Solar-driven electrocatalytic formation of hydrogen and syngas for downstream catalytic hydrogenation and hydroformylation reactions

Mina Anis Amin Ibrahim Meseha

Doctor of Philosophy

University of York

Chemistry

September 2019

Abstract

The aim of this thesis is to use solar driven electrocatalysis to produce hydrogen and hydrogen/carbon monoxide from water and water/carbon dioxide, respectively, to support downstream production of useful chemicals using catalytic hydrogenation and hydroformylation. Metal and metal phosphide electrocatalysts were investigated for the electrochemical reduction of CO_2 and water into CO and hydrogen, respectively. For the hydrogen evolution reaction, iron phosphide was prepared using two different methods: electroplating and spray-pyrolysis on carbon cloth (FeP/C). The catalytic activities of the two FeP/CC electrocatalysts were compared in terms of overpotential, Tafel slopes, stability and durability in acidic and neutral media. Both electrocatalysts were able to produce H_2 at a sufficient rate to support hydrogenation at room temperature and pressure.

Copper and copper phosphide electrocatalysts were used for the CO_2 reduction reaction. Copper based electrocatalyst were either based on Cu foils (commercial) or prepared by a novel 3D printing methodology followed by phosphidation. The electrochemical reduction of CO_2 using Cu_3P favoured proton reduction over CO_2 reduction. The water oxidation reaction occurred at a carbon plate in acidic media or using cobalt/phosphate (CoPi) on stainless steel in neutral media.

The electrocatalysts were used as part of a home built proof-of-principle solar powered reactor. The reactor was used to couple the electrocatalytic reactions with downstream catalytic reactions operating at room temperature and pressure. Two different catalytic systems were investigated: firstly the hydrogenation reaction of styrene using a commercially available catalyst Pd/C and secondly the hydroformylation of styrene using Rh/6-DPPon. Regarding the hydrogenation of styrene, the reactor succeeded in converting all the styrene (100 %) within 6 h. For hydroformylation a known catalyst system was used based on Rh/6-DPPon which operates in water under 1atm of H_2:CO. Several engineering and reaction issues emerged which primarily originated from the need to use a continuous flow of CO_2 that resulted in significant foaming and loss of substrate. Recommendations for overcoming these issues are presented in proposed future work.

Table of Contents

ABSTRACT 2
TABLE OF CONTENTS 3
LIST OF FIGURES 5
LIST OF SCHEME 13
LIST OF TABLES 13
ACKNOWLEDGEMENTS 14
DECLARATION 15
AIMS 16
1. INTRODUCTION 16
1.1. General considerations 16
1.2. General context and State-of-the-art 17
1.3. Hydrogen evolution reaction 21
  1.3.1. Thermodynamics and kinetics of hydrogen evolution reaction 23
  1.3.2. Transition metals volcano plot 26
  1.3.3. Preparations of iron phosphides 29
  1.3.4. State-of-the-art 31
1.4. Electrochemical reduction of CO_2 based on/ derived from copper binary compounds 35
  1.4.1. General considerations 38
  1.4.2. Beyond Bulk Monometallic Copper 42
  1.4.3. Copper Oxides and Monometallic Cu Derived from Copper Oxides 43
  1.4.4. Subsurface Oxides, Grain Boundaries, and Cu Oxidation State 46
  1.4.5. Copper chalcogenides (S and Se) modified or derived copper based electrocatalysts 50
  1.4.6. Electrocatalysts based on copper nitrides and phosphides 53
  1.4.7. Copper halide derived electrocatalysts and halide effects 54
1.5. 3D printing 56
  1.5.1. General mechanism of 3D printing through fused deposition modelling (FDM) 56
2. EXPERIMENTAL 59
2.1. Materials 59
2.2. Physical characterization 59
  2.2.1. The preparation of TEM samples 60
2.3. Hydrogen evolution reaction 60
  2.3.1. Preparations of FeP/CC electrocatalysts 60
  2.3.2. Electrochemical measurements for HER 62
  2.3.3. Quantification of hydrogen gas from HER 63
2.4. Electrochemical reduction of CO_2 64
  2.4.1. Copper phosphide foils 64
  2.4.2. 3D printing work 65
  2.4.3. Electrochemical measurements 67
  2.4.4. Quantification of gaseous and liquid products 70
2.5. Preparation of CoPi electrode 75
  2.5.1. Preparation of CoPi on stainless steel mesh 75
2.6. Catalysts 75
  2.6.1. Preparations of compounds 75
  2.6.2. Catalytic reactions 80
2.7. Solar powered reactor 81
  2.7.1. Reactor setup 81
  2.7.2. Reactor components 81
3. IRON PHOSPHIDE ELECTROCATALYSTS FOR HYDROGEN EVOLUTION REACTION; A COMPARISON STUDY IN ACIDIC AND NEAR NEUTRAL MEDIA 83

3.1. Results and Discussions 84
Physical characterization 84
3.1.1. Electrochemical measurements in acidic medium 91
3.1.2. Electrochemical performance in near neutral medium 99
3.1.3. Comments on the reproducibility of the results 105
3.1.4. Conclusions 105
4. ELECTROCHEMICAL REDUCTION OF CARBON DIOXIDE USING COPPER AND COPPER PHOSPHIDE ELECTROCATALYSTS; 3D PRINTING AS A NEW METHODOLOGY 107
4.1. Results and Discussion 108
4.1.1. Physical characterization of the Cu based electrodes 108
4.1.2. 3D ink development, printing and characterisation 118
4.1.3. Electrochemical characterisation and electrocatalysis of Cu based electrocatalysts 131
4.1.4. Electrochemical impedance measurements 151
4.2. Discussion 154
4.3. Conclusions 156
5. OXYGEN EVOLUTION REACTION 157
Introduction 157
5.2. Results and discussions 160
5.3. Conclusion 164
6. WATER-TOLERANT, LOW PRESSURE CATALYTIC HYDROGENATION AND HYDROFORMYLATION OF ALKENES 165
Aims 165
Abstract 165
6.2. Results and discussions 165
6.2.1. Preparation of Ru@MOF catalyst for the hydrogenation of alkenes ... 165
Introduction 165
6.3. Results and discussions 168
Physical characterization of MIL-101(SO3H) 168
6.3.1. Catalysis 170
6.4. Conclusions 177
7. MINI-CHEMICAL REACTOR 178
7.2. Mini-reactor components 178
7.3. Example of calculations for mini-reactor 179
7.4. Results and Discussion 180
7.4.1. Chemical reactor for hydrogenation reaction 180
7.4.2. Chemical reactor for hydroformylation reaction 185
7.4.3. Conclusions 185
8. CONCLUSIONS AND FUTURE WORK 186
8.1. The consumption of relatively low energy 186
8.2. Working with an electrocatalyst in aqueous media without using any sacrificial agents 188
8.3. Working under room temperature and atmospheric pressure 188
8.4. Catalysts for the hydrogenation and hydroformylation of styrene 188
8.5. The complementary oxidation reaction 189
8.6. Using solar panel. 189
8.7. Reactor experiments 190
APPENDIX-1 191
APPENDIX-2 200
APPENDIX-3 206
ABBREVIATION LIST 212
REFERENCES 213

List of Figures

Figure 1.1: Thermodynamic consideration of the proposed electrochemical reactions in water. CO2RR: CO_2 reduction reaction, HER: hydrogen evolution reaction, ORR: oxygen reduction reaction, HOR: hydrogen oxidation reaction and OER: oxygen evolution reaction.. 19
Figure 1.2: The suggested hydroformylation catalyst.[16].. 20
Figure 1.3: Skrydstrup's system. [17] 21
Figure 1.4: Typical water splitting system. 22
Figure 1.5: Schematic representation of three-electrode electrode cell.[37] 23
Figure 1.6: Schematic diagram illustrates the thermodynamics considerations for HER (A: activation energy, B overpotential and C Tafel plot).[42]............................ 24
Figure 1.7: Tafel plot.[37] 25
Figure 1.8: effects of charge transfer coefficient (α) on the symmetry of the electrochemical reaction barrier.[38].. 25
Figure 1.9: (Left) Volmer−Tafel and Volmer−Heyrovsky mechanisms on platinum electrodes [45] and (right) the Free energy diagram for HOR and HER processes at 0 V on Pt electrode in acidic medium (Volmer–Tafel pathway in red and Volmer–Heyrovsky pathway in blue). [54-56] 26
Figure 1.10: Exchange current density as a function of M-H bond strength (a) and of the calculated hydrogen chemisorption energy per atom (b).[57] 26
Figure 1.11: Summary of non-noble TM based electrocatalysts for HER in different pH media.[48]... 27
Figure 1.12: Polarization curves of iron phosphide prepared at different temperature.[70]... 28
Figure 1.13: Potentials phosphorus sources for phosphidation reactions. 30
Figure 1.14: Polarization curves of different iron phosphides prepared on FTO and their Tafel plots.[101] 32
Figure 1.15: Crystal structure of iron phosphide (a) Fe_2P and (b) FeP (Fe: red and orange, P: green).[100] 32
Figure 1.16: Molecular iron precursor for FeP nanoparticles.[102] 33
Figure 1.17: Free energy diagram based on theoretical studies.[104] 33
Figure 1.18: Polarization curves of P-Fe_2N/rGO (a) and Tafel plots (b).[106] 34
Figure 1.19: Examples of electrocatalytic CO2RRproducts reported in the literature.[39, 122-129] 36
Figure 1.20: prices of some carbon based compounds.[130] The prices of these products change on a daily basis depending on the markets. 37
Figure 1.21: A citation report by Web of science about electrochemical reduction of CO_2 with and without copper starting from 1990 to 2018. 37
Figure 1.22: Electocatalytic half reactions for general CO2RR............................... 38
Figure 1.23: Mechanism for the electrochemical reduction of CO_2 via two pathways:[145] The first one is pH dependent as reported by Norskov et al[147, 148] and the second pathway is pH independent as reported by Koper et al. [146] 39
Figure 1.24: Top: LSV of CO2RR using polycrystalline Cu, (below: Faradaic efficiencies of different products using polycrystalline Cu at each corresponding potential.[147] 40
Figure 1.25: Electrochemical performance of different transition metal toward CO2RR: (a) Volcano plot of partial current densities at -0.8 V vs CO binding strength and (b) the onset potentials vs CO binding energies for CO2RR and methane/methanol.[4]... 41
Figure 1.26: Geometric current densities for > $2e^-$ products using Au/Cu (bimetallic) and other reported Cu based electrocatalysts:[178] Cu, Au/Cu (bimetallic),[178] Cu/Pt(111) (overlayers),[179] Cu,[180, 181] Cu-Zn (bimetallic),[181] OD-Cu,[122] OD-Cu +

$PdCl_2$ (added to the electrolyte),[122] Cu(100),[182] Cu(100)-Ag (alloy),[182] Cu-Ni (alloy),[183] Fe/Cu(bimetallic)[184] and Ni/Cu (bimetallic).[184] 43
Figure 1.27: CO2RR performance of(a) chemical generation rate as a function of potential for Cu_2O derived inverse opals; (b) chemical generation rate as a function of potential for Cu particles, (c) carbon atom conversion rate as a function of voltage and (d) FE of all the products in 0.1 M $KHCO_3$.[196] 45
Figure 1.28: SEM images of Cu hollow fibre (a-e) and (f) Electrochemical system with Cu fibre as WE for CO2RR.[163] 46
Figure 1.29: The effect of oxygen percentage on the current densities and on FE% of C_2H_4 after 1 h of CO2RR at -1.0 V vs RHE in 0.1 M $KHCO_3$.[205] 47
Figure 1.30: Electron microscopic images of Cu nanoparticles (a-c), and OD-Cu-1 (d-f) and OD-Cu 2 (g-i) electrocatalysts: SEM images (a, d and g), low-magnification TEM images (b, e and h) and HRTEM (c, f and i).[209] 48
Figure 1.31: Energy profile of CO dimerization.[201] 48
Figure 1.32: Porbaix diagram with electrochemical performance of different Cu based electrocatalysts.[210] 49
Figure 1.33: In situ SEIRAS during CO2RR for (A) Cu foil and (B) SD-Cu.[216] 51
Figure 1.34: (a) LSV in 0.1 M $KHCO_3$ saturated with CO_2, (b) constant voltage experiments at -0.95 V RGE, (c)faradaic efficiencies of different products using core shell valence system and (d) FE% of alkene and alcohols from the different electrocatalysts at -0.95 V (RHE) in 0.1 M $KHCO_3$.[131] 52
Figure 1.35: FE% of each products using different electrocatalysts as a function of voltage, (b)FE% of multi-carbon products at -0.95 V (RHE), (c) geometric partial current densities of at different voltages on the electrocatalysts and (d) long term stability test.[220] 53
Figure 1.36: Relative ratio of Cu(I) during CO2RR at -0.95 V (RHE) in 0.1 M $KHCO_3$ (measured through a Cu K-edge XAS spectra).[220] 54
Figure 1.37: Electrochemical performance of reconstructed electrocatalyst toward CO2RR (a) the effect of H_2O_2 in the C_2H_4:CH_4 ratio, (b) FE% for CH_4 and C_2H_4 as a function of potentials, (c) LSV chart in 0.05 M $KHCO_3$ and (d) FE% of all C_{2+} products as function of voltages.[223] 55
Figure 1.38: (left) LSV of CO2RR upon using different electrolyte solution and (right) SEM images showing the role of the iodide on the morphology.[225] 56
Figure 1.39: mechanism of 3D printing using a filament.[231] 57
Figure 1.40: SEM images of Cu hollow fibre (a-e) and (f) Electrochemical system with Cu fibre as WE for CO2RR.[163] 57
Figure 1.41: Woodpile heterogeneous Cu/Al_2O_3 based catalyst.[228] 58
Figure 1.42: (a) optical and (b) SEM images of the 3D printed microbattery after annealing.[229] 58
Figure 2.1: Iron oxides prepared by (a) electroplating (FeOOH) and (b) spray-pyrolysis (Fe_2O_3). 61
Figure 2.2: Spray-pyrolysis setup. 61
Figure 2.3: (a) blank carbon cloth, FeP/CC electrocatalysts prepared by (b) electroplating and (c) spray-pyrolysis. 62
Figure 2.4: Calibration of Ag/AgCl (3.0 M NaCl) reference electrode. 63
Figure 2.5: Calibration of GC response to hydrogen gas. 64
Figure 2.6: 3D printed Cu based electrocatalysts. 65
Figure 2.7: 3D printing process: a) 3D printer stage, b) 3D printed Cu electrocatalyst, c) Syringe barrel filled with Cu based ink and d) 3D printer head... 66
Figure 2.8: Custom-made electrochemical cell: a) 1/4″ glass tubing as inlet for CO_2 and outlet to the GC, b) Luggin capillary for reference electrode, c) plastic cap, d) Keck clip, e) plastic screws, f) Cu wire connected to crocodile clips, g and k) the cell holder, h and j) the electrochemical cell glass body and i) Rubber gasket for Nafion membrane. 69

Figure 2.9: A representative ^1H NMR spectrum for characterization of the electro produced liquid hydrocarbons by the water suppression method. 70
Figure 2.10: GC analysis parameters.. 71
Figure 2.11: Typical chromatogram resulted from the FID detector....................... 72
Figure 2.12: Calibration curves of (a) H_2, (b) CO, (c) CH_4, (d) C_2H_4 and (e) C_2H_6 (The retention time of hydrogen gas based on TCD detector's chromatogram and the other gases based on FID dectector's chromatograms). 73
Figure 2.13: Farnell's solar panel... 81
Figure 2.14: (left) a diagram of the mini-reactor components and (right) real components of the reactor; (a) solar panel, (b) electrochemical cell, (c) catalysis vessel and (d) bubbler. 82
Figure 3.1: XRD patterns of different films prepared by (a) electroplating and (b) spray pyrolysis methods together with literature patterns for FeP, Fe_2O_3 and FeOOH taken from Inorganic Crystal Structure Database (ICSD). Red circles belong to Fe (ICSD # 44863).. 85
Figure 3.2: SEM images of the top-view of (a) Blank CC, (b) FeP/CC prepared by spray pyrolysis and (c) FeP/CC prepared by electroplating.................................. 86
Figure 3.3: Elemental mapping of the top-view of the FeP/CC electrocatalyst prepared by electroplating (a) SEM image (b) distribution of P measured by the (K-shell) and (c) distribution of Fe measured by (K-shell). 86
Figure 3.4: Elemental mapping of the top-view of the FeP/CC electrocatalyst prepared by spray-pyrolysis (a) SEM image (b) distribution of P measured by the (K-shell) and (c) distribution of Fe measured by the (K-shell). 87
Figure 3.5: EDX spectrum of FeP/CC prepared by electroplating (%Fe was 47.91 % and %P was 52.09%). 87
Figure 3.6: EDX spectrum of FeP/CC prepared by spray-pyrolysis (%Fe was 52.48 % and %P was 47.52%). 87
Figure 3.7: SEM of the cross-section of FeP/CC electrocatalyst prepared by spray-pyrolysis on carbon cloth fibres.. 88
Figure 3.8: Elemental mapping of the cross-section of FeP/CC prepared by spray-pyrolysis; (a) SEM image, (b) distribution of P measured by the (K-shell) and (c) distribution of Fe (K-shell).. 88
Figure 3.9: TEM of FeP/CC prepared by electroplating; a and b TEM images of the FeP particles on the carbon cloth, c: diffraction resulted from FeP particles and d: HRTEM image.. 89
Figure 3.10: TEM of FeP/CC prepared by spray-pyrolysis; a and b TEM images of the FeP particles on the carbon cloth, c: diffraction resulted from FeP particles and d: HRTEM image. 90
Figure 3.11: The diffraction of carbon cloth.. 90
Figure 3.12: LSV of FeP/CC electrocatalysts prepared by the two methods; electroplating (black) and spray-pyrolysis (red) in 0.5 M H_2SO_4 with a scan rate of 5 mV/s. 91
Figure 3.13: LSV of Iron oxides prepared via the two methods in 0.5 M H_2SO_4 with a scan rate of 5 mV/s... 92
Figure 3.14: Tafel plots of the electrocatalysts derived from the LSV curves in 0.5 M H_2SO_4. 93
Figure 3.15: EIS of blank CC at η_{10} = - 10 mV/cm^2 in 0.5 M H_2SO_4. 94
Figure 3.16: EIS of FeP/CC prepared by electroplating method at η_{10} = - 10 mV/cm^2 in 0.5 M H_2SO_4.. 94
Figure 3.17: EIS of FeP/CC prepared by spray-pyrolysis method at η_{10}= -10 mV/cm^2 in 0.5 M H_2SO_4.. 95
Figure 3.18: Equivalent one-time-constant circuit used to fit the EIS data of the two electrocatalysts.. 95
Figure 3.19: Double layer capacitance measurements of blank CC; the curves were taken in non-faradaic region in 0.5 M H_2SO_4... 95

Figure 3.20: Double layer capacitance measurements of FeP/CC prepared by electroplating method; the curves were taken in non-faradaic region in 0.5 M H_2SO_4. 96
Figure 3.21: Double layer capacitance measurements of FeP/CC prepared by spray-pyrolysis; the curves were taken in non-faradaic region in 0.5 M H_2SO_4....... 96
Figure 3.22: Stability test for the two FeP/CC electrocatalysts in 0.5 M H_2SO_4....... 97
Figure 3.23: Durability of FeP/CC prepared by electroplating in 0.5 M H_2SO_4 at a scan rate of 5 mV/sec before and after 3000 cycles at a scan rate of 100 mV/sec between +0.1 and -0.1 V (vs. RHE). 98
Figure 3.24: Durability of FeP/CC prepared by spray pyrolysis method in 0.5 M H_2SO_4 at a scan rate of 5 mV/sec before and after 3000 cycles at a scan rate of 100 mV/sec between +0.1 and -0.1 V (vs. RHE). 98
Figure 3.25: LSV of FeP/CC electrocatalysts prepared by the two methods; electroplating (black) and spray-pyrolysis (red) in 0.1 M phosphate buffer. 99
Figure 3.26: Tafel plot of the two FeP/CC electrocatalysts in 0.1 M KPi. 100
Figure 3.27: EIS of blank CC at η_{10}= - 10 mV/cm^2 in 0.1 M KPi. 101
Figure 3.28: EIS of FeP/CC prepared by electroplating method at η_{10}= - 10 mV/cm^2 in 0.1 M KPi. 101
Figure 3.29: EIS of FeP/CC prepared by spray-pyrolysis method at η_{10}= - 10 mV/cm^2 in 0.1 M KPi. 101
Figure 3.30: Stability test for the two FeP/CC electrocatalysts in 0.1 M KPi. 102
Figure 3.31: LSV curves for FeP/CC prepared by electroplating in 0.1 M phosphate buffer at a scan rate of 5 mV/sec before and after 3000 cycles at a scan rate of 100 mV/sec between +0.1 and -0.1 V (vs. RHE). 103
Figure 3.32: LSV curves for FeP/CC prepared by spray pyrolysis in 0.1 M phosphate buffer at a scan rate of 5 mV/sec before and after 3000 cycles at a scan rate of 100 mV/sec between +0.1 and -0.1 V (vs. RHE). 103
Figure 3.33: Quantification of H_2 gas for FeP/CC electrocatalyst prepared via electroplating in 0.5 M H_2SO_4. 104
Figure 3.34: Quantification of H_2 gas for FeP/CC electrocatalyst prepared via spray-pyrolysis in 0.5 M H_2SO_4. 104
Figure 3.35: Quantification of H_2 gas for FeP/CC electrocatalyst prepared via electroplating in 0.1 M KPi. 104
Figure 3.36: Quantification of H_2 gas for FeP/CC electrocatalyst prepared via spray-pyrolysis in 0.1 M KPi. 105
Figure 4.1: XRD patterns for the copper foil after electropolishing. 108
Figure 4.2: SEM images of Cu foil before (a-c) and (d-f) after electropolishing. ... 109
Figure 4.3: XRD patterns for the Cu_2O/Cu foil before electrochemical reduction of the oxides. Blue balls belong to Cu peaks and red balls belong to Cu_2O. 110
Figure 4.4: SEM images of the copper foils: (a-c) Cu_2O/Cu foil and (d-f) OD-Cu foil before electrochemical measurements. 111
Figure 4.5: Elemental mapping of the OD-Cu foil, (a) SEM of top-down OD-Cu foil, (b) the distribution of oxygen and (c) the distribution of Cu measured by the K-shell absorption. 112
Figure 4.6: XRD patterns for the electropolished Cu, Cu_2O/Cu foil before electrochemical reduction of the oxides and Cu_3P/Cu foil. Red balls: Cu, blue balls: Cu_2O and green balls: Cu_3P. 113
Figure 4.7: SEM of Cu_3P/Cu foil before electrochemical measurements. 114
Figure 4.8: SEM images of the cross-section of Cu_3P films on the sides of the Cu foil. 115
Figure 4.9: EDX spectrum of the 3D printed Cu_3P/Cu foil before electrochemical measurements (%Cu was 89.69% and %P was 10.31 %). 115
Figure 4.10: Elemental mapping of the the Cu_3P/Cu foil before electrochemistry. (a) SEM of top-down of the Cu_3P/Cu foil, (b) the distribution of oxygen, (c) the

distribution of phosphorous and (d) the distribution of Cu measured by the K-shell absorption. 116
Figure 4.11: Elemental mapping of the cross-section of the Cu_3P/Cu foil. (a) SEM of cross-section of the Cu_3P/Cu foil, (b) the distribution of silicon, (c) the distribution of phosphorous and (d) the distribution of Cu measured by the K-shell absorption (Sample was sandwiched between two Si plates). 116
Figure 4.12: TEM of Cu_3P foil; a and b: low magnification TEM images of the Cu_3P film, c: diffraction resulted from Cu_3P film and d: HRTEM image. 117
Figure 4.13: X-ray photoelectron spectroscopy (XPS) characterizations of Cu_3P/Cu foil before electrochemical measurements: (a) Cu 2p, (b) P 2p and (c) O 1s regions. 118
Figure 4.14: The structure/shape of the proposed Cu based electrocatalyst. 119
Figure 4.15: XRD patterns of the 3D printed OD-Cu electrode before the electrochemical measurements. Red circles belong to Cu peaks and blue circles for Cu_2O peaks. 120
Figure 4.16: (a-c) SEM images of the top-down view of the 3D printed OD-Cu electrode before electrochemical measurements. 121
Figure 4.17: Elemental mapping of the top-down view of the 3D printed OD-Cu. (a) SEM of top-down view of 3D printed OD-Cu before electrochemical measurements, (b) the distribution of oxygen and (c) Cu measured by the K-shell absorption. 122
Figure 4.18: Elemental mapping of the top-down view of the 3D printed OD-Cu after electrochemical measurements. (a) SEM of top-down view of the 3D printed OD-Cu (top-left), the distribution of oxygen, (b) the distribution of phosphorous and (c) the distribution of Cu measured by the K-shell absorption. 122
Figure 4.19: SEM image of the cross section of 3D printed OD-Cu electrocatalyst before electrochemical measurements (thickness of the electrocatalyst lies between 975 μm and 789 μm). 123
Figure 4.20: Elemental mapping of the cross-section view of 3D OD-Cu electrocatalyst before electrochemical measurements. (a) SEM images of the 3D OD-Cu electrocatalyst before electrochemical measurements, (b) the distribution of oxygen, (c) Si (below-left) and (d) the distribution of Cu measured by the K-shell absorption (sample was sandwiched between two Si plates for SEM scanning). 123
Figure 4.21: EDX spectrum of the 3D printed OD-Cu before electrochemistry (%Cu was 89.40% and %O was 10.60 %). 124
Figure 4.22: TEM images of 3D printed of OD-Cu electrocatalyst. 124
Figure 4.23: X-ray photoelectron spectroscopy (XPS) characterizations of the 3D printed OD-Cu electrocatalyst before electrochemical measurements: (a) Cu 2p and (b) O 1s regions. 125
Figure 4.24: XRD patterns of the 3D printed PD/OD-Cu electrode before the electrochemical measurements. Red circles belong to Cu peaks and green squares belong to Cu_3P. 126
Figure 4.25: (a-c) SEM images of the 3D printed PD/OD Cu electrode before electrochemical measurements. 127
Figure 4.26: Elemental mapping of the top-view of the 3D printed PD/OD Cu electrode before electrochemical measurements. (a) SEM image of the 3D printed PD/OD-Cu electrode, (b) the distribution of phosphorous and (c) the distribution of Cu measured by the K-shell absorption. 128
Figure 4.27: SEM image of the cross-section of the 3D printed PD/OD-Cu electrode. 128
Figure 4.28: Elemental mapping of the cross-section view of the 3D printed PD/OD-Cu electrode. (a) SEM image of 3D printed the 3D printed PD/OD-Cu electrocatalyst, (b) the distribution of phosphorous and (c) Cu (below-left) measured by the K-shell absorption. 129
Figure 4.29: EDX spectrum of the 3D printed PD/OD Cu electrode before electrochemical measurements (%Cu was 84.10 % and %P was 15.90 %). 129

Figure 4.30: TEM images of the 3D printed PD/OD-Cu electrode before electrochemistry: a,b) low magnification TEM images, c) diffraction and d) HETEM image. 130
Figure 4.31: X-ray photoelectron spectroscopy (XPS) characterizations of the 3D printed PD/OD-Cu (before the electrochemical reduction of Cu_3P layer): (a) Cu 2p, (b) P 2p and (c) O 1s regions. 131
Figure 4.32: LSVs of Electropolished Cu foil in 0.1 M $KHCO_3$ saturated by N_2 and CO_2 with a scan rate of 20 mV/s. 132
Figure 4.33: CAs experiments of electropolished Cu foil in 0.1 M $KHCO_3$ saturated by CO_2. 132
Figure 4.34: Current efficiencies % of all the detected products through CO2RR by the electropolished Cu foil. 133
Figure 4.35: LSVs of OD-Cu foil in 0.1 M $KHCO_3$ saturated by N_2 and CO_2 with a scan rate of 20 mV/s. 134
Figure 4.36: CA experiments of OD-Cu foil in 0.1 M $KHCO_3$ saturated by CO_2. 134
Figure 4.37: Measurement of the capacitance of the OD-Cu foil under N_2 in 0.1 M $KHCO_3$. 135
Figure 4.38: Current efficiencies % of all the detected products through CO2RR by the OD-Cu foil. 135
Figure 4.39: LSVs of Cu_3P/Cu foil in 0.1 M $KHCO_3$ saturated by N_2 and CO_2 with a scan rate of 20 mV/s. 136
Figure 4.40: Measurement of the capacitance of the Cu_3P/Cu foil under N_2 in 0.1 M $KHCO_3$. 136
Figure 4.41: CA experiments of Cu_3P/Cu foil in 0.1 M $KHCO_3$ saturated by CO_2. 137
Figure 4.42: Current efficiencies % of all the detected products through CO2RR by the Cu_3P/Cu foil. 137
Figure 4.43: XRD patterns of the Cu_3P/Cu foil before and after electrochemical measurements (CA). Red balls belong to Cu peaks and green squares belong to Cu_3P. 138
Figure 4.44: X-ray photoelectron spectroscopy (XPS) characterizations of Cu_3P/Cu foil after electrochemical measurements: (a) Cu 2p, (b) P 2p and (c) O 1s regions. 139
Figure 4.45: SEM images of the Cu_3P/Cu foil before (a-c) and after (d-f) electrochemistry. 140
Figure 4.46: LSVs of the 3D printed OD-Cu electrode in 0.1 M $KHCO_3$ saturated by N_2 and CO_2 with a scan rate of 20 mV/s. 141
Figure 4.47: Measurement of the capacitance of the 3D printed OD-Cu electrode under N_2 in 0.1 M $KHCO_3$. 141
Figure 4.48: CA experiments of the 3D printed OD-Cu electrocatalyst in 0.1 M $KHCO_3$ saturated by CO_2. 142
Figure 4.49: Current efficiencies % of all the detected products through CO2RR by the 3D printed OD-Cu electrocatalyst. 143
Figure 4.50: XRD patterns of the 3D printed OD-Cu electrode before and after electrochemistry. Red balls belong to Cu peaks and blue triangles for Cu_2O peaks. 144
Figure 4.51: X-ray photoelectron spectroscopy (XPS) characterizations of the 3D printed OD-Cu electrocatalyst after electrochemical measurements: (a) Cu 2p and (b) O 1s regions. 144
Figure 4.52: SEM images of the top-down view of the 3D printed OD-Cu electrode before (a-c) and after (d-f) electrochemical measurements. 145
Figure 4.53: LSVs of the 3D printed PD/OD Cu electrode in 0.1 M $KHCO_3$ saturated by N_2 and CO_2 with a scan rate of 20 mV/s. 146
Figure 4.54: Measurement of the capacitance of the 3D printed PD/OD-Cu electrode under N_2 in 0.1 M $KHCO_3$. 146

Figure 4.55: CA experiments of the 3D printed PD/OD-Cu electrode in 0.1 M $KHCO_3$ saturated by CO_2. 147
Figure 4.56: Current efficiencies % of all the detected products through CO2RR by the 3D printed PD/OD-Cu electrocatalyst. 147
Figure 4.57: XRD patterns of the 3D printed PD/OD-Cu electrode before and after electrochemistry. Red balls belong to Cu peaks, green squares belong to Cu_3P and blue triangles for Cu_2O peaks. 148
Figure 4.58: X-ray photoelectron spectroscopy (XPS) characterizations of 3D printed PD/OD-Cu electrocatalyst after the electrochemical measurements: (a) Cu 2p, (b) P 2p and (c) O 1s regions. 149
Figure 4.59: SEM images of the 3D printed PD/OD Cu electrode before (a-c) and after (d-f) electrochemical measurements. 150
Figure 4.60: EIS spectra of electropolished Cu foil in 0.1 M $KHCO_3$ saturated by CO_2. 152
Figure 4.61: EIS spectra of OD-Cu foil in 0.1 M $KHCO_3$ saturated by CO_2. 152
Figure 4.62: EIS spectra of Cu_3P/Cu foil in 0.1 M $KHCO_3$ saturated by CO_2. 152
Figure 4.63: EIS spectra of the 3D printed OD-Cu electrocatalyst in 0.1 M $KHCO_3$ saturated by CO_2. 153
Figure 4.64: EIS spectra of the 3D printed PD/OD-Cu electrocatalyst in 0.1 M $KHCO_3$ saturated by CO_2. 153
Figure 4.65: The equivalent electric circuit used for fitting the EIS data; R: resistance and Q: constant phase element. 153
Figure 5.1: Structural models for CoPi (a) Edge-sharing molecular cobaltate cluster (MCC) of CoPi films deposited at 1.1 V (surface). Bridging oxo/hydroxo ligands are shown in red, and non-bridging oxygen ligands (including water, hydroxide, and phosphate, light red) complete the octahedral coordination geometry of each peripheral Co ion (blue). (b) Corner-sharing model for surface, (c) edge-sharing MCC for bulk CoPi and (d) Corner-sharing model for CoPi bulk. [268] 158
Figure 5.2: Structural sketch of CoPi films.[269] 158
Figure 5.3: (a) Cyclic voltammogram in 0.1 M KPi electrolyte at pH 7.0 with 0.5 mM Co^{2+} present on SS (b) CA experiment in 0.1 M KPi electrolyte at pH 7.0 containing 0.5 mM at 1.1 V (Ag/AgCl). 160
Figure 5.4: SEM images of CoPi/SS (a-c) and CoPi/CC (d-f). 161
Figure 5.5: EDX spectrum of CoPi/SS (% Co: 1.32 %, % Fe: 89.56 %, % K: 0.76 %, % O: 7.20 % and % P: 1.16 %). 161
Figure 5.6: (a) SEM of the top-down of CoPi/SS), (b) the distribution of O, (c) the distribution of P, (d) the distribution of K, (e) the distribution of Fe and (f) the distribution of Co by the K-shell absorption. 162
Figure 5.7: LSV of carbon cloth in 0.5 M H_2SO_4 at scan rate of 20 mV/s. 163
Figure 5.8: LSV of carbon plate in 0.5 M H_2SO_4 at scan rate of 20 mV/s. 163
Figure 5.9: LSV of CoPi/SS and blank carbon cloth in 0.1 M KPi (pH=6.63) at scan rate of 20 mV/s. 163
Figure 5.10: LSV of CoPi/SS plate in 0.1 M $KHCO_3$. 164
Figure 6.1: Structures of (a) MIL-101(SO3H) pores, (b) their pore apertures, and (c) Wilkinson's catalyst.[240] 167
Figure 6.2: Interaction between Crabtree's catalyst (blue sphere) and sulfonated MIL-101(Cr) (1-SO3Na, cube) by exchange of the charge-balancing Na^+ cations (red sphere).[241] 167
Figure 6.3: Structures of $[CpRu(PTA)_2Cl]$ complex and PTA ligand. 168
Figure 6.4: $[CpRu(PTA)_2Cl]$ complex's dimensions.[243] 168
Figure 6.5: XRD pattern of MIL-101(SO3H). 169
Figure 6.6: TGA of all MOFs. 169
Figure 6.7: Hydrogenation of styrene using [Ru@MOF] catalyst under H_2 balloon. 171

Figure 6.8: ^{1}H-NMR (MeOD-d_4) spectrum of products of hydrogenation of styrene under 1 atm of H_2 gas (Balloon). 172
Figure 6.9: ^{1}H-NMR (MeOD-d_4) spectrum of products of hydrogenation of styrene under 1 atm of H_2 gas (balloon) for 4 h. 172
Figure 6.10: ^{1}H-NMR ($CDCl_3$) of products of the hydroformylation reaction of styrene under 1 atm of syngas under standard conditions. 174
Figure 6.11: ^{1}H-NMR spectrum of products hydroformylation reaction of styrene under CO/H_2 and CO_2 balloons for 20 h. 175
Figure 6.12: ^{1}H-NMR ($CDCl_3$) spectrum of products hydroformylation reaction of styrene under CO_2 and CO/H_2 balloons for 8 h in 3% (wt%) of PTS/H_2O. 175
Figure 6.13: ^{1}H-NMR ($CDCl_3$) spectrum of products hydroformylation reaction of styrene under CO_2 and CO/H_2 balloons for 8 h in 3% (wt%) of PTS/H_2O in addition to silicon antifoam. 176
Figure 7.1: (left) a diagram of the mini-reactor components and (right) real components of the reactor; (a) solar panel, (b) electrochemical cell, (c) catalysis vessel and (d) bubbler. 179
Figure 7.2: ^{1}H-NMR (MeOD-d_4) spectrum of the product of hydrogenation of styrene using the mini-reactor for 4 h (≈34 mA/cm^2) powered by solar panel. 181
Figure 7.3: Electrochemical parameters (cell voltage and current) for the solar powered reactor in 0.5 M H_2SO_4. 182
Figure 7.4: ^{1}H-NMR (MeOD-d_4) spectrum of products hydrogenation reaction of styrene under using the mini-reactor for 6 h (≈31 mA/cm^2) powered by solar panel in 0.5 M H_2SO_4. 183
Figure 7.5: Electrochemical parameters (cell voltage and current) for the solar powered reactor in 0.1 M KPi. 184
Figure 7.6: ^{1}H-NMR (MeOD-d_4) spectrum of products hydrogenation reaction of styrene using the mini-reactor for 6 h (≈31 mA/cm^2) powered by solar panel. 184
Figure A2.1: ^{31}P-NMR spectrum of triphenylphosphine in C_6H_6. 200
Figure A2.2: ^{1}H-NMR spectrum of 2-tert-butoxy-6-chloro-pyridine (1) in $CDCl_3$. 200
Figure A2.3: ^{13}C-NMR spectrum of 2-tert-butoxy-6-chloro-pyridine (1) in $CDCl_3$. . 201
Figure A2.4: ^{1}H-NMR spectrum of 2-tert-butoxy-6-diphenylphosphanyl-pyridine (2) in C_6D_6. 201
Figure A2.5: ^{13}C-NMR spectrum of 2-tert-butoxy-6-diphenylphosphanyl-pyridine (2) in C_6D_6. 202
Figure A2.6: ^{31}P-NMR spectrum of 2-tert-butoxy-6-diphenylphosphanyl-pyridine (2) in C_6D_6. 202
Figure A2.7: ^{1}H-NMR spectrum of 6-diphenylphosphanyl-1H-pyridin-2-one (6-DPPon) (3) in $CDCl_3$. 203
Figure A2.8: ^{13}C-NMR spectrum of 6-diphenylphosphanyl-1H-pyridin-2-one (6-DPPon) (3) in $CDCl_3$. 203
Figure A2.9: ^{31}P-NMR spectrum of 6-diphenylphosphanyl-1H-pyridin-2-one (6-DPPon) (3) in $CDCl_3$. 204
Figure A2.10: ^{1}H-NMR spectrum of [Rh(CO)$_2$(acac)] in $CDCl_3$. 204
Figure A2.11: ^{13}C-NMR spectrum of [Rh(CO)$_2$(acac)] in $CDCl_3$. 205
Figure A2.12: IR spectrum of [Rh(CO)$_2$(acac)] in hexane. 205
Figure A3.1: Schematic diagram of CO2RR in water in absence (solid) and presence (dashed) of electrocatalyst.[380] 206
Figure A3.2: Current density-voltage curve of electrolyser able to produce CO (cathode) and O_2 (anode) including limiting factors (kinetic, ohmic and mass transport limitations).[381] 207
Figure A3.3: Randles circuit and its Nyquist plot. 209
Figure A3.4: Distribution species diagram of carbonate species as a function of pH.[386] 210
Figure A3.5: ^{1}H NMR spectrum upon using $^{13}CO_2$.[390] 211

List of Scheme

Scheme 1-1: Hydrogenation and hydroformylation reactions of styrene................ 19
Scheme 2-1: Preparation of (6-DPPon) ligand according to literature.[15, 16]............ 76
Scheme 2-2: Preparation of [Rh(CO)$_2$(acac)] to literature.[239]................................ 78
Scheme 2-3: Preparation of [CpRu(PTA)$_2$Cl) complex.[244] 79

List of Tables

Table 1-1: The abundance of several elements in Earth's crust. [90] 29
Table 1-2: Different methods for phosphidation reaction and their conditions. 30
Table 2-1: Retention times for all gases based on FID detector's chromatograms. [a]composition of the standard gas mixture used for the calibration curves of the gases, [b]based on TCD detector's chromatograms. 71
Table 2-2: Technical specifications of the solar panel. 81
Table 3-1: EIS data of the FeP/CC electrocatalysts prepared by electroplating and spray-pyrolysis methods in acidic medium (0.5 M H_2SO_4).................................... 94
Table 3-2: EIS data of the FeP/CC electrocatalysts prepared by electroplating method and by spray-pyrolysis in 0.1 M phosphate buffer. 100
Table 4-1: Capacitance and roughness factor measurements of the Cu foils in 0.1 M $KHCO_3$ under N_2. 112
Table 4-2: Current efficiencies of all the products using different copper based electrocatalysts in 0.1 M $KHCO_3$ saturated with CO_2.. 133
Table 4-3: Capacitance and roughness factor measurements of the 3D printed Cu electrocatalyst in 0.1 M $KHCO_3$ under N_2. 142
Table 4-4: Current efficiencies of all the products using different electrocatalysts and the total current densities in 0.1 M $KHCO_3$ saturated with CO_2. 142
Table 4-5: EIS data of all Cu based electrocatalysts foils in 0.1 M $KHCO_3$ saturated by CO_2. 154
Table 5-1: Different non-noble electrocatalysts for OER in acidic and neutral media[270]. 159
Table 6-1: Elemental analysis of each MOF ([a] from CHN, S elemental analysis). 170
Table 6-2: BET surface area measurements of all prepared MOFs. *reported by Rosseinsky et al.[241] 170
Table 6-3: Summary of the results of the two hydrogenation reaction systems.... 171
Table 6-4: Summary of the results of the two hydroformylation systems............. 173
Table 7-1: Summary of the results of the two hydrogenation reaction systems.... 181
Table 7-2: Summary of the results of the two hydroformylation systems............. 185
Table A1.1: Possible half-reactions of electrochemical reduction of CO_2. 191
Table A1.2: Different electrocatalysts for hydrogen evolution reaction in 0.5 M H_2SO_4. 193
Table A1.3: Reported data of different electrocatalysts for hydrogen evolution reaction in neutral solution. 194
Table A1.4: Reported Copper based electrocatalysts for CO2RR. 196

Acknowledgements

I would like to express my deep gratitude to Dr Richard E. Douthwaite and Prof Robin N. Perutz, my research supervisors, for their patient guidance, support, enthusiastic encouragement and useful critiques of this research work. Also my IPM Dr Alison Parkin for her guidance and useful discussions during the TAP meetings.

I am profoundly grateful to Dr Ben Coulson and Dr Joyashish Debgupta for their help and fruitful discussions. I would like to thank my labmates Khanittha Walaijai, Thorsten Dreher, William Swansborough-Aston, Dr Barbara Procacci and all the current and former RED and RNP group members.

My sincere thanks Dr Jon Barnard for his time and help with microscopy work at the nanocentre and to Dr Martyn Ward for his valuable help and support with the GC analyses. I would like to acknowledge the assistance of Dr Naser Jasim, Dr Emma Dux, Dr Adrian Whitwood, Dr Heather Fish and Dr Alexander Heyam for training, technical support and advice.

My research would have been impossible without the aid, brilliant work and support of Mrs Abigail Mortimer, Mr Chris Rhodes, Mr Stuart Murray, Mr Timothy Ayers and Mr Mark Roper.

Finally, I wish to thank my mother and my brothers for their support and encouragement throughout my study.

Declaration

The research presented in this thesis was carried out at the University of York between September 2015 and September 2019. This work is, to the best of my knowledge, original and my own, except for the following:

1- TEM images were taken by Dr Jon Barnard.
2- XPS analyses and the data fitting were performed by Harwell XPS facility.
3- Elemental Analyses were performed by Dr Graeme McAllister.
4- TGA analysis was performed by Dr Emma Dux.

This thesis has not been submitted for any other degree at this or any other University.

Mina Meseha

Aims

The current project aims to demonstrate the proof of principle of complex chemical synthesis using only solar energy as the energy input via:

1- Generation of solar electricity using a commercial photovoltaic.
2- The electrocatalytic production of H_2 using FeP supported on carbon cloth.
3- The electroreduction of CO_2 to CO using copper based electrodes:
    a. Fabricated by 3D printing.
    b. Based on Cu_3P/Cu.
4- The preparation of CoP_i supported on a stainless steel electrode for the complementary water oxidation reaction in neutral medium.
5- Thermal catalytic hydrogenation and hydroformylation of alkenes (styrene).
6- Coupling of the electrocatalytic and thermal catalytic system within a mini-chemical reactor powered only by solar energy.

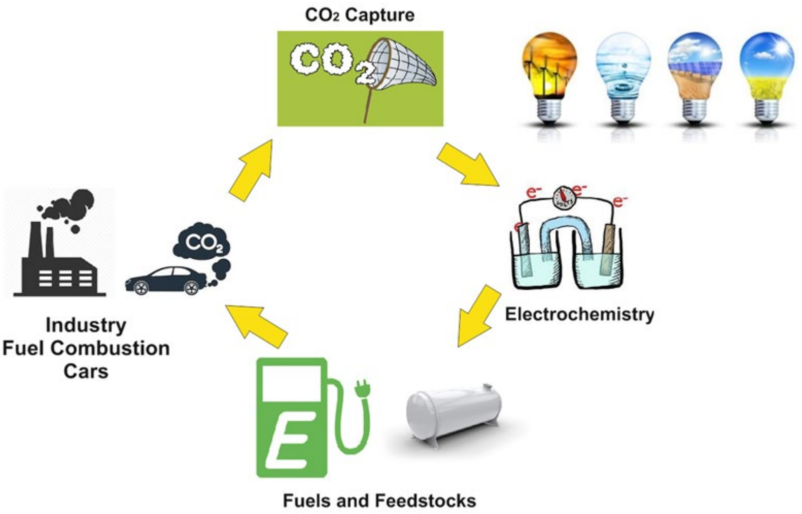

1. Introduction

1.1. General considerations

The ultimate goal of the work described in this thesis is to use solar energy and water/CO_2 as feedstocks for the production of useful chemicals. The methodology chosen in this thesis was to use PV-driven electrocatalysis of water/CO_2 to produce H_2 or H_2/CO (syngas) for catalytic hydrogenation and hydroformylation of alkenes, respectively. In order to increase the practicality of the reactor we wished to avoid the use of precious metal elements in electrochemical and thermal reactions and to use water as a reaction medium. Additional considerations include **i)** the use of a suitable electrode/electrocatalyst for the complementary oxidation of water to dioxygen that also functions in neutral media,

ii) the need to generate reduction products (H_2 and H_2/CO) at a sufficient rate to support the thermal catalysis, **iii)** the thermal catalytic reactions need to be tolerant to water (and CO_2 for hydroformylation) and probably oxygen to be compatible with aqueous electrocatalysis. In addition, hydrogenation chemistry can be performed in a closed system, whereas a continuous flow system is required to continually introduce CO_2 for H_2/CO production. Therefore in the absence of sophisticated pressure engineering, the thermal catalytic chemistry has to occur at an appreciable rate (hour timescale) at low overpressure (ca. 1 atm). These are a very demanding set of criteria.

Various electrocatalysts and thermal catalysts were considered and partially investigated. To generate sufficient reduction products > 1000 C of charge is required to support catalysis on the mmol scale over several hours **(Chapter 7 for further details p.178)**. Generally, commercial electrolysers usually work with 70% efficiency and current densities above 200 mA/cm^2. [1] This requirement limits the selection of electrocatalysts and effectively rules out homogeneous metal complex electrocatalysts that tend to support much lower currents and are prone to degradation on the required timescale. We therefore concentrated our efforts on inorganic catalysts that can support high current/current density and have sufficient stability over at least several hours.

1.2. General context and State-of-the-art

Extensive efforts have been made to find efficient and active catalysts for the electrochemical reduction of protons and carbon dioxide into hydrogen and carbon monoxide, respectively. These efforts have concentrated on the use of metal complexes and compounds such metalloporphyrins, pure transition metals and their oxides, carbides, phosphides, and sulphides.[2-6] Most ongoing studies are focused on the production of these gases without showing the ability of the system to be used in the real word. Independently, several researchers are focusing on improving and designing novel catalytic systems for hydrogenation, hydroformylation, cross coupling and other applications, which can be performed under low pressure or are tolerant to water and/or oxygen. The question is can we produce hydrocarbons from CO_2 directly or indirectly? There are a few potential pathways such as the direct production of hydrocarbons through electrocatalytic and photocatalytic based systems. Each of them have several advantages but using them on an industrial scale is far from certain. For any application to be applied on an industrial scale, it needs to be economic, requiring high efficiency, easy scale-up, and have a long life time. For photocatalytic systems, sun light is the source of energy while for electrocatalytic systems, other renewable sources can be used to avoid CO_2 emissions. In the current project, two mini-reactors were designed and built, which are powered by solar panels. The electrocatalytic electrodes were prepared from inexpensive earth abundant elements; FeP/C and Cu based for reductions and C and CoPi electrodes for the complementary oxidation reactions. The electroproduced gases (CO/H_2), either hydrogen or a syngas mixture were to be used directly in subsequent catalytic hydrogenation or hydroformylation reactions, respectively. For electrocatalysis, the thermodynamic considerations **(Figure 1.1)** for all the electrochemical reactions included within the project are summarized in following equations:

The cathodic (reduction) reactions:

$$2H^+ + 2e^- \rightarrow H_2, \qquad E^o = 0.0\,V$$

$$CO_2 + 2H^+ + 2e^- \rightarrow \mathrm{CO} + H_2O, \qquad E^o = -0.51\,V$$

$$CO_2 + 2H^+ + 2e^- \rightarrow \mathrm{HCOOH}, \qquad E^o = -0.61\,V$$

The anodic (oxidation) reaction:

$$H_2O \rightarrow 2H^+ + 2e^- + 1/2\,O_2, \qquad E^o = 1.23\,V$$

To operate under low energy demand, an electrocatalyst should work efficiently at low overpotential ($\eta = E_{applied} - E^o$). For proton reduction in water FeP/C has been reported to operate at low over potential, and for CO_2 reduction, many copper electrodes are reported to reduce CO_2 in water to products including CO and H_2. CoPi was chosen as the anode in order to minimize the overpotential required for the water oxidation reaction. CoPi operates efficiently in aqueous media especially in neutral solution under the same conditions of operation as the electrochemical reduction of CO_2 ($pH = 6.8$).[7] In an electrochemical cell to reduce CO_2 into CO, CH_4 etc, the required thermodynamic cell voltage lies between 1.47 V and 1.94 V compared to water oxidation at $E^o = 1.23\,V\,vs\,NHE$. An additional potential (to the thermodynamic barrier) is always required in order to begin the reduction of CO_2 to overcome the kinetic barriers **(Table A1.1)**. [3, 8]

Choice of the electrochemical solvent should also be considered as it will affect product separation and the solubility of substrate CO_2 in the case of CO2RR. In the absence of additional separation steps, the electrochemical solvent will also be present in the H_2 and CO_2/H_2 product stream and the thermal catalyst has to be compatible with its presence. Generally, working in aqueous media is highly recommended from an environmental and economic point of view.

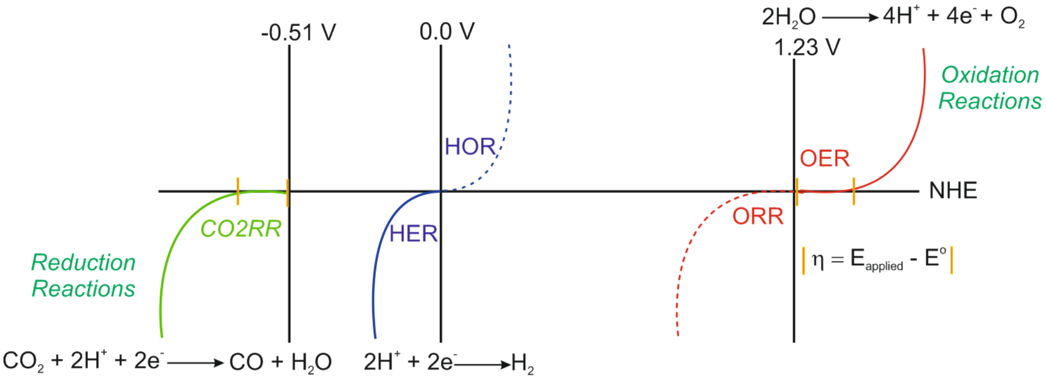

Figure 1.1: Thermodynamic consideration of the proposed electrochemical reactions in water. CO2RR: CO_2 reduction reaction, HER: hydrogen evolution reaction, ORR: oxygen reduction reaction, HOR: hydrogen oxidation reaction and OER: oxygen evolution reaction.

To achieve the goal of the project within the criteria outlined above the, choice of thermal catalyst is also crucial. In the proposed chemical reactor, CO_2 and/or protons are expected to electroreduced at the cathode and water oxidation is supposed to occur at the anode in aqueous media. The existence of O_2 (resulted from water oxidation) may cause problems to the catalyst such as deactivation. Thus, a membrane (Nafion-117) is required to separate the two electrochemical chambers to minimize the presence of oxygen gas within the catalytic chamber. Although the theme of the project is based on using earth abundant metals, most of the published commercial, reliable catalysts for hydrogenation and hydroformylation (particularly at low pressure) are based on precious metals like Pd, Pt, Rh, Ir and Ru **(Scheme 1-1)**.

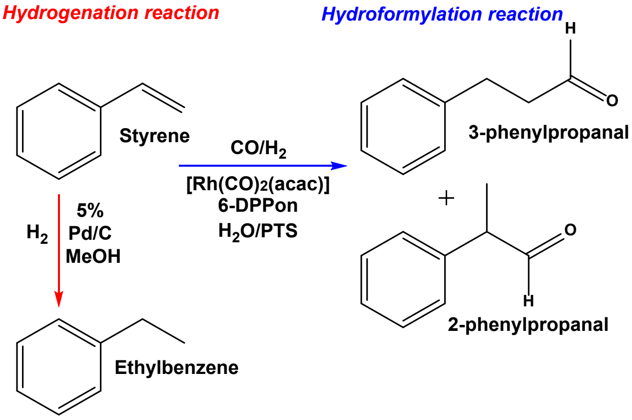

Scheme 1-1: Hydrogenation and hydroformylation reactions of styrene.

Many earth abundant based metal complexes like Co and Fe[9] can mediate catalytic reactions such as the hydrogenation of alkenes. However, these complexes either operate under high pressure/temperature or are very air sensitive making them impractical. For hydrogenation, we chose a 5% Pd/C commercial catalyst to perform the hydrogenation reaction of an alkene. About 75% of the industrial hydrogenation processes are performed using Pd/C catalysts.[10-14] It is generally tolerant to water and can operate under low hydrogen pressure. The main disadvantage of the Pd/C system is that in the presence of oxygen and methanol vapour ignition can occur.[10] For the hydroformylation reaction we chose a catalytic system using Rh/(6-DPPon) which is reported to operate in water under 1 atm of syngas **(Figure 1.2)**.[15, 16] A further consideration for CO_2 reduction is that the product gas stream is dilute in a relatively high concentration of CO_2. Typically, the effect of CO_2 on hydroformylation is not reported, so its effect required investigation.

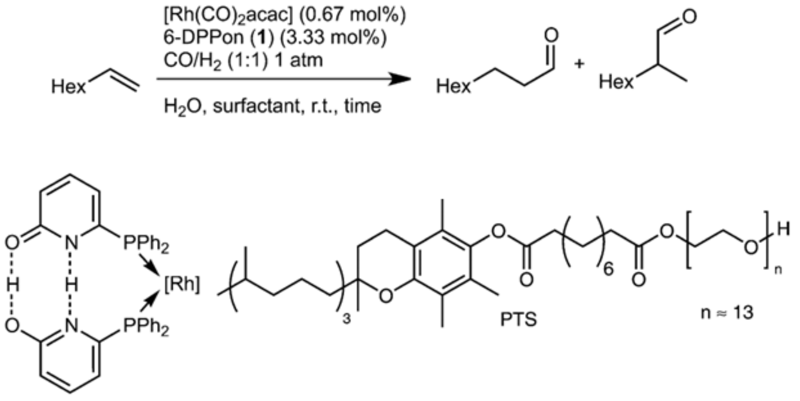

Figure 1.2: The suggested hydroformylation catalyst.[16]

During the time I was working on my PhD, Skrydstrup et al described a mini-reactor using an H-cell design to couple an electrocatalysis to a catalytic system (carbonylation).[17] In their system, an iron porphyrin (FeTPP) was used to electroreduce CO_2-to-CO in DMF at high overpotential with trifluoroethanol (TFE) as a proton source and a Pd-based catalyst was used to produce an antidepressant drug via carbonylation **(Figure 1.3)**. This built on their earlier work to perform low pressure carbonylation chemistry in a bespoke sealed reactor.[17] By comparison, our proposed system should operate in water without any sacrificial agents. In addition, our approach uses a commercially available cheap solar panel (£30-50) to drive the reaction (Skrydstrup used a potentiostat) and operates under flowing conditions.

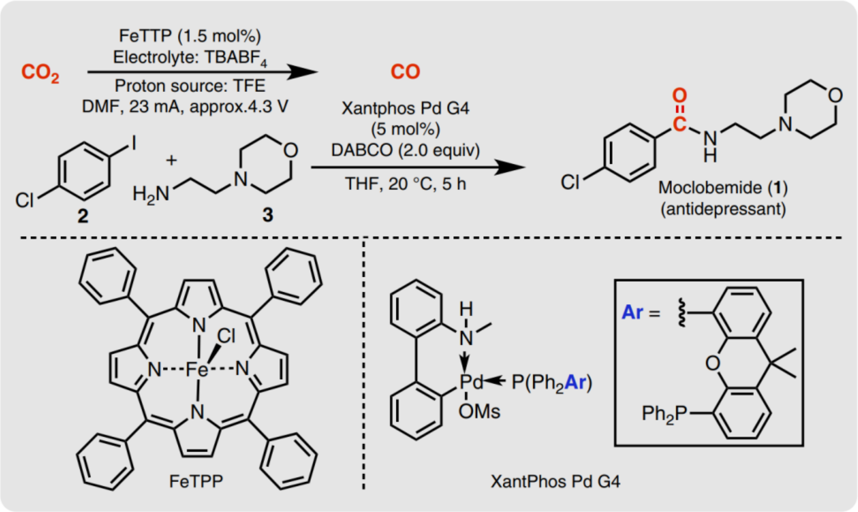

Figure 1.3: Skrydstrup's system. [17]

A large part of this thesis has concentrated on understanding the use of reported electrocatalysts for the production of hydrogen and syngas in water to provide sufficient product to support catalysis. The following sections describe in greater detail the background of electrocatalysis, particularly in the context of materials for electrocatalytic reduction of protons and CO_2.

1.3. Hydrogen evolution reaction

Global energy demand is greatly increasing and many energy sources, particularly fossil fuels, produce CO_2 emissions which lead to global warming and climate change. Hydrogen as a source of energy avoids carbon emissions as it produces energy and water upon combustion with oxygen. The reverse reaction (water-splitting) **(Eq. 1-1)** generates hydrogen and provides a way of storing energy in chemical bonds that can be converted to electricity in fuel cells or to heat by burning. The production of hydrogen gas without generating carbon emissions is a major challenge if it is to be used on a global scale. Currently, the vast majority of global hydrogen production is achieved using steam reforming of natural gas, which directly leads to carbon emissions.[18] Although energy demand for the hydrogen evolution reaction (HER) is one of the main challenges, H_2 gas storage is also a major issue.

Potential methods that do not result in direct carbon emissions for the production of hydrogen gas include electrocatalytic water splitting (water electrolysis), photoelectrochemical or photo-biological water splitting, fermentation, high temperature water splitting and renewable liquid reforming.[19] Of all these clean approaches water electrolysis is the only one currently used on a larger than laboratory scale usually in conjunction with a nearby renewable source of energy such as hydroelectricity.[20]

To increase the efficiency of energy storage using electrocatalytic water splitting, electrocatalysts are required in order to overcome the kinetic barrier (overpotential) to hydrogen and oxygen production. Generally, platinum is the best metal to be used for this purpose as it operates efficiently at low overpotential in acidic and alkaline media.[21] The high cost and rarity of Pt prohibits its usage on an industrial scale. Huge efforts from researchers all over the world have been exerted to prepare/find efficient alternatives to Pt including pure transition metals like gold[22] and binary compounds including transition metal phosphides,[23, 24] sulphides,[25, 26] selenides,[27, 28] nitrides,[29, 30] borides[31] and carbides.[32, 33]

During water electrolysis there are two electrochemical operations that take place simultaneously; at the anode (oxidation reaction; oxygen evolution reaction **OER**) and at the cathode (reduction reaction; hydrogen evolution reaction **HER**) **(Figure 1.4)**. The overall reaction of water splitting is:

$$H_2O \rightarrow H_2 + 1/2\,O_2 \qquad \text{Eq. 1-1}$$

The thermodynamic barrier of the reaction $E^o = 1.23\,V\,(NHE)$ regardless of the medium (25 °C, 1 atm).[34, 35] In acidic medium:

Cathode: $2H^+ + 2e^- \rightarrow H_2$ Eq. 1-2

Anode: $H_2O \rightarrow 2H^+ + 2e^- + 1/2\,O_2$ Eq. 1-3

In neutral and basic medium:

Cathode: $2H_2O + 2e^- \rightarrow H_2 + 2OH^-$ Eq. 1-4

Anode: $2OH^- \rightarrow H_2O + 1/2\,O_2 + 2e^-$ Eq. 1-5

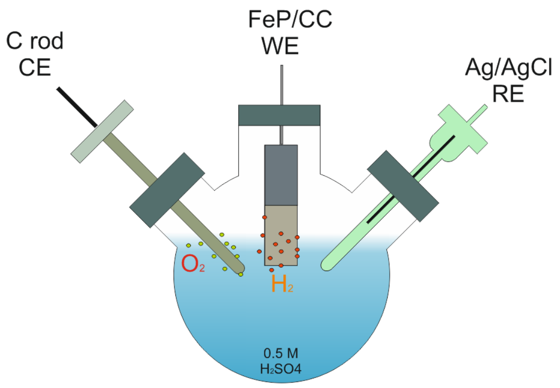

Figure 1.4: Typical water splitting system.

1.3.1. Thermodynamics and kinetics of hydrogen evolution reaction

HER electrocatalysts are characterized by the overpotential value, the exchange current density and Tafel slope. It's worth noting that the best electrocatalyst for the hydrogen evolution reaction is the one which operates at low overpotential ($\eta = E_{applied} - E^{o}$), has high exchange current density (J^{o}) and a small Tafel slope as is the case for Pt.[35] Pt is the best electrocatalyst for HER as the adsorption free energy of H is close to zero (ΔG ≈0).[36] The practical cell voltage E_{cell} of water splitting $E_{cell} = 1.23 + \eta_a + \eta_c + \eta_{ohmic}$ where η_a and η_c are the overpotential on anode and cathode, respectively.[34] Both overpotentials can be small values when using efficient electrocatalysts.

In three-electrode electrochemical cell **(Figure 1.5)**, ohmic drop is always included (iR_s) resulted from solution resistance (R_s); the solution resistance corresponds to compensated resistance (Rc) and uncompensated resistance (R_u).[37, 38] Most of the current flows between working electrode (WE) and counter electrode (CE), thus the ohmic drop can be minimised. The uncompensated resistance (R_u) between the working electrode (WE) and reference electrode (RE) causes ohmic drop.[37, 38]

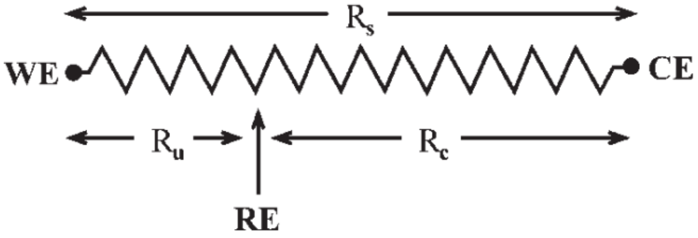

Figure 1.5: Schematic representation of three-electrode electrode cell.[37]

Generally, the ohmic drop (η_{ohmic}) can be minimized through efficient electrochemical cell design, increasing the conductivity of the electrolyte solution and decreasing the distance between working and reference electrode.[34, 39] The equilibrium potential for HER is expressed (at room temperature and 1 atm) in **(Eq. 1-6)** and is pH dependent.

$$E_{HER} = E^{o}_{H_2} - \frac{RT}{nF} ln\left(\frac{a_{H^+}}{P^{1/2}_{H_2}}\right) = 0 - 0.059\, x\, pH\ V\ (NHE) \qquad \text{Eq. 1-6}$$

Although the value of the equilibrium potential is 0 V at pH = 0, in practice, the reaction does not start at the equilibrium potential, because of the activation energy barrier of the chemical reaction **(Figure 1.6)**.[40-42] The height of the activation barrier depends on the nature of the interaction at which HER takes place.[42]

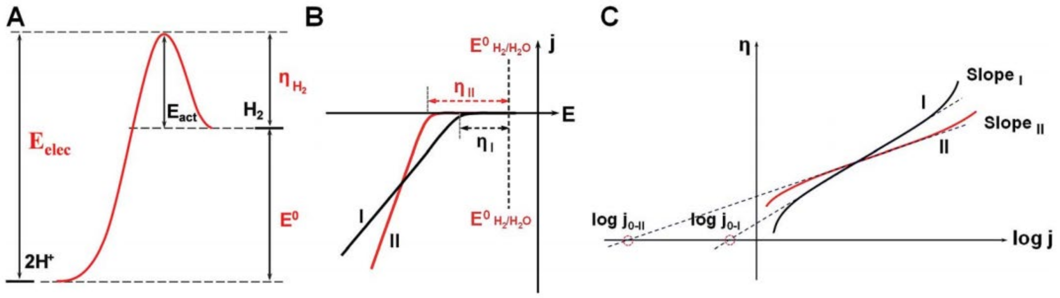

Figure 1.6: Schematic diagram illustrates the thermodynamics considerations for HER (A: activation energy, B overpotential and C Tafel plot).[42]

The reaction cannot begin until enough reduction potential is applied; overpotential ($\eta = E_{applied} - E^{o}$). The kinetics of HER are dependent on electrochemical potential; Butler-Volmer equation **(Eq. 1-7)**;[38, 43]

$$J = J^{o}[-e^{\alpha nF\eta/RT} + e^{(1-\alpha)nF\eta/RT}]$$ Eq. 1-7

Where J and J^{o} are the current and the exchange current densities, respectively, α: charge transfer coefficient, n: number of electrons transferred, F: Faraday constant, R: ideal gas constant, and T is the temperature. Exchange current density represents the rate of the reaction at equilibrium (no applied potential).[26] At equilibrium, the two terms (cathodic and anodic) are important $-e^{\alpha nF\eta/RT}$ and $e^{(1-\alpha)nF\eta/RT}$. At very low overpotential ($\eta < 0.05$) the Butler-Volmer equation is simplified to the following form: $\eta = (\frac{RT}{nF}J^{o})J$, where overpotential is linearly proportional to current density. Away from the equilibrium, one term becomes more important and dominates the behaviour (either the cathodic or the anodic term). At higher overpotential the equation can expressed in a form like the Tafel equation:

$$\eta = a + b\, Log\, J = \frac{-2.3RT}{\alpha nF} Log\, J^{o} + \frac{2.3RT}{\alpha nF} Log\, J$$ Eq. 1-8

Where the overpotential is linearly proportional to log J and slope $b = \frac{2.3\mathrm{RT}}{\alpha\mathrm{nF}}$. The Tafel slope can be calculated from the Tafel plot **(Figure 1.7)** which is a plot between ($Log\, J$) vs overpotential (η) and subsequently calculating the charge transfer coefficient (α) **(Figure 1.8)**.[37]

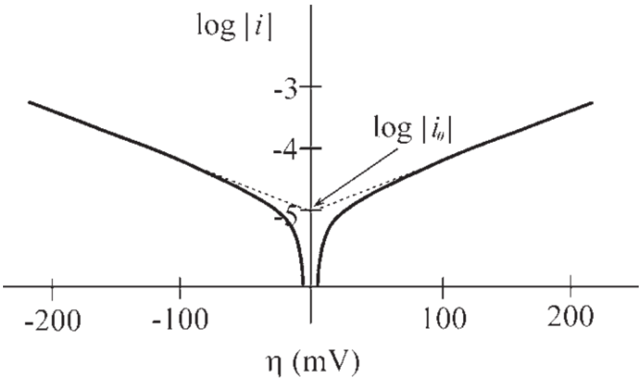

Figure 1.7: Tafel plot.[37]

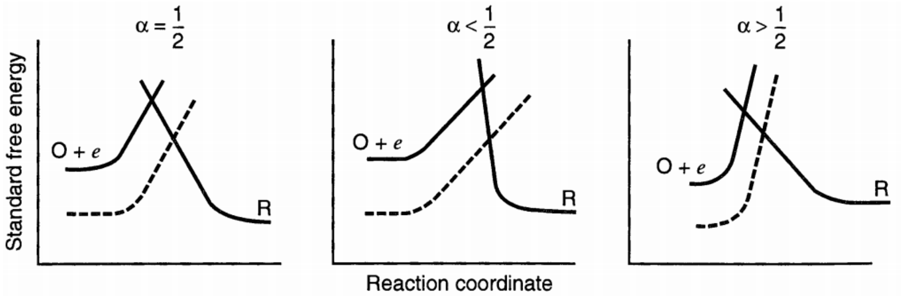

Figure 1.8: effects of charge transfer coefficient (α) on the symmetry of the electrochemical reaction barrier.[38]

The Tafel slope can be used to assign the mechanism of HER and the rate determining step. Experimentally, the Tafel slope provides a tool to know how to increase the current density by ten-fold. The HER can be preceded via three possible steps in acidic media with different thermodynamic consequences; **Figure 1.9A**.[38, 41, 43-48]

(1) Volmer step which involves the electrochemical hydrogen adsorption.
(2) Heyrovsky step which is an electrochemical desorption.
(3) Tafel step which is a chemical desorption step.

The value of Tafel slope depends on factors like the reaction mechanism and the number of active sites available for adsorption.[44] Butler-Volmer kinetics can use Tafel slope values to suggest the rate determining step of reactions, where Tafel slope values of 120, 40 and 30 mV/dec have a Volmer, Heyrovsky and Tafel rate-determining step, respectively.[42] According to the literature when Tafel slope equals 30 mV per decade, the HER proceeds via the Volmer-Tafel mechanism and recombination is the rate determining step.[49, 50] When the Tafel slope equals 40 mV/dec the reaction proceeds through the Volmer-Heyrovsky mechanism and the rate determining step is the electrochemical desorption step.[51, 52] A high Tafel slope ($b \approx 120\, mV/dec$) indicates the existence of many pathways occurring depending on the coverage of the surface of the adsorbed hydrogen.[49, 51] The free energy of hydrogen adsorption (ΔG_H) is important as the hydrogen evolution passes through the hydrogen adsorption step regardless of the pathway **(Figure 1.9B)**. Ideal non-precious electrocatalysts should have (ΔG_H) close to zero.[53]

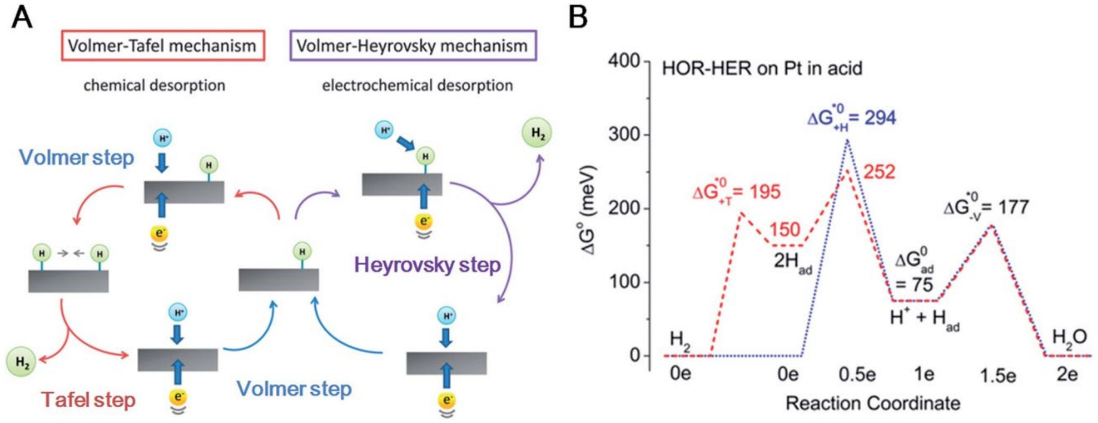

Figure 1.9: (Left) Volmer−Tafel and Volmer−Heyrovsky mechanisms on platinum electrodes [45] and (right) the Free energy diagram for HOR and HER processes at 0 V on Pt electrode in acidic medium (Volmer–Tafel pathway in red and Volmer–Heyrovsky pathway in blue). [54-56]

1.3.2. Transition metals volcano plot

The electrocatalytic activity of any transition metal (TM) HER electrocatalyst relies on the free energy of hydrogen adsorption.[36, 57, 58] On plotting Gibbs free energy (ΔG_H) versus current exchange densities of various HER electrocatalysts, a volcano plot is observed with Pt at the peak position; **(Figure 1.10)**.[36] Pt is on the top of the volcano plot and is an excellent HER catalyst.[36, 57, 58] The superiority of Pt as an electrocatalyst for HER can be explained by the Sabatier principle, the binding ability of the Pt is moderate, neither too strong nor too weak for both hydrides and hydrogen. The volcano plot is a convenient visualisation classifying different HER electrocatalysts.[26] Other pure metals can electrocatalyse HER but inefficiently compared to that of Pt.

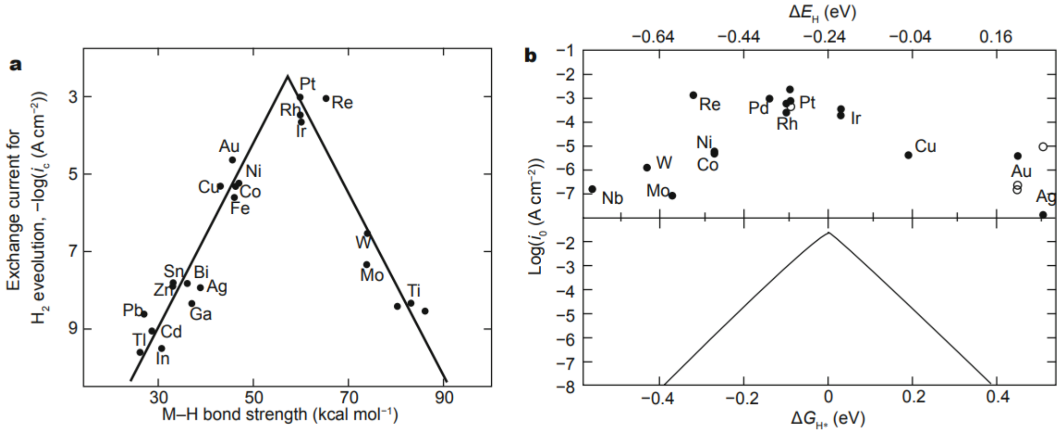

Figure 1.10: Exchange current density as a function of M-H bond strength (a) and of the calculated hydrogen chemisorption energy per atom (b).[57]

In order to tune and control the electrocatalytic activities of such metals, many binary and ternary TM based electrocatalysts have been prepared. Transition metal based carbides, sulphides, selenides, nitrides, borides, carbides and phosphides have been used for HER in different pH ranges **(Figure 1.11)**. The electrocatalytic performances and parameters of different TM based electrocatalysts are tabulated in **(Table A1.2)** and **(Table A1.3)**.

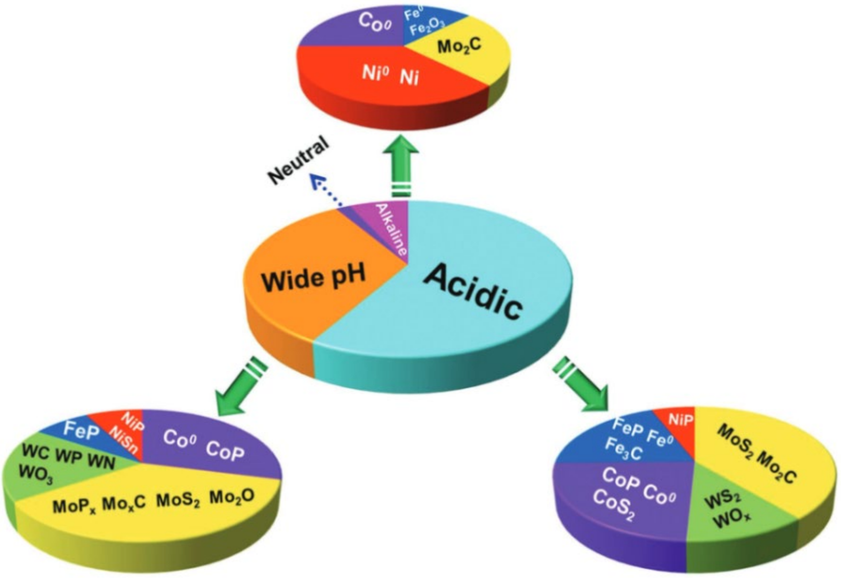

Figure 1.11: Summary of non-noble TM based electrocatalysts for HER in different pH media.[48]

In the current project we decided to use an electrocatalyst that can operate efficiently in acidic medium (0.5 M H_2SO_4) in order to avoid problems like passivation side reactions and to lower the resistance losses.[59]

Transition metal sulphides are promising electrocatalysts for HER. They can operate with low H coverage on the surface of the electrocatalyst but the low coverage reduces their electrical conductivities.[36, 60, 61] Molybdenum sulphide is the a common electrocatalyst as it is cheap, easy to prepare and easy to design.[62-64] **Transition metal carbides** are considered as potential alternatives to Pt for HER. Molybdenum carbide is called quasi-platinum as both share the same electronic structure.[34, 65, 66] Li et al studied molybdenum carbide as a potential electrocatalyst for HER. The overpotential required for -10 mA/cm^2 was between 140 mV and 160 mV.[34, 67, 68] **Transition metal selenides** were studied as electrocatalysts for HER as Se is in the same group as S. Se has more metallic properties, larger atomic radius and lower ionization energy compared to S. Such properties suggested the ability of selenides to reduce protons like sulphides.[35] $MoSe_2$ is the best example for a TM selenide in terms of working under low overpotential and small Tafel slope.[66]

Transition metal borides have been investigated as potential electrocatalysts for HER. Amorphous metal borides showed enhanced stability and activities toward HER.[65, 67, 68] **Transition metal nitrides** were prepared as an attempt to tune the transition metal catalytic activities. They are prepared through nitridation of the metal precursors. Molybdenum nitride as an electrocatalyst showed current density of -38.5 mA/cm^2 at $\eta = 300\,mV$ [42]. All the mentioned TM classes have pros and cons and there is no favourability of one class over other one. Benchmarking these different TM classes for their electrocatalytic toward HER can be done through different terms like overpotential, Tafel slopes, ease of preparation, expense of metals and properties like conductivities. In the current project, the energy demand is one of the main criteria of choosing the electrocatalyst.

Transition metal phosphides were chosen for their ability to operate in a wide range of pH and being non-toxic and high conductivity (heat and electricity) and they are thermally stable.[69] FeP was chosen as an electrocatalyst to work as an electrocatalyst for HER in acidic medium. There are different iron phosphides based electrocatalysts reported in literature **(Table A1.2)**. The criteria for choosing the electrocatalyst for the reactor was the ability to operate under low overpotential, easy to prepare, stable and durable. Rugae like iron phosphide (FeP) based on carbon cloth reported by Li et al[70] (2015) was chosen to be used in the proposed reactor. The electrocatalyst is one of the best electrocatalysts reported for HER in acidic medium in the literature **(Table A1.2)**. FeP was prepared through electroplating followed by phosphidation at different temperatures (250 - 500 °C). Li et al reported that FeP/CC prepared at 300 °C provide a high surface area morphology with excellent HER activity in 0.5 M H_2SO_4 with η_{10} = 34 mV (η_{10} is the overpotential required to afford -10 mA/cm^2) and a Tafel slope of 29.2 mV/dec **(Figure 1.12)**. Such a Tafel slope is close to that of Pt suggesting that the evolution of H_2 proceeds through Volmer-Tafel mechanism.

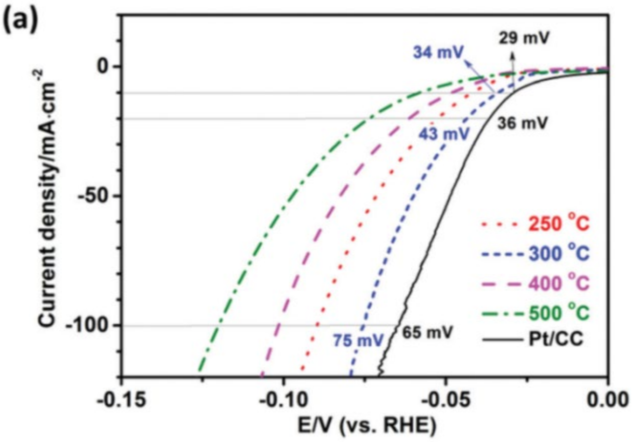

Figure 1.12: Polarization curves of iron phosphide prepared at different temperature.[70]

Iron phosphides exist in different stoichiometries and polymorphs including FeP, Fe_2P, FeP_2 and Fe_3P. Iron phosphide based electrocatalysts have shown excellent catalytic activity compared to other TMPs (transition metal phosphides) in acidic and neutral media. Many researchers reported the ability of FeP electrocatalysts to operate at low overpotential and showed their high stability and long durability.[71] TMPs have many advantages over other materials for instance they are often based on earth abundant elements **(Table 1-1)**,[72] are easy to prepare, cheap, and their electronic properties can be tuned. TMPs electronic properties vary with the ratio between the metal and phosphorus where increasing the phosphorus content can change the conductivity gradually from metallic, to semi-conductive or even insulating materials.[65, 73] This phenomenon is attributed to the electronegative nature of P which limits the electron delocalization in the metal leading to reduced conductivity of the TMP.[65, 73] Increasing the metal ratio can lead to materials with properties of the corresponding pure metals indicating the high conductivity of these materials.[74] Theoretically, TMPs form a cationic metal centre and anionic P atom. Such anionic states of P are active positions for proton discharge in HER.[75-77] Many transition metal phosphides have been investigated as potential electrocatalysts for HER like Co,[26, 78] Fe,[79-82] Mo,[83-85] Ni[86-88] and W.[89]

Table 1-1: The abundance of several elements in Earth's crust. [90]

Atomic no.	Element	Abundance in earth's crust (ppm)	Atomic no.	Element	Abundance in earth's crust (ppm)
8	O	4.61×10^5	29	Cu	60
26	**Fe**	$\mathbf{5.63 \times 10^4}$	27	Co	25
19	K	2.09×10^4	46	Pd	1.5×10^{-2}
22	Ti	5.56×10^3	78	Pt	5×10^{-3}
1	H	1.40×10^3	79	Au	4×10^{-3}
15	**P**	$\mathbf{1.05 \times 10^3}$	44	Ru	1×10^{-3}
6	C	200	45	Rh	1×10^{-3}

1.3.3. Preparations of iron phosphides

Iron phosphides are usually prepared through two main steps: formation of an iron phosphide precursor on the substrates followed by the phosphidation process:

1.3.3.1. Methods of preparation of iron phosphides precursors:

Several methods have been used to prepare FeO(OH) or Fe_2O_3 on different substrates, which can be converted to FeP_x. These include ***electroplating*** (electrodeposition of iron metal on the substrate),[70] ***spray pyrolysis*** (spraying iron source on heated substrate),[71] ***solvothermal*** (liquid phase reaction and precipitation),[82] ***hydrothermal*** (the substrate is heated in an aqueous solution containing the iron source),[21] ***solvent-deficient*** (grinding an iron salt with ammonium bicarbonate in a mortar without using a solvent)[91] and ***dip-coating*** (immersing the substrate in a solution containing the iron precursor at room temperature).[61] **(Table A1.2 and Table A1.3)** shows the electrocatalytic activities of nominally the same material on different substrates varies with respect to overpotential and Tafel slope. Different iron compounds, MOF and metal complexes ($FeSO_4$, $FeCl_3$) were used as precursors to prepare intermediates like FeO(OH) or Fe_2O_3 followed by the phosphidation process.

1.3.3.2. Phosphidation process

Different sources for P **(Figure 1.13 and Table 1-2)** have been used for phosphidation including hypophosphites ($2NaH_2PO_2 \rightarrow PH_3 + Na_2PO_4$),[53] n-trioctylphosphine (TOP)[79] and red phosphorus.[78] Using the red phosphorous directly for phosphidation required high temperature up to 800 °C. Relatively low temperatures are required for the other phosphidation processes compared to the red phosphorus. As main advantage of using sodium hypophosphite as a source of P is that it is not toxic as TOP.

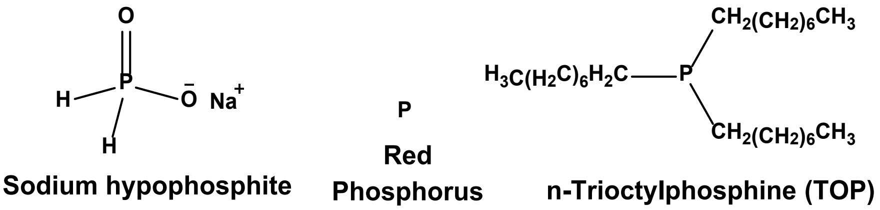

Sodium hypophosphite **Red Phosphorus** **n-Trioctylphosphine (TOP)**

Figure 1.13: Potentials phosphorus sources for phosphidation reactions.

Table 1-2: Different methods for phosphidation reaction and their conditions.

Catalyst	P source	Conditions
FeP[78]	n-trioctylphosphine	320 °C, 5 h, under Ar
FeP[92]	Sodium hypophosphite	300 °C, 2 h, under Ar
WP[86]	Red phosphorus	800 °C, 1 h, under Ar

1.3.3.3. Substrates

Several materials were used as substrates for electrocatalysts for HER like Ni foam,[87] Cu disk,[93] Cu foam,[94] Ti foil [95] and carbon-based materials such as glassy carbon electrode[83] (GCE), carbon cloth[70] carbon soot[96] and graphene sheets.[82]. Carbon cloth is relatively cheap, very conductive and provides a self-standing 3D structure/network for any electrocatalytic system.[97] It proved its ability to act as a substrate for many electrocatalysts including CoP,[24] FeP[98] particles. For these reasons carbon cloth was chosen as a substrate for FeP in the current project.

1.3.4. State-of-the-art

Iron phosphides have been used for the hydrogen evolution reaction in acidic and neutral media. Different forms of iron phosphides have been used for HER including FeP, FeP_2, Fe_2P and Fe_3P. The overpotential values depend on many factors such as the interaction between the electrocatalyst particles with the substrate and the substrate itself, morphology which is usually defined in most of the cases from the starting precursors, structure, and composition. HER involves charge transfer from the substrate to the electrocatalyst then to its surface. In most cases, researchers were trying to improve the interactions between the electrocatalyst and the substrates through designing electrocatalysts with different structures and morphologies including nanorods, nanosheets, nanowires, nanoparticles, and films in order to increase the exposed surface and number of active sites.[99] In the following section, some of the reported work based on iron phosphides including different phosphide forms, substrates and methods of preparations:

Different forms of iron phosphide were prepared and used as ellectrocatalysts for HER including FeP, Fe_3P, FeP_2 and Fe_2P. Park et al[80] (2016) succeeded in preparing controlled-composition of iron phosphide (FeP and FeP_2) nanowire. The richer P material exhibited an excellent performance. The Tafel slopes of HER were 39 and 37 mV/dec for FeP and FeP_2, respectively in 0.5 M H_2SO_4. The same behaviour was observed in 1.0 M KOH with Tafel slope value of 75 and 67 mV/dec for for FeP and FeP_2, respectively.[80] Ha et al[100] (2018) also proved the phase dependency of iron phosphide nanoparticles towards HER activity. Unlike the previous example, Whitmire et al[101] (2018) investigated the catalytic activities for HER of pure phase iron phosphides (Fe_xP; x: 1- 3). All samples were supported on FTO. Whitmire et al reported that the Fe_3P required that lowest η_{10} =49 mV in 0.5 M H_2SO_4 (Fe_3P > Fe_2P > FeP with respect to the electrocatalytic activity) **(Figure 1.14)**. The results suggested that the P rich iron phosphide are less active that the Fe rich ones. It is not clear yet what is more critical for the iron phosphides for their electrocatalytic activity for HER; the more metal content or the more P content.

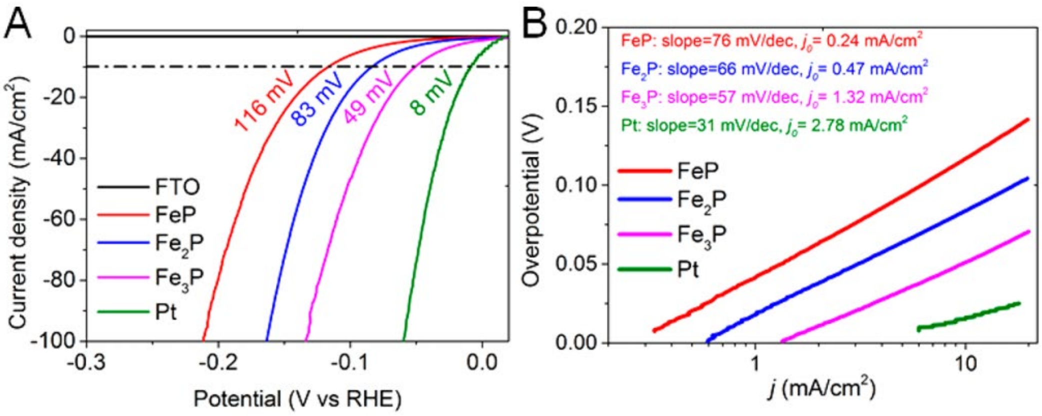

Figure 1.14: Polarization curves of different iron phosphides prepared on FTO and their Tafel plots.[101]

Ha et al prepared iron phosphide nanoparticles with two distinct phases **(Figure 1.15)** (FeP and Fe_2P) on Ti foil by changing the temperature of the reaction system. FeP nanoparticles exhibited a better performance compared to that of FeP_2 particles and both of them have similar Tafel slopes. The overpotential required to afford -10 mA/cm^2 at 300 °C was 250 mV but after increasing the temperature up to 320 °C, Fe_2P appeared and the overpotential value was η_{10} =155 mV. At 340 °C FeP exhibited the best electrocatalytic performance with η_{10} = 135 mV.[100]

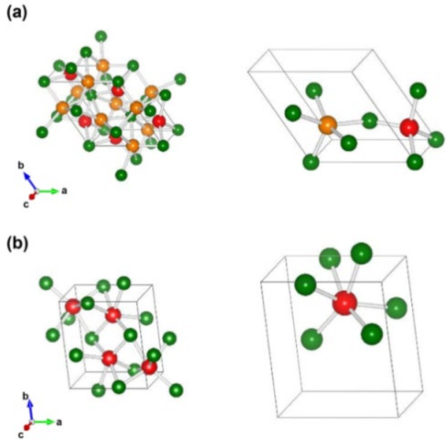

Figure 1.15: Crystal structure of iron phosphide (a) Fe_2P and (b) FeP (Fe: red and orange, P: green).[100]

Generally, iron phosphides can be prepared through different routes like starting with inorganic salts like $FeCl_3$ and $FeSO_4$. Different reported iron phosphide based electrocatalyst were prepared from different precursor including metal complexes,[102] inorganic-organic hybrid,[78] MOF[103] and polymers.[83] Using different precursors can support the prepared iron phosphide with the macro-size morphology of the precursor such as the preparation of nanoporous FeP nanosheet reported by Zhang et al[78] (2013) which synthesised using the anion-exchange reaction of inorganic–organic hybrid $Fe_{18}S_{25}$–TETAH (TETAH = protonated triethylenetetramine). Starting with metal complexes **(Figure 1.16)** was also reported to prepared FeP nanoparticles for water splitting in basic medium (1 M KOH). The preparation of FeP nanoparticles from iron molecular precursor **(Figure 1.16)** resulted in the formation of ultra-small, efficient and bifunctional electrocatalyst capable of working for long time (weeks).[102] The molecular precursor was subjected to hot injection condition in oleylamine that resulted into the formation of FeP NPs. The prepared electrocatalyst can afford -10 mA/cm^2 at overpotential of 165 mV in 1 M KOH (pH=14).[102]

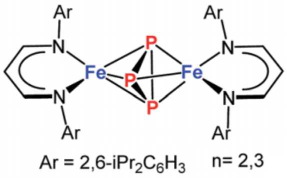

Figure 1.16: Molecular iron precursor for FeP nanoparticles.[102]

Engineering of the iron phosphide was reported also to tune the intrinsic properties by creating Fe vacancies.[104] The vacancies were created by using a sacrificial dopant (Mg) followed by a chemical leaching **(Figure 1.17)**. The catalytic activities towards HER of the obtained materials were studied and overpotential values were η_{10} = 108 in 1.0 M KOH and 65 mV in 0.5m H_2SO_4. The faradaic efficiencies were close to 100%.

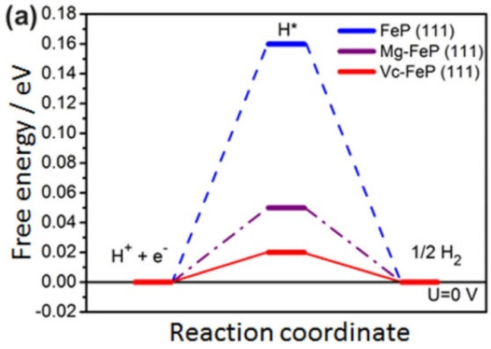

Figure 1.17: Free energy diagram based on theoretical studies.[104]

The improving of the electrocatalyst did not stop at the iron phosphide alone but it extended to involve the substrates too. Doping the substrates (carbon or Ti based substrates) with elements like P and N were reported. [79, 105-107] FeP supported on nitrogen-doped carbon nanotube (NCNT) was prepared in order to improve the immobilization of catalyst.[79] FeP/NCNT showed a good catalytic activity with η_{10} = 113 mV with Tafel slope of 59 mV/dec and FE% about 100% in 0.5 M H_2SO_4.[79] Mu et al[105] (2017) prepared FeP eleactrocatalyst encapsulated in N,P-codoped carbon (FeP NPs@NPC). FeP NPs@NPC exhibited η_{10} = 130, 386 and 214 mV in 0.5 M H_2SO_4, 1.0 M phosphate buffer solution (PBS) and 1.0 M KOH, respectively.[105] Fu et al[106] (2018) developed an efficient and stable electrocatalyst for HER based on amorphous Fe_xP coated Fe_2N supported on reduced graphene oxide (P-Fe_2N/rGO).

Fu et al reported that the η_{10} =64.8 mV and the Tafel slope was 48.7 mV/dec **(Figure 1.18)**. Theoretical studies suggested that the hydrogen binding free energy $|\Delta G_H*|$ value is close to zero and this is the reason for the enhanced performance.[106] Chu et al (2018) doped iron phosphide supported on TiN nanowire arrays with N. The produced structure works efficiently as an electrocatalyst for HER in alkaline medium.[107] Chu et al attributed this behaviour to the effects of N doping, amorphous surface and the conductive nanowire scaffold that provides a large number of active sites, enhances the charge transfer and prevents the catalysts from migration and aggregation.[107]

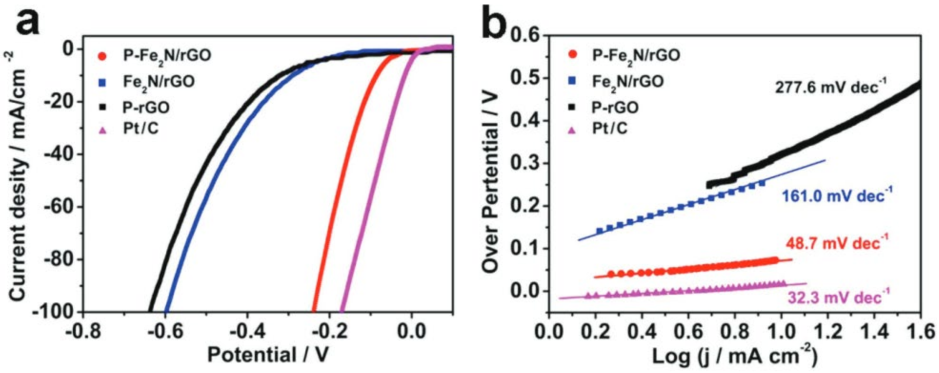

Figure 1.18: Polarization curves of P-Fe_2N/rGO (a) and Tafel plots (b).[106]

Most of the reported FeP based HER electrocatalysts were in nanoscale with different shapes including nanowires and nanorods.[92, 108] Sun et al[108] (2014) prepared FeP nanowires on Ti to work as electrocatalyst for HER. The precursor of FeP was β-FeOOH NA/Ti, prepared hydrothermally, followed by a low temperature phosphidation process. The electrocatalyst showed a high performance with η_{10} = 55 mV, a Tafel slope of 38 mV/dec in 0.5 M H_2SO_4. Sun et al[92] (2014) synthesised highly active self-supported FeP nanorods arrays for HER. The authors tried to prepare the catalyst without using any binder on a current collector causing an increase the resistance by blocking active sites through preparing the electrocatalyst directly on the substrate (current collector). The electrocatalyst can afford -10 mA/cm^2 with η_{10} = 58 mV and Tafel slope = 45 mV/dec and nearly 100% Faradaic efficiency. The electrocatalyst can operate for 20 h.[92] Sun et al also investigated the ability of their catalyst to operate in 1.0 M PBS (phosphate buffer solution) and the overpotential value was larger than that in acidic medium η_{10} = 202 mV and the Tafel slope was 71 mV/dec.[92] Wang et al[109] (2017), prepared electrocatalyst made from core-shell of Fe@FeP nanoparticles on carbon nanotubes (CNTs) for HER. The prepared electrocatalyst exhibited η_{10} = 53 mV in 0.5 M H_2SO_4 with Tafel slope of 55 mV/dec. Wang et al concluded that the strong interaction between metal and the phosphide strengthened the binding of the intermediates. Not all the iron phosphide based electrocatalysts were in nanoscale, some FeP were in the microscale like FeP hollow microspheres electrocatalyst for HER developed by Li et al.[110] The electrocatalyst exhibited electrocatalytic activity with η_{10} = 144 mV in 0.5 M H_2SO_4 and a Tafel slope of 58 mV/dec and long term stability.

1.4. Electrochemical reduction of CO_2 based on/ derived from copper binary compounds

The atmospheric accumulation of greenhouse gases must be lowered to reduce the probability of catastrophic climate change and related natural disasters.[111-115] A major contributor to greenhouse effects is carbon dioxide, which is a consequence of increasing global industrialisation since the late 1700's. Currently, there are two broad approaches suggested for reducing emissions, neither of which have yet to be realized on an effective scale, carbon capture and storage (CCS), and carbon capture and utilization (CCU). In this part of the introduction, we will focus on one strategy for CCU, where CO_2 is electrocatalytically reduced (CO2RR) directly to liquid oxygenates and hydrocarbons, or to their precursors CO and H_2 (syngas) for downstream conversion using Fischer-Tropsch synthesis. Several other approaches to CCU have been proposed including photocatalysis, biological (microbial CO_2 fixation), copolymerisation, and power-to-gas technologies, which have been reviewed elsewhere.[116-120]

To minimize upstream CO_2 emissions, it is envisaged that the electricity for electrocatalysis will be supplied by a renewable energy source such as solar, wind, or tidal. Whilst in principle the liquid products of CORRs could be stored for CCS, they have value as chemical feedstocks. Furthermore, all the relevant chemical reactions are endergonic, potentially allowing the products to be used as fuels. However, this later strategy will not eliminate CO_2 emissions or reduce currently accumulated levels unless an efficient process for concentrating atmospheric CO_2 is developed. Nevertheless, the rate of current emissions can be reduced significantly if concentrated waste streams of CO_2 could be captured and utilised. It has even been suggested that electrocatalytic methods could be available commercially within the next decade due to the current intensity of global research activities.[121] The electrocatalytic CO_2RR can be performed under homogeneous or heterogeneous conditions. Typically, homogeneous CO2RR uses soluble metal complex catalysts, whereas heterogeneous CO2RR uses either immobilized metal complexes, metalloproteins, or more commonly a metal electrode. Heterogeneous electrocatalytic CO2RR also has the advantage that for practical application it can build on existing infrastructure and knowledge of large scale industrial electrolysis.

At least 22 different compounds have been reported as CO2RR products **(Figure 1.19)** using transition metal based electrocatalysts,[39, 122-129] with the voltage dependent on a multitude of interdependent parameters. These include the pH, temperature, current density, CO_2 and product solubility and mass transfer in the reaction medium, electrode geometry as well as intrinsic catalyst properties including adsorption/desorption, which also collectively control the relative rates of competing reactions such as proton reduction and those resulting in catalyst degradation. Many CO2RR products are of economic importance, and are produced globally on an industrial scale **(Figure 1.20)**.[130] Many also have high energy densities such as ethanol (21 MJ/L) and propanol (27 MJ/L) for potential use as fuels.[131] Of the multitude of known electrocataysts, metallic copper has attracted the most attention due to a combination of simplicity, low cost, and critically, the electrochemical properties uniquely support significant C-C coupled products in water. Other monometallic electrocatalysts favour CO (e.g. Au, Ag. Zn), formate (e.g. Sn, Pb, In) and in aqueous solution competing proton reduction to dihydrogen can be dominant (e.g. Ni, Fe). This behaviour is consistent with relative adsorption energies of CO_2, CO, H^+ and associated products and reactive intermediates.[132] However, in common with many metallic heterogeneous electrocatalysts, copper suffers from a limited lifetime due to surface contamination, and control of product selectivity remains a major challenge.

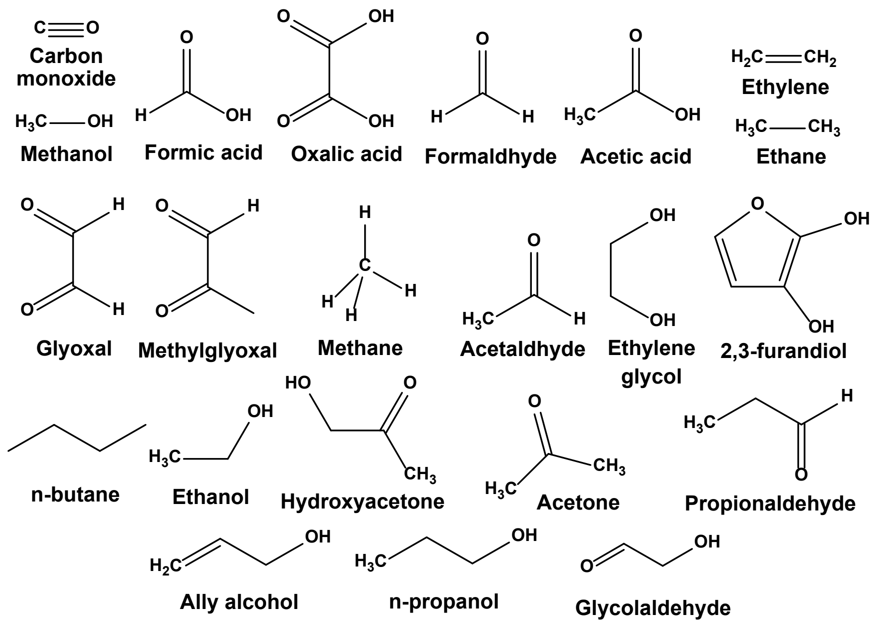

Figure 1.19: Examples of electrocatalytic CO2RRproducts reported in the literature.[39, 122-129]

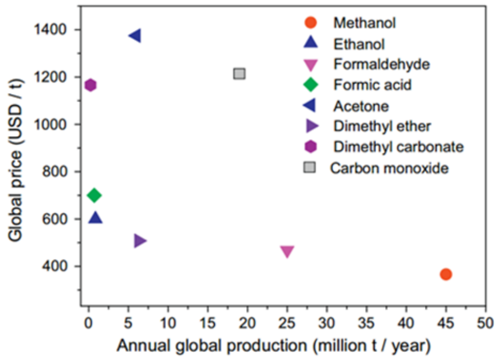

Figure 1.20: prices of some carbon based compounds.[130] The prices of these products change on a daily basis depending on the markets.

In the last decade there has been a vast increase in the number of publications for CO2RR with about 20 % based on Cu **(Figure 1.21)**. There are some contradictions between different studies identifying the key factors that have been suggested for enhanced electrocatalytic performance in copper based electrocatalysts. These include the role of grain boundaries, copper oxidation state, and the stability of surface oxides during the CO2RR, which will be briefly addressed below. Although significant advances have been reported there remains doubt that monometallic copper will be viable due to limited selectivity and lifetime, and therefore more complex materials such as alloys and compounds are required. Several reviews have recently been published addressing the fundamentals, strategies, mechanism and challenges that are facing the development and industrial implementation of heterogeneous CO2RR.[3, 116, 121, 133, 134] These include general CO2RR using transition metals including Cu,[6] electrocatalysts exhibiting selectivity for syngas,[3] methane,[129] methanol,[129] formic acid,[135, 6, 136-138] bimetallic alloys and factors affecting the product selectivity,[139-141] and copper specific reviews addressing surface morphology, microstructure, strain, particles size, and mass transport effects.[141, 142]

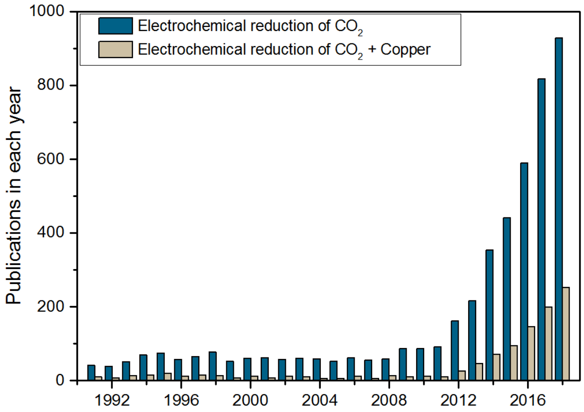

Figure 1.21: A citation report by Web of science about electrochemical reduction of CO_2 with and without copper starting from 1990 to 2018.

1.4.1. General considerations

Ideally, an efficient electrocatalyst should operate at high current density close to the equilibrium potential, which is characterized by a low overpotential (η). The reaction should also be selective for the desired product.

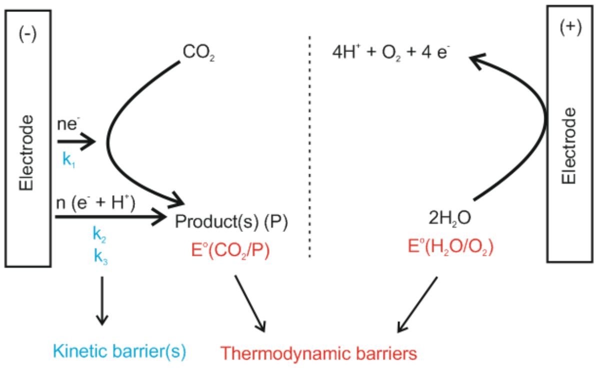

Figure 1.22: Electocatalytic half reactions for general CO2RR.

For CO2RR **(Figure 1.22)** many potentially desirable products have similar standard electrochemical potentials (E°) **(Table A1.1)**, have common intermediates, and all are multi-electron and often multi-proton processes that are kinetically complicated. Consequently, copper electrodes have typically been found to exhibit low selectivity due to variations in catalytic sites at metal surfaces, and high overpotentials due to slow kinetics.

Direct one electron reduction of CO_2 to the intermediate $CO_2^{\cdot}$ is energetically demanding ($E^\circ = -1.90V$) because of the LUMO energy and reorganization of the linear CO_2 molecule to the bent radical anion.[143] However, direct reduction can be circumvented by proton coupled electron transfer (PCET) processes, which provide more practical lower energy pathways **(Table A1.1)**. Given the complexity of these heterogeneous reactions it is no surprise that overpotential and selectivity are very dependent on electrochemical conditions as well as the composition, morphology, and microstructure of the electrocatalyst, making comparisons across studies extremely challenging.

For example product selectivities for CO2RR using Cu nanoparticles varies as a function of CO_2 pressure and electrolyte concentration ($KHCO_3$).[144] Low concentration of $KHCO_3$ (0.1M) favours ethylene whereas greater concentrations (0.5M) favour methane, but under 9 atm of CO_2 ethylene again predominates.[144] Similarly results are found for bulk Cu.[145] Product selectivity can be partially rationalized on the basis of local pH, where a higher concentration of bicarbonate at the electrode surface favours PCET leading to more CH_4 (and H_2) and higher overall current density. At lower bicarbonate concentrations, overpotentials, and overall current density, the formation of ethylene is independent of local pH because the reductive CO dimerization is the rate determining step for ethylene formation **(Figure 1.23)**.[145, 146]

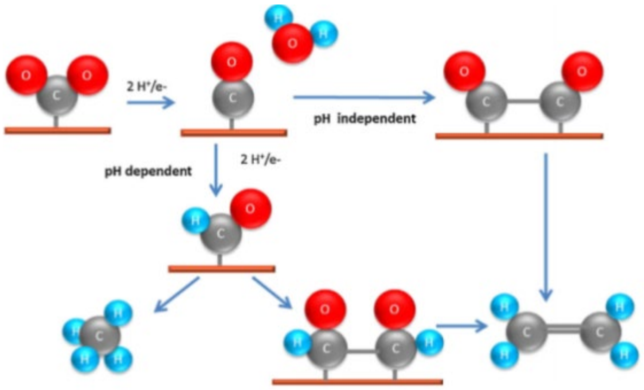

Figure 1.23: Mechanism for the electrochemical reduction of CO_2 via two pathways:[145] The first one is pH dependent as reported by Norskov et al[147, 148] and the second pathway is pH independent as reported by Koper et al. [146]

Notwithstanding the reported role of various parameters, a recent comparison of twenty monometallic copper electrodes has shown that selectivity across a diversity of systems can be interpreted based on the current density.[149] The product selectivity for each electrode, represented by the faradaic efficiency (FE), fall into voltage ranges that drive similar current density. In addition, it is well established that on polarisation the local pH at the surface of an electrode will differ from the bulk and recent experimental studies have shown that the local pH can change by several orders of magnitude.[150] Therefore irrespective of the voltage, the current density will largely define the local pH, and consequently modify the concentration of CO_2 and PCET rates at the electrode surface, overall controlling product selectivity of CO_2RR. Therefore, perhaps the most critical feature when comparing copper electrocatalysts is the electrochemically active surface area (ECSA) ($ECSA = R_f\ x\ S = C_{dl}/C_s\ x\ S$); ($R_f$: roughness factor, C_{dl}: the capacitance of the electrocatalyst, C_s: capacitance of reference and S is the geometric surface area). Unfortunately this is not always reported.

CO2RR using a copper electrocatalyst was first discovered and studied by Hori et al,[151-153] demonstrating oxygenate (EtOH and PrOH) and hydrocarbon formation at room temperature. This is in contrast to the industrial process of Fisher–Tropsch synthesis which takes place at high temperature and pressure using CO and H_2 (Syngas). The overpotential required by monometallic Cu for the production of oxygenates and hydrocarbons ranges between (0.6 to 1.0 V)[147, 154-157] representing a significant energy loss and reduction in overall efficiency **(Figure**

1.24).[147] Experiments and theory comparing electrochemical reduction of CO_2 and CO under identical conditions give similar product selectivity and overpotential. These data strongly suggest that where CO_2 mass transport is not limiting, the rate-limiting reaction which determines the high overpotential is not the initial reduction of CO_2 but occurs after formation of CO.[147]

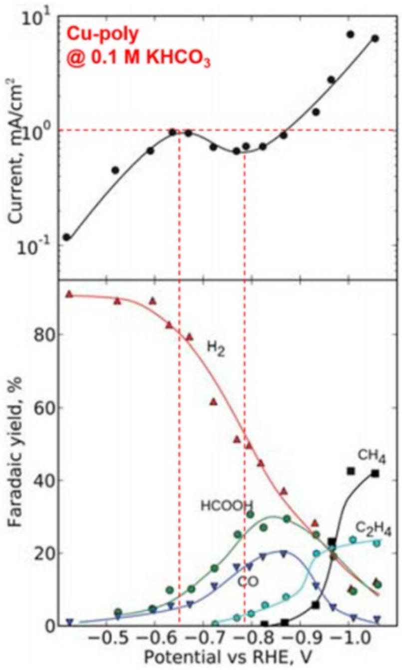

Figure 1.24: Top: LSV of CO2RR using polycrystalline Cu, (below: Faradaic efficiencies of different products using polycrystalline Cu at each corresponding potential.[147]

Mass transfer of CO_2 and reaction intermediates also play a critical role in determining the product distribution by limiting the CO2RR partial current density(ies) that are determined by the solubility of CO_2 in water ($[CO_2]$ = 30 mM at STP) and the pH dependent ($CO_2/HCO_3^-/CO_3^{2-}$) equilibria.[158] The flow rate of CO_2 and fluid dynamics of the electrochemical apparatus and electrode geometry modify the concentration of CO_2 at the electrode surface and the probability of intermediates such as CO being readsorbed on the electrode. The role of the flow rate of CO_2 on the FE showed that the partial current densities vary with the thickness of the hydrodynamic boundary layer. Increasing the flow rate decreases the thickness, increasing the partial current density for CO.[159] A range of electrode geometries including Cu foil,[156] foams,[160] nanoparticles,[161] nanowires,[162] hollow fibres[163] and gas diffusion electrodes (GDEs) [164] have aimed to increase the current density and product selectivity by increasing the surface area of the electrode and modifying flow dynamics. An outstanding example is provided by a GDE apparatus capable of CO_2RR to ethene with a partial current density of up to ca. 70 mAcm^{-2} and FE = 70%.[165]

The unique reactivity of copper amongst monometallic electrocatalysts for oxygenates and hydrocarbon products are primarily due to the relative adsorption behaviour of CO_2, H^+, and critically the volatile intermediate CO. For example, desorption/adsorption of the reactive CO intermediate has been compared for the electrocatalytic CO2RR using several monometallic transition metals **(Figure 1.22)**,[4] showing that metals having relatively high binding strength allow further reduction of CO intermediate whilst those with low CO binding strength release CO as a gas.[4] Theoretical calculations also support experimental data indicating that protonation of the adsorbed CO intermediate determines the CO2RR overpotential.[132] Increasing the number of adsorbed CO enhances the formation of C_2H_4 [166] and other adsorbed species such as H, COOH and CH_3O can help explain observed product selectivity.[167] Many other studies also support the 'goldilocks' electrochemical properties of Cu leading to hydrocarbon and oxygentate formation. Nonetheless, the picture still remains far from clear because of the challenge in unravelling the interdependence of extrinsic reaction conditions and intrinsic electrocatalytic parameters that collectively control overall performance. Furthermore, for economic viability, an electrocatalyst must have sufficient lifetime, ideally years, however, to date copper electrodes exhibit too short a lifetime for commercial use. Lifetimes up to 150 h for CO2RR have been reported[165] but commonly show decreasing current density within minutes-hours.

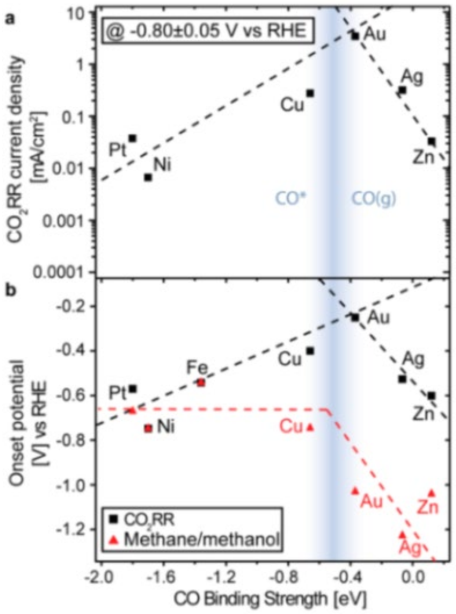

Figure 1.25: Electrochemical performance of different transition metal toward CO2RR: (a) Volcano plot of partial current densities at -0.8 V vs CO binding strength and (b) the onset potentials vs CO binding energies for CO2RR and methane/methanol.[4]

1.4.2. Beyond Bulk Monometallic Copper

Many modifications of bulk copper have been investigated to reduce overpotential, increase selectivity and lifetime.[165] These approaches include tuning the intrinsic properties of bulk copper electrocatalysts through morphological[168] and microstructural modification,[156, 157] and using supported copper nanoparticles.[156] However, there is increasing evidence that restructuring occurs during CO2RR and the ECSA largely determines the partial current density and consequently the product selectivity. There have also been huge efforts to use copper as the basis of more complex compositions and structures by electrodepositing other metal cations,[169-171] adding overlayers[172], forming binary alloys,[139, 141, 168, 173, 174] and phase separated structures such as core shell,[175, 176] and Janus structures.[174] For example, CO2RR using phase separated Cu-Pd Janus nanoparticles was compared with ordered and disordered Cu-Pd alloy nanoparticles, where the ordered alloy exhibited the highest faradaic efficiencies for C1 (>80%),[174] and the phase separated Cu-Pd particles for C2 products (>60%). An implication is that the product selectivity is more sensitive to the spatial arrangement of the two metals than the electronic effects arising from alloying.[174] Sequential electrocatalysis using micro-patterned Cu-Ag can control the ratio of oxygenate and hydrocarbon products, by forming high local concentrations of CO on Ag close to active Cu sites, resulting in a higher oxygenate to ethylene ratio compared to that of Cu.[177] Adjusting the Cu:Ag ratio and pattern of the electrocatalyst led to an enhanced oxygenates:ethylene ratio from 0.59 to 2.39 with FE% of oxygenates increased from 21.4% to 41.1% which was attributed to a sequential pathway for the production of oxygenates.[177] Similarly CO2RR on gold nanoparticles supported on a copper substrate is superior to monometallic Au, Cu, and their alloys.[178] The electrocatalyst (Au/Cu), was 100 times more selective toward formation of alcohols over hydrocarbons, with the formation of alcohols passing through tandem steps: first the electrochemical conversion of CO_2 into CO on Au nanoparticles followed by further reduction of CO (with high local concentration) on the copper surface. The selectivity of >2e- hydrocarbons increase by Cu based bimetallic compared to standard Cu electrocatalyst **(Figure 1.26)**. The Au/Cu exhibited an enhanced selectivity with increase in the current density **(Figure 1.26)**.[178]

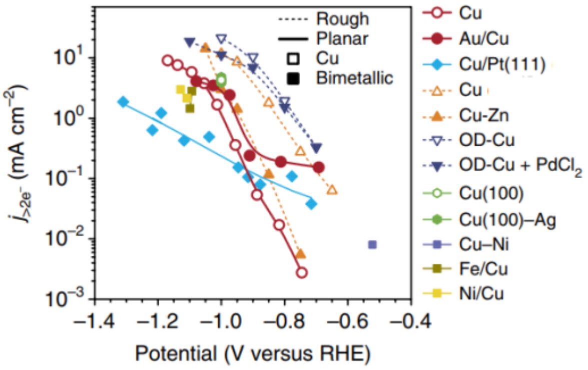

Figure 1.26: Geometric current densities for > $2e^-$ products using Au/Cu (bimetallic) and other reported Cu based electrocatalysts:[178] Cu, Au/Cu (bimetallic),[178] Cu/Pt(111) (overlayers),[179] Cu,[180, 181] Cu-Zn (bimetallic),[181] OD-Cu,[122] OD-Cu + $PdCl_2$ (added to the electrolyte),[122] Cu(100),[182] Cu(100)-Ag (alloy),[182] Cu-Ni (alloy),[183] Fe/Cu(bimetallic)[184] and Ni/Cu (bimetallic).[184]

These studies show that combinations of monometallic catalysts either as Janus nanoparticles, patterned arrays, or substrate-nanoparticle structures can exhibit synergistic behaviour, potentially overcoming the scaling problem of metal alloys, providing an opportunity for significant improvements in performance. In addition to multimetallic systems, a further option is to investigate copper containing compounds. Metal oxides, sulphides, phosphides and nitrides are common compound classes that have been investigated for a range of electrocatalytic redox reactions including CO2RR. This is in part because under the conditions of CO2RR, reduction to lower oxidation state copper species, including metallic copper, can occur. Indeed, copper compounds have also been used as a source of monometallic copper electrocatalysts that exhibit modified microstructure (and hence ESCA), which controls selectivity.[156] Recently, several groups have reported interesting results using doped or binary copper compounds which may suggest p-block elements have a direct role in modifying selectivity. Theoretical studies also suggest the potential of p-block elements to bond to intermediates which can tune the product selectivity of CO2RR[185, 186] and overcome the scaling problem of d-block metals. These topics are addressed below.

1.4.3. Copper Oxides and Monometallic Cu Derived from Copper Oxides

Copper electrocatalysts can be prepared by reduction of copper compounds which can cause topological reconstruction, modify the ESCA and defect distribution and grain boundaries,[187] in addition to compositional variation at the surface and subsurface. The most common strategy is to intentionally oxidize copper followed by electrochemical or chemical reduction. Structurally, the selectivity of copper CO2RR has been shown to be dependent on the exposed facets. For example Cu(100) shows a preference for C_2 products compared to Cu(111). Cu(100) promotes C-C bond formation to ethene and ethanol due to the low barrier for C-C bond formation through CO dimerization, although a complete interpretation is complicated by the observation of surface reconstruction under CO2RR conditions.[123, 188] Several studies have investigated the copper source, topology, route of oxidation and subsequent reduction. Copper derived from copper oxides has the ability to electroreduce CO_2 into CO and ethylene at low overpotential.[156, 189, 190] A Cu electrocatalyst with a thin film of Cu_2O resulted in an electrocatalyst of activity similar to that of polycrystalline Cu, whereas thicker films ($\geq$ 3 μm) resulted in an electrocatalyst with high roughness factors and electrochemical reduction of CO_2 at an overpotential 0.5 V lower than that of polycrystalline Cu.[156] Oxide films of thickness between 1.7 - 3.6 μm showed the best selectivity towards C_2 hydrocarbons (FE% = 34 - 39 % for ethylene and 9-16% for ethanol).[191] Cu^o was observed by in situ Raman spectroscopy analysis due to the rapid reduction of Cu_2O.[191] An O_2 plasma has also been used to control the morphology of the copper surface and the thickness of the oxide layer followed by in situ partial reduction during CO2RR.[189] The electrocatalyst exhibited a low onset potential and high faradaic efficiencies toward ethylene up to 60%.[189]

Cu nanocrystals prepared by anodising a Cu disk followed by electrochemical reduction of the formed oxides[126] gave n-propanol at an onset potential of 200-300 mV lower than that of an electropolished Cu surface[126]. The effect of crystallite size of Cu_2O-derived Cu particles showed as the crystallite size decreased from 41 to 18 nm, the FE for C_2H_4 increases greater than 4 times, which was attributed to greater concentration of adsorption sites for intermediate CO.[192] The role of CuO_x nanoparticle areal density on the product selectivity of CO2RR showed an enhancement of formation of C_2H_4 over methane using areal dense NP due to the increase in the number of active sites and the decline in the interparticle distances.[193] At low areal particle density, CO tends to leave the surface as a gas while at high areal density (small IP distance), the desorbed gas tends to be readsorbed allowing further reduction to ethylene.

CuO derived Cu nanowires show enhanced activity for CO with FE up to 50% compared to that of Cu foil.[194] Increasing the density of the Cu nanowires increases the local pH leading to enhancement of a CO coupling mechanism[124] giving greater proportions of ethylene, ethanol and ethane.[124] Mesoporous oxide-derived Cu foams increase the production rate of H_2, C_2H_4, $HCOO^-$, C_2H_6 and CH_4

on moving toward more negative voltages, whereas CO production peaks before declining, confirming its role as an intermediate for the formation of C_1 and C_2 hydrocarbons.[195] The maximum production of C_2 hydrocarbons reached a FE = 55%, which was attributed to the in operando reduction of Cu_2O causing the formation of a large number of active sites available for C-C bond formation.[195] An ordered porous Cu electrode derived from a Cu_2O inverse opal exhibited an enhanced performance toward the conversion of CO_2 into CO and HCOOH with FE of 45.3% and 33.6% **(Figure 1.27)**, respectively, which are higher than Cu particles prepared under the same conditions.[196] The authors attributed the enhancement to the stabilization of $CO_2^{\cdot}$ radical on the electrocatalyst surface of the inverse opal. Electro-redeposition of Cu from a sol-gel was used to control the nanoscale morphology and stabilize Cu(I) at negative potential,[197] giving an enhanced ethylene:methane ratio of 200:1 and current densities of 160 mA/cm^2 at -1.0 V (RHE).[197] A chrysanthemum-like Cu nanoflower electrode derived from CuO suppressed H_2 evolution by 25% and can reduce CO_2 at lower overpotential than Cu foil giving HCOOH (~50%), C_2H_4 (~10%), and CH_4 (~5%).[198]

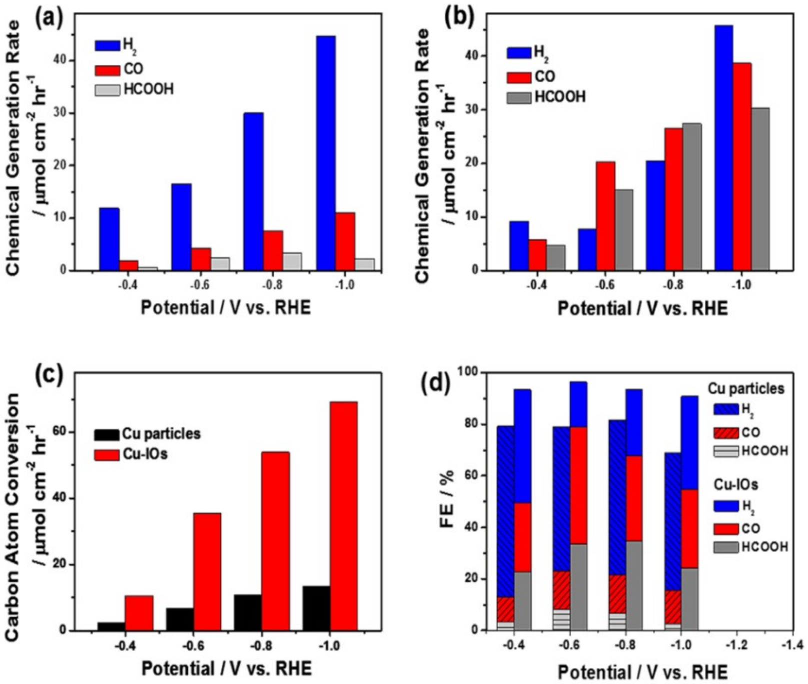

Figure 1.27: CO2RR performance of(a) chemical generation rate as a function of potential for Cu_2O derived inverse opals; (b) chemical generation rate as a function of potential for Cu particles, (c) carbon atom conversion rate as a function of voltage and (d) FE of all the products in 0.1 M $KHCO_3$.[196]

A 3D porous hollow Cu fibre was prepared by spinning a CuO nanoparticle-polymer composite showed an enhanced performance toward the production of CO with FE of 72% at -0.4 V (RHE) **(Figure 1.28)**.[163] The fibres can operate efficiently for 24 h.[163] The high percentage of CO was attributed to the defect rich porous structure and favourable mass transport in the fibre that removes CO before further reduction to C_{2+} hydrocarbons. Porous dendritic copper containing ca. 10 % Cu_2O gave formic acid with FE = 90% using ionic liquid/water as electrolyte[199] and was reduced in situ to <5% Cu_2O. Sponge-like Cu electrocatalysts have been prepared by electro-deposition and annealing which induces the formation of Cu_2O,[200] where the annealed electrode exhibits FE of 32.3% for (C_2H_4, C_2H_6) while electrodeposition give an FE of 29.1%.[200]

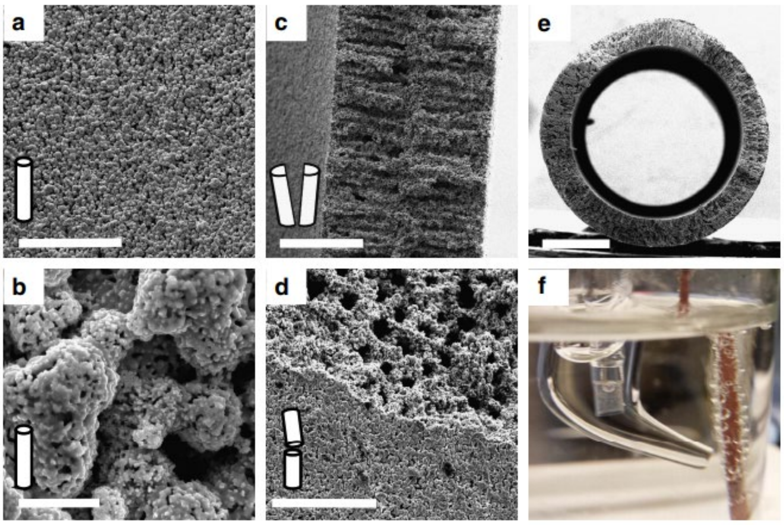

Figure 1.28: SEM images of Cu hollow fibre (a-e) and (f) Electrochemical system with Cu fibre as WE for CO2RR.[163]

A bi-phasic Cu_2O-Cu electrocatalyst succeeded in converting CO_2 into C_3 and C_4 hydrocarbons and oxygenates such as n-propanol and n-butane.[128] Cu_2O was reported to be stabilised by the existence of Cl^- ions, which resulted in the formation of multi-carbon products due to the ability of Cu(I) to bind the intermediate strongly enough to allow further reduction.[128] Collectively these studies suggest that the topology and route to fabrication dramatically affect CO2RR selectivity. However, as stated, the critical feature of the multitude of morphologies and macrostructures is likely to be the ECSA, which is complicated by the possibility of CO2RR induced topological reconstruction. Furthermore, it is also clear that oxide formation occurs on fabrication, either intentionally or not, and most discussion is based on ex-situ analysis before and after CO2RR which does not represent the in operando surface chemistry of CO2RR.

1.4.4. Subsurface Oxides, Grain Boundaries, and Cu Oxidation State

Several studies have proposed that subsurface oxygen in oxide derived Cu electrocatalysts enhances CO2RR .[201, 202] The role of subsurface oxygen in CO2RR has been studied theoretically using DFT, which predicts that the subsurface oxygen can strengthen the CO_2 and CO adsorption energies explaining the difference in product distribution between pure copper and copper oxides.[203] The role of Cu^+ species on the surface of the plasma-activated Cu electrode using Operando X-ray absorption spectroscopy and cross-sectional scanning transmission electron microscopy,[189] showed the unusual stability of Cu^+ and its prominent role in lowering onset potential and enhancing C_2H_4 formation.[189] An in situ ambient pressure XPS and STEM-EELS study supported by DFT simulations shows the presence of residual oxygen but no copper oxide suggesting that subsurface oxygen enhanced selective CO2RR to ethylene.[204] The importance of surface and subsurface oxygen has also been studied on a cubic morphology with predominantly Cu(100) facets.[205] The oxygen content was modified using an O_2 plasma and showed enhanced FE for ethylene and current density **(Figure 1.29)**.[205]

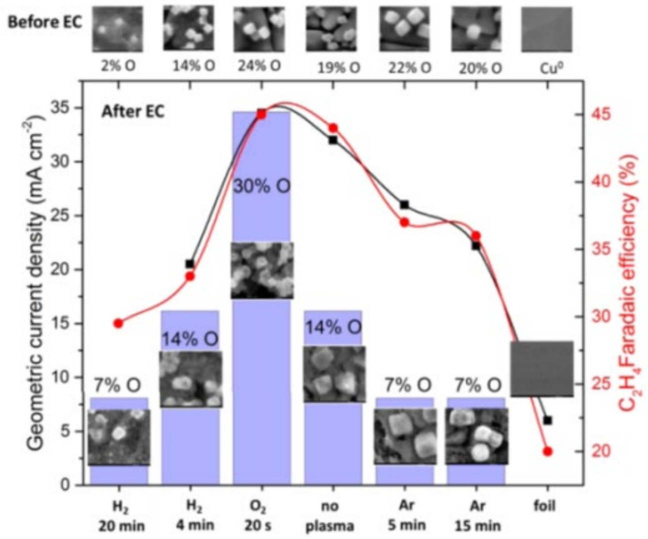

Figure 1.29: The effect of oxygen percentage on the current densities and on FE% of C_2H_4 after 1 h of CO2RR at -1.0 V vs RHE in 0.1 M $KHCO_3$.[205]

However, other studies using labelled ^{18}O show that <1% of ^{18}O remained after CO2RR. Copper oxides prepared using ^{18}O labelled oxygen gave FE for C_2/C_3 of 60 % and it was shown that oxide-derived copper can be rapidly reoxidized, thus compromising ex situ analyses.[206] The enhanced electocatalytic performance compared to copper foil was attributed to the high density of grain boundaries.[207, 208] Earlier work has suggested that grain boundaries play a role in modifying the selectivity of CO2RR. Electroreduction of CO into hydrocarbons using oxide-derived nanocrystalline copper was investigated using three different electrocatalysts prepared by annealing and reducing electrochemically (OD-Cu 1), by hydrogenation (OD-Cu 2) or commercial copper nanoparticles (prepared by vapour condensation).[209] HRTEM images showed different boundaries; commercial nano-particles showed aggregation of overlapping particles while the other two electrodes exhibited distinct grain boundaries between nanocrystallites **(Figure 1.30)**.[209] The oxide-derived copper electrocatalyst showed enhanced performance toward the production of oxygenates (ethanol, acetate and n-propanol) with FE of 57% at -0.25 volts to -0.5 V (RHE) compared to the Cu nanoparticles which produce H_2 (FE = 96 %), which was attributed to strong CO binding at grain boundaries .[209]

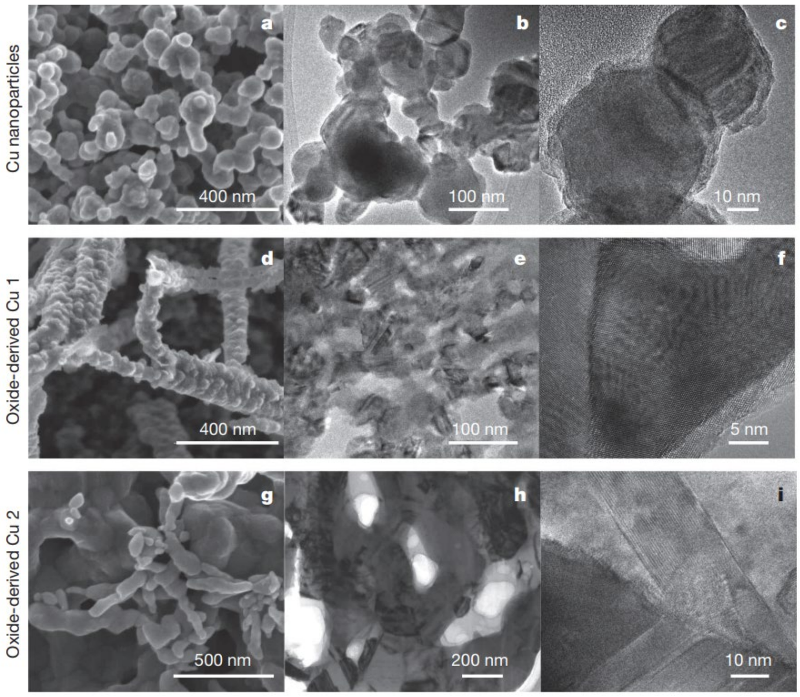

Figure 1.30: Electron microscopic images of Cu nanoparticles (a-c), and OD-Cu-1 (d-f) and OD-Cu 2 (g-i) electrocatalysts: SEM images (a, d and g), low-magnification TEM images (b, e and h) and HRTEM (c, f and i).[209]

Studies on the role of Cu oxidation state have suggested additional phenomena should be considered. Theoretical studies have predicted a synergistic effect between Cu^+ and Cu^o on the surface of Cu results in improved kinetics of CO_2 activation and CO dimerization,suppressing the formation of C1 compounds **(Figure 1.31).**[187, 201]

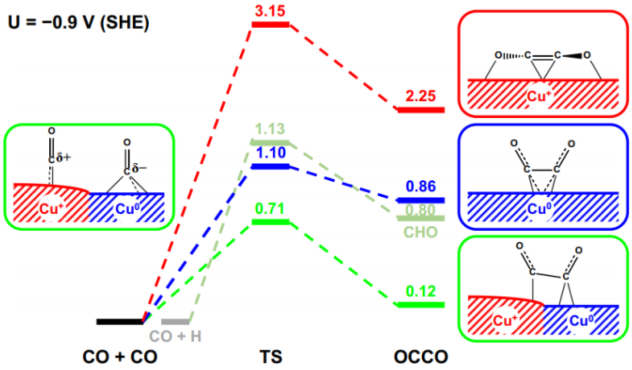

Figure 1.31: Energy profile of CO dimerization.[201]

In an experimental study three Cu electrocatalysts were prepared with different oxidation states (Cu°, Cu^+ and Cu^{2+}).[210] and investigated using x-ray spectroscopy and in situ microreactors to monitor the electronic structure during the preparation and electrocatalysis. During CO2RR, Cu° and Cu^+ exhibted the same behavior starting with 100% H_2 at -0.9 V vs Ag/AgCl followed by CO at -1.2 V, then C_2H_4 and CH_4 appeared at more negative voltages. Cu^{2+} showed less activity for carbonaceous species compared to Cu° and Cu^+. The properties of the electrocatalyst surface, subsurface and bulk were affected by the formation of Cu^{2+} carbonates giving rise to a passivation layer which blocks electron transfer causing catalyst deactivation. Desorption requires partial reduction of the electrode and the layer can be dissolved by applying a negative potential in an acidic medium **(Figure 1.32)**.[210]

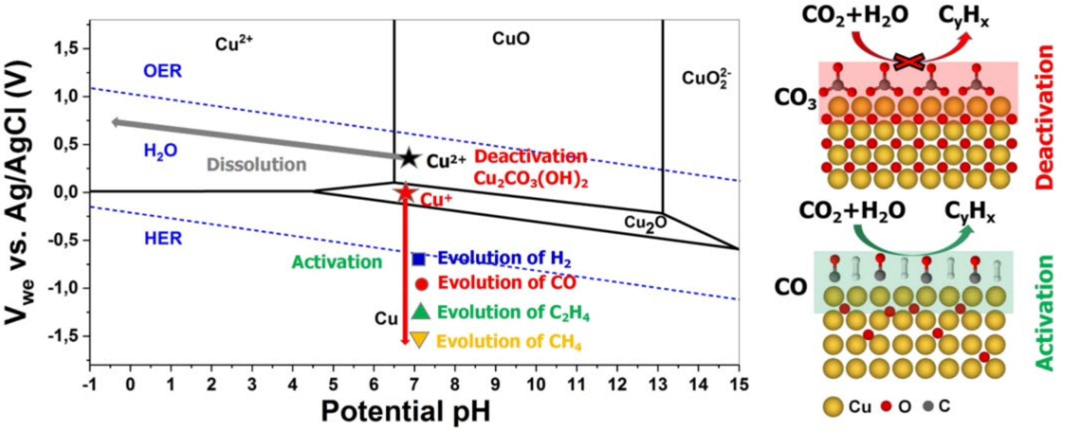

Figure 1.32: Porbaix diagram with electrochemical performance of different Cu based electrocatalysts.[210]

More recently CO2RR using mixed $^{12}CO_2$ and ^{13}CO showed that there are product-specific active sites on oxide derived Cu electrocatalysts.[211] Three types of active site are proposed, for ethanol and acetate, for ethylene, and for 1-propanol, respectively, based on the isotopic fraction of ^{13}C found in each product as a function of the voltage (current density).[211] These sites are not found on polycrystalline copper or orientated (100) and (111) surfaces, showing that CO2RR does not result in surface reconstruction of the oxide derived electrocatalyst to a surface identical to polycrystalline copper. Therefore Cu compounds can exhibit intrinsically different reactivity than monometallic Cu and do not just represent an alternative route to Cu electrocatalysts with a modified ECSA.

1.4.5. Copper chalcogenides (S and Se) modified or derived copper based electrocatalysts

Given that oxide modification causes an intrinsic change to the selectivity of Cu electrocatalysts, there has been growing motivation to investigate other Cu compounds. The study of Cu sulfides has also been partly motivated by the anticipated reduced hydrogen bond strength of sulfur compounds compared to oxides, which would likely reduce competing proton reduction to dihydrogen. Density function theory studies have been used to investigate the ability of transition metal chalcogenides to act as potential electrocatalyst for CO_2. The active edges sites of TMC (Mo based chalcogenides) are selective and can stabilize COOH and CHO intermediates through S or Se bridging at the edges. [212, 213]

Indeed recent studies have shown that formate production from CO2RR in particular is enhanced at low potentials on sulphur modification of copper.[214, 215] For example when a Cu_2O film is reduced and immersed in an ammonium polysulfide solution the surface reconstructs acquiring 1-2 at% of S giving a surface of Cu and CuS_x. Sulfur doping converted the regular behaviour of oxide-derived copper from the production of various products to the production of formate with 75% FE at -0.8 V (RHE). HER is suppressed and no CO is detected which likely explains the absence of any other hydrocarbon or oxygenate products, which are formed via CO.[215] In a complementary study, copper sulphide electrocatalysts prepared from hydrothermally synthesized CuS particles electroreduce CO_2 into formate with faradaic efficiency reaching 80% at -0.8 V (RHE).[185] Under the reducing conditions of CO2RR all electrocatalysts undergo rapid reconstruction to smaller particle sizes, with larger initial starting particles giving the greatest FE. Less than 2 at% of S remains after reconstruction again suggesting that very low surface concentrations are required to significantly affect selectivity.[185] CO2RR in an ionic liquid ($BmimBF_4$/MeCN) has also been reported using electrodeposited Cu_2S on a copper foam giving a maximum FE of 85% for formate at -2.0 (Ag/Ag^+) and a current density of 5.3 mA/cm^2 indicating the ability of Cu_2S to stabilize the CO_2^- intermediate leading to formate.[214] H_2 was the only detectable gaseous product.[214]

More recently, experiments to elucidate mechanistic features have been undertaken using surface enhanced infrared absorption spectroscopy (SEIRAS). [216] Electrodeposited sulphur on copper gave reconstruction to a nanowire morphology and post electrocatalysis analysis by XPS and EDS showed the presence of sulphur in unquantified trace amounts.CO2RR using sulphur derived copper (SD-Cu) gave a FE of ca. 70 and 30% for formate and dihydrogen, respectively at -0.8V. SEIRAS was used to probe the surface species and showed that SD-Cu strongly adsorbs CO in comparison to OD-Cu and that formate production is consistent with direct hydrogenation of surface bound CO_2 **(Figure 1.33)**.[216] No CO product was detected for SD-Cu in contrast to OD-Cu and it has been suggested that subsurface S could be responsible for increasing CO adsorption energy in a similar way suggested for the OD-Cu compared to monometallic Cu. Overall, strong CO adsorption retards HER increasing the selectivity for formate.[216] In related work it has previously been shown that on a Cu(100) surface, S atoms induce long-range modifications affecting the CO binding**.**[217] CO binding is modulated at second and third nearest neighbour sites giving weaker and stronger CO adsorption, respectively.[217]

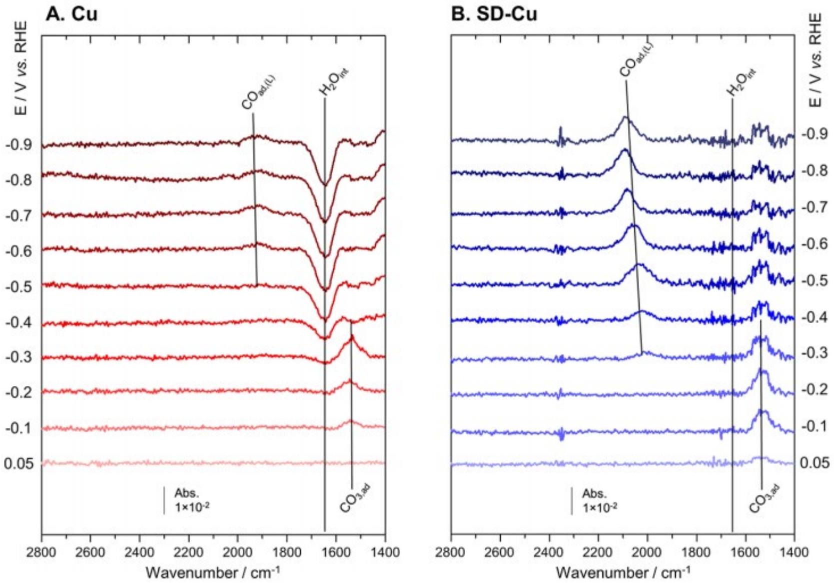

Figure 1.33: In situ SEIRAS during CO2RR for (A) Cu foil and (B) SD-Cu.[216]

A combined experimental and DFT study investigated S, Se and Te modified Cu showed only S gives enhanced formate selectivity. Time-of-flight secondary ion mass spectrometry (ToF-SIMS) showed that the chalcogenide is present on the surface after CO2RR and DFT implies the S surface adatoms act as basic sites, aiding transfer of H to adsorbed CO_2 and also preventing CO_2 dissociation to CO.[218] Overall these studies suggest formate production is promoted by basic S atoms for H transfer to $CO_2^{\cdot}$ and the strong CO bonding prevents HER and the formation of C_{2+} products.

Core shell nanoparticles comprising a Cu_2S core covered with vacancy rich Cu (Cu_2S-Cu-V) exhibit CO2RR with increased selectivity for C_{2+} alcohols. At 0.95 V vs RHE, the FE of ethanol and propanol was at a maximum of 8 and 15 % respectively, representing a 44-fold increase compared to bulk copper at -0.95 V

(RHE).[131] At lower potentials, formate predominates with 66% observed at 0.85 V, similar to other Cu-S systems. After CO2RR, the sulphur content of the particles reduces but it is not clear if surface S atoms are present. An interesting feature of this work was to perform CO2RR in 1M KOH which increased the FE of C_{2+} liquid alcohols to 32% with a partial current density of 126 ± 5 mA cm^{-2}, which represents a greater than 2-fold increase in FE and partial current density compared to bulk copper **(Figure 1.34)**.[131] DFT calculations predict that metal vacancy defects on the copper surface enhance the electrocatalytic performance of the Cu electrocatalyst towards C_{2+} through tuning of the electronic structure of neighbouring atoms and the energy barriers of the rate-limiting reaction intermediates.[131, 219] Mechanistically, electrochemical reduction of CO_2 into ethene and ethanol share the same pathway via dimerization of a CO intermediate to an CH_3CHO intermediate that can undergo either a loss of the adsorbed oxygen atom to form ethylene or further reduction to ethanol. DFT showed that pristine Cu has a low energy barrier towards C_2H_4 and C_2H_5OH while Cu_2S-Cu-V has a low barrier for ethanol compared to that of ethylene attributed to modification of the Cu(0) surface by the $Cu(I)_2S$ support **(Figure 1.34)**.

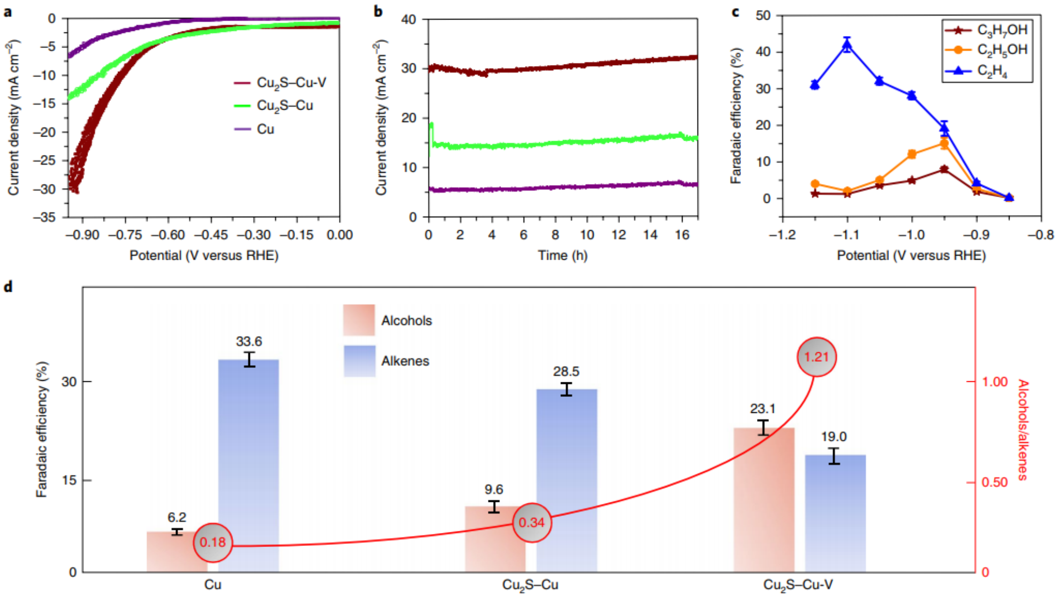

Figure 1.34: (a) LSV in 0.1 M $KHCO_3$ saturated with CO_2, (b) constant voltage experiments at -0.95 V RGE, (c)faradaic efficiencies of different products using core shell valence system and (d) FE% of alkene and alcohols from the different electrocatalysts at -0.95 V (RHE) in 0.1 M $KHCO_3$.[131]

Copper selenide based electrocatalysts were investigated for CO2RR. The electrocatalyst was efficient for the electrochemical reduction of CO_2 into methanol with FE% reaching 77.6% at overpotential of 285 mV. The reported current density was relatively high (41.5 mA/cm^2) compared to previous literature.

1.4.6. Electrocatalysts based on copper nitrides and phosphides

In work related to that of Cu_2S-Cu-V, core shell Cu on Cu_3N exhibits the formation of C_{2+} products up to a combined Fe of 64 % (ethane 39%, ethanol 16% and propanol 6%) at -0.95 V (RHE), representing a 40-fold increase over bulk Cu primarily at the expense of methane **(Figure 1.35)**.[220] Again the inner support (Cu_3N) is proposed to modify the electronic structure of the Cu(0) surface, affecting the interaction of CO with the surface, thus modifying adsorption and CO dimerization. The suppression of methane production in the case of Cu on Cu_3N (and Cu on Cu_2O) compared to bulk Cu was not attributed to a rise in local pH on the basis of similar current densities indicating comparable proton consumption. Grain boundary effects were also excluded on the basis of the rapid conversion of Cu(I) to Cu(0) observed for Cu-on-Cu_2O under CO2RR conditions compared to Cu-on-Cu_3N. The > 30 h stable production of multi-carbon products observed for Cu-on-Cu_3N **(Figure 1.36)** is consistent with reduction in the energy barrier of CO dimerization in the rate determining step, promoted by the $Cu(I)_3N$ core and is supported by DFT calculations.[220]

Copper phosphide (Cu_3P/C) electrocatalyst was prepared through the direct phosphidation of Cu based metal organic framework (HKUST-1) for CO2RR. The authors reported the ability of their electrocatalyst to electroreduce CO_2 to CO with FE = 47% at a relatively low overpotential of -0.3 V RHE with a low current density of (≈0.05 mA/cm^2).[221]

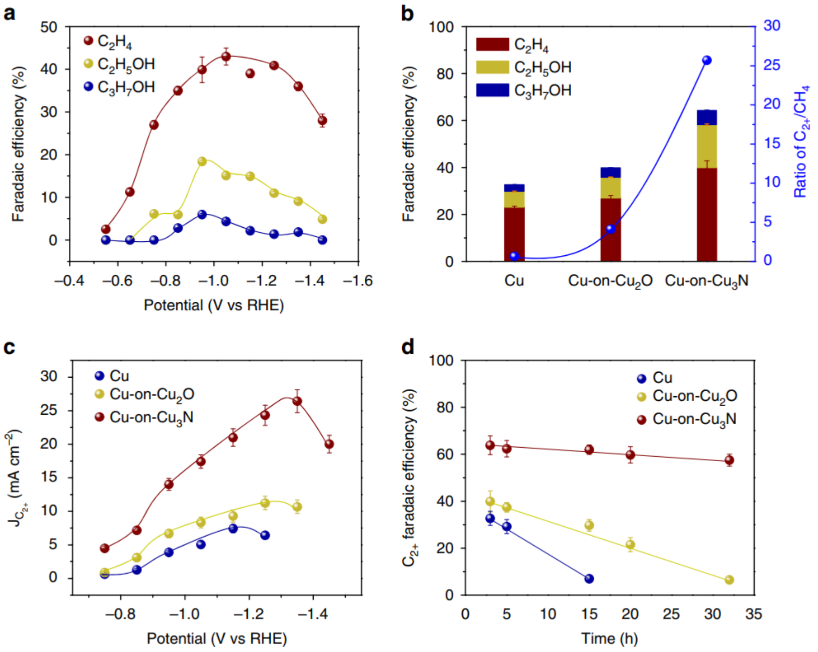

Figure 1.35: FE% of each products using different electrocatalysts as a function of voltage, (b)FE% of multi-carbon products at -0.95 V (RHE), (c) geometric partial current densities of at different voltages on the electrocatalysts and (d) long term stability test.[220]

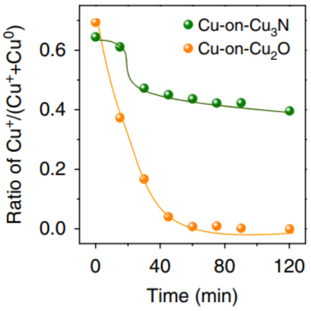

Figure 1.36: Relative ratio of Cu(I) during CO2RR at -0.95 V (RHE) in 0.1 M $KHCO_3$ (measured through a Cu K-edge XAS spectra).[220]

1.4.7. Copper halide derived electrocatalysts and halide effects

Electroreduction of bulk Cu in KCl leads to the formation of CuCl films that on reduction under CO2RR conditions at -0.99 V (RHE) result in Cu mesocrystals.[222] At -0.99 V the mesocrystals are selective for the production of C_2H_4 with an FE = 81%, which is 18-fold more than copper nanoparticles and can operate for 6 h. HRTEM images revealed the predominance of Cu(100) facets which are known to be active sites for the conversion of CO_2 into C_2H_4 due to strong CO adsorption.[205, 222] In a related study, bulk Cu was covered by a film of CuCl by reaction with H_2O_2 and HCl followed by oxidation to Cu_2O and electrochemical reduction under CO2RR conditions to give a reconstructed Cu surface. Again selectivity for C_{2+} hydrocarbons was observed with FE = 73% at ca -2.6 V (Ag/AgCl) with current density of ≈17 mA/cm^2 in H-Cell configuration.[223] The authors proposed reconstructed morphologies as a strategy to tune the selectivity toward multi-carbon products **(Figure 1.37)**. Using a flow cell configuration, current densities reached 336 mA/cm^2 with 84% selectivity for C_{2+} products.[223] Copper oxide and copper bromide composite films were prepared electrochemically on a GDE. Ethylene and hydrogen were the main products (FE% of C_2H_4 was about 10 %). Interestingly, lowering the temperature to 3 °C enhance the FE% of ethylene massively which reached 68%.[224]

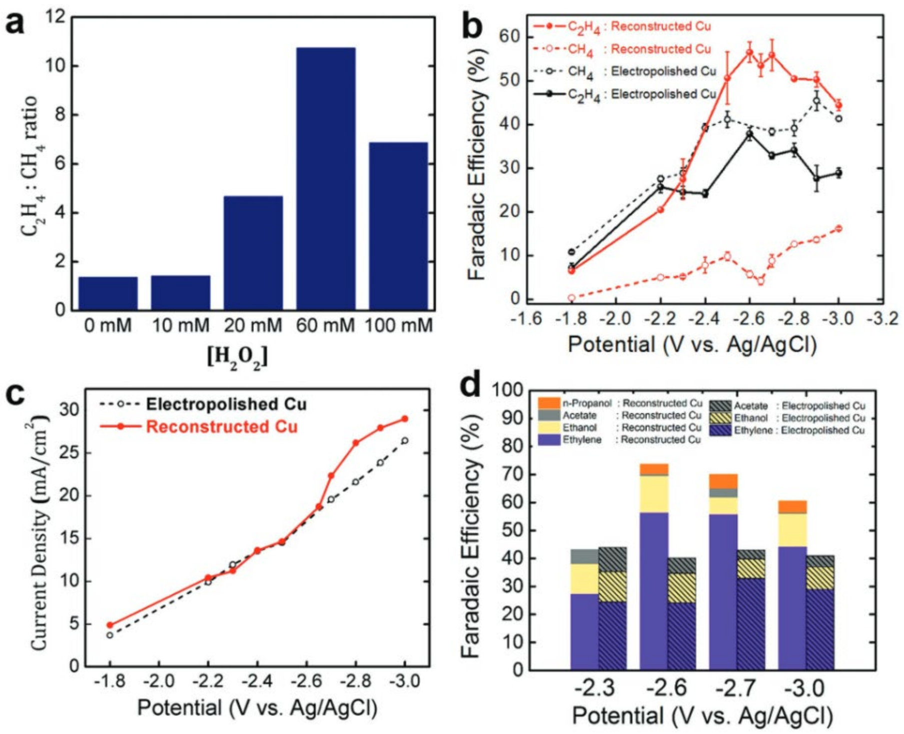

Figure 1.37: Electrochemical performance of reconstructed electrocatalyst toward CO2RR (a) the effect of H_2O_2 in the C_2H_4:CH_4 ratio, (b) FE% for CH_4 and C_2H_4 as a function of potentials, (c) LSV chart in 0.05 M $KHCO_3$ and (d) FE% of all C_{2+} products as function of voltages.[223]

1.4.7.1. Effect of halides

Halides are a common electrolyte component and CO2RR is found to be dependent on the halide and its concentration. Possible roles include reaction with Cu to induce electrode reconstruction, the formation of Cu-halide compounds, and interaction with adsorbed surface species. Upon using iodide ion well-defined Cu nanostructures have been observed in contrast to the other halides **(Figure 1.38)**.[225] Interestingly, halides help to lower the overpotential and increase the current densities without affecting the product selectivity toward C_2-C_3 (≈65% at -1.0 V (RHE) in the order Cl^- < Br^- < I^-. The role of the halides was attributed to specific adsorption on the Cu surface during CO2RR.[225] Halide anions can cause nanostructuring of the oxidized Cu surface even at open-circuit potential forming Cu nanocrystals.[225] In a related study, CO2RR using an O_2-plasma activated Cu electrocatalyst was investigated in a series of electrolytes, which showed that Cs^+ and I^- results in an increase the C_{2+}/C_1 ratio giving FE = 69% and i_{C2+} = -45 mAcm^{-2} at -1.0V (RHE).[226] The increase is attributed to surface reconstruction and the formation of CuI, and DFT studies indicate the presence of Cs^+ and I^- at the surface promotes the formation of CO2RR intermediates which is also enhanced by subsurface oxygen.[226]

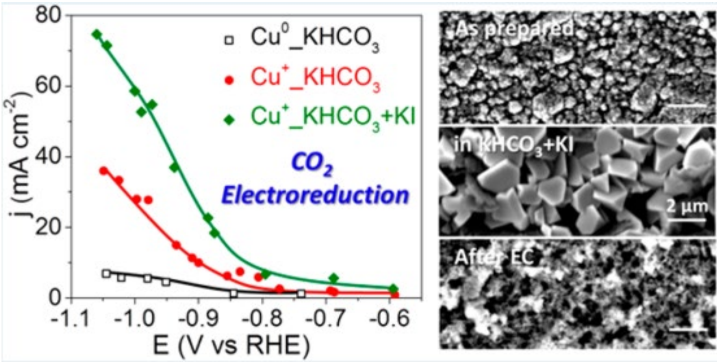

Figure 1.38: (left) LSV of CO2RR upon using different electrolyte solution and (right) SEM images showing the role of the iodide on the morphology.[225]

1.5. 3D printing

This thesis describes the use of a 3D printer to build copper-based electrocatalysts through preparing a very viscous ink (direct writing). 3D printers have been used in different aspects of science and a wide range of practical applications. Recently, 3D printers have shown success in building catalyst monoliths,[227, 228] batteries,[229] and structures for chemical synthesis.[230] 3D printers have the capability to be used in mass production of the desired product. This advantage reduces the distance between research and industry.

Our aim was to print copper oxide structures to be reduced either electrochemically or by hydrogenation. To improve the intrinsic properties of the copper electrocatalyst, a copper phosphide layer was prepared on the surface of the copper plate. Physico-chemical characterizations have been performed to investigate the properties of the prepared copper-based electrocatalysts and to prove the ability of 3D printer to be used for building electrocatalysts.

1.5.1. General mechanism of 3D printing through fused deposition modelling (FDM)

A filament is used to be connected to an extruder then melts at the hot end of the 3D printer head. The molten filament flows through a nozzle **(Figure 1.39)**. The motion of the 3D printer head controls and builds the desired structure on the bed. The commercial filament usually contains 35% of Cu and the remaining percentage is polymer like PLA. It is very easy to build a Cu based structure using Cu based filament. The problem is that the removal of the polymer (organic content), through thermal treatment, would cause deformation of the structure.

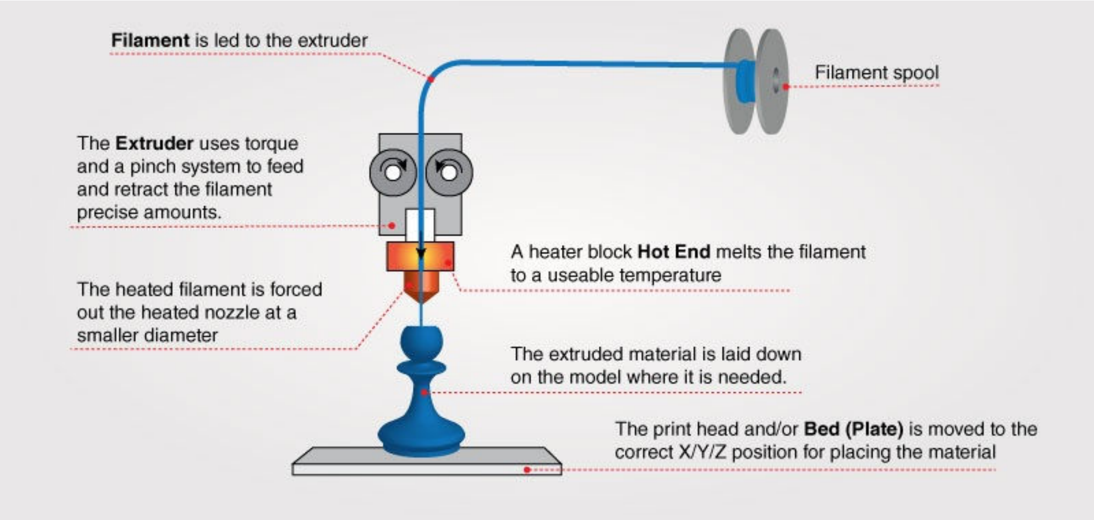

Figure 1.39: mechanism of 3D printing using a filament.[231]

The current work is not the first time to use 3D structure in chemistry nor the first time to use 3D printing. The current project was inspired by previous works in different fields including CO2RR[163], catalysis[228] and batteries.[229] Mul et al (2016) fabricated a 3D porous hollow Cu fibre for CO2RR. The Cu based fibre prepared by spinning showed an enhanced performance toward the production of CO with FE% of 72% at -0.4 V (RHE) **(Figure 1.40)**.[163] Mul et al used Cu powder, PEI polymer and N-methylpyrrolidone as a solvent. After mixing, the spinning was performed at room temperature through stainless steel vessel under pressurised nitrogen (1 bar).[163]

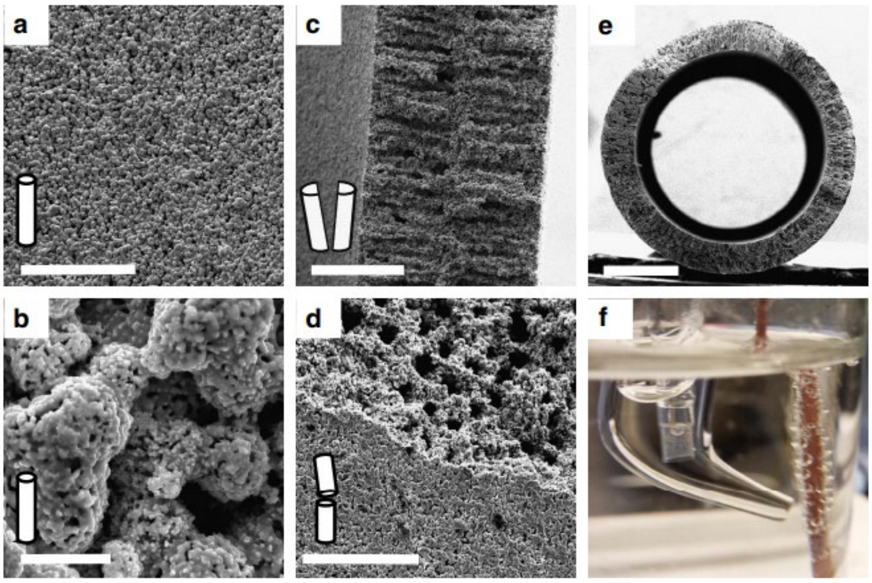

Figure 1.40: SEM images of Cu hollow fibre (a-e) and (f) Electrochemical system with Cu fibre as WE for CO2RR.[163]

Gil et al (2016) developed a heterogeneous Cu/Al_2O_3 catalyst with a woodpile porous structure **(Figure 1.41)**.[228] The Cu based structure was built using a Cu based ink consisting of Cu powder, Al_2O_3, copper nitrate and viscosity modifier (hydroxypropyl methylcellulose). The prepared ink was loaded in a syringe and the structure was built using a robotic deposition A3200 system (Aerotech) under pressure 21 bar.[228]

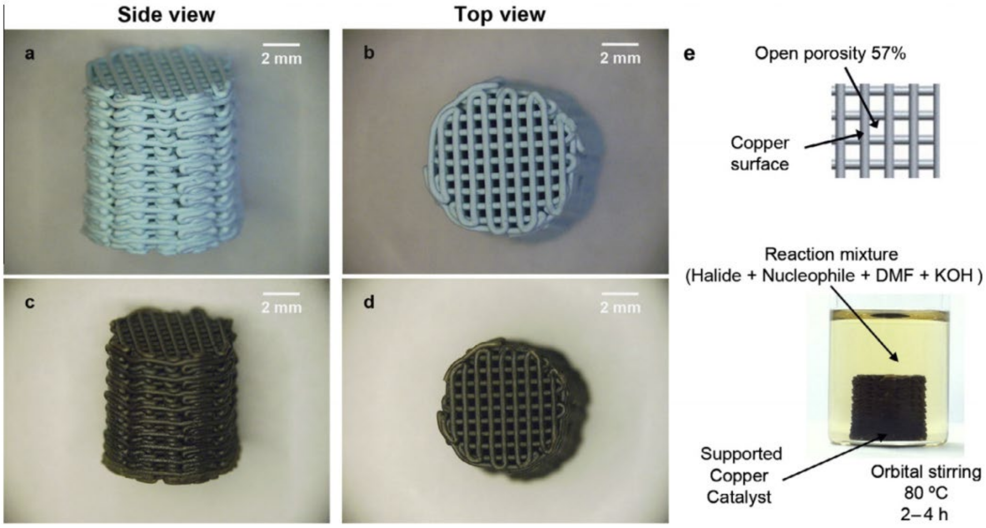

Figure 1.41: Woodpile heterogeneous Cu/Al_2O_3 based catalyst.[228]

Lewis et al (2013) developed a 3D printed Li-ion microbattery **(Figure 1.42)**.[229] The microbattery was 3D printed prepared using two inks for the anode ($Li_4Ti_5O_{12}$) and for the cathode ($LiFePO_4$), the two inks also contained deionized water, ethylene glycol, glycerol, and cellulose-based viscosifiers. After building the 3D structures, the structures were annealed at 600 °C for 2 h.[229]

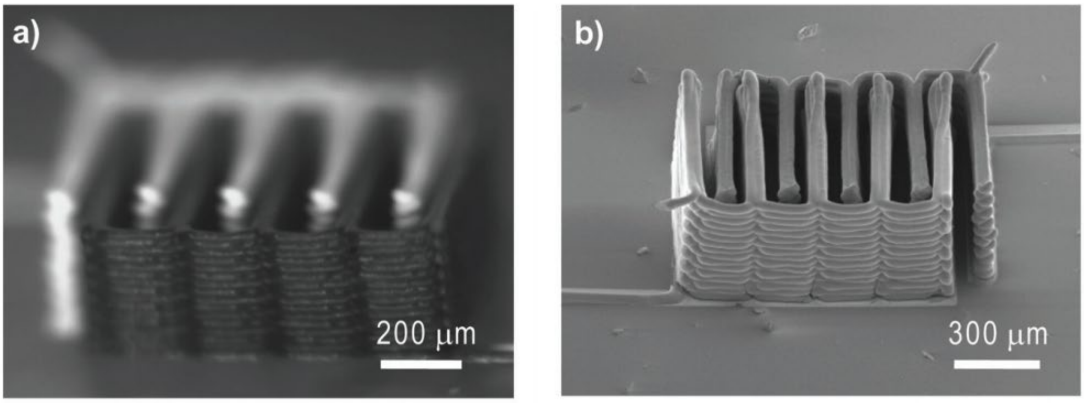

Figure 1.42: (a) optical and (b) SEM images of the 3D printed microbattery after annealing.[229]

The current project aims to build a 3D printed Cu based electrode. To avoid using low Cu content based filament or preparing new filament, we decided to prepare a viscous ink. Using a viscous ink can allow also avoid the melting step using hot end. The viscous ink was filled in a barrel and connected directly to the extruder with passing through the melting step. The prepared structures were subjected to thermal treatment to remove any organic content (polymer and solvents) followed by reduction by hydrogenation and electrochemical reduction.

2. Experimental

2.1. Materials

All the chemicals were of analytical grade. All solutions were prepared using ultrapure water (18.2 MΩ.cm). Carbon cloth (Spectracarb 2050A-1550) and Nafion-117 were purchased from Fuel Cell Store. Stainless steel gauze type-316 and $KHCO_3$, copper powder (0.5-1.5 micron), 1,3,5 trimethoxybenzene were purchased from Alfa Aesar. A copper foil of thickness 0.25 mm, 99.98% trace metals basis was purchased from Goodfellow. $FeSO_4.7H_2O$, $FeCl_3.6H_2O$, $Co(NO_3)_2.6H_2O$ Polyoxyethanyl-alpha-tocopheryl sebacte (PTS), formic acid, Pd/C (5%wt), polyethylineimine, hydroxylpropyl methyl cellulose potassium-*tert*-butylate, triphenylphosphine, silicon antifoam (30%, emulsion) and H_2SO_4 were purchased from Sigma Aldrich. $KHCO_3$ and NaH_2PO_2 and K_2HPO_4 were purchased from Fisher and Acros chemicals. K_2HPO_4 and glycerol were purchased form Fisher. 2,6-dichloro-pyridine was from TCI. Gas cylinders (NH_3, CO_2, H_2(5%)/N_2 and standard mixture cylinders) were purchased from BOC. Ethylene glycol was purchased from Lancaster. Gold foil (0.1mm was purchased from Testbourne Ltd. Chromium trioxide (CrO_3) and 2-sulfoterphthalic acid monosodium salt were purchased from BDH and TCI, respectively.

2.2. Physical characterization

The electrocatalysts were characterized using scanning electron microscopy (SEM) using JEOL-7800F Prime. X-ray diffraction (XRD) of the electrocatalysts was performed using a Bruker D8 powder diffractometer with a Cu source (Cu Kα, 40 kV, 40 mA). The transmission electron microscope imaging was performed by Dr Jon Barnard using a JEOL 2010 TEM with a LaB6 electron source. It operates at 200 kV, which gives the electrons a wavelength of 2.51 pm. It uses the digital camera Gatan MultiScan 794 CCD. X-ray photoelectron spectroscopy (XPS) spectrum was measured on a Kratos Axis Supra spectrometer equipped with a monochromated Al kα (Al Kα = 1486.9 eV). XPS analyses were performed in the EPSRC National Facility for XPS ('HarwellXPS'). The fitting of the XPS data was also performed by the Harwell facility. NMR spectra were run on Bruker (^{1}H NMR 500 MHz) spectrometer. PerkinElmer Spectrum Two FT-IR Spectrometer was used to recorded IR spectra. CHN elemental analysis, thermal gravimetric analysis (TGA), Brunauer–Emmett–Teller (BET) (77 K N_2-adsorption) using TriStar 3000. The samples were degassed with Ar at 110 ^oC for 4 h.

2.2.1. The preparation of TEM samples

The TEM images were taken using samples prepared using focused ion beam SEM.[232, 233] The focused ion beam SEM (FIBSEM) was performed using a FEI Nova 200. The liquid metal ion source is Ga. The bulk milling is done at 30 keV with between 3 nA (for fast, rough cutting) down to 10 pA for final milling. The samples were lightly milled with the Ga ion beam at 5 keV. This reduces the amount of beam damage on the sample surface, from about 25 nm down to about 3-5 nm (the lower energy ions penetrate less than the faster ones). All the SEM images were taken with a 1.3 nA 5 keV beam. All the samples were extracted using the FIB 'lift-out' technique in which a fine tungsten needle is used to extract a thin lamella which was attached to a copper OmniProbe pillared 'grid' using ion-beam deposited platinum (the precursor is Methylcyclopentadienyl (trimethyl) Platinum (IV)).

The iron phosphide samples and 3D printed OD-Cu electrocatalyst based samples were prepared using FIB techniques. The Cu_3P samples were prepared by scratching some of the iron phosphide particles from the electrocatalyst surface. After grinding the samples using a mortar, the powders of the samples were placed on a Cu grid.

2.3. Hydrogen evolution reaction

2.3.1. Preparations of FeP/CC electrocatalysts

FeP/CC electrocatalysts were prepared according to procedures reported in the literature.[70, 71]

Electrodeposition: carbon cloth (1 x 2 cm^2) was electroplated in a single compartment electrochemical cell in 0.1 M $FeSO_4.7H_2O$ by applying -10 mA/cm^2 for 20 min at room temperature. The electroplated cloth was rinsed with milli-pore water and then left to oxidize/dry the iron overnight. Pt wire and Ag/AgCl were used as counter and reference electrode, respectively. After the electrodeposition process, a grey layer of Fe appeared on the surface of the carbon cloth, after the oxidation the grey film converted to orange film of the FeO(OH) **(Figure 2.1a)**.

Spray-pyrolysis: Portable ultrasonic Nebulizer (MY-520A) was filled with 0.1 M $FeCl_3$ (aqueous) to produce vapours that were directed through a metallic tube of diameter 1.0 cm at 1.0 cm above the carbon cloth substrate (1 x 2 cm^2) which was heated at 500 ^{o}C for 20 min prior the spraying **(Figure 2.2)**. After the spraying process, a red film **(Figure 2.1b)** immediately appeared on the surface of carbon cloth then the carbon cloth transferred to the tube furnace for the phosphidation process.

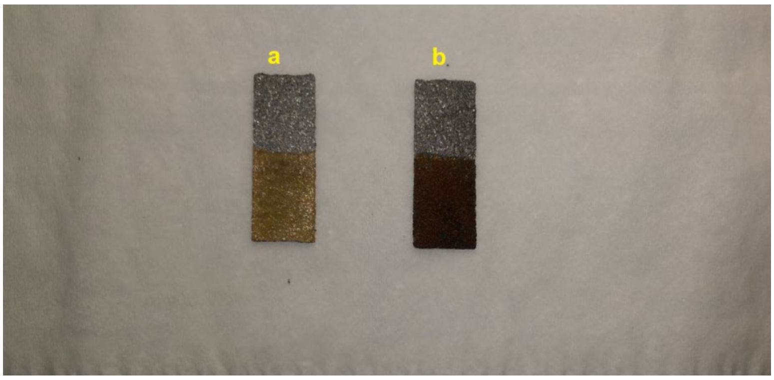

Figure 2.1: Iron oxides prepared by (a) electroplating (FeOOH) and (b) spray-pyrolysis (Fe_2O_3).

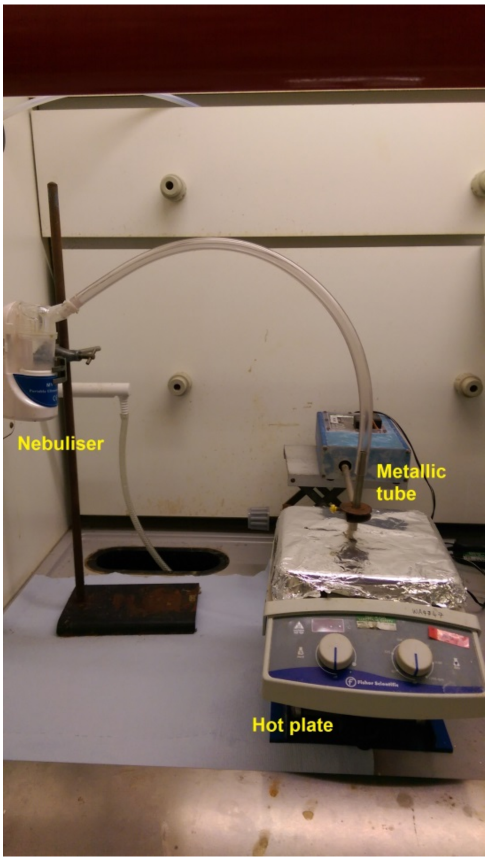

Figure 2.2: Spray-pyrolysis setup.

Phosphidation: each of the carbon cloth substrates with deposited FeO_x was subjected to a low temperature phosphidation process by heating an excess of NaH_2PO_2 (1: 10 FeO_x: NaH_2PO_2) within a tube furnace using two alumina boats. The first boat contains NaH_2PO_2 and the second one contains the carbon cloth substrates. The furnace was heated to 300 °C with a heating rate of 1.5 °C/min for 2 h with an Ar flow rate of 5 mL/min. After the phosphidation process, a black films appeared on the carbon cloth **(Figure 2.3)**. The mass of FeP_x on the carbon cloth ranged between 0.40 – 0.50 mg for spray-pyrolysis and 4.66 – 4.96 mg for the electroplating method (mass loadings were measured by a high precision balance).

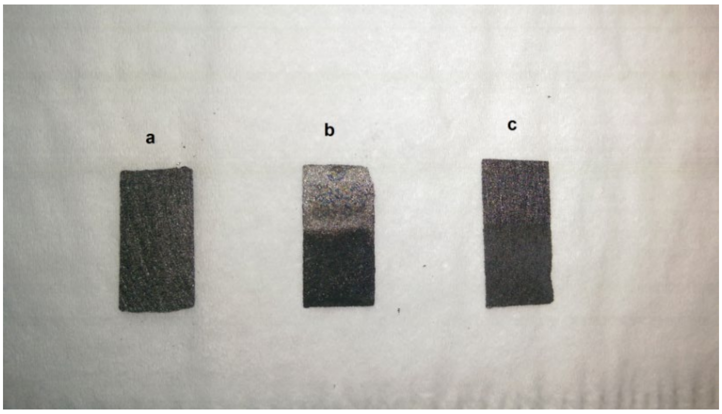

Figure 2.3: (a) blank carbon cloth, FeP/CC electrocatalysts prepared by (b) electroplating and (c) spray-pyrolysis.

2.3.2. Electrochemical measurements for HER

General: All electrochemical measurements were performed using Biologic potentiostat (SP-150) at room temperature in a custom-made electrochemical cell. The reference electrode was Ag/AgCl (in a 3 M NaCl solution, E° = 0.197 V). A carbon rod was used as the auxiliary counter electrode. Linear sweep voltammetry (LSV) experiments were used to investigate the catalytic performance and performed using a scan rate of 5 mV/s. All LSVs experiments were reported after applying 85% iR compensation using Biologic potentiostat otherwise mentioned. All the electrochemical measurements were performed either in 0.5 M H_2SO_4 or 0.1 M KPi solutions. In 0.5 M H_2SO_4 (pH=0.47), the potentials were converted to the reversible hydrogen electrode (RHE) according to the following equation: $E(RHE) = E(Ag/AgCl) + 0.225$. In 0.1 M KPi, the potentials were converted to the reversible hydrogen electrode (RHE) according to the following equation $E(RHE) = E(Ag/AgCl) + 0.197 + 0.059\, x\, pH$. These corrections values were based on the calibration of the reference electrode, as described below. Tafel plots were drawn using LSV data after applying iR compensation by the potentiostat. Electrochemical impedance spectroscopy (EIS) was performed at η_{10} with the frequency range 100 mHz - 10 kHz and amplitude of 10 mV.

2.3.2.1. Calibration of Ag/AgCl and conversion to RHE

The reference electrode Ag/AgCl (3.0 M NaCl) calibration method was based on a reported method.[234, 235] The calibration was performed using a three-electrode system. A Pt disc (1.6 mm diameter, 99.95% purity) was cleaned through 30 CVs in 0.5 M H_2SO_4 prior to the calibration and was used as a working electrode.

Pt wire and Ag/AgCl (3.0 M NaCl) were used as counter and reference electrodes, respectively. The electrolyte solution (0.5 M H_2SO_4) was pre-purged and saturated with high purity H_2 gas. Linear sweep voltammetry was used for the calibration with a scan rate of 1 mV/sec **(Figure 2.4)**. The thermodynamic potential for hydrogen electrode is the potential at which the current crosses zero.[234, 235] For example, in 0.5 M H_2SO_4 the zero current point was at -0.225 V, so $E(RHE) = E(Ag/AgCl) + 0.225\ V$ at pH=0.47.

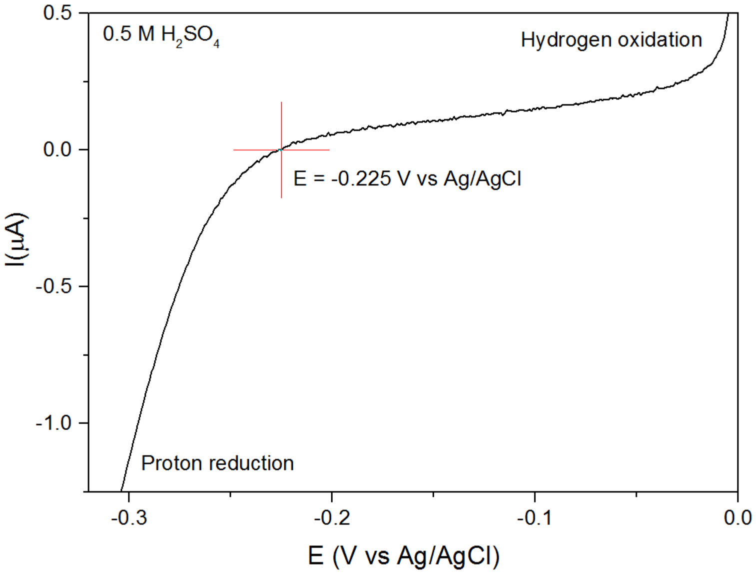

Figure 2.4: Calibration of Ag/AgCl (3.0 M NaCl) reference electrode.

2.3.3. Quantification of hydrogen gas from HER

Quantification of hydrogen gas was performed using a Shimadzu GC-2014 fitted with a ShinCarbon ST column and TCD detector. The temperatures of the injector, oven and TCD were held at 120, 40 and 120 °C, respectively. Ar was used as a carrier gas with a flow rate of 20 mL/min. A calibration curve was prepared using known volumes of pure hydrogen gas **(Figure 2.5)**. The produced hydrogen gas was collected using a Hamilton gastight syringe (250 µl).

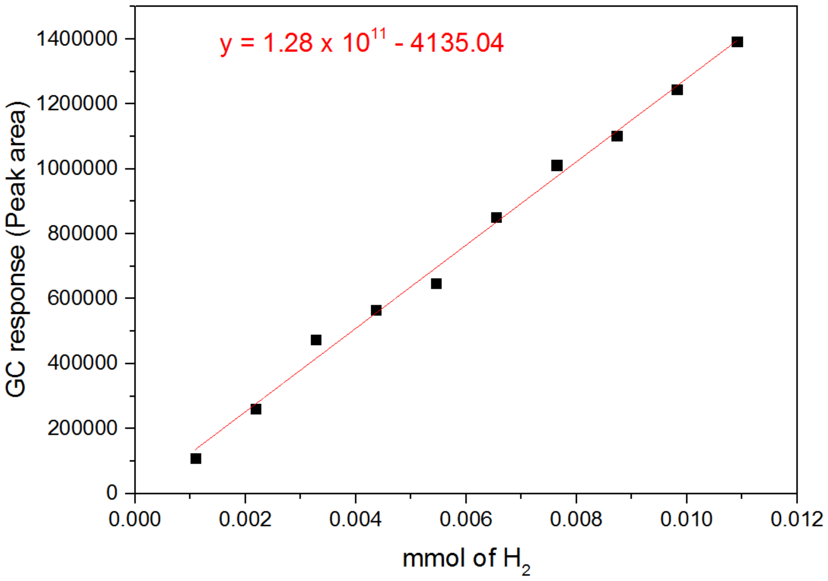

Figure 2.5: Calibration of GC response to hydrogen gas.

2.4. Electrochemical reduction of CO_2

2.4.1. Copper phosphide foils

2.4.1.1. Electropolished copper foil

Copper foils were electropolished by applying 4.0 V for 5 min in 85 % phosphoric acid. The foils were rinsed with Millipore water then either used directly for CO2RR or oxidised to prepare OD-Cu before phosphidation process.

2.4.1.2. Preparation of Cu_3P/Cu foil

Electropolished Cu foil (1 x 1 cm^2) was used to make copper phosphide via phosphidation process. Cu foil and sodium hypophosphite were placed in two separate alumina boats within a tube furnace. The furnace was heated to 300 °C with a heating rate of 1.5 °C/min for 2 h with an Ar flow of 5 mL/min.

2.4.1.3. Preparation of OD-Cu foil

An OD-Cu foil electrode was prepared using a reported method.[191] A Cu_2O layer was electodeposited on an electropolished Cu foil galvanostatically by applying -1.82 mA/cm^2 for 10 min in electrolyte solution containing 0.3 M $CuSO_4$, 3.2 M NaOH and 2.3 M lactic acid.[191] The CuO_x layer was then reduced electrochemically by applying -0.8 V (RHE) for 5 min in 0.1 M $KHCO_3$.[215]

2.4.1.4. Preparation of Cu_3P/OD-Cu foil

The OD-Cu electrode was prepared as mentioned above then subjected to the phosphidation process as follows: OD-Cu foil and sodium hypophosphite were placed in two separated alumina boats within a tube furnace. The furnace was heated to 300 °C with a heating rate of 1.5 °C/min for 2 h with an Ar flow of 5 ml/min.

2.4.2. 3D printing work

A 3D printer MakerBot Replicator 2x was used to print copper-based structures using a home-made viscous ink. Autodesk Inventor 2016 software was used for designing the structures. All the 3D printed copper based structures were subjected to the following steps to obtain the active copper electrocatalyst:

1- Building and designing the Cu based electrocatalyst using a 3D printer.
2- Thermal treatment up to 600 °C to sinter the copper powder and remove organic content.
3- Reduction of the Cu_xO structure chemical reduction using dihydrogen and electrochemical reduction.

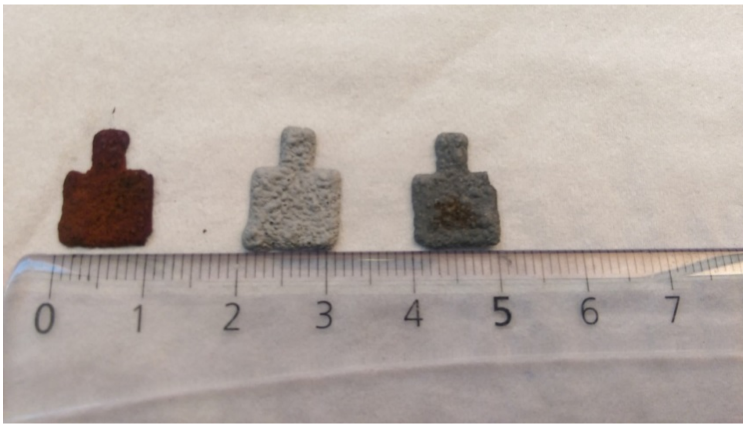

Figure 2.6: 3D printed Cu based electrocatalysts.

2.4.2.1. Preparation of 3D printed OD-Cu electrocatalyst

The ink was prepared using copper powder (20 g), polyethylineimine (PEI) (2 mL), and hydroxylpropyl methyl cellulose (HPMC) (0.200 g). Ethylene glycol (2 mL) and glycerol (1 mL) were used as binding additives.[229] The components were mixed strongly for 5 min then left to relax for 1 h. The viscosity of the ink was controlled by evaporating volatiles at 150 - 220 °C over a graphite bath. It is worth noting that the physical behaviour of the ink can be controlled by changing the percentage of the ingredients for instance increasing the polymer content produced an ink with gum-like consistency. After reaching the required viscosity (410 Pa s) the prepared ink was placed within a syringe barrel which was connected to the 3D printer head. The ink starts to flow under a pressure of 6.5 bar. The 3D printer was used to build a plate of dimensions (1 cm x 1 cm) with an additional tip for connection **(Figure 2.7)**. The organic contents in the prepared structures were decomposed by heating in a muffle furnace up to 600 °C with a slow heating rate (1 °C/min) to avoid extreme deformations in the structures. The Cu_xO plates were reduced by hydrogenation (300 °C 8 h 1.5 °C/min under 5% H_2/N_2 atmosphere) followed by electrochemical reduction (by applying -1.4 V vs Ag/AgCl for 15 min) prior to any electrochemical measurements.

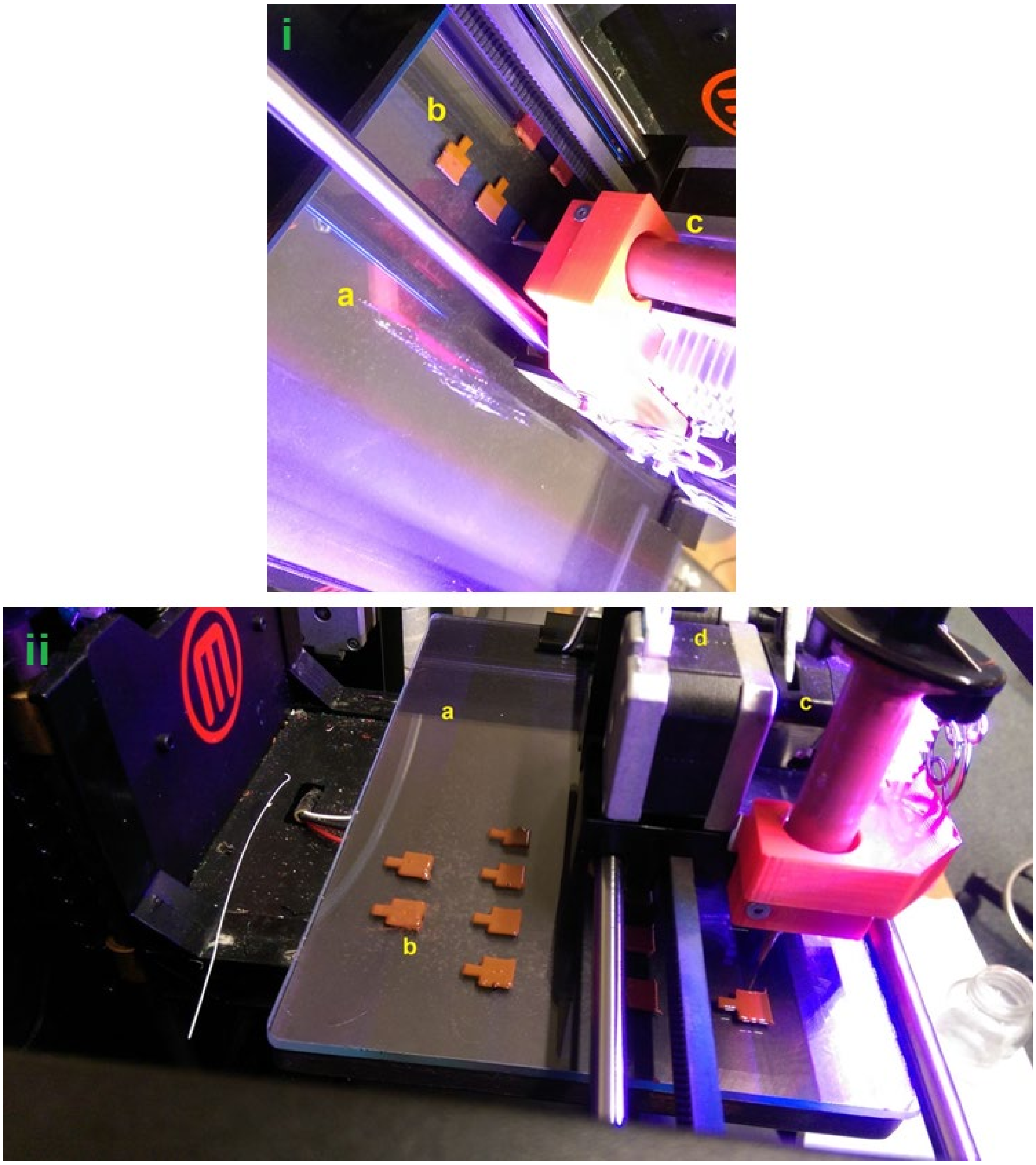

Figure 2.7: 3D printing process: a) 3D printer stage, b) 3D printed Cu electrocatalyst, c) Syringe barrel filled with Cu based ink and d) 3D printer head.

2.4.2.1.1. Viscosity measurements

The viscosity of a Cu ink (ca. 0.3 mL per replicate) was measured using Brookfield CPS+ Rheometer fitted with a cone. The cone had a diameter of 25 mm, angle of 2° and the gap from the bottom plate was 0.045 mm and a Peltier PTS-2 temperature controller (21 °C). Application of both immiscible, low viscosity silicone oil (5 cSt at 25 °C) and a solvent trap were used to prevent moisture loss during experimentation. The viscosity was measured with shear rate of 5.0 (s^{-1}) at room temperature and the average viscosity measured over 10 min and was 412 (Pa.s). The average viscosity value was collected by calculating the average value over 10 min as the viscosity measurement did not reach a constant value and it was decreasing with time may be due to the evaporation of the solvent.

2.4.2.2. Preparation of PD/OD-Cu electrocatalyst

The 3D printed OD-Cu electrocatalyst was subjected to the phosphidation process by heating NaH_2PO_2 (Cu: NaH_2PO_2 was 5:1) within a tube furnace up to 300 °C with heating rate of 1.5 °C/min for 15 min under Ar flow (5 mL/min). Before any electrochemical measurement, the electrode was electroreduced electrochemically by applying a constant voltage -1.4 V (Ag/AgCl) for 20 min in 0.1 M $KHCO_3$.

2.4.3. Electrochemical measurements

All the electrochemical measurements were performed using a Biologic (SP-150) potentiostat at room temperature in a custom-made electrochemical cell **(Figure 2.8)**. Ag/AgCl (in a 3.0 M NaCl solution, $E^o = 0.197$ V RHE) electrodes were used as reference electrodes. All the potentials were converted to reversible hydrogen electrode (RHE). Platinum mesh was used as the counter electrode.

The working chamber was separated from the counter electrode chamber via a Nafion-117 membrane, in order to avoid the re-oxidation of CO_2 electrochemical reduction products like formic acid back to CO_2 according to the following equation:

$$HCOOH \rightarrow CO_2 + 2H^+ + 2e^-$$

The electrolyte solution was bubbled by CO_2 with a flow rate of 20ml/min and was stirred in order to enhance the transport of CO_2 to the electrocatalyst.[166] The CO_2 saturated solution of 0.1 M $KHCO_3$ has a pH of 6.8.

All measurements were performed with ohmic drop compensation unless otherwise mentioned. Electrochemical impedance spectroscopy (EIS) was performed using a Biologic (SP-150) potentiostat at each voltage with frequency range 100 kHz - 100 mHz and amplitude of 10 mV. Biologic potentiostat was used to perform 85% compensation automatically by the potentiostat.

2.4.3.1. Electrochemical active surface area measurements (ECSA)

The roughness factor (RF) can be defined as the ratio between the capacitance of the working electrode compared to that of a smooth surface. In order to measure the roughness factor, multiple CV cycles were measured in the non-faradaic region at different scan rates and plotted on a graph of $\Delta J = J_a - J_c$ versus scan rate. For copper-based electrocatalysts the capacitance of the polycrystalline copper was used as a reference for RF calculations $(C_{dl_{Cu}} = 29\ \mu F)$. For CO2RR, the CVs performed using the same cell and Nafion membrane in the same electrolyte solution (0.1 M KHCO$_3$).

$$\Delta J = J_a - J_c = v\ C_{dl} \qquad \text{Eq. 2-1}$$

$$Roughness\ Factor\ (R_f) = \frac{C_{dl\ of\ sample}}{C_{dl\ of\ smooth\ Cu\ foil}} = \frac{C_{dl_{Cu_3P}}}{C_{dl_{Cu}}} \qquad \text{Eq. 2-2}$$

ECSA is dependent on the morphology of the working electrode surface. The ECSA is directly proportional to the double layer capacitance $(C_{dl})^{19, 21, 23, 24}$ and the linear slope corresponds to the ECSA, where S is the geometric surface area of the working electrode.

$$ECSA = R_f\ x\ S = C_{dl}/C_s\ x\ S \qquad \text{Eq. 2-3}$$

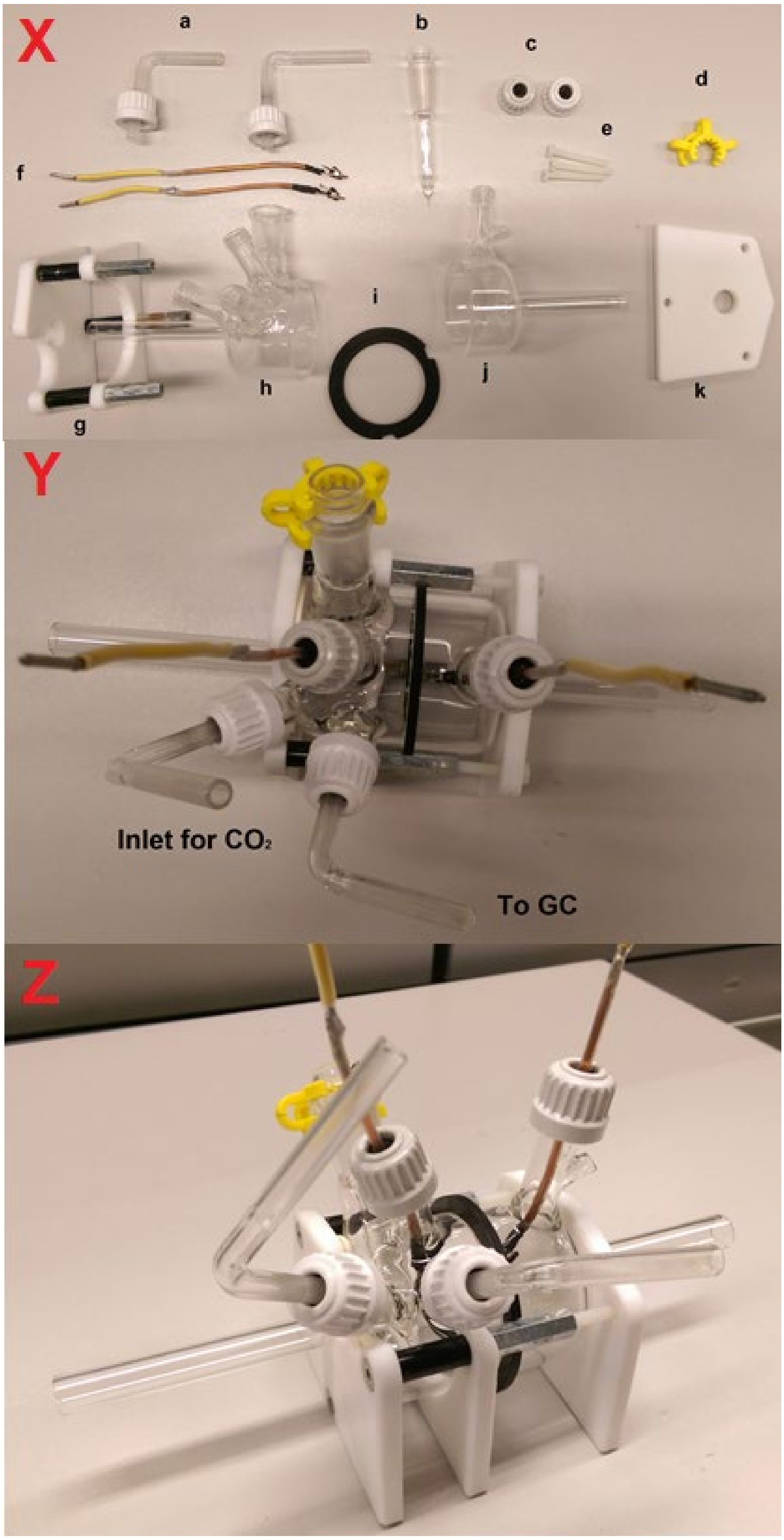

Figure 2.8: Custom-made electrochemical cell: a) 1/4″ glass tubing as inlet for CO_2 and outlet to the GC, b) Luggin capillary for reference electrode, c) plastic cap, d) Keck clip, e) plastic screws, f) Cu wire connected to crocodile clips, g and k) the cell holder, h and j) the electrochemical cell glass body and i) Rubber gasket for Nafion membrane.

2.4.4. Quantification of gaseous and liquid products

2.4.4.1. Quantification of liquid products

For accurate measurements, Hamilton syringes were used to measure volumes. ^{1}H NMR spectra were recorded with water suppression (zgesgp) and 2048 scans were collected so that the liquid product peaks can be detected **(Figure 2.9)**. DMSO was used as an internal standard and was added directly to the NMR tube. The concentrations of products were obtained using the following equations:

$$\frac{6\ x\ C_{ref\,(ppm)}}{(Peak\ area)_{ref}} = \frac{n\ x\ C_{product(ppm)}}{(Peak\ area)_{product}}$$

$$C_{product(mol/L)} = \frac{C_{product(ppm)}\ x\ 10^{-3}}{Mwt_{(\frac{g}{mol})}}$$

$$Q_{total}\ (C) = \int_{t_i}^{t_f} i\ dt$$

$$FE\% = \frac{C_{product\ (mol/L)}\ x\ V_{catholyte}\ x\ n\ x\ F}{Q_{total}}\ x\ 100$$

All electrochemical experiments were performed using 25 mL of catholyte in the working electrode chamber. (n): no of corresponding protons in the desired product in balanced equations **(Table A1.1)**.[39, 122-126] $C_{product}$ is the concentration of product, the concentration of reference DMSO is 1.87 ppm and F is Faraday constant. The expected positions of peaks of ^{1}H in NMR spectra are summarized in **(Table A1.1)**.[39, 122-126]

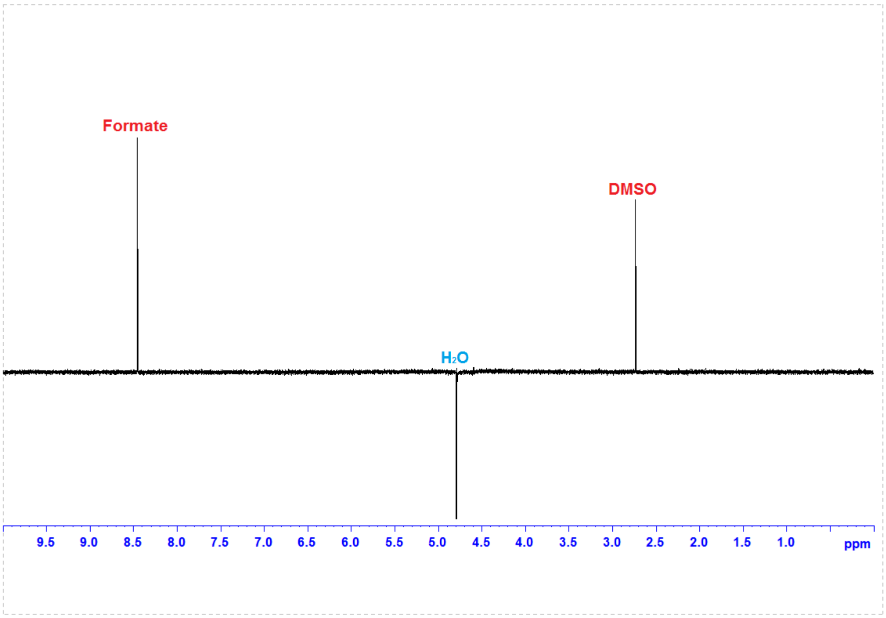

Figure 2.9: A representative ^{1}H NMR spectrum for characterization of the electro produced liquid hydrocarbons by the water suppression method.

2.4.4.2. Quantification of gaseous products for CO2RR

GC analyses were performed using a Shimadzu GC-2014 fitted with ShinCarbon ST column. A gas sampling loop of volume 1.0 mL was used to inject a sample every 20 min. The oven temperature was held at 40 °C for 4.5 min followed by heating the oven to 200 °C from 3.5 min with a heating rate of 80 °C/min **(Figure 2.10)**. Two detectors, connected in series, were used for the analysis: TCD and FID (connected to a methaniser). Argon was used as the carrier gas.

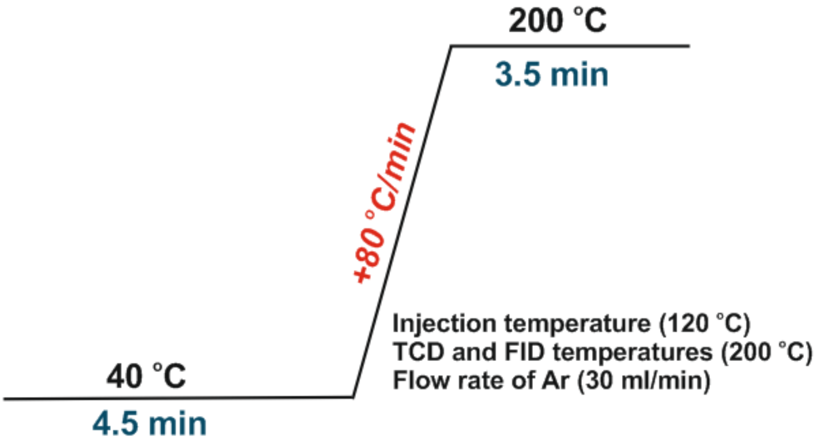

Figure 2.10: GC analysis parameters.

The mentioned method **(Figure 2.10)** can be used to detect gases (H_2, CO, CO_2, C_2H_4, C_2H_6 and CH_4) **(Figure 2.11)**. The temperatures of the two detectors were kept at 200 °C. For each 80 min of electrolysis four gas samples were injected and analysed via the gas sampling loop. The retention times for the permanent gases are tabulated in **(Table 2-1)**.

Gas	Formula	Volume % [a]	Retention time (min)
Argon	Ar	-	-
Hydrogen [b]	H_2	2.38	0.76
Air	(mainly O_2/N_2)	-	1.45
Carbon monoxide	CO	2.423	1.83
Methane	CH_4	2.462	3.62
Carbon dioxide	CO_2	87.725	6.20
Ethylene	C_2H_4	2.435	8.30
Ethane	C_3H_6	2.575	9.20

Table 2-1: Retention times for all gases based on FID detector's chromatograms. [a]composition of the standard gas mixture used for the calibration curves of the gases, [b]based on TCD detector's chromatograms.

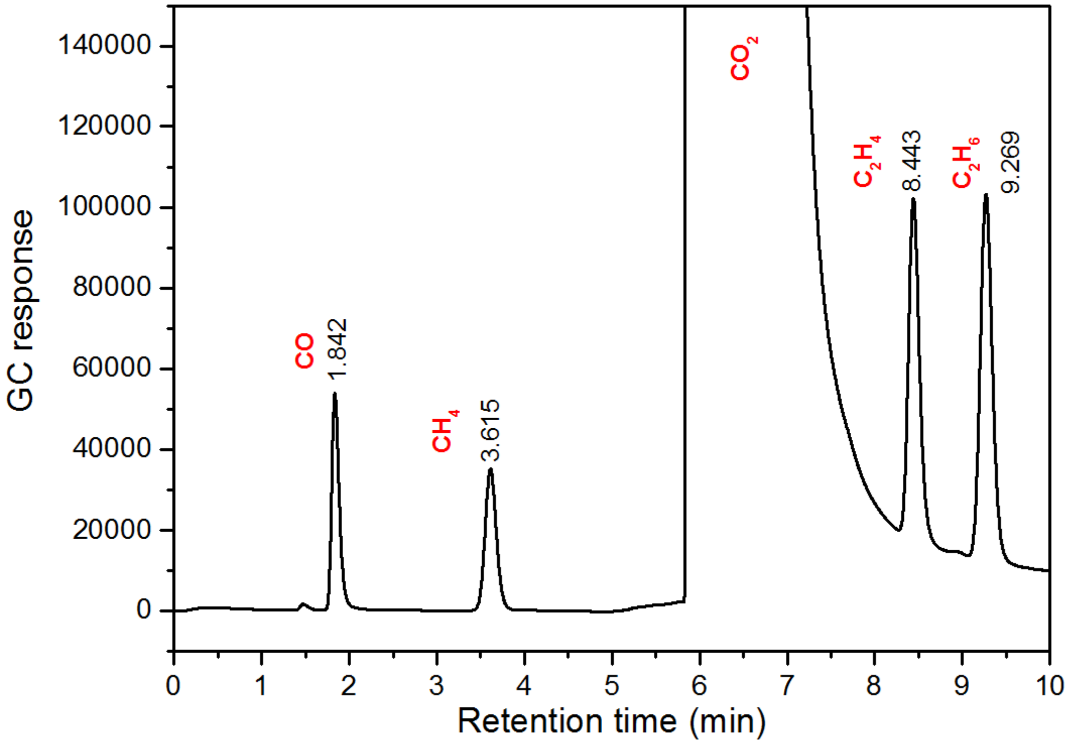

Figure 2.11: Typical chromatogram resulted from the FID detector.

2.4.4.3. Building Calibration curves for gaseous products

Calibration curves of each gas (H_2, CO and CH_4) were built to determine the no of moles produced during chronoamperometry (CA). Calibration curves were built by diluting the desired gases in pure CO_2. A standard gas mixture was used to build the calibration curves **(Table 2-1)**. The calibration curves of the gases are plotted as peak area (GC response) versus $(Vol\,\%)$ **(Figure 2.12)**.

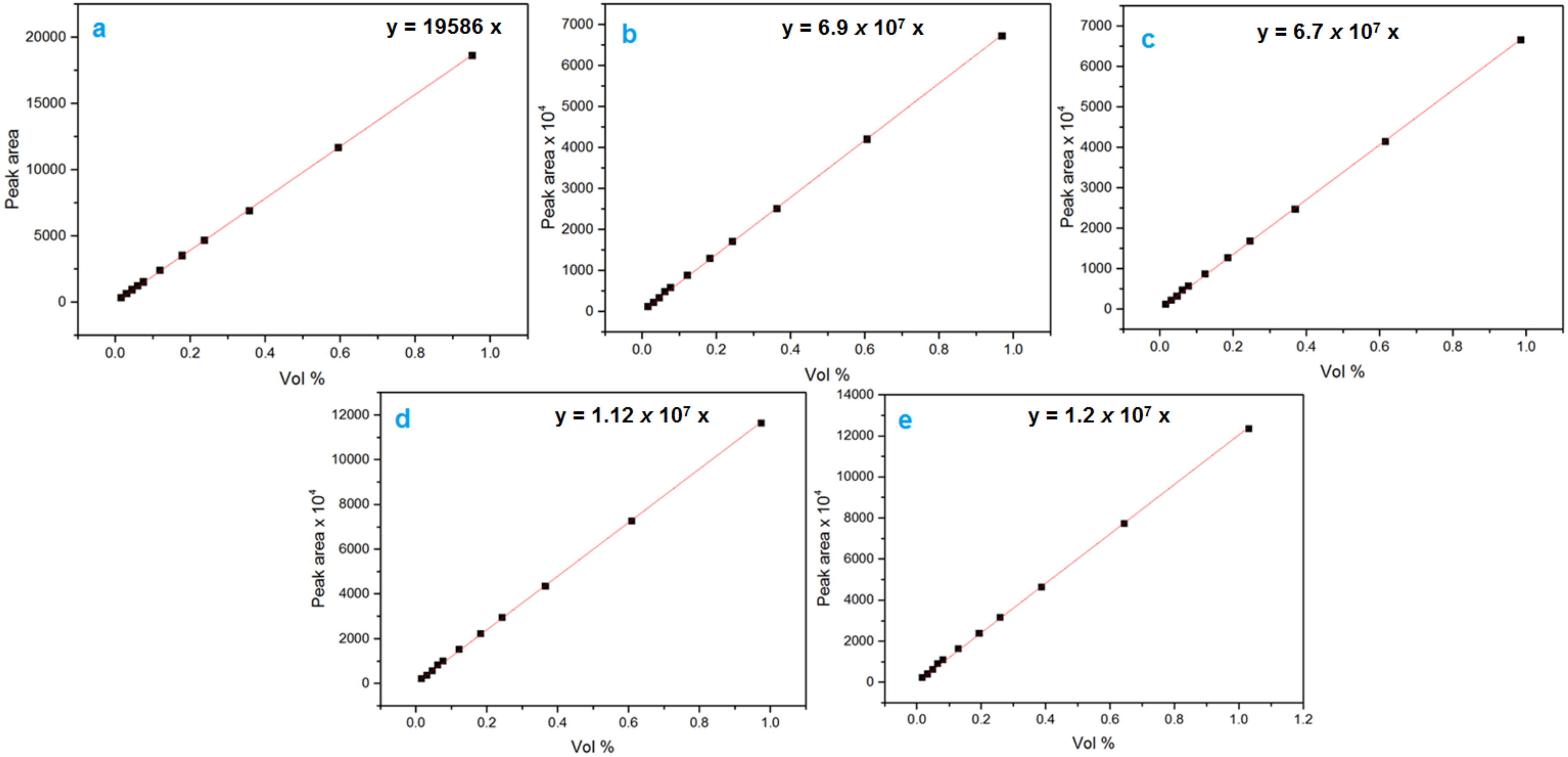

Figure 2.12: Calibration curves of (a) H_2, (b) CO, (c) CH_4, (d) C_2H_4 and (e) C_2H_6 (The retention time of hydrogen gas based on TCD detector's chromatogram and the other gases based on FID dectector's chromatograms).

2.4.4.4. Calculations of the current efficiencies of gaseous products

The current efficiencies of each product were calculated according to a reported method.[222, 236, 237] The average between the 2nd and the 3rd GC measurements was used for calculating the average current efficiency $(CE\%)$ of each product gas in order to ensure that the reported results were under equilibrium conditions.[222] The electrochemical measurements were performed under continuous flow of CO_2 and samples were injected through an auto sample valve fitted to the GC. The calibration curves exhibited linear relationships $(y = ax + b)$ between peak area and $Vol\,\%$.

$$Vol\,(\%) = \frac{Peak\ area}{Slope}\ and\ Vol_{ratio} = \frac{Vol\,\%}{100}$$

$$i_{product}\,(A) = (n_{product})\ x\ (z_{e}-)\ x\ F$$

$$i_{product}\,(A) = \left(\frac{PV}{RT}\right)\ x\ (z_{e}-)\ x\ F$$

$$i_{product}(mA) = \left(\frac{PV}{RT}\right)(z_{e}-)\ x\ F\ x\ 1000$$

Where (R) is the general gas constant $= 8.314\,(m^3.\ Pa/K.mol)$, atmospheric pressure $(P) = 101325\ Pa$, the flow rate of CO_2 during the electrochemical reduction of CO_2 was $20\ (ml/\mathrm{min})$ and (F) is the faraday constant $96485\,(A\,.sec/mol)$. For example, the calculations of the $CE\%$ for the electrochemical reduction of CO_2–to–CO:

$$(CO_2 +\ 2H^+ +\ 2e^- \rightleftharpoons CO +\ H_2O\,, \qquad z = 2)$$

$$Q\ (C) = n\ x\ z\ x\ F = i\ x\ t = \frac{PV}{RT}\ x\ z\ x\ F$$

$$i_{CO}\ (A) = \frac{PV}{RTt}\ (z)\ x\ F$$

$i_{CO}\ (mA)\ =$

$$\left(\frac{101325\ \cancel{(Pa)}\ x\ \left(Vol_{ratio}\ x\ 20\ (\cancel{m^3}/\cancel{min})\right)}{8.314\ (\cancel{m^3}.\ \cancel{Pa}/\cancel{K}.\ \cancel{mol})\ x\ 294.15\ (\cancel{K})\ x\ 60\ (\cancel{\mathrm{min}})\ x\ 10^6}\right) x\ 2\ x\ 96485\ \ (A\ .\cancel{s}/\cancel{mol})\ x\ 1000$$

$$J_{CO}\ (mA/cm^2) = \frac{i_{CO}\ (mA)}{Geometric\ surface\ area\ of\ the\ working\ electrode\ (cm^2)}$$

$$Current\ efficiency\ (CE\%) = \frac{J_{CO}\ (\cancel{mA}/\cancel{cm^2})}{J_{Total}\ (\cancel{mA}/\cancel{cm^2})}\ x\ 100$$

2.5. Preparation of CoPi electrode

2.5.1. Preparation of CoPi on stainless steel mesh

The preparation of CoPi was prepared according to a reported method.[7, 238] In a custom-made two-chamber electrochemical cell separated by a Nafion-117 membrane CoPi was prepared. The working electrode was stainless steel (SS) (2 x 2 cm^2), working electrode chamber was filled with 0.5 mM of $Co(NO_3)_2.6H_2O$ salt in potassium phosphate buffer (pH=7). The counter electrode chamber was filled with potassium phosphate buffer (pH=7). The electrode becomes ready after electrolysis at a potential of 1.1 V (Ag/AgCl) until a charge density between 50-60 mC/cm^2 is achieved.[7] The electrode was characterized by SEM and EDS.

2.6. Catalysts

2.6.1. Preparations of compounds

2.6.1.1. Preparation of 6-DPPon ligand

Breit et al[15] described a hydroformylation reaction for alkenes that fulfil the required criteria for the mini-reactor mentioned above. It can operate at low pressure (1 atm) of syngas in water/surfactant solution; it can also work at room temperature and the Rh complex is not water or air sensitive. The 6-DPPon ligand was prepared according to **(Scheme 2-1)**[16] with slight modifications according to the following steps: All the recorded spectra are in **Appendix-2, p. 200**.

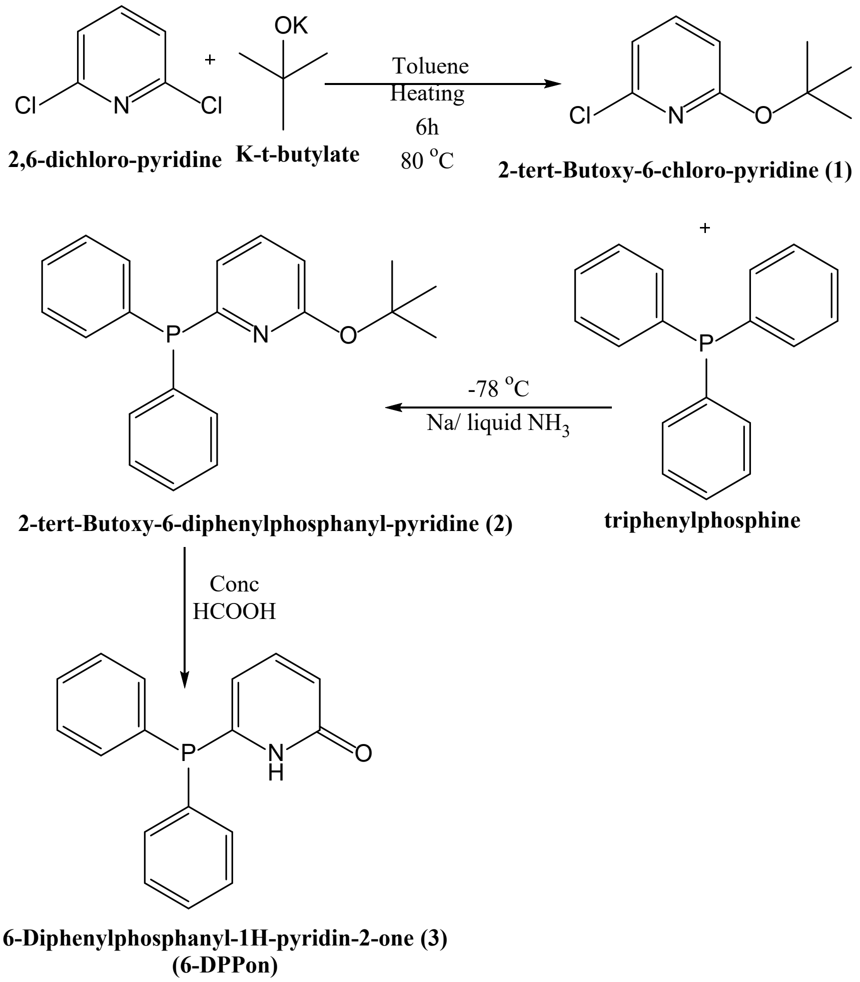

Scheme 2-1: Preparation of (6-DPPon) ligand according to literature.[15, 16]

2.6.1.2. Preparation of 2-*tert*-Butoxy-6-chloro-pyridine (1)

In a glove box, a solution of 2,6-dichloro-pyridine (10.00 g, 67.6 mmol, 1.0 eq) in 150 mL toluene was mixed with potassium-*tert*-butylate (9.10 g, 81.1 mmol, 1.2 eq) to give a pale yellow solution. After heating and stirring for 6 h at 80 °C, a white precipitate formed, then after cooling the mixture was filtered through a plug of silica to give a pale yellow filtrate which was concentrated under vacuum to give a yellow oil. The oil was purified via bulb to bulb distillation using a high vacuum line (vacuum) gently with a heat gun to give **(1)** as a colourless liquid (9.05 g, 72.14 %). The product was characterised by ^{1}H and ^{13}C{^{1}H} nmr spectroscopy. The data was consistent with that reported in the literature.[15]

***^{1}H** NMR (500 MHz, $CDCl_3$, ppm) 7.41 (t, J = 7.78 Hz, 1H), 6.79 (d, J = 7.13 Hz, 1H), 6.52 (d, J = 8.20 Hz, 1H), 1.57 (s, 9H).*

***^{13}C** NMR ($CDCl_3$, ppm) 163.4, 147.7, 140.3, 115.63, 111.25, 80.86, 28.48.*

2.6.1.3. Preparation of 2-*tert*-Butoxy-6-diphenylphosphanyl-pyridine (2)

In a 2 L 3-neck round flask, liquid ammonia (ca. 500 mL) at -78 °C was stirred with was 4.6 g of sodium metal pieces (200 mmol) during 10 min. A dark blue solution was formed and turned into brown (orange) gradually after adding 25.72 g of Ph_3P (98.05 mmol). The mixture was left at -78 °C for 2 h with stirring then 18.1 (98 mmol) of 2-*tert*-butoxy-6-chloro-pyridine **(1)** was added followed by the addition of 175 mL of THF (drop-wise) then ammonia was allowed to evaporate overnight. Deionized water (200 mL) was added slowly to quench the reaction to avoid violent reaction with any Na residues. The compound was extracted three times with 150 mL of diethyl ether and dried over Na_2SO_4. The solution was left overnight and white crystals of **(2)** appeared and recrystallized with methanol. Triphenylphosphine was observed with the product and has been removed from the product by dissolving the crude with hexane (i.e the product was insoluble in hexane and Ph_3P is soluble).

*^{1}**H** NMR (500 MHz, C_6D_6, ppm) 7.61-7.55 (m, 4H), 7.20-7.11 (m, 6H), 6.99 (ddd, J = 8.38, 7.80, 2.64 Hz, 1H), 6.84 (dd, J = 7.19, 2.78 Hz, 1H), 6.55 (d, J = 9.00 Hz, 1H), 1.51 (s, 9H).*
*^{13}**C** NMR (C_6D_6, ppm) 163.80 (d, $J_{C,P}$ = 10.15 Hz), 160.16, 137.74 (d, $J_{C,P}$ = 5.53 Hz), 137.23 (d, $J_{C,P}$ = 11.06 Hz), 134.37 (d, $J_{C,P}$ = 21 Hz), 128.59, 128.35 (d, $J_{C,P}$ = 7.17 Hz), 121.07 (d, $J_{C,P}$ = 25.15),111.89, 79.30, 28.2.*
*^{31}**P** NMR (C_6D_6, ppm) -2.37.*

2.6.1.4. Preparation of 6-Diphenylphosphanyl-*1H*-pyridin-2-one (6-DPPon) (3)

In a Schlenk tube, 2-tert-butoxy-6-diphenylphosphanyl-pyridine **(2)** (4.85 g, 14.46 mmol) was dissolved in Ar saturated 50 mL of conc. formic acid. After stirring for 1 h the pale yellow solution was diluted with 60 mL DI water. A white precipitate started to appear. The precipitate was collected by filtration, washed with 30 mL aqueous formic acid (2:1, v/v) and dried. 6-Diphenylphosphanyl-1H-pyridin-2-on **(3)** was obtained as a white solid and stored in a glove box (4.0 g, 82.4%).

*^{1}**H** NMR (500 MHz, $CDCl_3$, ppm) 8.95 (br s, 1H), 7.6-7.44 (m, 11H), 6.63 (d, J = 9.24 Hz, 1H), 6.40 (t, J = 6.32 Hz, 1H).*
*^{13}**C** NMR ($CDCl_3$, ppm) 163.8, 145.8 (d, $J_{C,P}$ = 26.92 Hz), 140.39 (d, $J_{C,P}$ =7.97 Hz), 133.8 (d, $J_{C,P}$ = 20.34 Hz), 132.44 (d, $J_{C,P}$ = 10.04 Hz), 130.27, 128.49 (d, $J_{C,P}$ = 6.90 Hz), 121.07, 113.81 (d, $J_{C,P}$= 24.13).*
*^{31}**P** NMR ($CDCl_3$, ppm) -9.12.*

2.6.1.5. Preparation of $[Rh(CO)_2(acac)]$ complex

$$RhCl_3.3H_2O + 2\ HC(O)NMe_2 \rightarrow [NH_2Me_2][Rh(CO)_2Cl_2] + [NH_2Me_2]Cl$$

$$[NH_2Me_2][Rh(CO)_2Cl_2] + CH_2(COMe)_2 + HC(O)NMe_2 \rightarrow$$

$$[Rh(CO)_2(acac)] + CO + 2\ [NH_2Me_2]Cl$$

The Rh compound was prepared according to a reported method[239] **(Scheme 2-2)**.

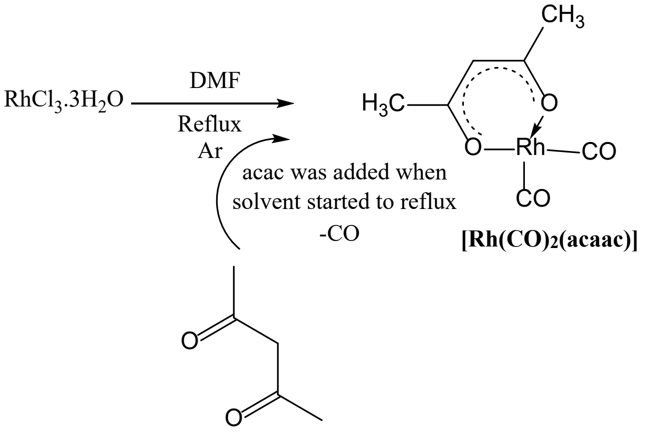

acetylaceetone (acacH)

Scheme 2-2: Preparation of $[Rh(CO)_2(acac)]$ to literature.[239]

In a 50 mL two-neck round-bottomed flask fitted with a condenser, 1.0 g of $RhCl_3.3H_2O$ was added and dissolved with 40 mL of a dried and degassed DMF. The solution colour was deep violet and the reaction was carried out under a continuous flow Ar gas and stirring. When the solvent started to reflux, 2 mL of (acacH) was added against the Ar flow. The deep violet solution turned into orange solution within a 10 min. The system was left for additional 20 min under reflux conditions. The solution was left to cool and transferred to 250 mL round-bottomed flask. Deionised water (100 mL) was added and fine purple precipitate started to appear. The precipitate was filtered through sintered glass and washed by 30 mL of DI water and 20 mL of cold methanol. The crude solid was then extracted with 20 mL of DCM and dried with $MgSO_4$ and filtered through Celite. The $MgSO_4$ and Celite paste were then washed with 40 mL of DCM and the two filtrates were combined. DCM was removed under vacuum and a green-bronze solid was obtained. The solid was washed with 20 mL of cold methanol giving solid of yield 20 %. The compound was characterized by IR and NMR (^1H and ^{13}C). IR: 2083 (s), 2036 (w), 2015 (s) and 1985 (w) cm^{-1}. The spectral data were in good agreement with literature.[239]

***^{1}H** NMR (500 MHz, $CDCl_3$, ppm) 2.06 (s, 6H), 5.58 (s, 1H).*

***^{13}C** NMR ($CDCl_3$, ppm) 26.9, 101.7, 183.6 (d, J_{Rh-CO}=72.2), 187.2.*

2.6.1.6. Preparation of [Ru@MIL-101(SO3H]

2.6.1.6.1. Preparation of the MOF [MIL-101(SO3H)]

[MIL-101(SO3H)] is a well-known MOF and was prepared according to the reported method in the literature.[240-242] A stock solution of chromium trioxide (CrO_3) was prepared (0.646 M) and 4.62 mL (mmol) of it was used to dissolve 0.8 g of 2-sulfoterephthalic acid monosodium salt (mmol) (H2BDC-SO3Na). 2 equivalents of HCl (mmol) was added to the mixture then the mixture was diluted up to 12 mL with H_2O. The prepared solution was left for 1 h with strong stirring until all the suspensions were dissolved. The reaction solution was transferred to a Teflon-lined autoclave and heated up to 190 °C under hydrothermal conditions for 6 days with a heating rate of 2 °C/min. The autoclave was left to cool naturally. Our first trial, using 1.5 equivalent of HCl did not work and the MOF did not form. The mixture was kept under rapid stirring for 30 min prior thermal treatment 180 °C for 6 days. The forest-green colour was filtered and washed with 250 mL of H_2O and 100 mL of methanol and dried under vacuum.

2.6.1.6.2. Preparation of [CpRu(PTA)$_2$Cl] complex

[CpRu(PTA)$_2$Cl] complex was prepared according to the method reported in the literature **(Scheme 2-3)**.[243, 244] In a Schlenk tube equipped with a magnet bar, 0.18 g (0.24 mmol) of [CpRuCl(PPh$_3$)$_2$] was mixed with 0.08 g (0.48 mmol) of PTA ligand in 15 mL of toluene. The orange solution was refluxed for 2 h under Ar. The complex was extracted with water. A yellow precipitate started to appear after 45 min of reflux. The mixture was left to cool overnight.

*^{1}**H** (500 MHz, CD_2Cl_2, ppm) 4.11 - 4.30 (AB spin system, 2J (HAHB) 14.94 Hz, 12H, PCH2N); 4.61-4.73 (m, 17H, NCH_2N + Cp).*

*^{13}**C** (CD_2Cl_2, ppm) 57.22 (t, $^{2}J(CP)$ 8.4 Hz, Cp), 73.38 (t, PCH_2N); 75.99 (t, NCH_2N).*

*^{31}**P** (CD_2Cl_2, ppm) -26.34 (s).*

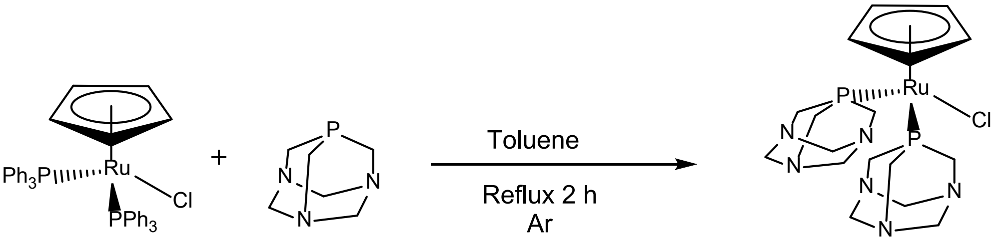

[CpRu(PPh3)$_2$Cl] **PTA Ligand** **[CpRu(PTA)$_2$Cl]**

Scheme 2-3: Preparation of [CpRu(PTA)$_2$Cl) complex.[244]

2.6.1.3. Preparation of Ru@-MIL-101(SO3H)

The ruthenium complex (50 mg) mixed with (30 mg) of MIL-101 in a two-neck round flask equipped with a magnet bar with a dry and degassed acetonitrile (7 mL). The mixture was refluxed for 24 h under Ar followed by a Soxhlet step to remove any excess complex.

2.6.2. Catalytic reactions

2.6.2.1. Hydrogenation reaction of styrene using the prepared Ru@-MIL-101(SO3H)

In 1 mL of CD_2Cl_2, 5 mg of the catalyst was mixed with the styrene and stirred for 24 h under a H_2 balloon. The products of the reaction were characterized via ^{1}HNMR.

2.6.2.2. Hydrogenation reaction using Pd/C (5%) (Standard method)

Hydrogenation of styrene was performed using a commercial 5% Pd/C catalyst. Two reactions were performed in Schlenk tubes equipped with magnetic stir bars. The two reactions were kept for 24 h under 1 atm of hydrogen gas using a balloon and characterized using ^{1}HNMR. According to the reported data,[10] only 12 h are required for the full conversion of alkenes into the corresponding alkanes upon using the 5% Pd/C as a heterogeneous catalyst. The reported method include the usage of 5% Pd/C as a catalyst (Pd 1 mol%), H_2 (1 atm, balloon) and 5 mmol of the substrate in methanol at 25 °C and for 12 h.[10] The solution was black due to the suspensions of Pd/C and the reaction was kept under continuous stirring.

2.6.2.3. Hydroformylation reaction using Rh/6-DPPon (Standard method)

The hydroformylation reaction was performed according to a reported procedure.[16] In a Schlenk tube equipped with a magnetic bar, 1 mmol of styrene was mixed with $[Rh(CO)_2(acac)]$ (1.73 mg, 6.70 µmol, 0.67 mol%) and 6-DPPon (9.30 mg, 33.3 µmol, 3.33 mol%) in H_2O (PTS wt% 1.0 %). The mixture was evacuated and filled with CO/H_2 three times and left with stirring for 24 h under a CO/H_2 balloon (1 atm) at room temperature. Two drops of antifoaming agent (commercially available silicon oil from Sigma Aldrich) were added to the solution to prevent the formation of foams. After 24 h (or 8 h in some cases), the solution was diluted with 5 mL of diethyl ether then filtered through a short silica gel column. The silica gel was washed with 200 mL of ether. The filtrates were mixed and reduced under vacuum to 6-7 mL. An additional volume of ether was used to prepare 10 mL solution of the filtrate in a volumetric flask. 1,3,5-trimethoxybenzene (16.8 mg, 0.100 mmol, 0.1 eq) was added into the solution as an internal standard for the ^{1}H NMR analysis.

2.7. Solar powered reactor

2.7.1. Reactor setup

A commercial solar panel **(Figure 2.13)** was purchased from Farnell (SR5-36) and was used to power the mini-reactor as the only input energy source. The solar panel was connected to a control box which contained a LT3080 (Linear Technology) low dropout regulator. The output voltage to the cell is controlled via a potentiometer on the front panel and the cell voltage and current were monitored by means of INA219 high side current sensor (Adafruit Industries LLC). The INA219 sends the digitized signals to an Arduino microcontroller which connects to a laptop computer via USB. The voltage and current are graphed and recorded to an Ascii file using Labview software (National Instruments). The technical specifications of the solar panel are tabulated in **(Table 2-2)** (as described in the manufacture's data sheet):

Table 2-2: Technical specifications of the solar panel.

Dimensions	L 194 * W 385 * H 28
Weight	0.8 Kg
Max. power voltage	17 V
Short-circuit current	330 mA
Open-circuit voltage	21.6 V
Max. power	5 W
Max. power current	300 mA

Figure 2.13: Farnell's solar panel.

2.7.2. Reactor components

A solar panel was used to supply the system with the required current flow as the only source of energy **(Figure 2.14)**.

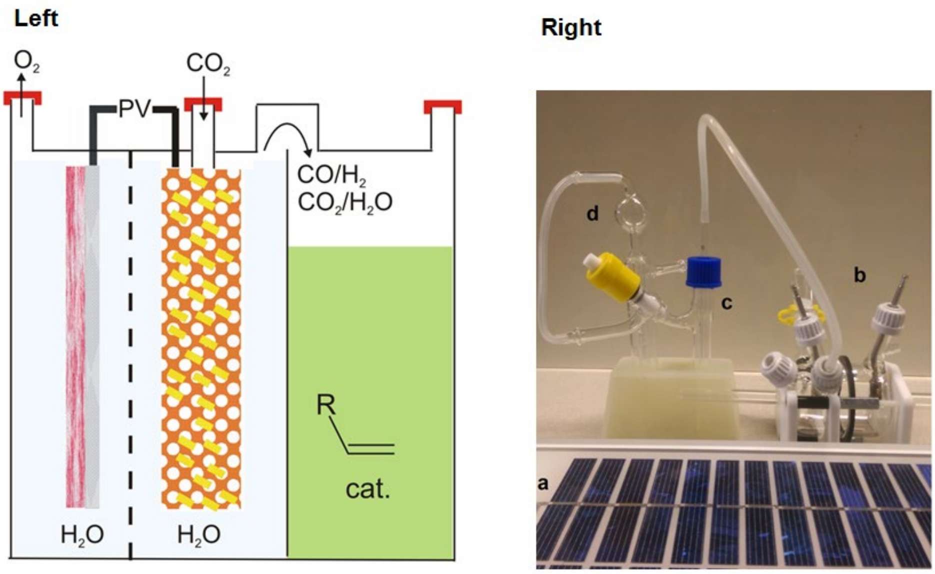

Figure 2.14: (left) a diagram of the mini-reactor components and (right) real components of the reactor; (a) solar panel, (b) electrochemical cell, (c) catalysis vessel and (d) bubbler.

2.7.2.1. Reactor for hydrocarbon production via hydrogenation of alkenes:

I. In a two-compartment custom-made electrochemical cell **(Figure 2.8)**, FeP/CC electrocatalyst and blank carbon plate were used as cathode and anode electrodes, respectively in in 0.5 M H_2SO_4. The reaction was performed also in neutral medium (0.1 M KPi) and the counter electrode was CoPi/SS.

II. The produced hydrogen gas will be used directly, without drying, for hydrogenation reaction. A glass frit will be used to dispense the electroproduced gas.

III. Commercially available catalyst Pd/C (5%) system (1g/14.10 £ from Sigma Aldrich, the price was recorded on the 21st of September 2019) was used for the hydrogenation of styrene.

IV. The percentage of the conversion of styrene was evaluated through ^{1}H-NMR spectra.

2.7.2.2. Reactor for hydrocarbon production via hydroformylation of alkenes:

I. In a two-compartment custom-made electrochemical cell **(Figure 2.8)**, Au foil was used as cathode and CoPi/SS as anode in 0.1 M $KHCO_3$ solution.

II. The produced gas (CO/H_2) will be used directly, without drying or separation, for hydroformylation reaction. A glass frit will be used to dispense the electroproduced gases.

III. Rh/6-DPPon catalytic system was used for the hydroformylation of styrene.

IV. The percentage of the conversion of styrene was evaluated through ^{1}H-NMR spectra.

3. Iron phosphide electrocatalysts for hydrogen evolution reaction; a comparison study in acidic and near neutral media

Aims

The aim of this work was to synthesis and characterize an inexpensive and efficient electrocatalyst for HER that could provide the required amount of hydrogen gas for the hydrogenation of styrene on a mmol scale. Iron phosphide was selected based on literature reports which suggest low over potential and good stability at lower pH's. There are a wide range of methods that can be used to prepare it and a number of conductive substrates. We used carbon cloth as the substrate because it is very inexpensive, conductive and can provide a high surface area 3D network support. Two methods were investigated for the synthesis of FeP/CC on carbon cloth; electroplating and spray-pyrolysis. The latter was used because it is simple, scalable, and can minimise the mass loading of the catalyst on the substrate.

Abstract

Iron phosphide based on carbon cloth (FeP/CC) electrocatalysts were prepared through two methods; electroplating based on a literature procedure, and using a new method spray-pyrolysis. FeP/C prepared by spray pyrolysis can operate with overpotential (η_{10}) of 98 ± 5 mV while that prepared by electroplating has an overpotential of 65 ± 10 mV in 0.5 M H_2SO_4. The mass loading of FeP/C electrocatalyst prepared by the electroplating was between 4.66 – 4.96 mg/cm^2 and that of the electrocatalyst prepared by spray-pyrolysis was between 0.4 – 0.5 mg/cm^2. The catalytic activities of the two FeP/CC electrocatalysts were compared in terms of overpotential, Tafel slopes, capacitance measurements, stability and durability. The ability of the two electrocatalysts to operate in near neutral medium (pH = 5.8 - 6.3) has also been investigated. The electrocatalyst prepared by spray pyrolysis operates at (η_{10}) 190 ± 60 mV while that prepared by electroplating is 136 ± 50 mV in phosphate buffer solution. Both demonstrate near 100% FE% for protons reduction in acidic and near neutral media.

3.1. Results and Discussions

Two iron phosphide based electrocatalyst were prepared on carbon cloth through two methods; electroplating and spray-pyrolysis. In the case of electroplating, iron was electrodeposited on a carbon cloth from an aqueous solution of $FeSO_4$ by applying -10 mA/cm^2 from 20 min. Fe was allowed to oxidize in air overnight. Then the orange FeOOH film formed on the carbon cloth fibres was subjected to phosphidation reaction in a tube furnace.

FeP/CC prepared by spray-pyrolysis was synthesized by spraying an aqueous solution of $FeCl_3$ (0.1 M) on a heated carbon cloth for 20 min. A red film of Fe_2O_3 was formed immediately and the film was subjected to the phosphidation process directly to form FeP/CC through phosphidation reaction in tube furnace.

Physical characterization

The electrocatalysts were characterized by x-ray diffraction **(XRD)**, scanning electron microscopy (**SEM**) and energy dispersive x-ray spectroscopy **(EDX)**. **XRD** patterns of films prepared through spray-pyrolysis method confirm the formation of Fe_2O_3 (ICSD # 15840) on the carbon cloth surface upon spraying **(Figure 3.1)**. XRD pattern did not confirm the formation of the FeP film which may be due to the particles sizes were too small.

For films prepared by electroplating, FeOOH formed upon the oxidation of the deposited iron then formation of FeP was formed via the phosphidation process **(Figure 3.1)**. It is worth noting that a peak related to iron metal **(Figure 3.1a)** (ICSD # 44863) appeared in the case of FeOOH (ICSD # 1544) and FeP films prepared through the electroplating was due to the incomplete oxidation of the electrodeposited iron **(Figure 3.1)**. Again, the formation of the FeP film on the carbon cloth was not confirmed by XRD patterns which may be due to the particles sizes were too small.

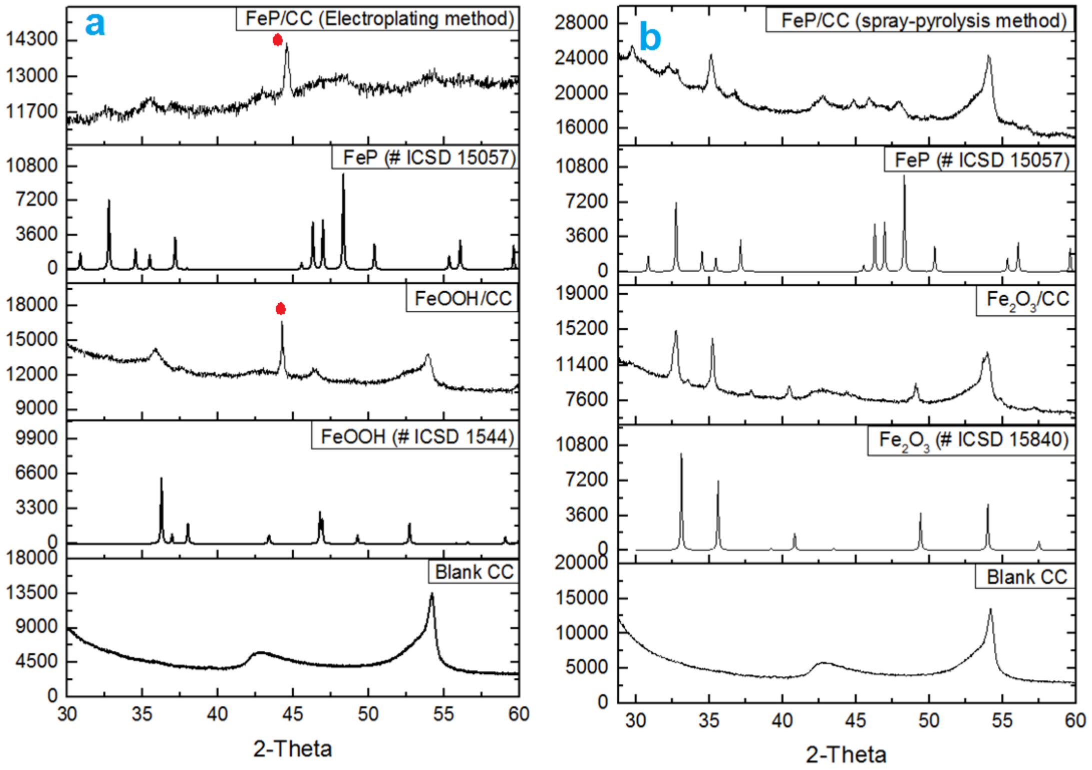

Figure 3.1: XRD patterns of different films prepared by (a) electroplating and (b) spray pyrolysis methods together with literature patterns for FeP, Fe_2O_3 and FeOOH taken from Inorganic Crystal Structure Database (ICSD). Red circles belong to Fe (ICSD # 44863).

SEM images of blank carbon cloth showed that the carbon cloth consists of 3D interconnected smooth fibres **(Figure 3.2a)**. **SEM** images **(Figure 3.2)** showed that the surface of blank carbon cloth changed upon addition of FeP. SEM images for FeP prepared via spray pyrolysis showed smooth fibres of carbon cloth were converted into rough fibres with cracks with small particles on the surface **(Figure 3.2b)**. **SEM** images of FeP/CC prepared through electroplating **(Figure 3.2c)** showed more material compared to spray-pyrolysis **(Figure 3.2b)** and FeP appeared as needles on the surface of the carbon cloth fibres. EDX spectral mapping **(Figure 3.3, Figure 3.4 and Figure 3.8)** indicated the existence of phosphorus in the same position as iron on the surface of carbon cloth with ratio (Fe:P) 1:1 for both spray pyrolysis and electroplating **(Figure 3.5 and Figure 3.6)** suggesting the formation of iron phosphide (FeP) compound.

The SEM images **(Figure 3.7)** and the EDX spectral mapping **(Figure 3.8)** of the cross-section of FeP/CC prepared by spray-pyrolysis were taken to confirm the existence of FeP on the surface of the carbon fibres. It was clear that the FeP particles were on the surface of the carbon cloth fibre as the surface of the carbon cloth, apparently, is rough. EDX spectral mapping also confirmed the formation of FeP film on the carbon cloth.

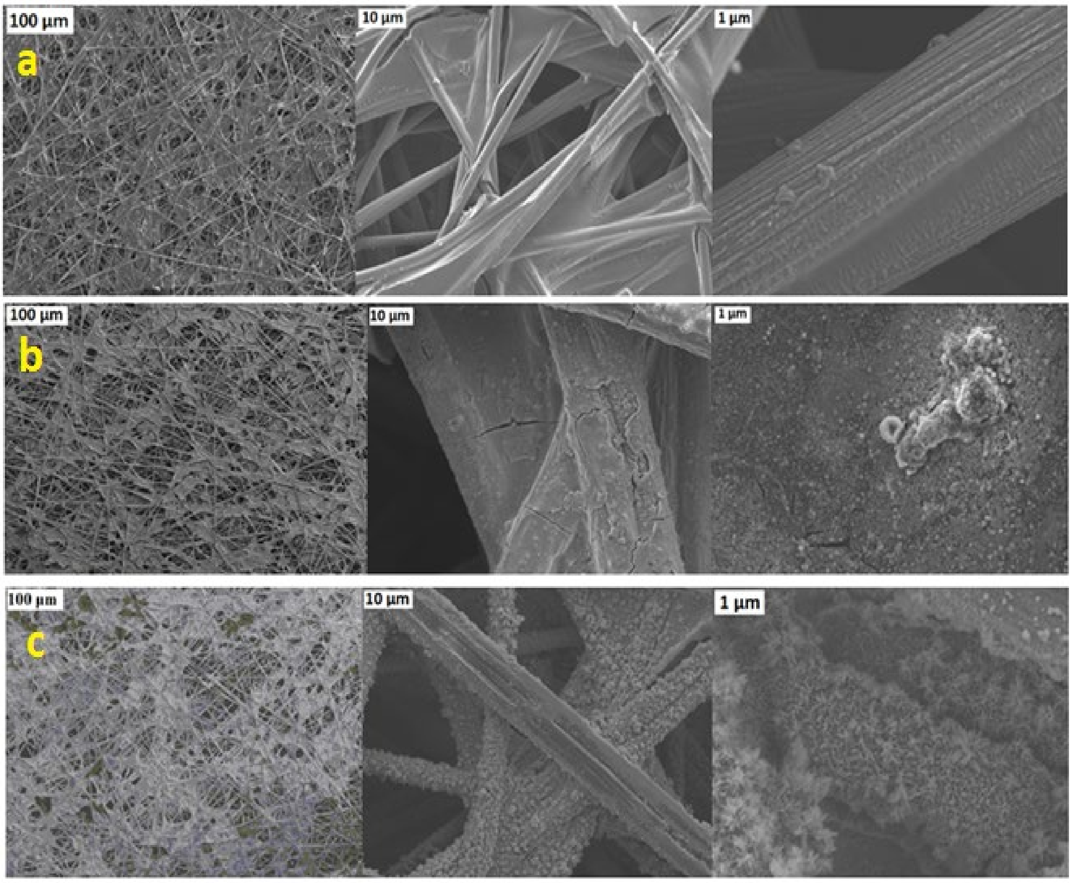

Figure 3.2: SEM images of the top-view of (a) Blank CC, (b) FeP/CC prepared by spray pyrolysis and (c) FeP/CC prepared by electroplating.

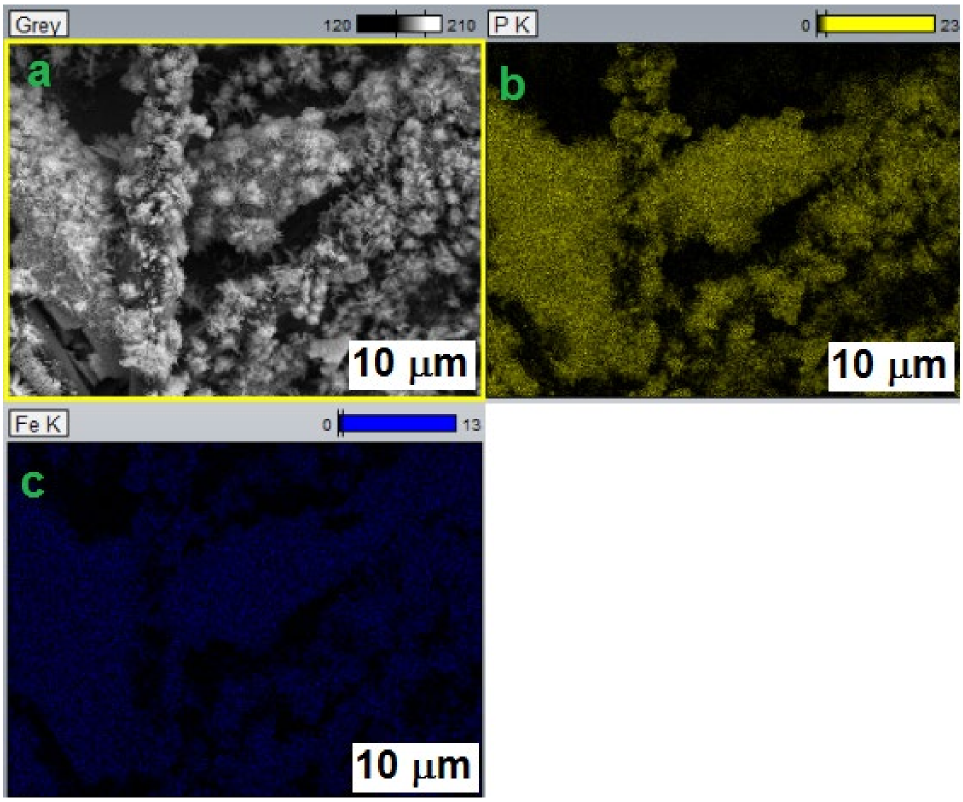

Figure 3.3: Elemental mapping of the top-view of the FeP/CC electrocatalyst prepared by electroplating (a) SEM image (b) distribution of P measured by the (K-shell) and (c) distribution of Fe measured by (K-shell).

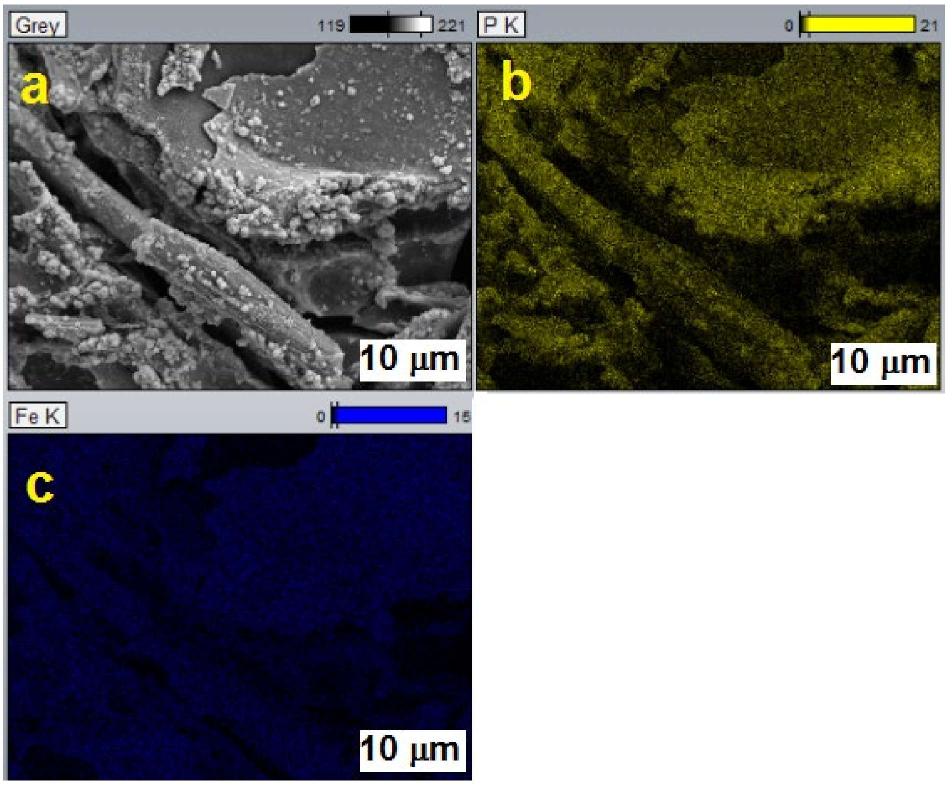

Figure 3.4: Elemental mapping of the top-view of the FeP/CC electrocatalyst prepared by spray-pyrolysis (a) SEM image (b) distribution of P measured by the (K-shell) and (c) distribution of Fe measured by the (K-shell).

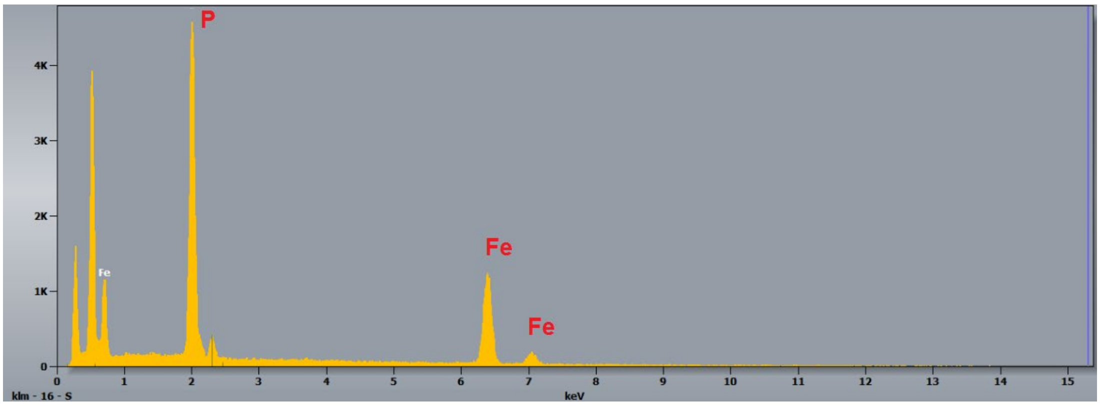

Figure 3.5: EDX spectrum of FeP/CC prepared by electroplating (%Fe was 47.91 % and %P was 52.09%).

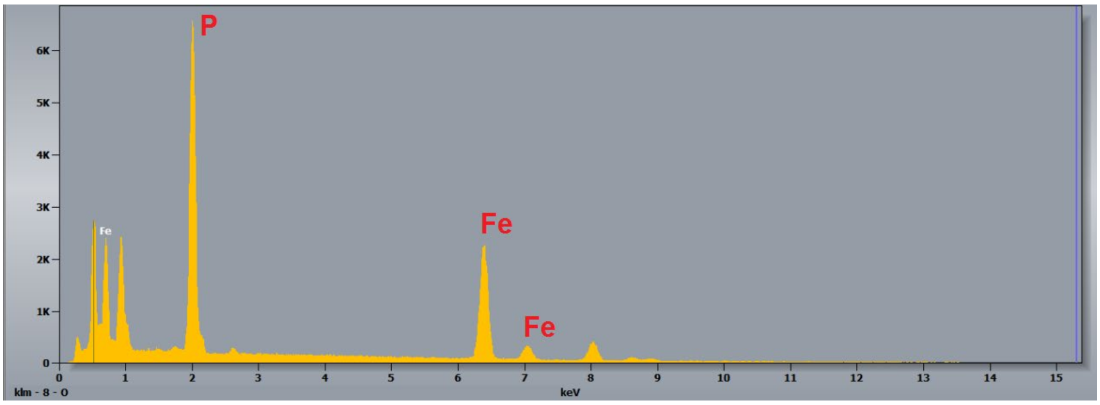

Figure 3.6: EDX spectrum of FeP/CC prepared by spray-pyrolysis (%Fe was 52.48 % and %P was 47.52%).

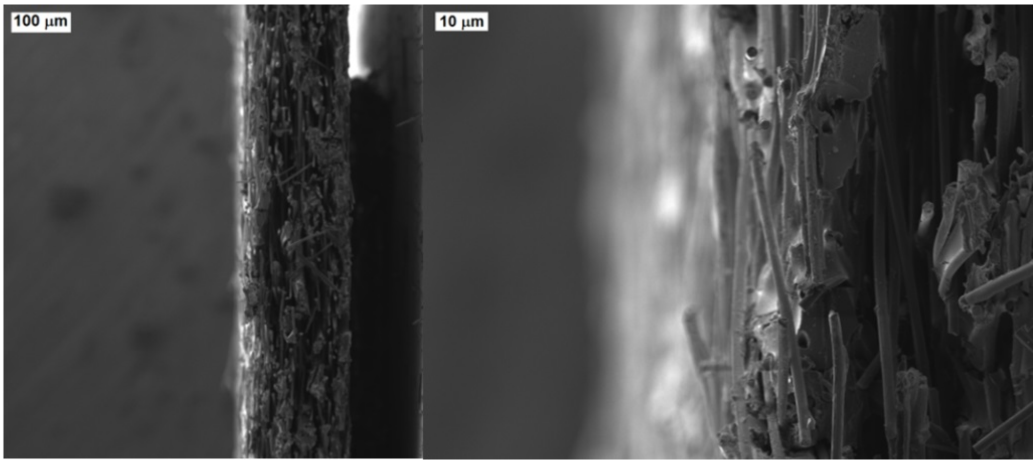

Figure 3.7: SEM of the cross-section of FeP/CC electrocatalyst prepared by spray-pyrolysis on carbon cloth fibres.

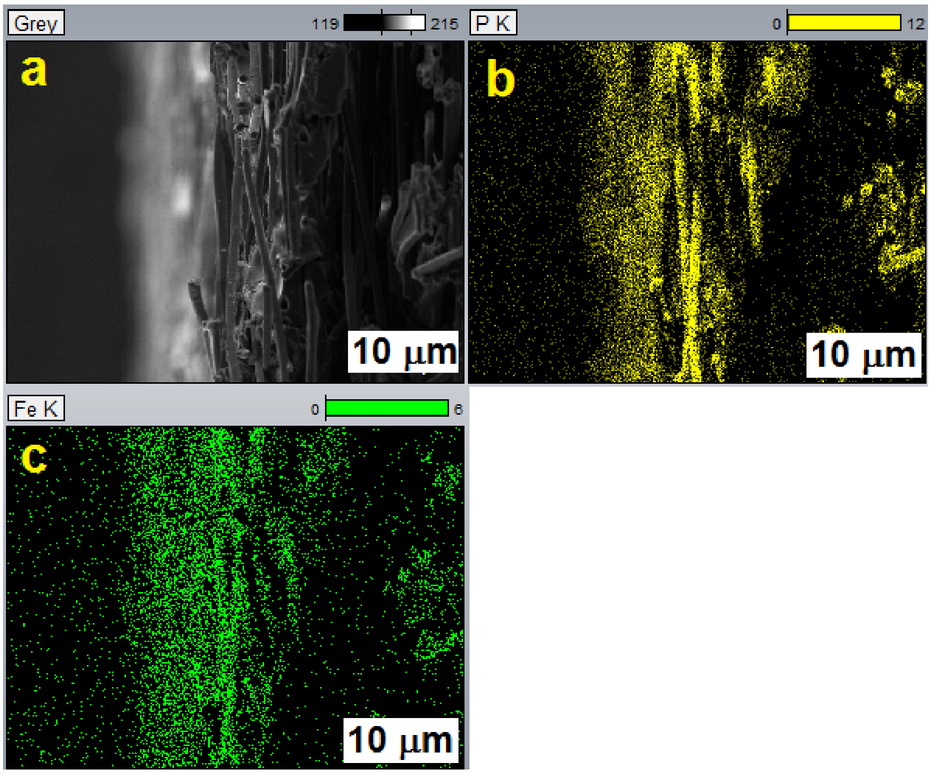

Figure 3.8: Elemental mapping of the cross-section of FeP/CC prepared by spray-pyrolysis; (a) SEM image, (b) distribution of P measured by the (K-shell) and (c) distribution of Fe (K-shell).

Transmission electron microscopy **(TEM)** images of FeP/CC, prepared by electroplating **(Figure 3.9)**, confirm the formation of FeP on the carbon cloth. The low magnification TEM images **(Figure 3.9a and Figure 3.9b)** showed dark areas of thick sample region and oval nanoparticles of FeP in the light middle region of **(Figure 3.9b)**. The particles sizes are ranged between 20 - 50 nm. The high-resolution TEM (HRTEM) image **(Figure 3.9c)** reveals clear lattice fringes with d-spacing of 0.19 nm corresponding to the (211) plane of FeP. The selective area electron diffraction (SAED) pattern **(Figure 3.9d)** of the nano-crystallites showed discrete spots which correspond to the (111), (112), (200), (211), and (212) planes of FeP.

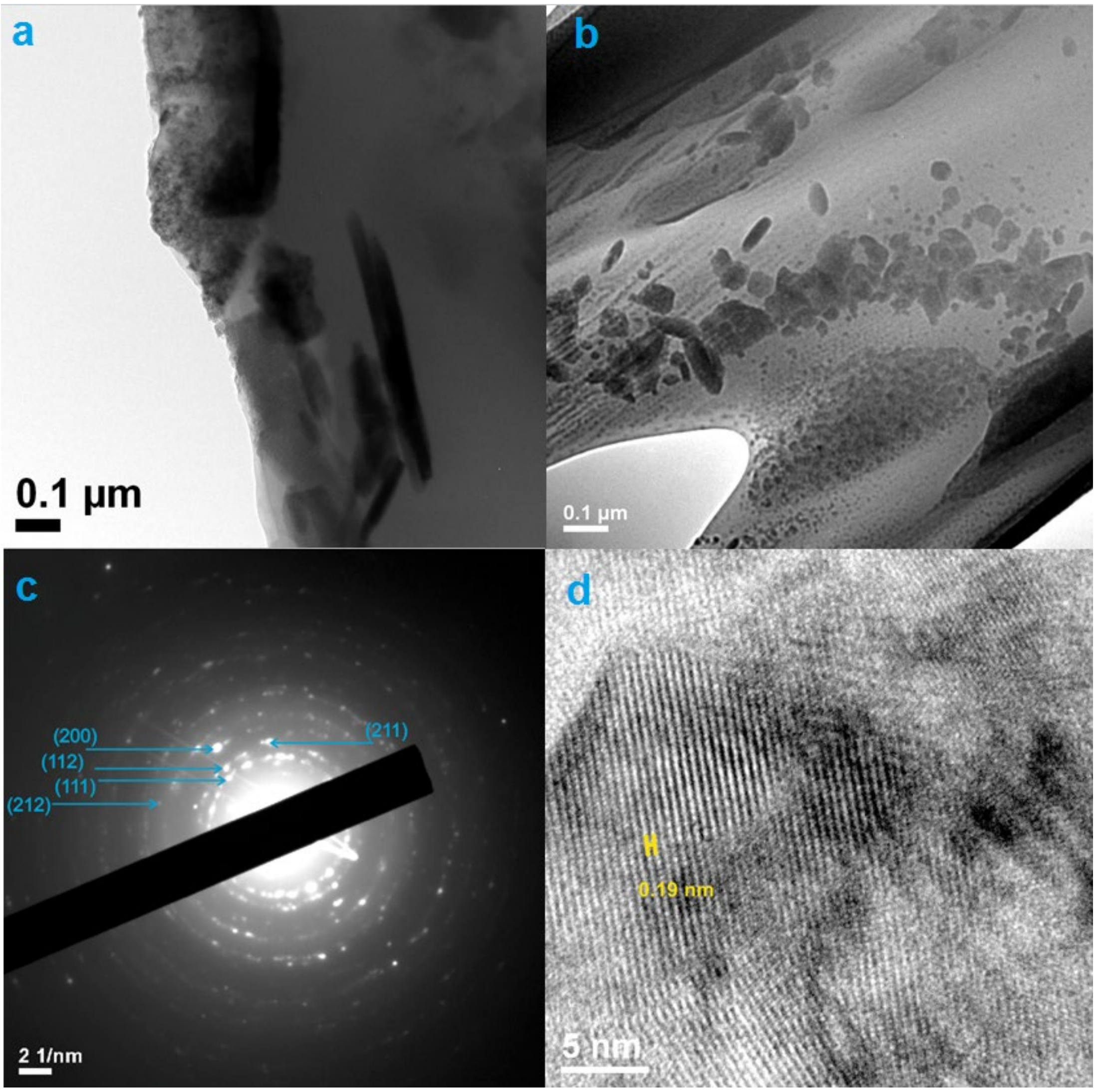

Figure 3.9: TEM of FeP/CC prepared by electroplating; a and b TEM images of the FeP particles on the carbon cloth, c: diffraction resulted from FeP particles and d: HRTEM image.

Transmission electron microscopy (TEM) images of FeP/CC, prepared by spray pyrolysis **(Figure 3.10)**, confirm the formation of FeP on the carbon cloth. The low magnification TEM images **(Figure 3.10a and Figure 3.10b)** showed dark areas of thick sample region and oval nanoparticles of FeP in the light middle region of **(Figure 3.10a)**. Generally, the FeP particles prepared by electroplating are smaller than that prepared by spray-pyrolysis. The majority of particles size of FeP particles prepared by spray-pyrolysis were of size ranged 50 - 60 nm. Few particles of reached 130 -160 nm were also observed. High-resolution TEM (HRTEM) image **(Figure 3.10c)** reveals clear lattice fringes with interplanar spacing of 0.24 nm corresponding to the (111) plane of FeP. The selective area electron diffraction

(SAED) pattern **(Figure 3.10d)** of the nano-crystallites showed discrete spots which correspond to the (111), (200), (211), and (212) planes of FeP.[23-26, 28] There is abundant evidence that the electrocatalyst contains iron phosphides including XRD, SEM, EDX and TEM.

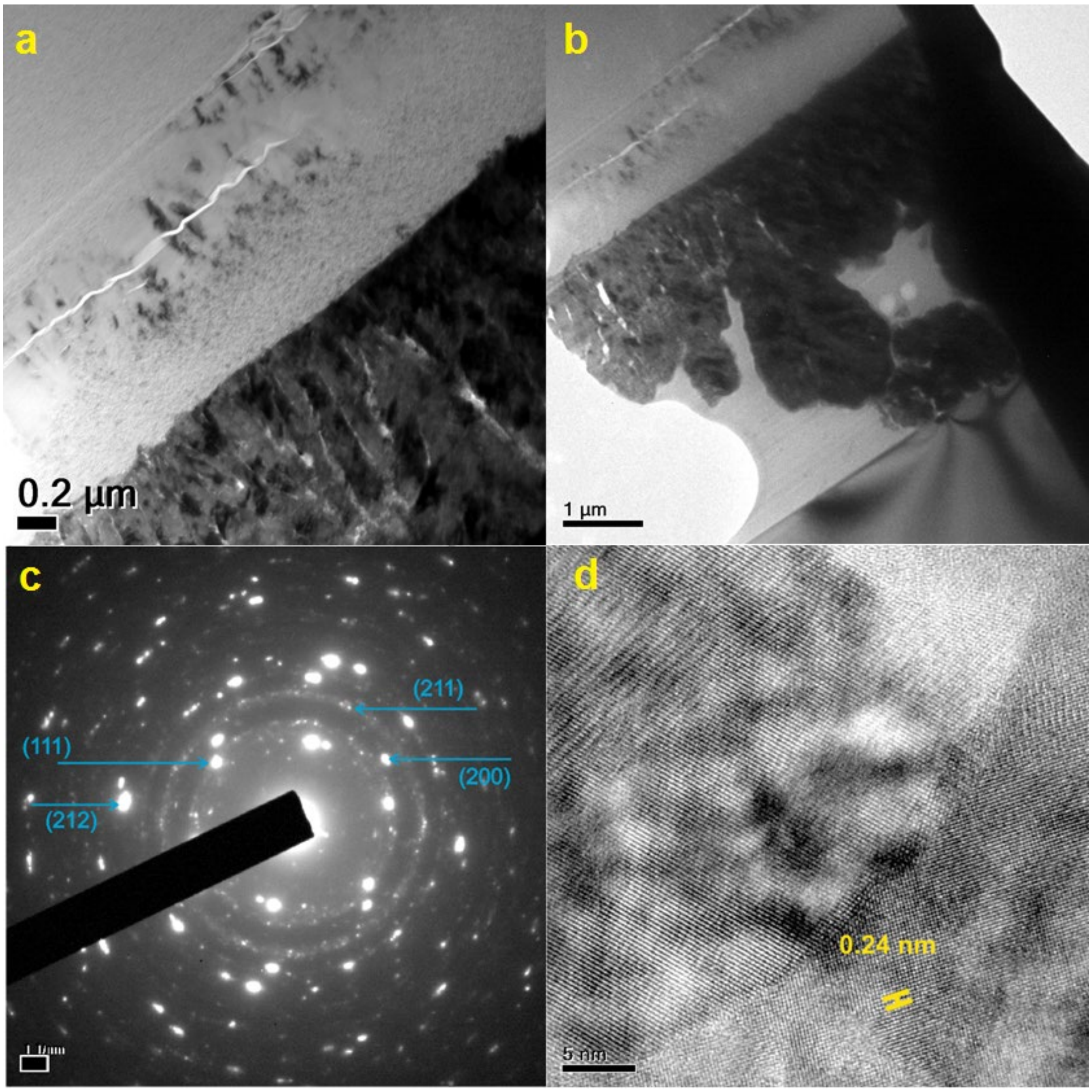

Figure 3.10: TEM of FeP/CC prepared by spray-pyrolysis; a and b TEM images of the FeP particles on the carbon cloth, c: diffraction resulted from FeP particles and d: HRTEM image.

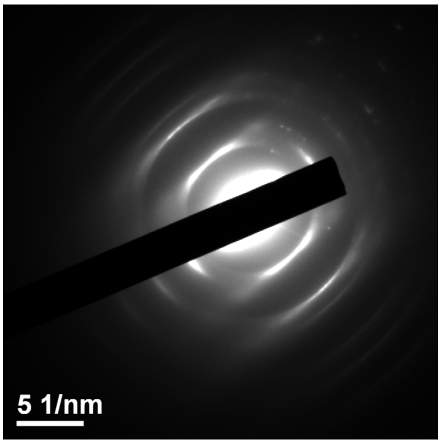

Figure 3.11: The diffraction of carbon cloth.

3.1.1. Electrochemical measurements in acidic medium

Linear sweep voltammetry (LSV) experiments **(Figure 3.12)** were used to study the catalytic activity of the two FeP/CC electrocatalysts. Blank carbon cloth showed a weak catalytic activity with a high onset potential (>0.60 V) **(Figure 3.13)**. The FeP/CC electrocatalysts prepared by spray pyrolysis and electroplating can afford current densities of -10 mA/cm^2 at 102 and 65 mV, respectively. η_{10} is the difference between the applied potential and standard potential at -10 mA/cm^2 ($\eta_{10} = E_{applied} - E^{o}$). The current densities values (-10 mA/cm^2) were chosen to benchmark the overpotential values with that reported in literature. The onset potential definition varies from article to article and it represents the potential at which the electrocatalytic activity can be detected and typically ranging between 0.5 - 1.0 mA/cm^2.[48] The electrocatalytic performances of the iron oxides precursors were very low compared to that of the iron phosphides based electrocatalysts.

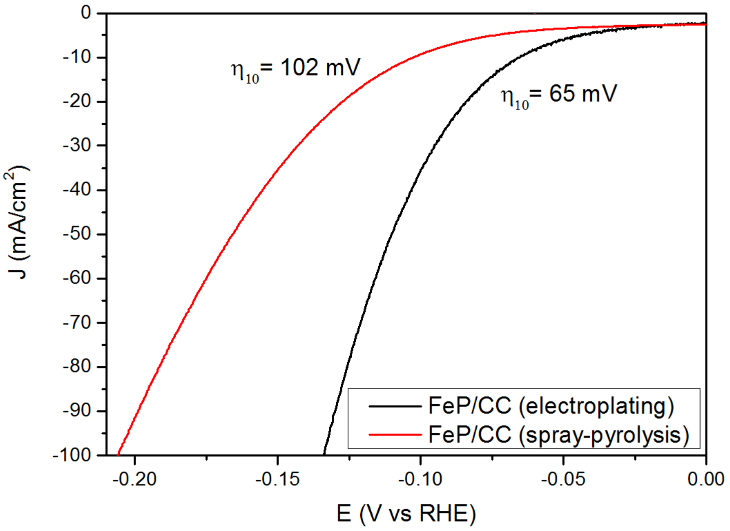

Figure 3.12: LSV of FeP/CC electrocatalysts prepared by the two methods; electroplating (black) and spray-pyrolysis (red) in 0.5 M H_2SO_4 with a scan rate of 5 mV/s.

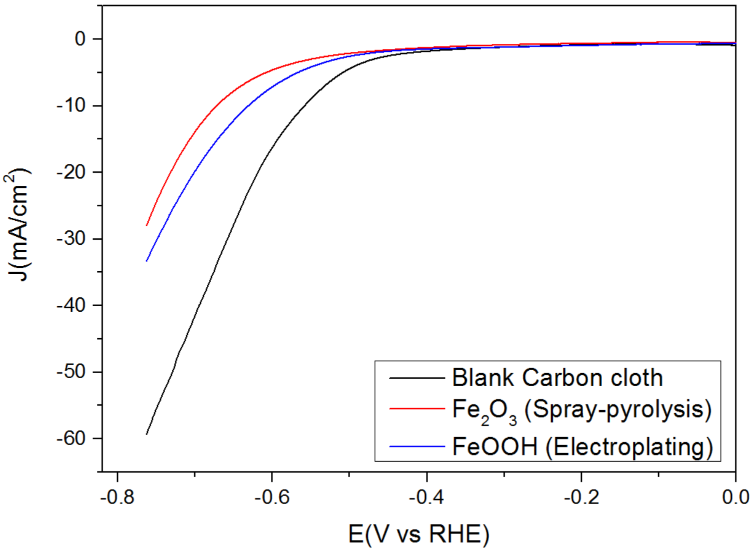

Figure 3.13: LSV of Iron oxides prepared via the two methods in 0.5 M H_2SO_4 with a scan rate of 5 mV/s.

3.1.1.1. Tafel plots

Tafel plots of FeP electrocatalysts were recorded with the linear regions fitted into the Tafel equation $\eta = a + b \log J$ where J is the current density and b is the Tafel slope. A Tafel slope of 120, 40, or 30 mV/dec is expected if the Volmer, Heyrovsky, or Tafel step is the rate determining step, respectively.[49, 85, 245, 246] The curves in the low current density region show Tafel slopes of 65 and 83 mV/dec for FeP/CC prepared by electroplating and spray-pyrolysis, respectively **(Figure 3.14)**. The Tafel slope for FeP/CC prepared through electroplating suggests that the HER might proceed through via Volmer-Heyrovsky mechanism (Volmer step: $H^+ + e^- \rightarrow H_{ads}$ and Heyrovsky process: chemical desorption: $H_{ads} + H^+ + e^- \rightarrow H_2$) and the rate-limiting step is the electrochemical desorption process.[95] It is worth noting that the Tafel slope reported by Li et al [70] was 29.2 and the reaction passed through Volmer-Tafel mechanism. The difference between these values may be due to different reasons including the properties of the carbon cloth. The carbon cloth substrate used in the current work was of a different brand from that used by Li et al therefore the properties may be different in a way that can cause changes in their interaction of the FeP particles and subsequently with protons.

The Tafel slope of FeP/CC electrocatalyst prepared by spray pyrolysis showed that HER proceeded via Volmer–Heyrovsky mechanism and the Volmer reaction is the rate-limiting step.[32, 49, 247] The differences in surface coverage (mass loading) and particles sizes of the two electrocatalyst may be the reason behind the difference between the Tafel slope and the pathways of the reaction.

The exchange current densities of the two electrocatalyst were determined by the intersection of Tafel plots **(Figure 3.14)**. The exchange current densities of the two FeP/CC electrocatalyst were 0.495 and 0.518 mA/cm^2 for electroplating and spray-pyrolysis, respectively. The close values confirm the two methods (electroplating and spray-pyrolysis) succeeded in the formation of the same materials as suggested by the physical characterization (SEM, EDX and TEM). It is worth noting that the reported exchange current densities are slightly lower than the value reported by Li et at (0.68 mA/cm^2) [70] reflecting the high electrocatalytic activity of Li et al compared to the prepared FeP/CC electrocatalysts.

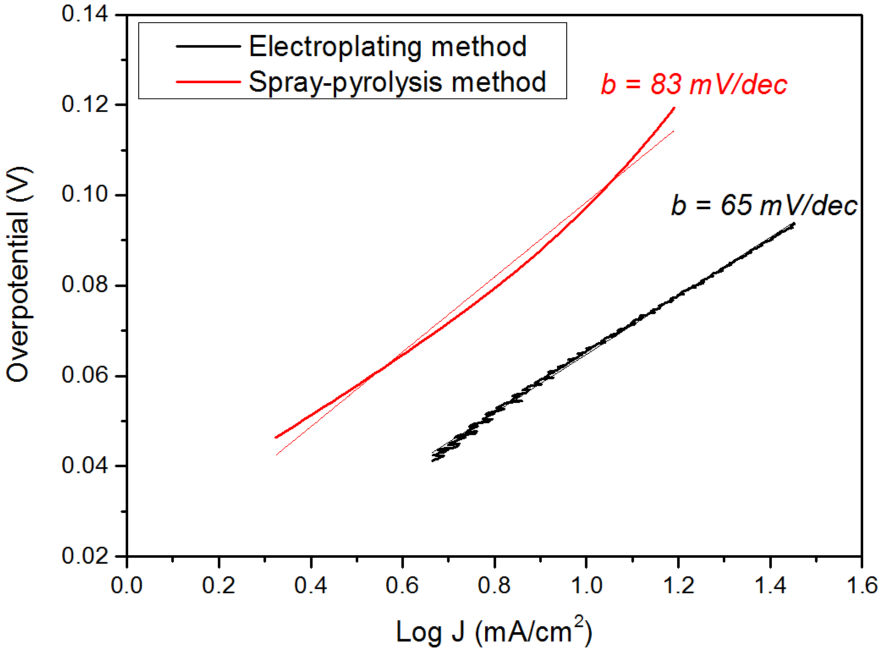

Figure 3.14: Tafel plots of the electrocatalysts derived from the LSV curves in 0.5 M H_2SO_4.

3.1.1.2. Electrochemical impedance spectroscopy in acidic medium

Electrochemical impedance measurements (EIS) were performed at the voltage that corresponds to η_{10} to give more insights into the kinetics of HER process at the electrode surface and are presented as Nyquist plots in **(Figure 3.15 - Figure 3.17)**. The Nyquist plots showed semi-circles that were fitted to an electrical equivalent circuit model of modified Randles circuit **(Figure 3.18)**. R1 is corresponds to the solution resistance. R2 and Q2 are the charge transfer resistance and the constant phase element, respectively, corresponding to the electron transport within the sample **(Table 3-1)**. The high frequency intersection with the *x*-axis (real impedance) represents the ohmic resistance (R1) which results from solution resistance and all contact resistances. The charge transfer resistance (R2) values can be calculated from the low frequency region and can be used to correlate the electrocatalytic kinetics; a low value suggests a fast reaction rate and vice versa.[248]

As expected the blank carbon cloth has a high charge transfer resistance (8.459 ohm) compared to the two electrocatalysts and low capacitance (37.09 μF) that reflects its poor electroactivity **(Figure 3.15) (Table 3-1)**. The two electrocatalysts showed the same semi-circular responses where the diameter represents the resistance for charge transfer (Rct) at the surface of the two electrocatalysts for HER.[249] The charge transfer resistance of FeP/CC prepared by electroplating was 2.77 ohm and for spray-pyrolysis was 4.72 ohm. The charge transfer resistance of the two electrocatalyst are low and close to what is reported in literature with FeP nanoparticles (4.75 ohm) [249] and with FeP based on carbon nanosheets (5.2 ohm).[250] The charge transfer resistance value of FeP/CC prepared by electroplating reflects its superiority over FeP/C prepared by spray-pyrolysis. The faster rate could be due to an intrinsic difference between the two FeP materials or the difference of the electrical conductivities and effective electron transport at the electrocatalyst and electrolyte solution interface.[251]

Table 3-1: EIS data of the FeP/CC electrocatalysts prepared by electroplating and spray-pyrolysis methods in acidic medium (0.5 M H_2SO_4).

FeP/CC	***Blank carbon cloth***	***Electroplating***	***Spray-pyrolysis***
R1 (ohm)	3.499	2.7	2.32
Q2 (F.S^(a-1)	37.09 x 10^{-6}	0.11	0.015
a2	0.9185	0.8	0.874
R2 (ohm)	8.459	2.77	4.72

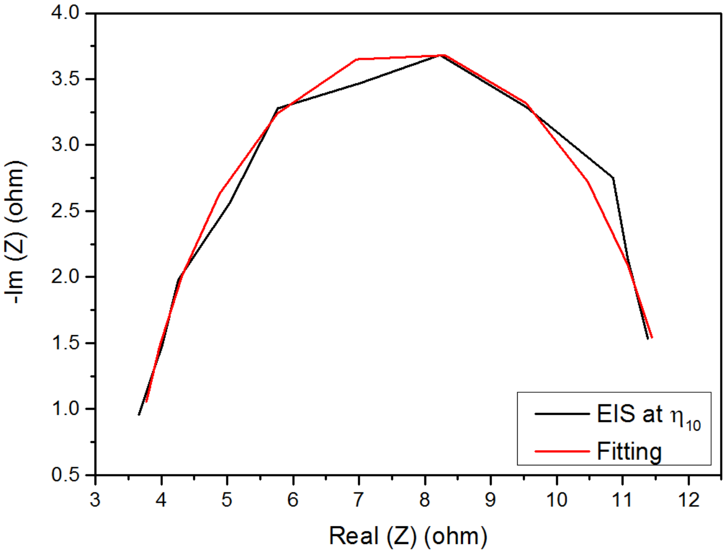

Figure 3.15: EIS of blank CC at η_{10} = - 10 mV/cm^2 in 0.5 M H_2SO_4.

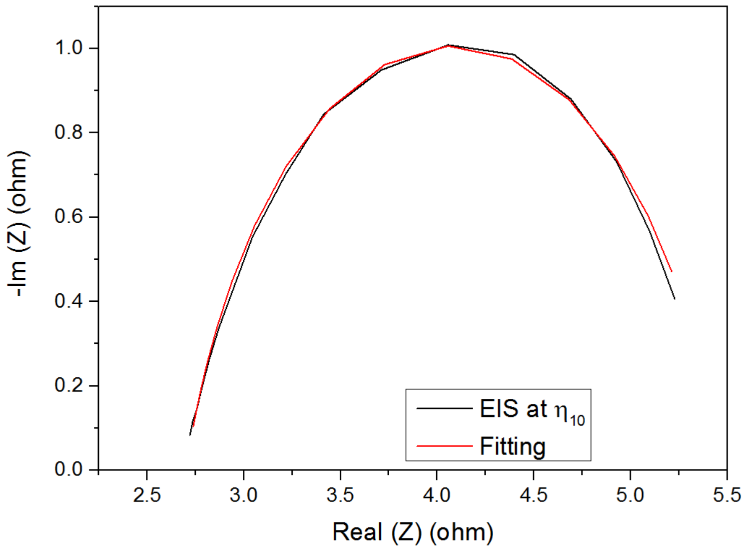

Figure 3.16: EIS of FeP/CC prepared by electroplating method at η_{10} = - 10 mV/cm^2 in 0.5 M H_2SO_4.

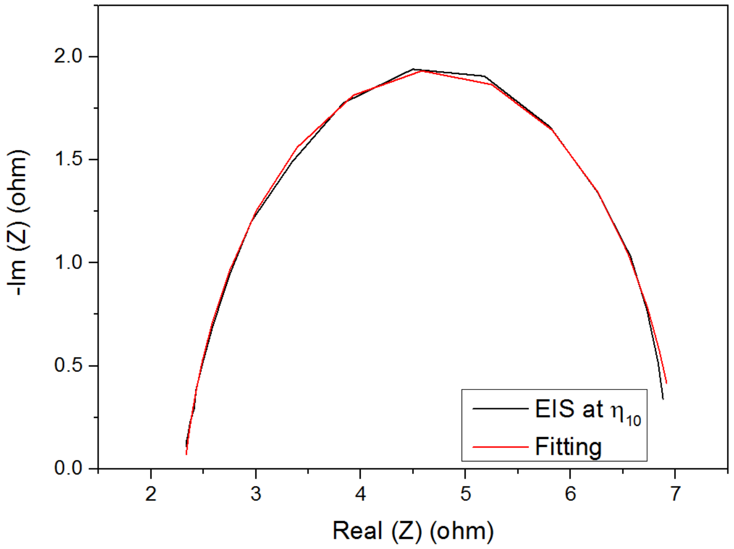

Figure 3.17: EIS of FeP/CC prepared by spray-pyrolysis method at η_{10}= -10 mV/cm^2 in 0.5 M H_2SO_4.

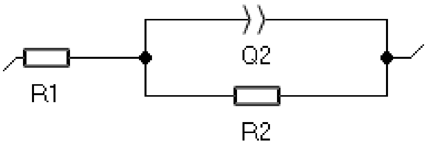

Figure 3.18: Equivalent one-time-constant circuit used to fit the EIS data of the two electrocatalysts.

3.1.1.3. Capacitance measurements

Capacitance measurements were made by performing multiple CV experiments in a non-faradaic region (charge associated with movement of electrolyte ions, reorientation of solvent dipoles and adsorption/desorption at the electrode-electrolyte interface) at different scan rates. The blank carbon cloth has a very low capacitance resulting from low electrochemical activity **(Figure 3.19)**.[252, 253]

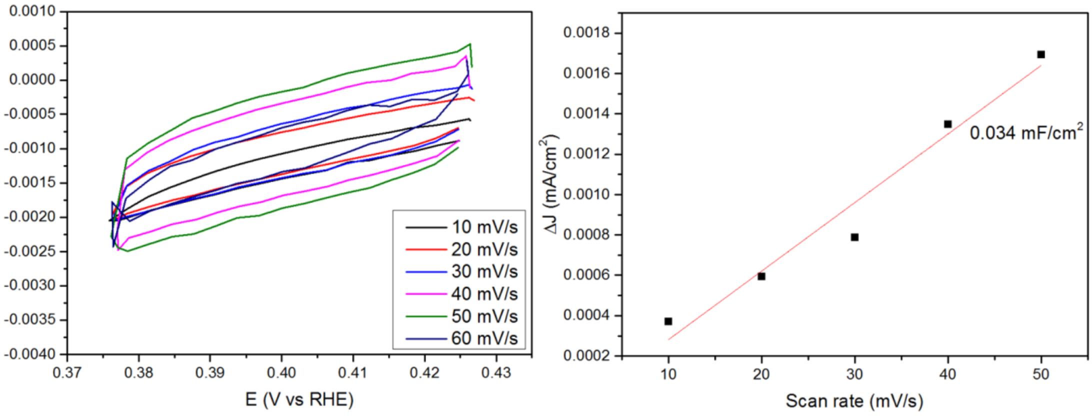

Figure 3.19: Double layer capacitance measurements of blank CC; the curves were taken in non-faradaic region in 0.5 M H_2SO_4.

The difference in the electrocatalytic activities of the two FeP electrocatalysts can be explained by the difference in the electrochemically active surface area (ECSA) which is a reflection of the amount of FeP on the carbon cloth. The ECSA is directly proportional to the **(Figure 3.20 and Figure 3.21)** double layer capacitance (C_{dl})$^{19, 21, 23, 24}$ and the linear slope corresponds to the ECSA, which is 2-fold C_{dl}.$^{23, 24}$ The slope for FeP/CC prepared by electroplating is higher than that prepared by spray pyrolysis reflecting the big difference in the electrocatalytic activities and difference between the mass loading of the two FeP in the two cases. The ECSA of FeP prepared by electroplating is about three times that of FeP prepared by spray-pyrolysis, not ten times, reflecting the difference in the mass loadings. The non-linear relation may be arising from the difference between the morphology in the two cases. FeP/CC prepared by electroplating showed needle like structure unlike the appearance of FeP prepared by spray pyrolysis which appears like cracks on the surface of carbon cloth fibres.^{254} The same trend was observed in the case of amorphous molybdenum sulfide catalysts at which the relation between the roughness factors and mass loadings was linear untill the morphology and structure changes with high mass loading.^{254}

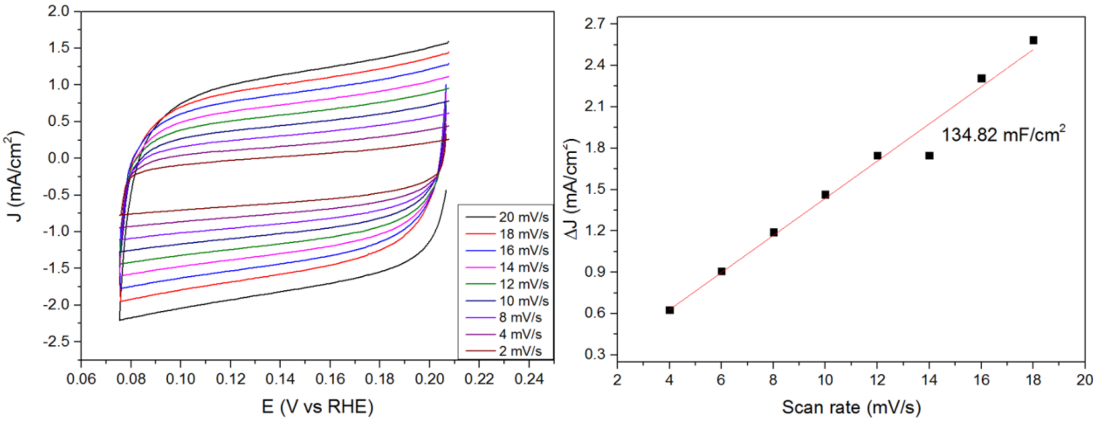

Figure 3.20: Double layer capacitance measurements of FeP/CC prepared by electroplating method; the curves were taken in non-faradaic region in 0.5 M H_2SO_4.

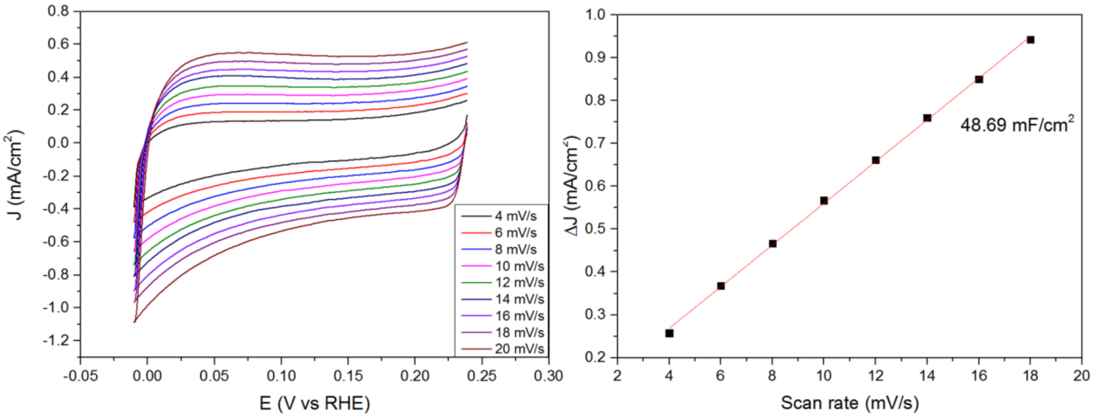

Figure 3.21: Double layer capacitance measurements of FeP/CC prepared by spray-pyrolysis; the curves were taken in non-faradaic region in 0.5 M H_2SO_4.

3.1.1.4. Stability in acidic medium

The stability of FeP electrocatalyts was investigated by applying -10 mA/cm^2 for approximately 18 hours without applying iR correction **(Figure 3.22)**. The overpotential increased by about 35 mV after 18 h in the case of FeP prepared by spray-pyrolysis. The overpotential increased by about 45 mV after 18 h of chronopotentiometry (CP) process for FeP prepared by electroplating. Such decay percentage is about the double of that reported (20 %) by Li et al upon applying 100 mA/cm^2 for 24 h.[70] The decline in the activity may be due to the leaching of FeP out of the surface of the carbon cloth or the deactivation of the active sites.

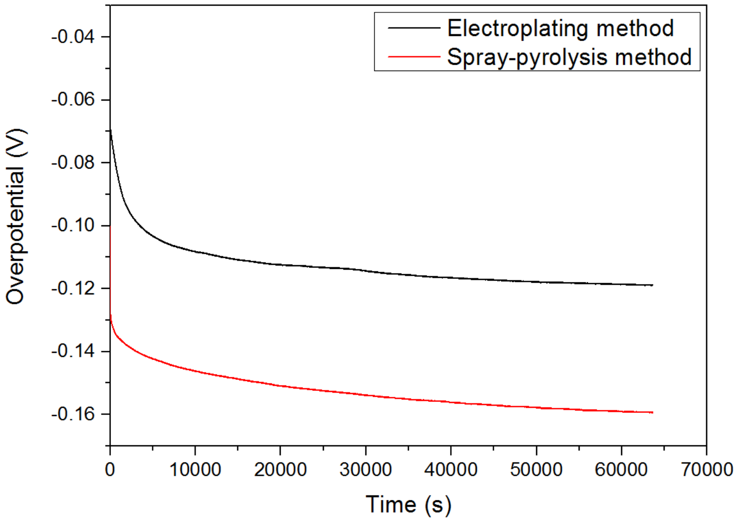

Figure 3.22: Stability test for the two FeP/CC electrocatalysts in 0.5 M H_2SO_4.

3.1.1.5. Durability in acidic medium

The durability of the electrocatalysts was tested by performing 3000 CV cycles (-0.1 to 0.1 V vs RHE with a scan rate of 100 mV/sec) **(Figure 3.23 and Figure 3.24)**. After applying 3000 cycles the overpotential value required to obtain a current density of -10 mA/cm^2 shifted from 65 mV to 136 mV for FeP prepared by electroplating. For FeP/CC prepared by the spray pyrolysis, after 3000 CV cycles, the overpotential value shifted from 102 to 144 mV. The shift in the overpotential value may be attributed to leaching of the catalyst particles out of the substrate or due to the deactivation of the electocatalyst. Some electrocatalyst based on FeP showed the same tend and exhibited a shift in the overpotential values like FeP nanowire arrays (3000 cycles)[108] and other electrocatalysts like FeP nanocrystals showed more durability and no significant change or small shift in the overpotential values after multiple thousands of CV cycles (5000 cycles).[255]

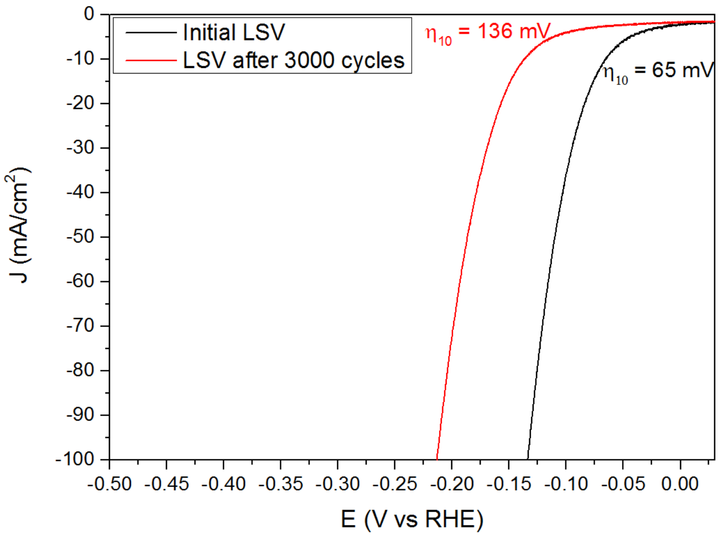

Figure 3.23: Durability of FeP/CC prepared by electroplating in 0.5 M H_2SO_4 at a scan rate of 5 mV/sec before and after 3000 cycles at a scan rate of 100 mV/sec between +0.1 and -0.1 V (vs. RHE).

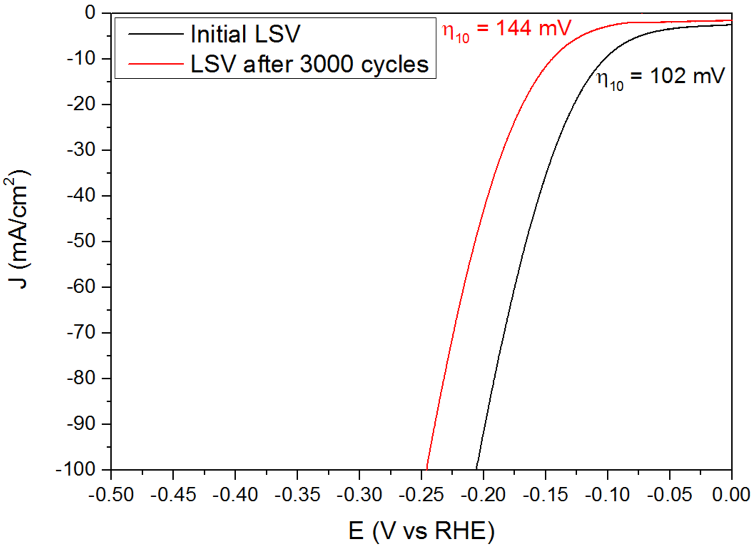

Figure 3.24: Durability of FeP/CC prepared by spray pyrolysis method in 0.5 M H_2SO_4 at a scan rate of 5 mV/sec before and after 3000 cycles at a scan rate of 100 mV/sec between +0.1 and -0.1 V (vs. RHE).

According to the stability and durability tests, it is clear that FeP/CC prepared by spray-pyrolysis was more stable than FeP/CC prepared by electroplating. FeP/CC prepared by spray pyrolysis showed relatively small shift in the overpotential values after the durability test (from 102 to 144 mV) and the overpotential vales also increased by 35 mV for FeP/CC prepared by spray-pyrolysis compared to 45 mV in the case of FeP/CC prepared by electroplating.

3.1.2. Electrochemical performance in near neutral medium

Generally, the hydrogen evolution reaction is controlled by thermodynamic $(E = 0.059\, x\, pH)$ and kinetic barriers. Working in neutral medium can solve many challenges that face industry. Working in near neutral medium would allow working with sea water without the need for any desalination process required for the pH maintenance and can also allow the usage of inexpensive metals. [256]

The electrochemical activities of the two FeP/CC electrocatalysts were investigated in near neutral solution (0.1 M KPi) (pH lies between 5.5 and 6.2) **(Figure 3.25)**. For FeP/CC prepared by electroplating, the overpotential required for -10 mA/cm^2 was 136 mV. In the case of FeP/CC prepared by spray-pyrolysis, the overpotential for -10 mA/cm^2 was 190 mV. The reported overpotential values for FeP based electrocatalyst are ranging between 102 - 386 mV **(Table A1.3)**.

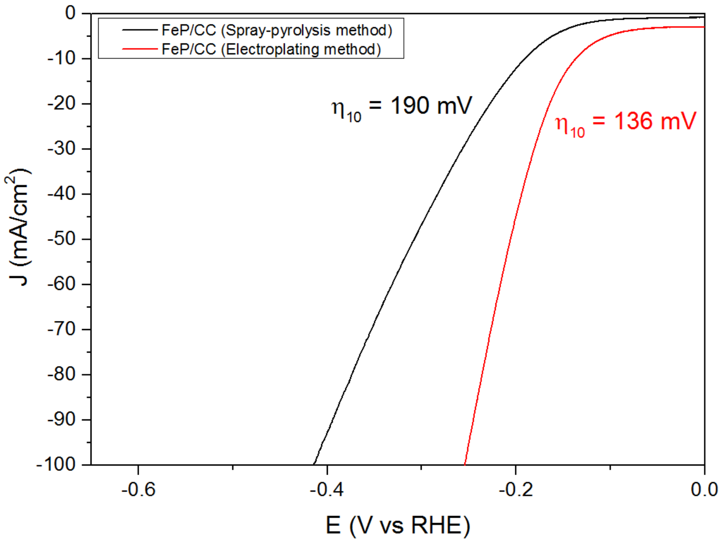

Figure 3.25: LSV of FeP/CC electrocatalysts prepared by the two methods; electroplating (black) and spray-pyrolysis (red) in 0.1 M phosphate buffer.

3.1.2.1. Tafel plots

Tafel plots were obtained from the slow scan rate polarization curves. In buffered near neutral media the HER electrocatalytic activity tends to be controlled by the mass transport of the phosphate.[257] Generally, the reported Tafel slope values in near neutral media tend to be higher than that in acidic media. The Tafel slopes of the FeP/CC electrocatalysts in 0.1 M KPi **(Figure 3.26)** were 94 and 104 mV/dec for electroplating and spray-pyrolysis, respectively. These values are close to Tafel slopes for similar systems based on FeP such as FeP/Ti (99 mV/dec).[95] The smaller Tafel slope value for FeP/CC prepared by electroplating indicate that the HER is faster than that of FeP/CC prepared by the spray pyrolysis method.[258]

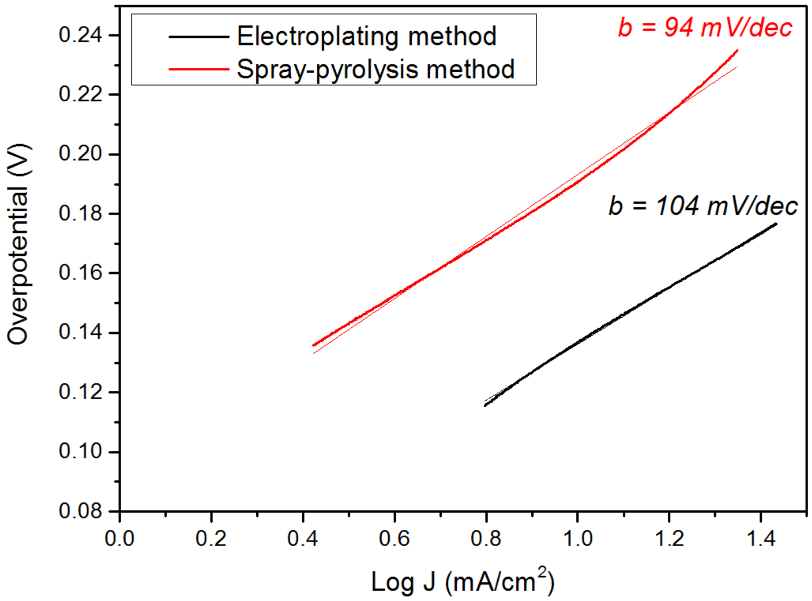

Figure 3.26: Tafel plot of the two FeP/CC electrocatalysts in 0.1 M KPi.

3.1.2.2. Electrochemical impedance spectroscopy in near neutral medium

Electrochemical impedance measurements were performed at the voltage that corresponds to $\eta_{10} = -10\, mA/cm^2$ in 0.1 M KPi and are presented as Nyquist plots in **(Figure 3.27 - Figure 3.29, Table 3-2)**. The electrical equivalent circuit model for fitting the EIS responses of HER on the FeP/CC electrocatalysts **(Figure 3.18)**. The charge transfer resistance (R2) values can be calculated from the low frequency region and can be used to correlate the electrocatalytic kinetics; a low value suggests a fast reaction rate and vice versa.[248] Blank carbon cloth exhibited a high charge transfer resistance (131.6 ohm) and low capacitance, this indicates poor electrocatalytic activity **(Figure 3.27) (Table 3-2)**. The interactions between FeP and carbon cloth in the case of FeP/CC prepared by electroplating method allowed faster kinetics compared to that prepared by spray-pyrolysis method. Specifically the high value of (R2) in the case of FeP/CC prepared by spray-pyrolysis, explains the high overpotential demand in this case compared to that of the electroplating method. In neutral medium the electrocatalytic kinetics seem to be slower than that in acidic medium. Such slow kinetics were reflected in the higher charge transfer resistance (R2) values in the near neutral medium compared to that in acidic medium (< 5 ohm) **(Table 3-1 and Table 3-2)**.

Table 3-2: EIS data of the FeP/CC electrocatalysts prepared by electroplating method and by spray-pyrolysis in 0.1 M phosphate buffer.

FeP/CC	***Blank carbon cloth***	***Electroplating***	***Spray-pyrolysis***
R1 (ohm)	15.57	12.84	14.4
Q2 (F.S^(a-1))	63.93 x 10^{-6}	0.06984	0.019
a2	0.9164	0.401	0.66
R2 (ohm)	131.6	35.45	43.5

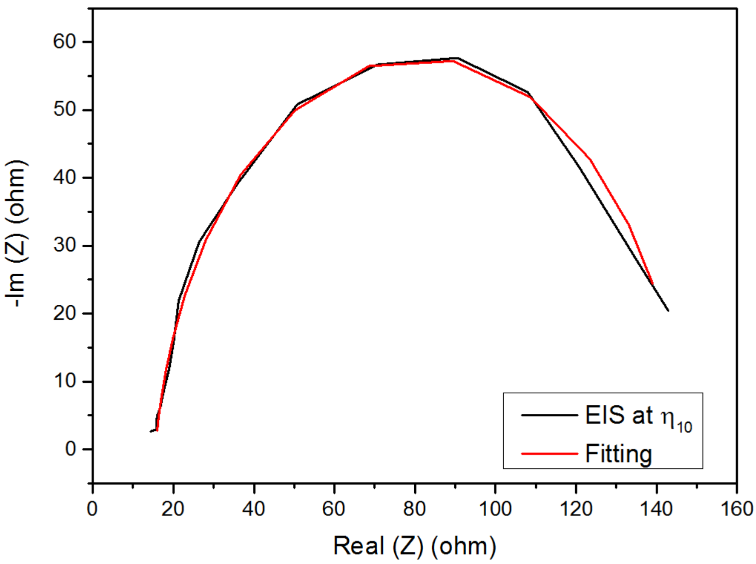

Figure 3.27: EIS of blank CC at η_{10}= - 10 mV/cm^2 in 0.1 M KPi.

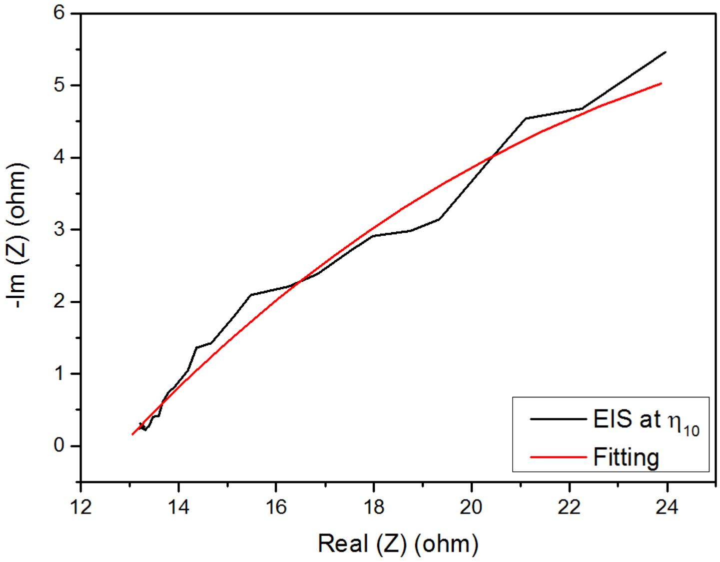

Figure 3.28: EIS of FeP/CC prepared by electroplating method at η_{10}= - 10 mV/cm^2 in 0.1 M KPi.

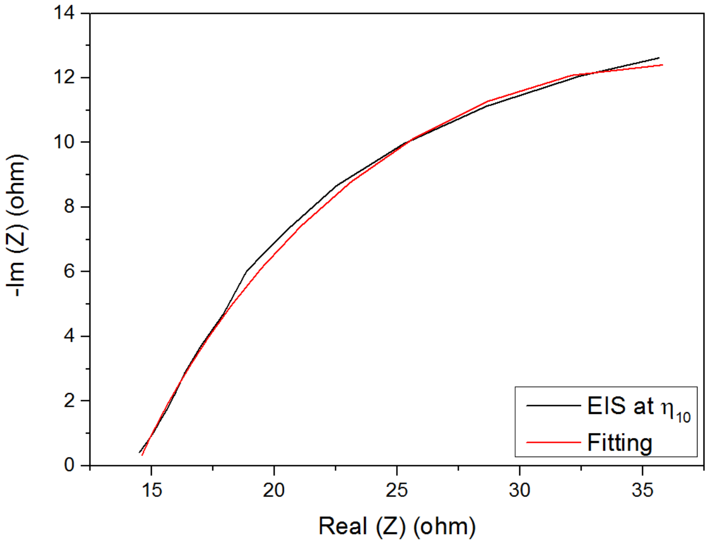

Figure 3.29: EIS of FeP/CC prepared by spray-pyrolysis method at η_{10}= - 10 mV/cm^2 in 0.1 M KPi.

3.1.2.3. Stability in near neutral medium

The stability of FeP electrocatalysts was investigated by applying -10 mA/cm^2 for about 18 h without applying iR correction **(Figure 3.30)**. The iron phosphide electrocatalyst prepared by spray-pyrolysis exhibited more stability in near neutral medium than that prepared by electroplating. There is no significant change in overpotential value after applying -10 mA/cm^2 for 18 h in the case of spray-pyrolysis method. There is about 28 mV increase in overpotential value after 18 h in case of electroplating method. Generally, the two electrocatalysts showed higher stability in near neutral medium comparted to that in acidic medium which may be attributed to the role of the buffer in the stability. Further investigations are required to study/prove such behaviour.

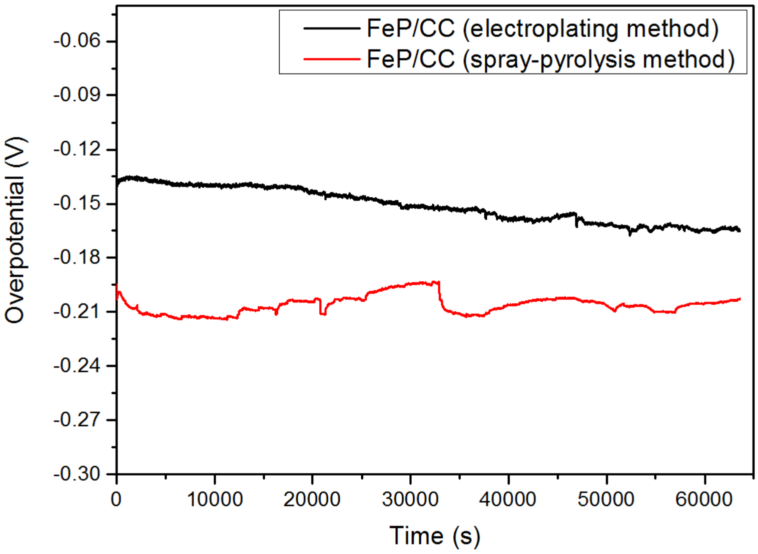

Figure 3.30: Stability test for the two FeP/CC electrocatalysts in 0.1 M KPi.

3.1.2.4. Durability in near neutral medium

The durability of the electrocatalysts was tested by performing 3000 CV cycles (-0.1 to 0.1 V vs RHE with a scan rate of 100 mV/sec) **(Figure 3.31 and Figure 3.32)**. After 3000 CV cycles the overpotential value shifted from 136 to 115 mV indicating that the phosphate buffer may activate/stabilize the FeP particles. The same behaviour was observed in the case of FeP/CC prepared by spray-pyrolysis method where the overpotential value shifted from 190 to 182 mV after 3000 cycles. It is worth mentioning that such behaviour is not common and further investigations are required to understand such behaviour. Chen et al reported the same behaviour with their FeP nanoparticles and they attributed that to the decline in the charge transfer resistance after the stability test. [249]

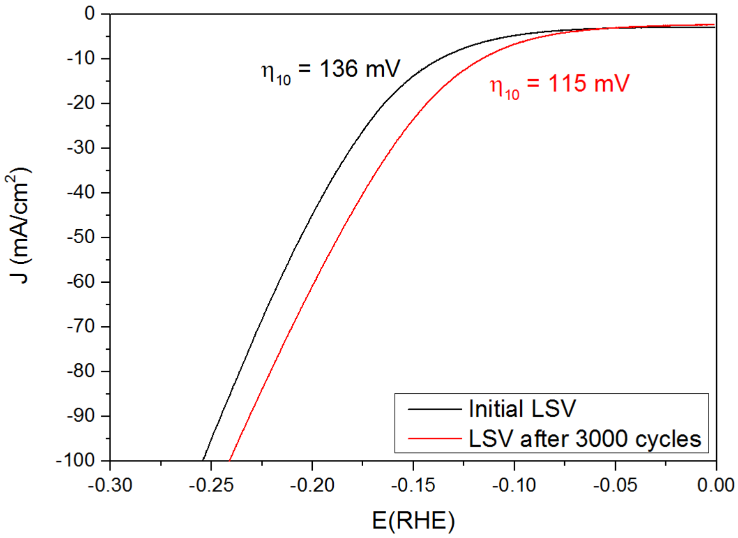

Figure 3.31: LSV curves for FeP/CC prepared by electroplating in 0.1 M phosphate buffer at a scan rate of 5 mV/sec before and after 3000 cycles at a scan rate of 100 mV/sec between +0.1 and -0.1 V (vs. RHE).

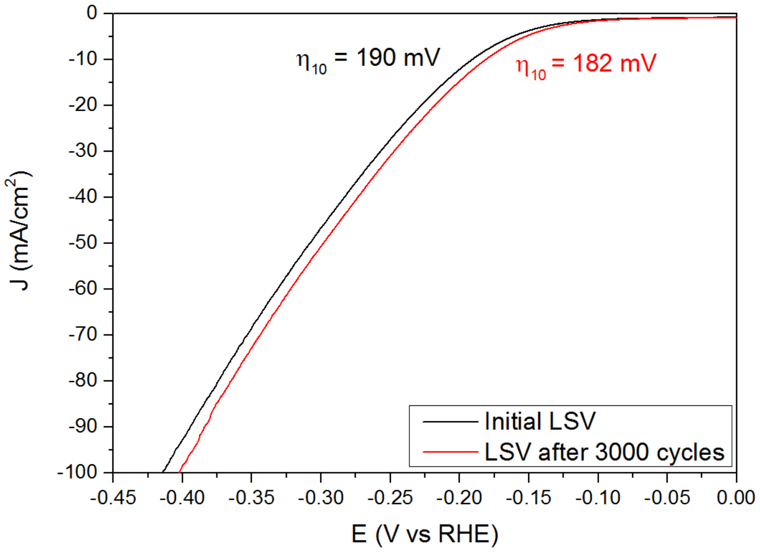

Figure 3.32: LSV curves for FeP/CC prepared by spray pyrolysis in 0.1 M phosphate buffer at a scan rate of 5 mV/sec before and after 3000 cycles at a scan rate of 100 mV/sec between +0.1 and -0.1 V (vs. RHE).

3.1.2.5. Quantification of the produced hydrogen gas

To quantify the produced hydrogen gas, a current density of -5.0 mA/cm^2 was applied for 60 min. The faradaic efficiency was calculated by dividing the experimental no moles of H_2 to the theoretical quantity **(Figure 3.33 - Figure 3.36)** based on the total charge that passed. The faradaic efficiencies were close to 100 % in 0.5 M H_2SO_4 and in 0.1 M KPi solutions for about 1 h. It is worth noting that after one hour a slight decline in the experimental values was observed due to the expansion of the Nafion membrane resulting from the build-up of the produced gas, which increased the volume of the cathodic chamber. In addition a small leak in the electrochemical cell cannot be excluded.

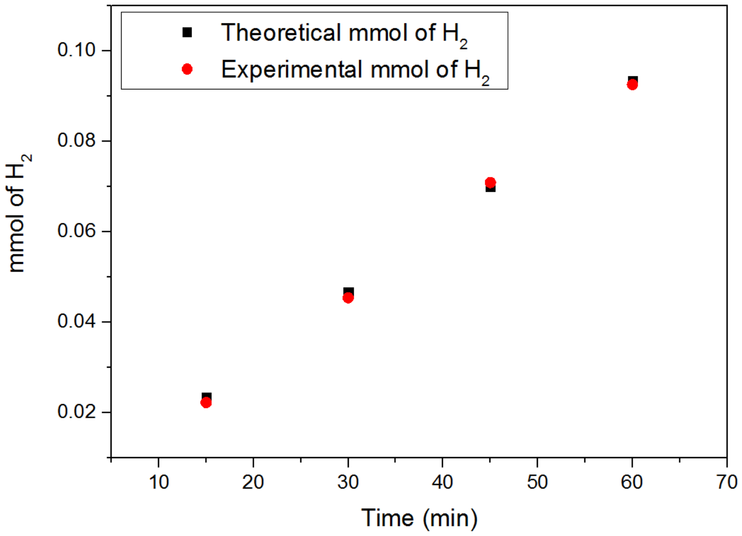

Figure 3.33: Quantification of H_2 gas for FeP/CC electrocatalyst prepared via electroplating in 0.5 M H_2SO_4.

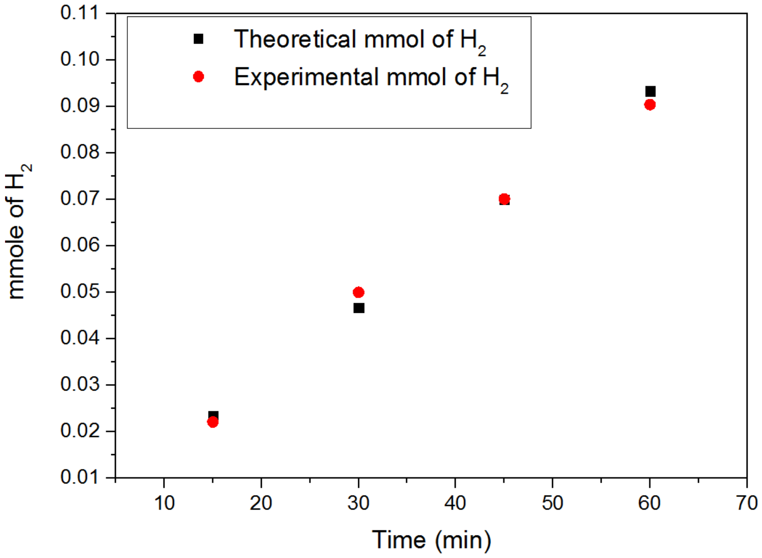

Figure 3.34: Quantification of H_2 gas for FeP/CC electrocatalyst prepared via spray-pyrolysis in 0.5 M H_2SO_4.

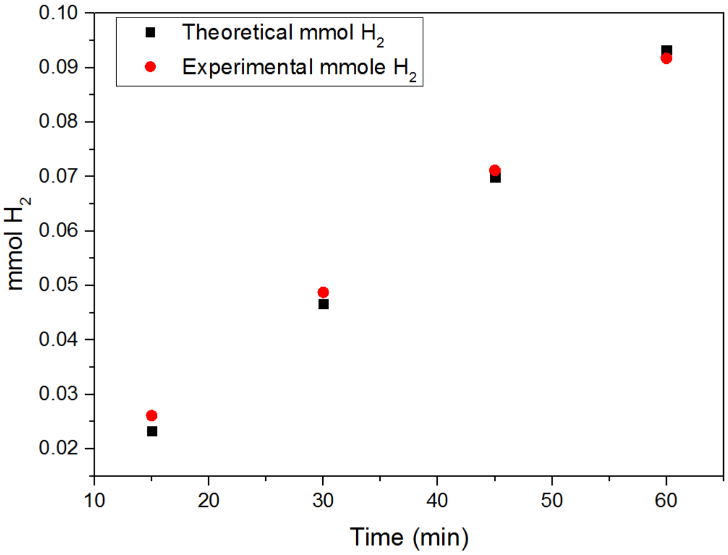

Figure 3.35: Quantification of H_2 gas for FeP/CC electrocatalyst prepared via electroplating in 0.1 M KPi.

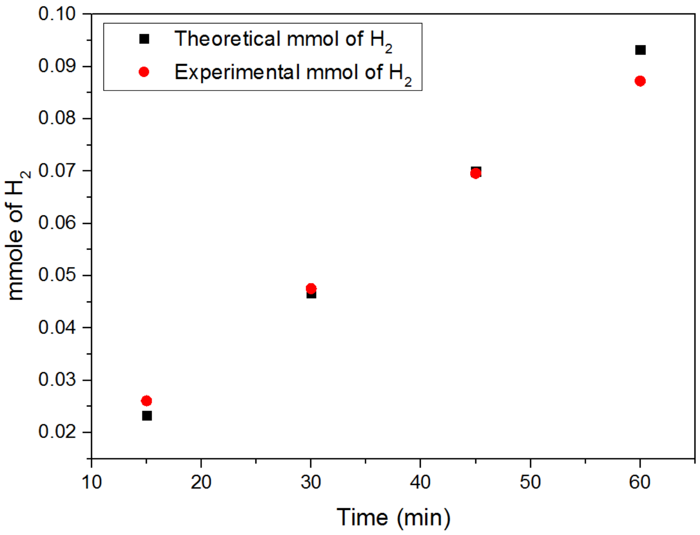

Figure 3.36: Quantification of H_2 gas for FeP/CC electrocatalyst prepared via spray-pyrolysis in 0.1 M KPi.

3.1.3. Comments on the reproducibility of the results

Multiple LSV experiments were used to study and check reproducibility. The changes in the overpotential values were measured and compared using different electrocatalysts and solutions. In the case of acidic medium (0.5 M H_2SO_4), the change in the overpotential values from one electrode to other was approximately 10 and 5 mV (the reported range were collected using 11 different freshly prepared electrocatalysts) for electroplating and spray-pyrolysis methods, respectively. In the case of the near neutral medium (0.1 M KPi), the change in the overpotential values is dependent on pH and higher than that in acidic medium and reached 50 mV or FeP/CC prepared by electroplating (the reported range were collected using 5 different freshly prepared electrocatalysts) and 60 mV for spray-pyrolysis (the reported range were collected using 3 different freshly prepared electrocatalysts).

The fluctuation of the pH of the solution over the used range (5.8 - 6.3) is responsible for change by up to 29.5 mV (*i.e.* 0.059*pH). The fluctuation in the pH values may be related to changes in the temperature. The pH values of the prepared solutions were not adjusted by adding of any additional base or acid and the pH was measured each time before any electrochemical measurements.

3.1.4. Conclusions

FeP/CC electrocatalysts were successfully prepared on carbon cloth via electroplating and by spray-pyrolysis. FeP/CC prepared by electroplating showed a better catalytic activity compared to that prepared by spray pyrolysis method in terms of overpotential, with η_{10} = 65 ± 10 mV compared to 102 ± 5 mV in 0.5 M H_2SO_4. These compare to literature values of FeP on carbon cloth made using electroplating and spray-pyrolysis of 34 and 140 mV, respectively. [70, 71] In addition at near neutral pH, FeP/CC prepared by spray-pyrolysis did not show a big change in overpotential on stability and durability testing compared to electroplating. With respect to use in a mini-reactor FeP/CC exhibits near 100% FE% and is suitable for producing hydrogen at sufficient rate to support hydrogenation catalysis. The charge (Q) that passed during the 18 h was 648 C, such value is very close to what is required (≈ 670 C) for the proposed reactor more details in **Chapter seven p.178**.

4. Electrochemical reduction of carbon dioxide using copper and copper phosphide electrocatalysts; 3D printing as a new methodology

Aims

This part of the project targets the electro-production of a CO/H_2 mixture through the electrochemical reduction of CO_2 using Cu based electrodes in water. Copper based electrocatalysts have been reported to electro-reduce CO_2 and protons into a mixture of products including CO and H_2 gases, respectively. The electro-produced syngas mixture could be used to support the hydroformylation reaction in a reactor powered by sunlight. Several copper based electrodes have been investigated for the production of syngas mixtures. A commercial copper foil and an oxide derived copper electrode (OD-Cu) were prepared using literature methods. OD-Cu is reported to increase the production of CO and C_{2+} products in comparison to copper foil. Two new electrodes were also investigated. Cu_3P/Cu (Cu_3P/Cu) was studied because a related compound is reported to promote CO production, and during work on this thesis a separate report[221] indicated that Cu_3P/C gives 47 % of CO at -0.3 V (RHE) (FE% of H_2 was 53 %).[221] In addition, the development of structured electrodes such as GDEs is an important challenge for the industrial implementation of electrocatalysis. A novel 3-D printing methodology was developed to prepare 3-D printed Cu electrodes.

Abstract

Cu foil, OD-Cu, Cu_3P/Cu, and 3D Cu structures were prepared and characterised using structural (SEM, TEM, PXRD), compositional (EDS), spectroscopic (XPS) and electrochemical techniques (CV, EIS, CA). Development of an ink containing >78 % Cu particles was successfully used to print 3D Cu/polymer composites. Composite structures were calcined to remove organic binder material to give CuO structures that could be chemically or electrochemically reduced. Electrochemical reduction of CO_2 in water was studied using a home-made electrochemical cell, and CO_2 reduction products were determined using a combination of NMR for the liquid products and in-line GC for gaseous products. Cu_3P/Cu gave almost exclusively hydrogen as the main reduction product. The other Cu based electrodes gave mixtures of products dependent on the voltage (partial current density).

4.1. Results and Discussion

4.1.1. Physical characterization of the Cu based electrodes

4.1.1.1. Cu foil

A Cu foil was used as a standard for all the electrochemical measurements. The electropolishing of Cu foil was performed in order to start the electrochemical measurements with a smooth surface.

The PXRD diffractogram **(Figure 4.1)** of Cu foil was recorded after the electropolishing process and it was clear that the intensity of (200) is higher than that of (111) unlike the standard Cu (ICSD # 43495).

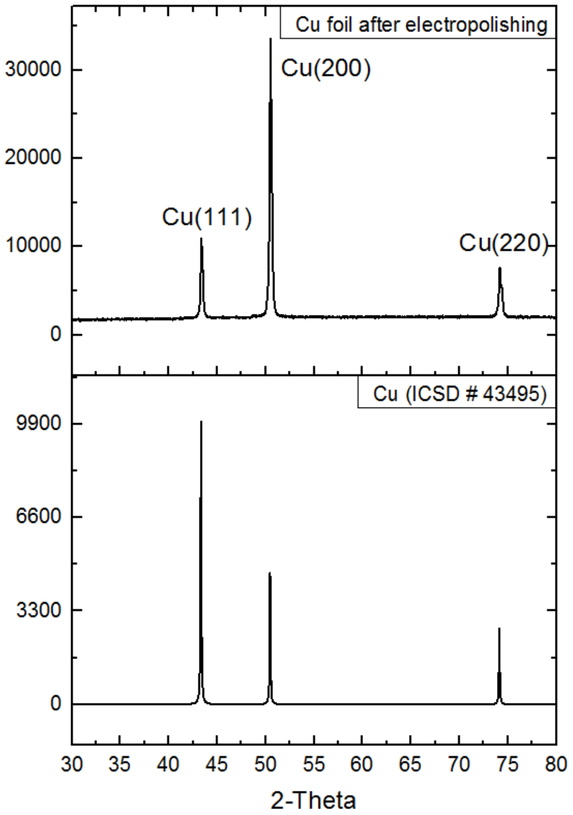

Figure 4.1: XRD patterns for the copper foil after electropolishing.

SEM images of the electropolished Cu foil confirmed that the surface was smooth after the electropolishing **(Figure 4.2)** and ready for the electrochemical measurements.

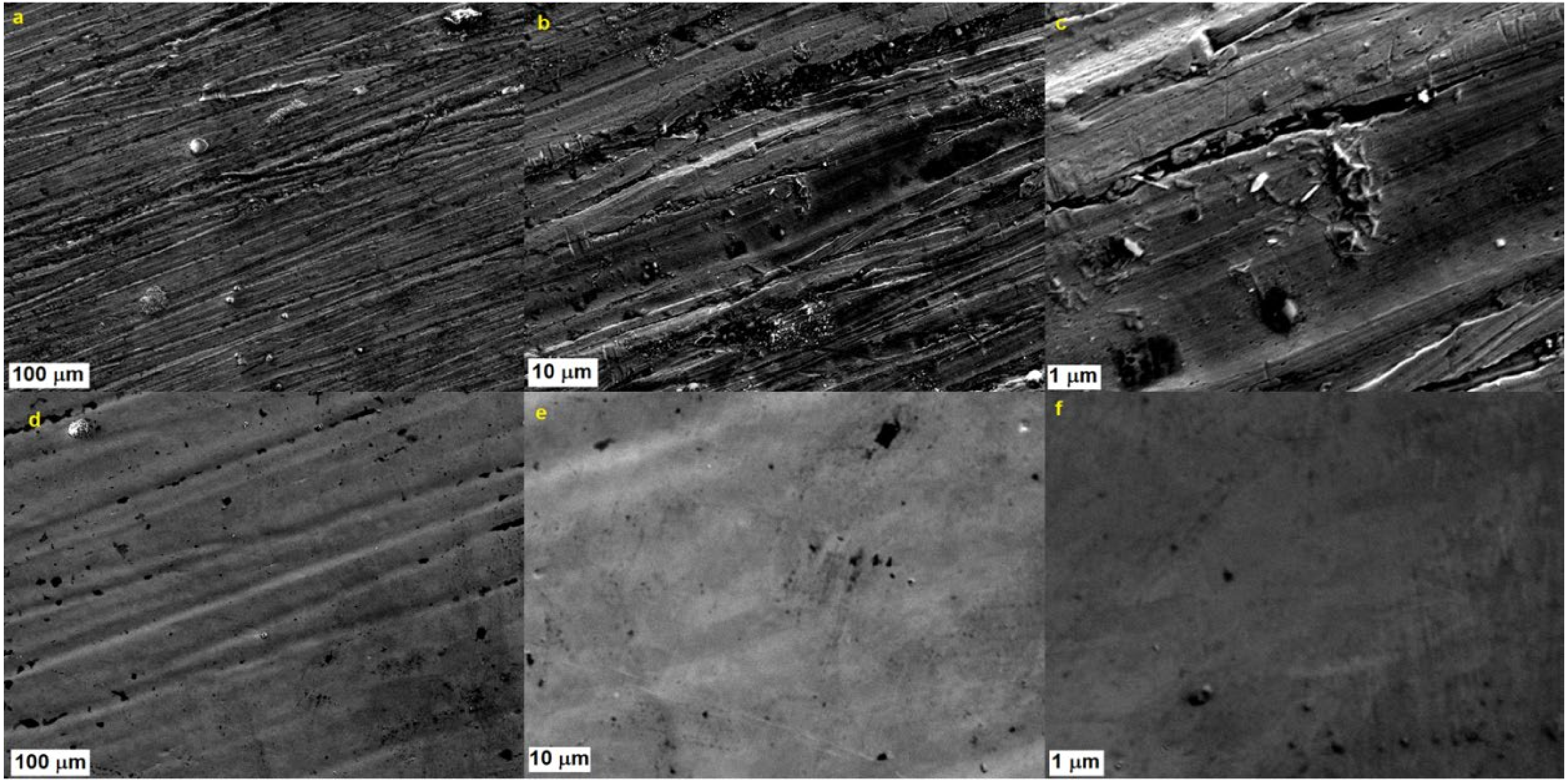

Figure 4.2: SEM images of Cu foil before (a-c) and (d-f) after electropolishing.

4.1.1.2. OD-Cu foil synthesis and physical characterisation

The OD-Cu electrocatalyst was prepared for two reasons: firstly as a standard to compare it with 3D printed OD-Cu electrocatalyst and secondly to use it as a precursor for Cu_3P/Cu foil (the 3D printed PD/OD-Cu was also prepared on 3D printed OD-Cu electrocatalyst). The OD-Cu was prepared according to a reported method.[191]

The roughness factor was measured by comparing the capacitance of the sample to that of smooth Cu surface ($R_f = C_{dl\ of\ sample}/C_{dl\ of\ Cu}$; $C_{dl\ of\ Cu} = 29\ \mu F$). It is worth noting that the roughness factor of the prepared OD-Cu (41.3) is about 10 times that of the reported value in literature (4.7)[191] **(Table 4-1)**. The XRD pattern of the Cu_2O **(Figure 4.3)** showed a preference for (200) over (111) unlike the standard Cu_2O (ICSD # 52043). It may follow the same pattern of the electropolished Cu foil **(Figure 4.1)**.

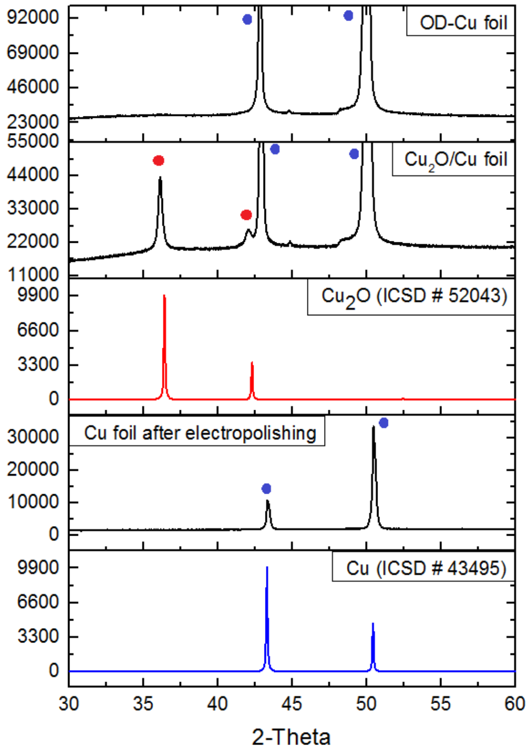

Figure 4.3: XRD patterns for the Cu_2O/Cu foil before electrochemical reduction of the oxides. Blue balls belong to Cu peaks and red balls belong to Cu_2O.

SEM images showed the formation of rough surface OD-Cu electrocatalyst. SEM images **(Figure 4.4)** also showed the existence of additional nanoparticles on the surface of the oxide layer and these particles are responsible for increasing the active surface area and this is reflected in a high roughness factor value **(Table 4-1)**. The roughness factor was calculated through measuring the capacitance of the electrocatalyst by performing multiple CV cycles with different scan rates.

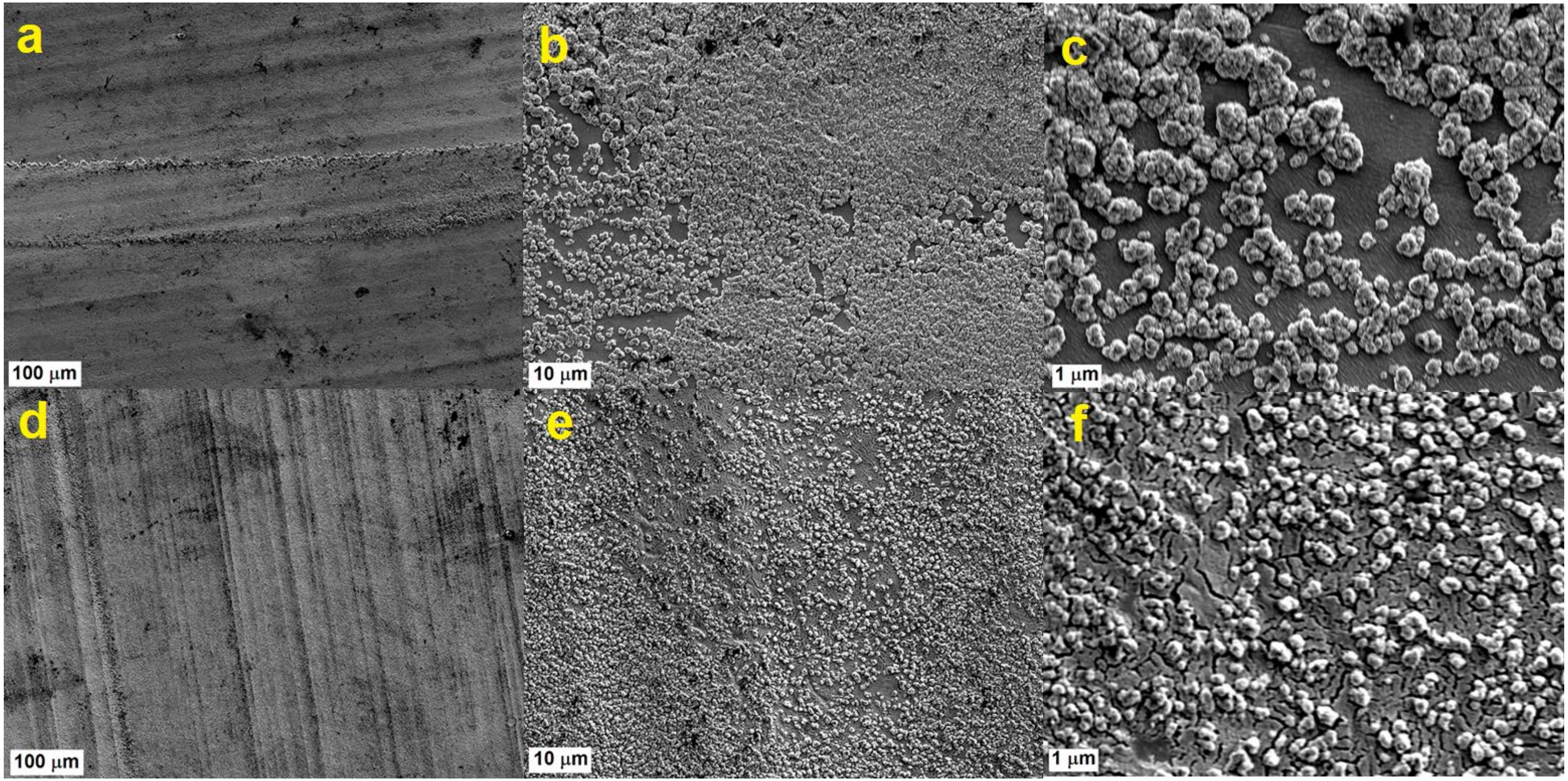

Figure 4.4: SEM images of the copper foils: (a-c) Cu_2O/Cu foil and (d-f) OD-Cu foil before electrochemical measurements.

Table 4-1: Capacitance and roughness factor measurements of the Cu foils in 0.1 M $KHCO_3$ under N_2.

Electrocatalyst	**Capacitance mF**	**Roughness factor**
Cu foil	0.029	1
OD-Cu foil	1.2	41.3
Cu_3P/Cu foil	0.65	22.4

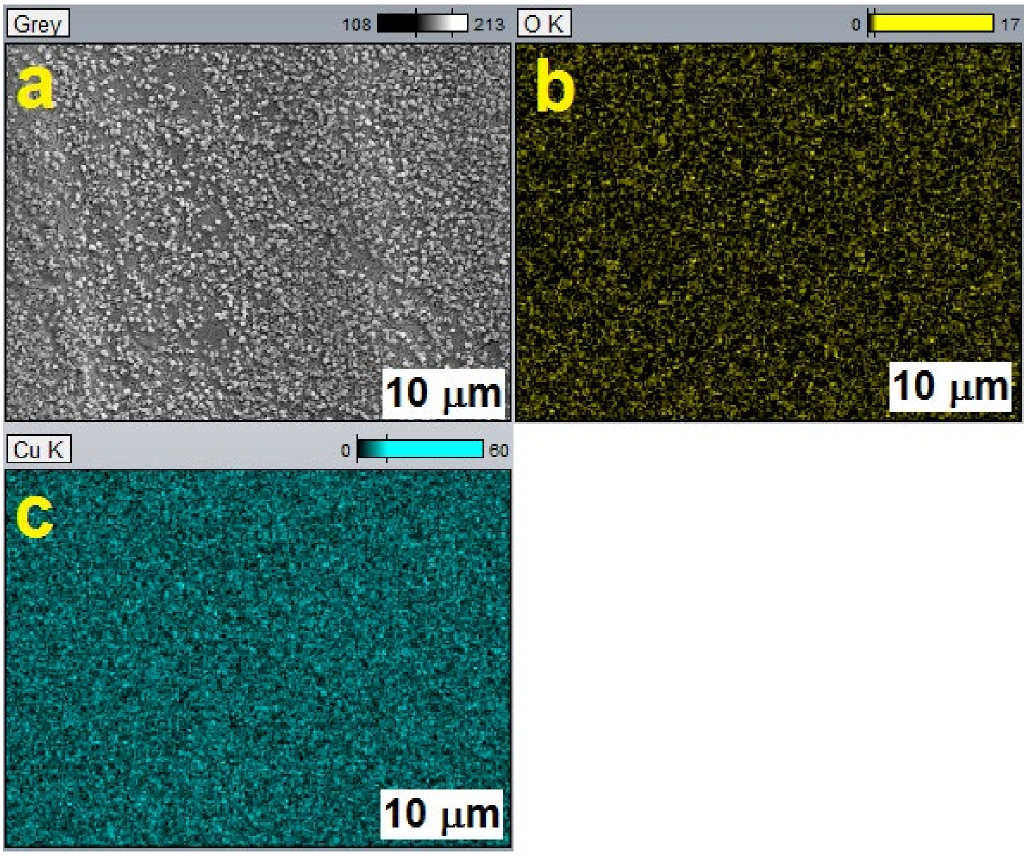

Figure 4.5: Elemental mapping of the OD-Cu foil, (a) SEM of top-down OD-Cu foil, (b) the distribution of oxygen and (c) the distribution of Cu measured by the K-shell absorption.

4.1.1.3. Cu_3P/Cu synthesis and physical characterisation

The OD-Cu foil was used as the precursor for the preparation of Cu_3P/Cu foil via low temperature phosphidation process and as standard for the 3D printed OD-Cu electrocatalyst.

The XRD patterns confirm the formation of copper phosphide on the surface of the copper foil **(Figure 4.6)**. The diffraction peaks **(Figure 4.6)** index to the hexagonal-phase of Cu_3P (ICSD # 15056). It is worth mentioning that the observed preferred orientation originates from the electropolished Cu foil and affects the Cu_2O and Cu_3P.

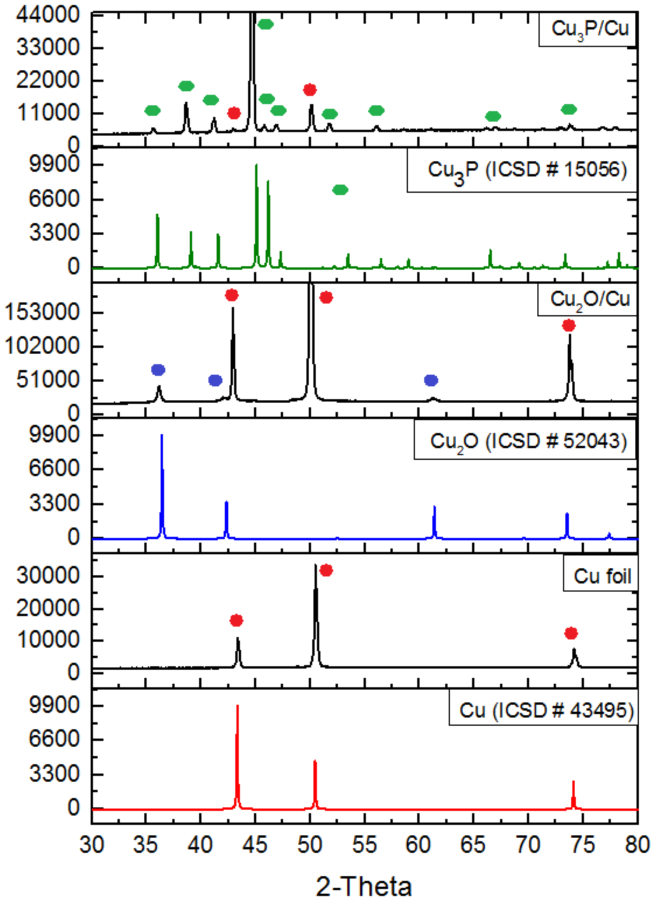

Figure 4.6: XRD patterns for the electropolished Cu, Cu_2O/Cu foil before electrochemical reduction of the oxides and Cu_3P/Cu foil. Red balls: Cu, blue balls: Cu_2O and green balls: Cu_3P.

SEM images showed the polycrystalline surface of the copper phosphide foil after phosphidation reaction **(Figure 4.7)**. The thickness of the copper phosphide layer was about 30 μm at each side **(Figure 4.8)**. The SEM images of the cross-section of Cu_3P show indicate an obvious separation between the Cu bulk and Cu_3P film which may suggest improper contact between them **(Figure 4.8)**. EDX spectrum of the top view of Cu_3P **(Figure 4.9)** confirm the existence of phosphorus and copper in the same region. The EDX mapping of the cross section view showed the existence of phosphorus within the outer film only without any existence in the bulk of the foil **(Figure 4.10)** the same behaviour was repeated again in the spectral mapping of the cross-section **(Figure 4.11)**. It is worth noting the spectral mapping supported the improper contact between bulk and film conclusion.

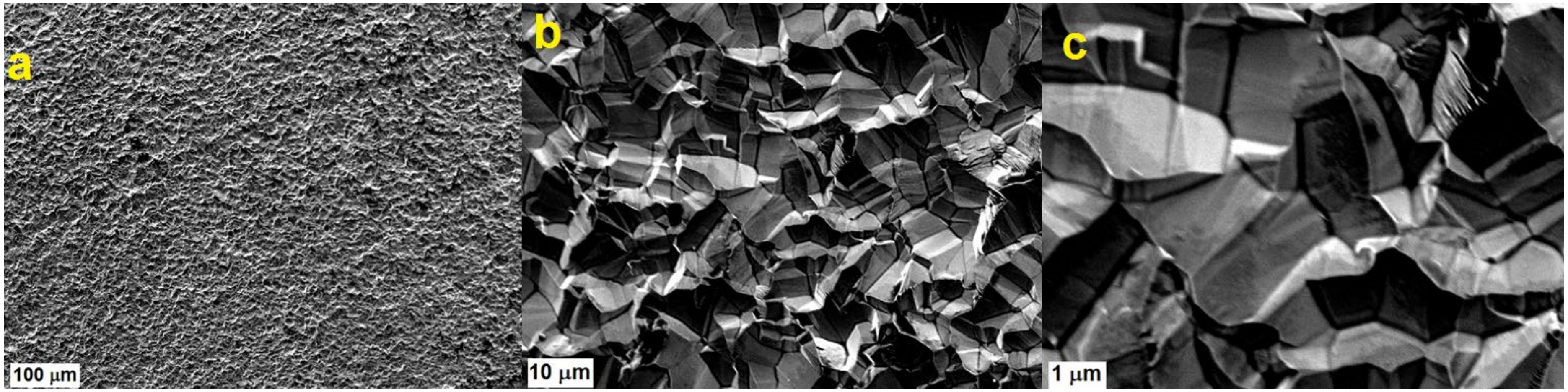

Figure 4.7: SEM of Cu_3P/Cu foil before electrochemical measurements.

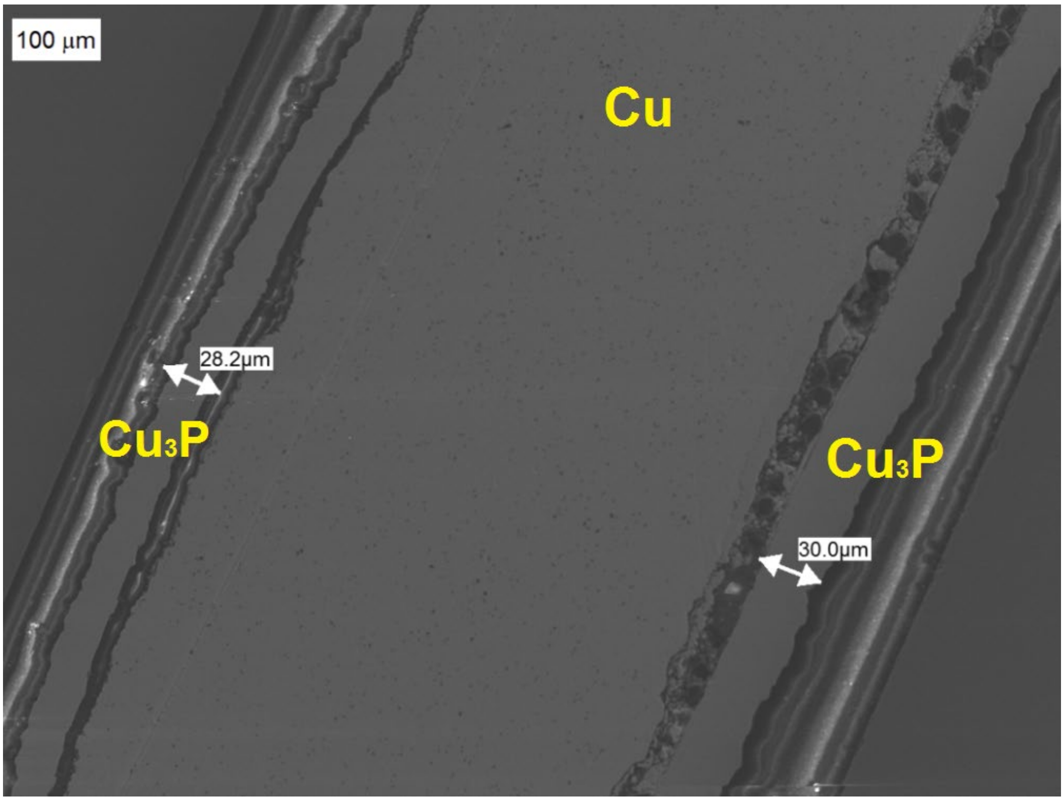

Figure 4.8: SEM images of the cross-section of Cu_3P films on the sides of the Cu foil.

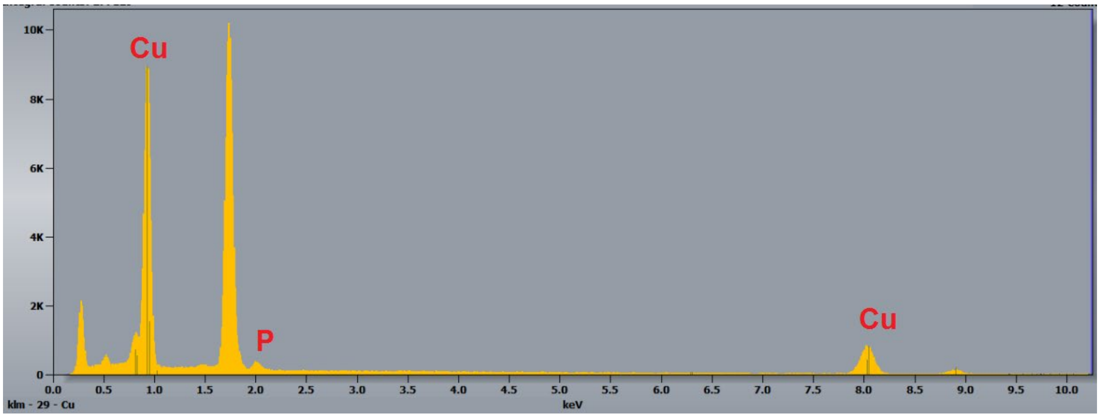

Figure 4.9: EDX spectrum of the 3D printed Cu_3P/Cu foil before electrochemical measurements (%Cu was 89.69% and %P was 10.31 %).

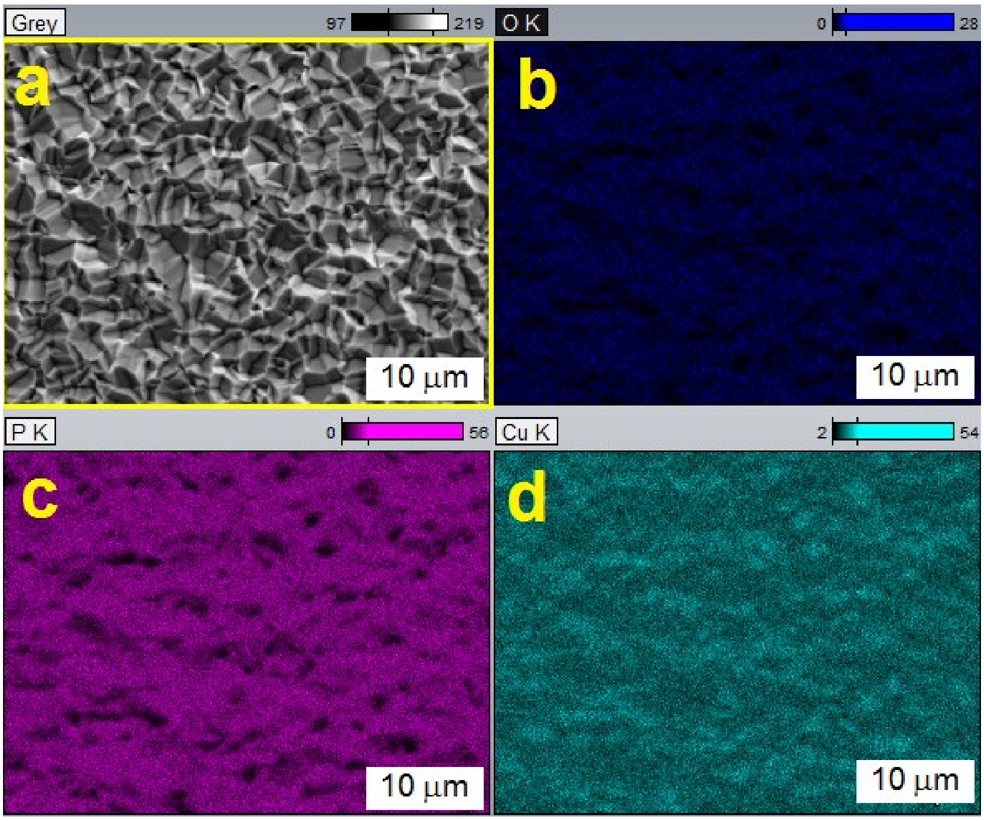

Figure 4.10: Elemental mapping of the the Cu_3P/Cu foil before electrochemistry. (a) SEM of top-down of the Cu_3P/Cu foil, (b) the distribution of oxygen, (c) the distribution of phosphorous and (d) the distribution of Cu measured by the K-shell absorption.

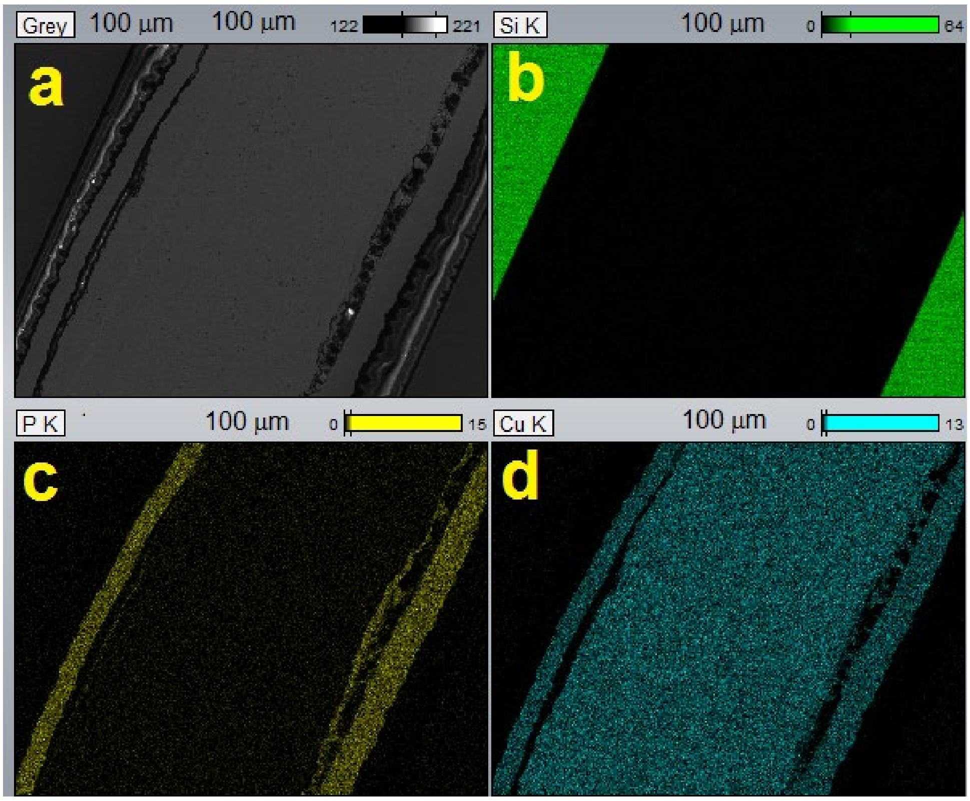

Figure 4.11: Elemental mapping of the cross-section of the Cu_3P/Cu foil. (a) SEM of cross-section of the Cu_3P/Cu foil, (b) the distribution of silicon, (c) the distribution of phosphorous and (d) the distribution of Cu measured by the K-shell absorption (Sample was sandwiched between two Si plates).

The low magnification TEM images **(Figure 4.12a,b)** of the copper phosphide film showed that it was covered with nanocrystallites of the same material (these appeared as darker spots, **Figure 4.12a and Figure 4.12b)**. A HRTEM image **(Figure 4.12d)** showed interplanar spacing of 0.25 nm, this corresponds to (112).[259-261] The diffraction rings appearing in **(Figure 4.12c)**, can be indexed as (300), (112), (113) and (220).

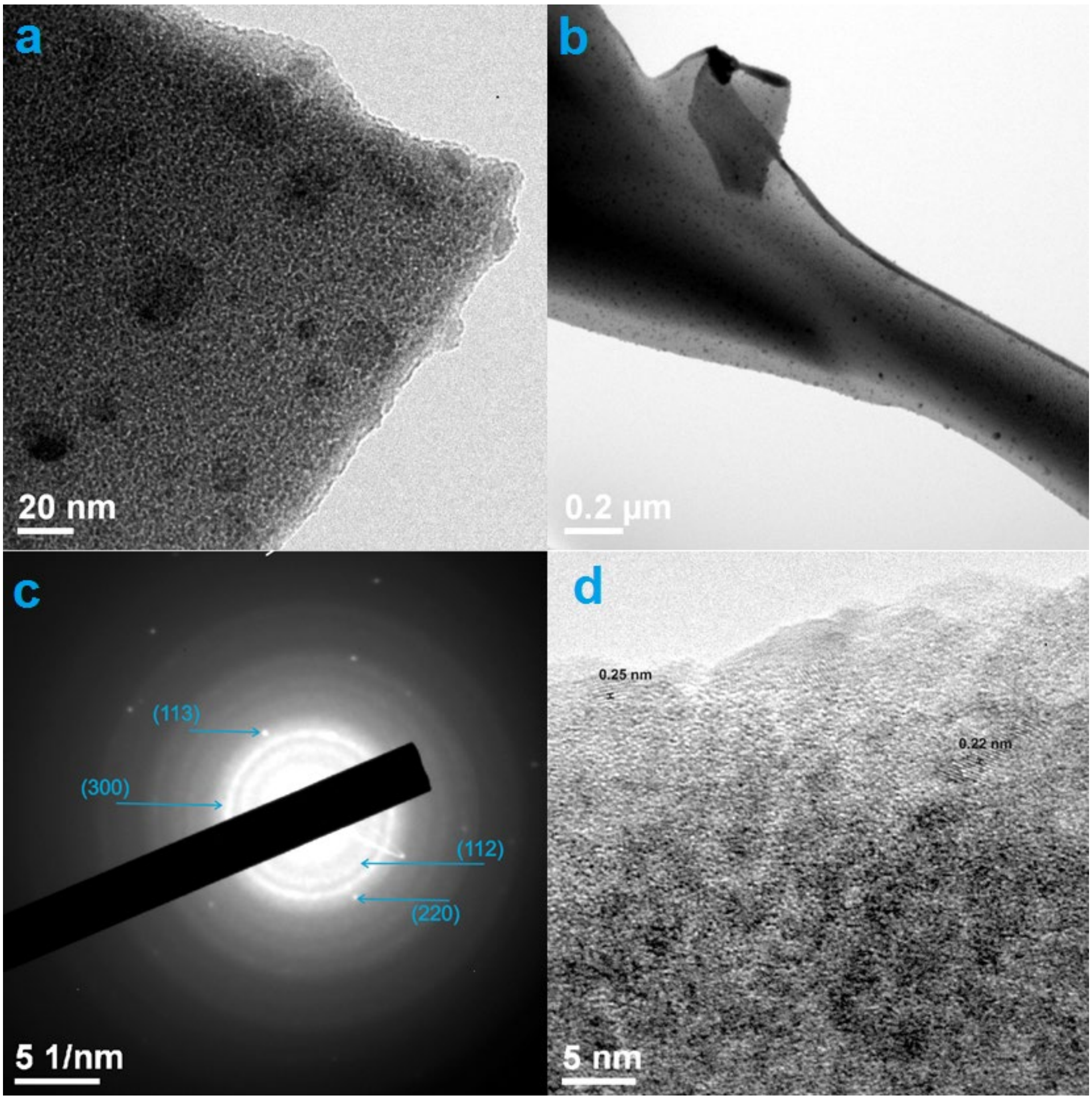

Figure 4.12: TEM of Cu_3P foil; a and b: low magnification TEM images of the Cu_3P film, c: diffraction resulted from Cu_3P film and d: HRTEM image.

The XPS spectra of Cu_3P/Cu foil confirmed the existence of Cu, P and O elements consistent with the EDX spectral data **(Figure 4.13)**. The XPS data showed the existence of Cu(II) and Cu(I) species on the surface of the electrocatalyst with ≈35 % for Cu(II) and ≈64 % for Cu(I), the majority of the Cu on the surface were either Cu_3P or Cu_2O (this latter species may result from oxidation in air). In the Cu 2p region **(Figure 4.13a)**, peaks were observed at 931.3 and 951.0

eV for Cu $2p_{3/2}$ assigned for corresponding to $Cu^{\delta+}$ in Cu_3P and Cu(I), respectively. Another two peaks at 934.8 and 952.7 eV assigned for $Cu^{\delta+}$ in Cu_3P and Cu(II) species of the Cu $2p_{1/2}$ peak, respectively.[259] The peaks at 942.6 and 962.8 eV are assigned for the satellites of Cu(II).[221] In the P 2p region **(Figure 4.13b)**, a big peak at 132.7 corresponds to the P ($2p_{3/2}$) and P ($2p_{1/2}$).[262] The existence of oxygen in the XPS spectrum resulted from the oxidation of Cu_3P in surface air during storage **(Figure 4.13c)**.[261]

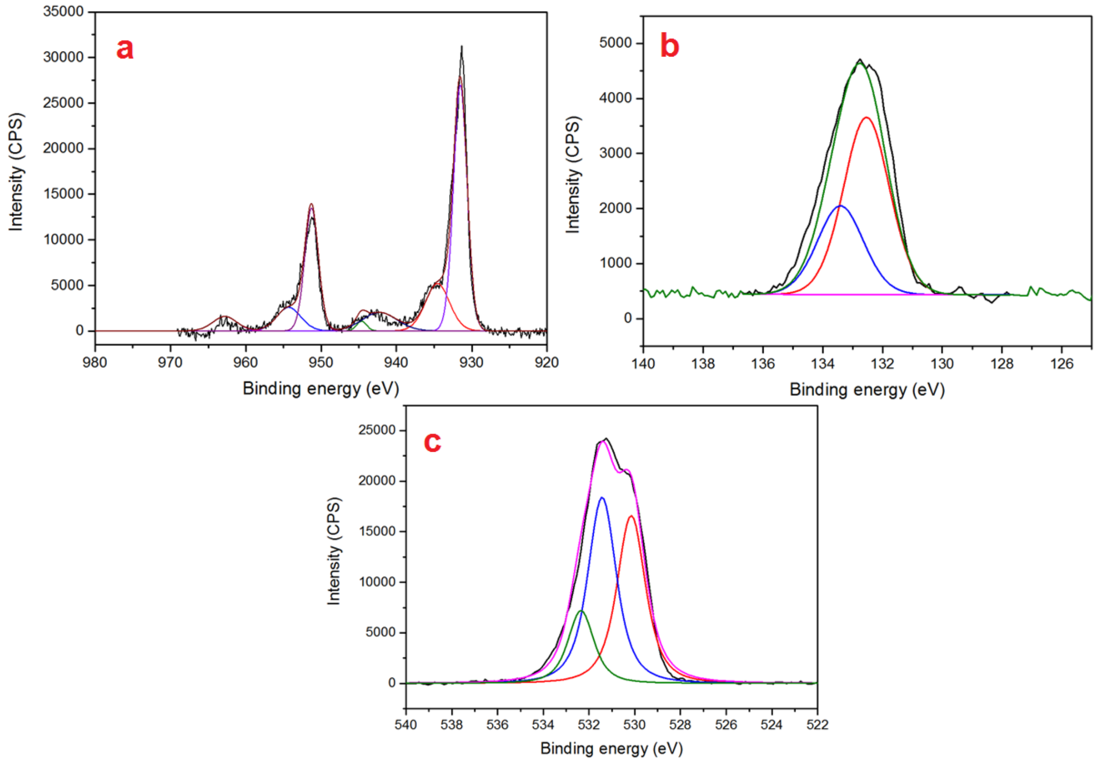

Figure 4.13: X-ray photoelectron spectroscopy (XPS) characterizations of Cu_3P/Cu foil before electrochemical measurements: (a) Cu 2p, (b) P 2p and (c) O 1s regions.

4.1.2. 3D ink development, printing and characterisation

3D printing was used to develop a new method for the preparation of Cu based electrocatalysts that can be used in the future potentially on an industrial scale. The 3D printing was performed using a very viscous ink and the 3D printer head motion was responsible for building the structure. The viscous ink consists of Cu powder, viscosity modifier (HMPC), DI water, ethylene glycol and glycerol. The mixture (ink) was stirred strongly to form homogenous solution. The viscosity of the ink was controlled through the viscosity modifier and through evaporation of the solvents (DI water, ethylene glycol and glycerol). After reaching the desired viscosity (ca. 410 Pa.s), the prepared ink was transferred to a syringe barrel and fitted on the head of the 3D printer and the barrel was fitted with a plastic nozzle. The viscous ink started to flow through the syringe nozzle after applying air pressure of 6.5 bar. We choose to prove the concept with simple structure of 1 x 1 cm^2 of thickness about 1 mm **(Figure 4.14)**.

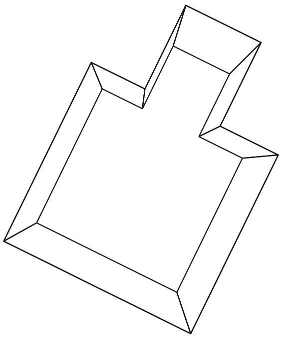

Figure 4.14: The structure/shape of the proposed Cu based electrocatalyst.

The 3D printed OD-Cu electrocatalyst was prepared through three steps: i) preparation of viscous ink, ii) building the Cu based structure using 3D printer and iii) thermal treatment. The thermal treatment is responsible for the removal of all the organic content and the expelled gases are responsible for the formation of a very rough OD-Cu electrode.

During the preparation trials we observed the following:

1- Increasing the polymer percentage resulted in the formation of ink with gum-like behaviour and it was difficult to force the ink out of the nozzle during the printing.

2- The addition of copper sulfate salt caused the expansion (swelling) of the structure like bread.

3- The evolution of gases during the thermal treatment resulted in the formation of very rough structures.

4- The evolution of the gases during the thermal treatment resulted in relatively low resolution of the prepared structure.

4.1.2.1. 3D printed OD-Cu electrocatalyst

XRD patterns of the 3D printed electrocatalysts **(Figure 4.15)** were recorded before and after the electrochemical measurements (CA). XRD patterns of the copper electrode showed the reduction of Cu_2O via hydrogenation reduction. For the 3D printed OD-Cu electrode, weak peaks appeared belonging to Cu_2O which may be formed during the storage of the plate (ICSD # 52043) before the electrochemical measurements.

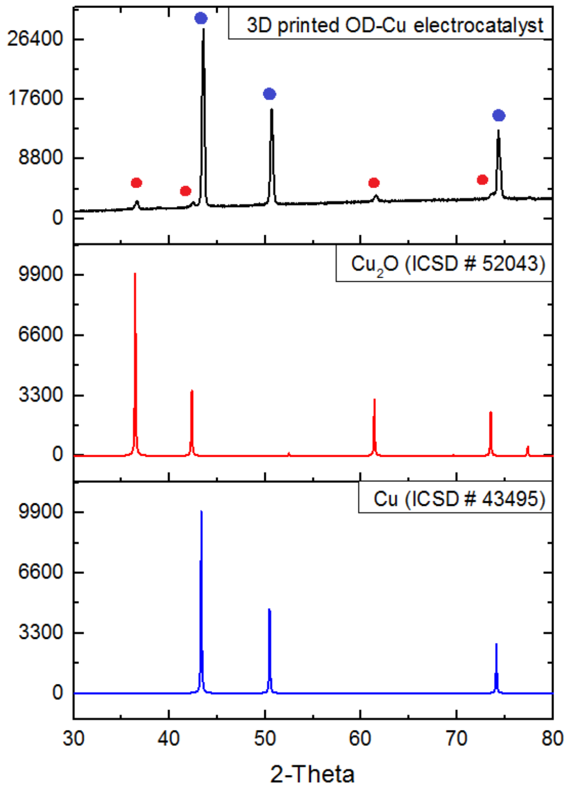

Figure 4.15: XRD patterns of the 3D printed OD-Cu electrode before the electrochemical measurements. Red circles belong to Cu peaks and blue circles for Cu_2O peaks.

SEM and EDX images **(Figure 4.16 - Figure 4.21)** of the top-down and cross-section views were used to study the morphology of the electrocatalysts and identify the composition of the outer and internal parts of the different electrocatalysts. SEM images of the 3D printed OD-Cu electrocatalyst showed that the surface of the electrode composed of rough polycrystalline copper **(Figure 4.16)** and the thickness of the 3D printed OD-Cu electrocatalyst ranged between 975 to 780 µm **(Figure 4.19)**. There was no significant change in the morphology before and after electrochemistry except the adsorption of carbonates on the electrode surface. The EDX spectrum and mapping showed the existence of amounts of oxides before the electrochemical measurements that may be formed during storage **(Figure 4.17 - Figure 4.18, Figure 4.20)**, the same behaviour also observed in the XRD patterns **(Figure 4.15)**.

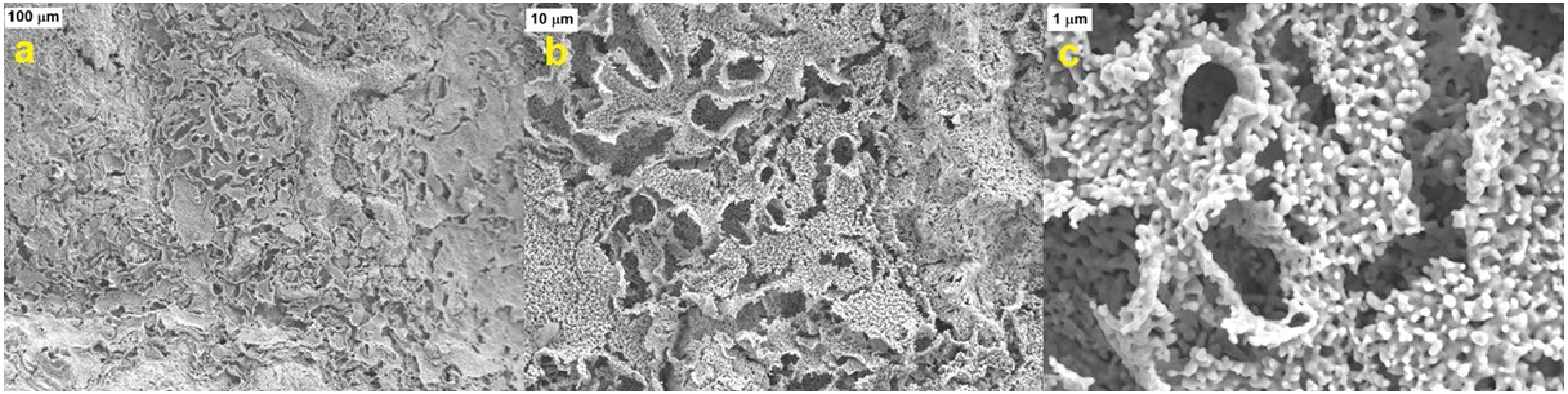

Figure 4.16: (a-c) SEM images of the top-down view of the 3D printed OD-Cu electrode before electrochemical measurements.

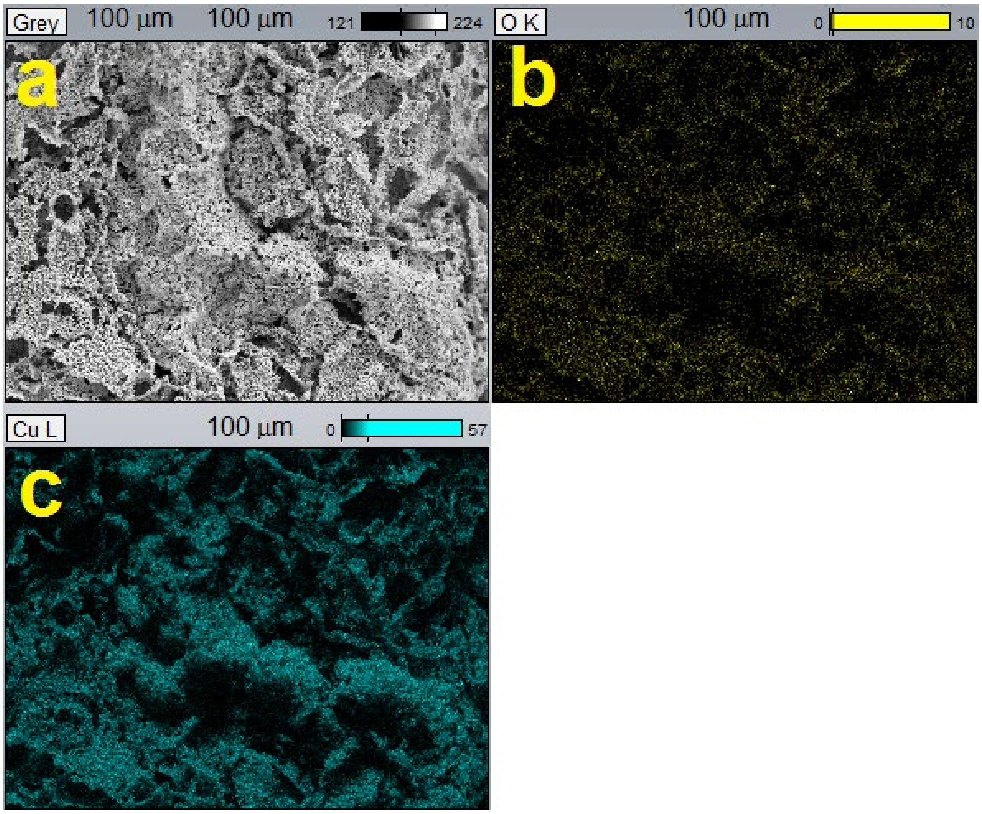

Figure 4.17: Elemental mapping of the top-down view of the 3D printed OD-Cu. (a) SEM of top-down view of 3D printed OD-Cu before electrochemical measurements, (b) the distribution of oxygen and (c) Cu measured by the K-shell absorption.

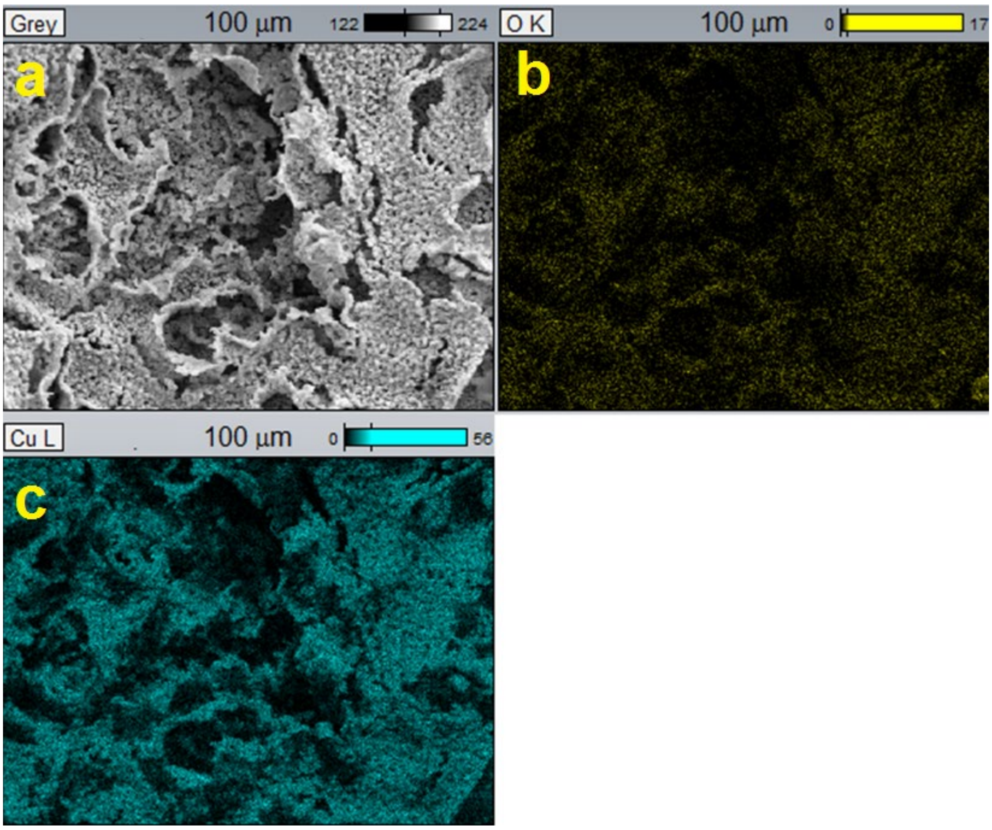

Figure 4.18: Elemental mapping of the top-down view of the 3D printed OD-Cu after electrochemical measurements. (a) SEM of top-down view of the 3D printed OD-Cu (top-left), the distribution of oxygen, (b) the distribution of phosphorous and (c) the distribution of Cu measured by the K-shell absorption.

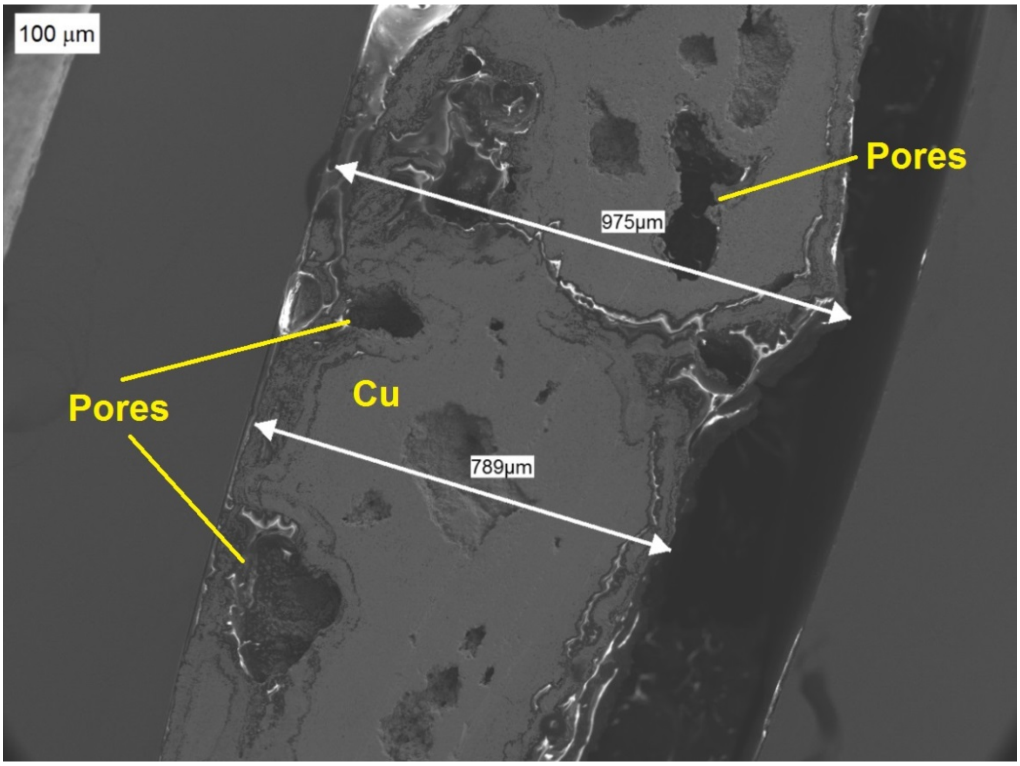

Figure 4.19: SEM image of the cross section of 3D printed OD-Cu electrocatalyst before electrochemical measurements (thickness of the electrocatalyst lies between 975 µm and 789 µm).

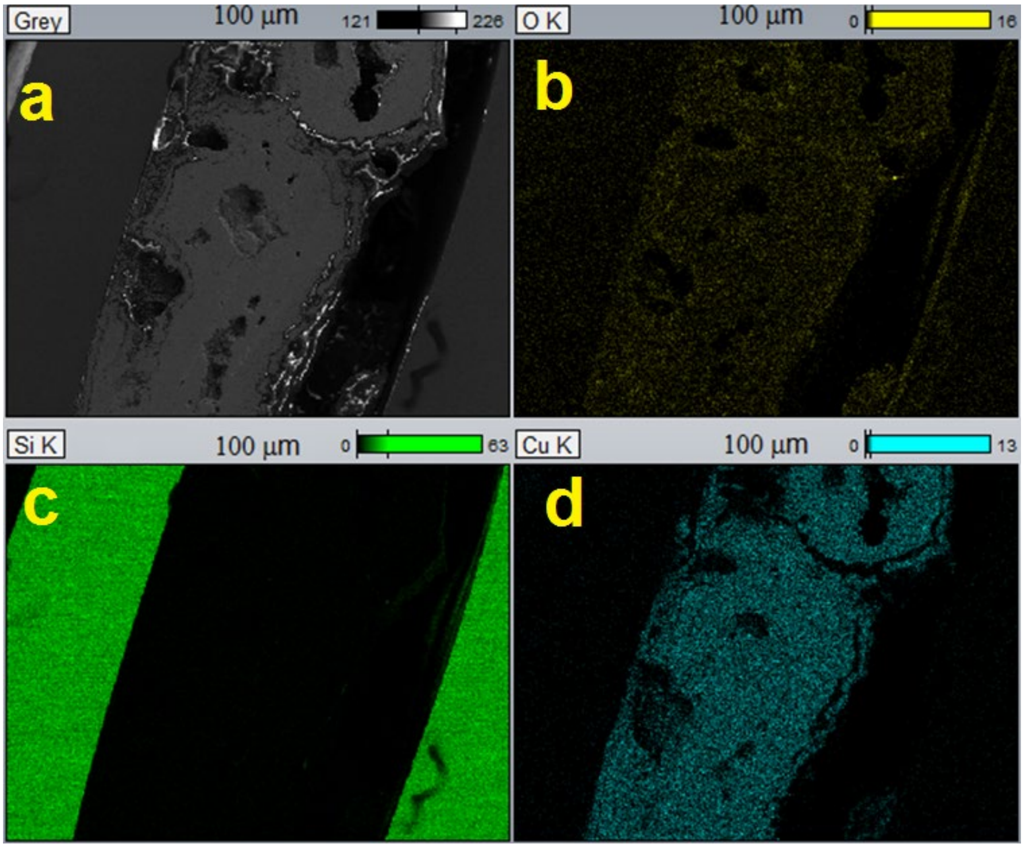

Figure 4.20: Elemental mapping of the cross-section view of 3D OD-Cu electrocatalyst before electrochemical measurements. (a) SEM images of the 3D OD-Cu electrocatalyst before electrochemical measurements, (b) the distribution of oxygen, (c) Si (below-left) and (d) the distribution of Cu measured by the K-shell absorption (sample was sandwiched between two Si plates for SEM scanning).

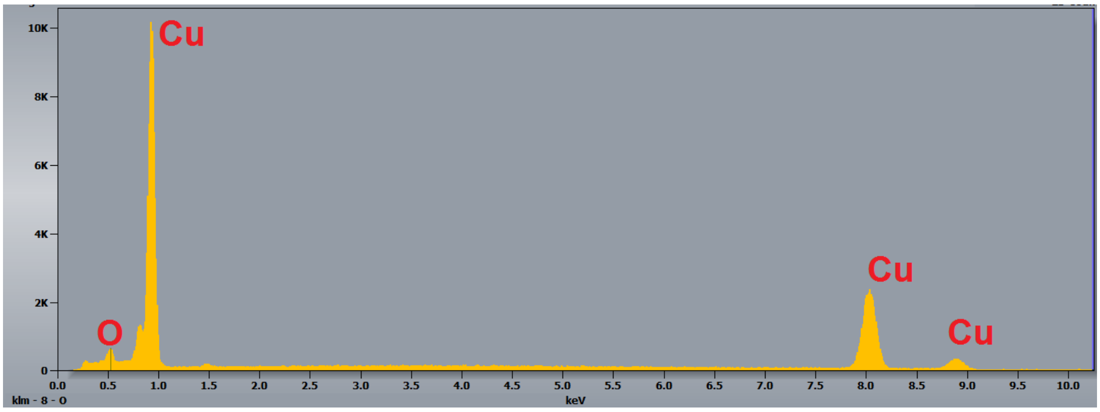

Figure 4.21: EDX spectrum of the 3D printed OD-Cu before electrochemistry (%Cu was 89.40% and %O was 10.60 %).

The low magnification TEM images of the 3D printed OD-Cu electrode are shown in **(Figure 4.21a-c)**. TEM images showed large crystals of copper metal with additional nanoparticles on the surface of the large crystal appearing as bright spots in **(Figure 4.21b)**. TEM images also showed bright spots due to the existence of nanocrystallites within the polycrystalline bulk.

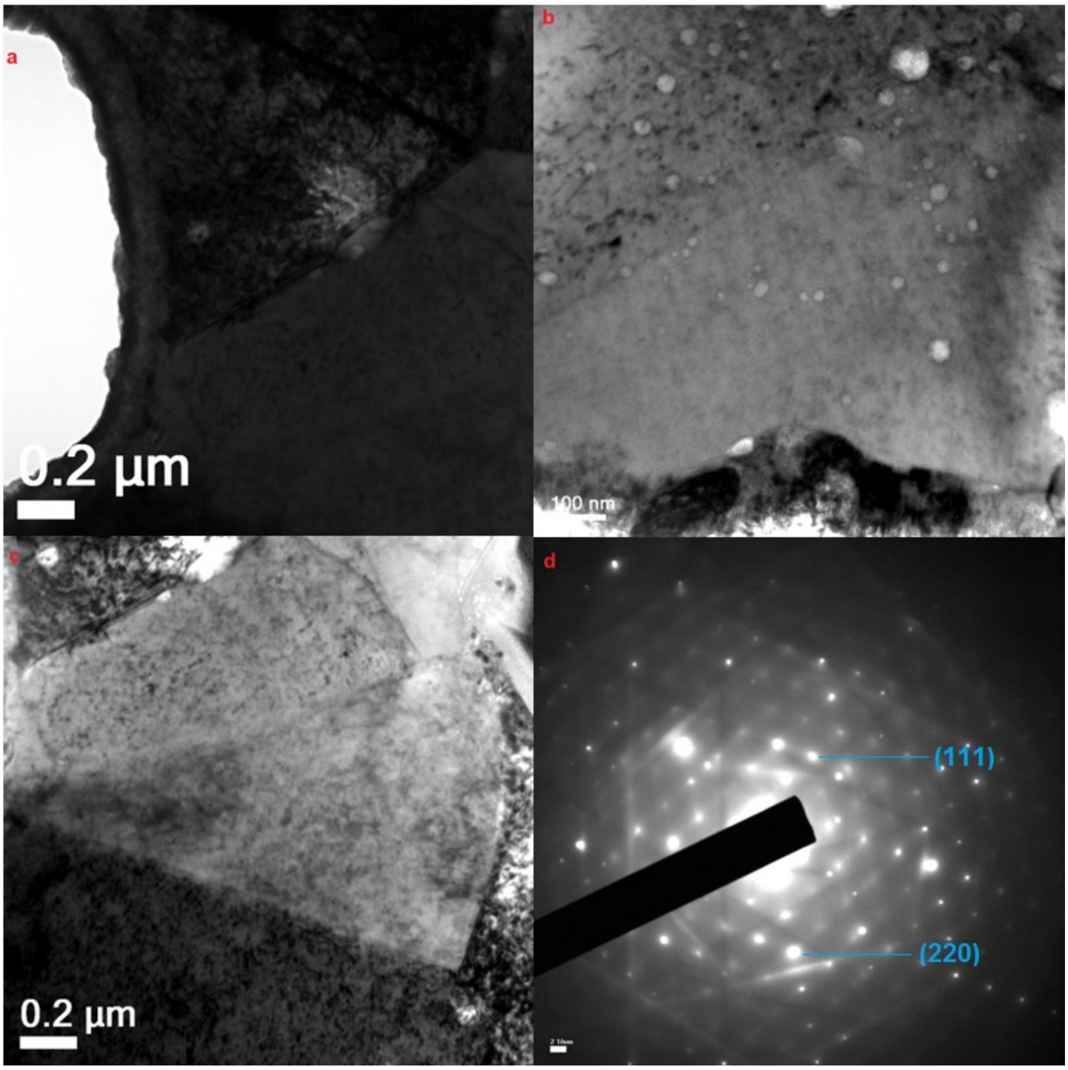

Figure 4.22: TEM images of 3D printed of OD-Cu electrocatalyst.

The XPS spectra of the 3D printed OD-Cu electrocatalyst confirmed the existence of Cu, and O elements consistent to the EDX spectral data **(Figure 4.23)**. The XPS data showed the existence of Cu(II) and Cu(I) species on the surface of the electrocatalyst with ≈9.6 % for Cu(II) and ≈90.3 % for Cu(I), the majority of the Cu on the surface were Cu_2O (may resulted from oxidation in air). The Cu 2p region **(Figure 4.23a)** showed peaks at 932.3 and 952.1 eV for Cu $2p_{3/2}$. These are assigned to Cu(I) of (Cu_2O). Another two peaks at 935.1 and 955.1 eV were assigned to Cu(II) of CuO.[259, 263] The peaks at 944.9 and 963.4 eV are assigned for the satellites of Cu(II).[221] The existence of oxygen in the XPS spectrum resulted from the oxidation of Cu in surface air during storage **(Figure 4.23b)**.

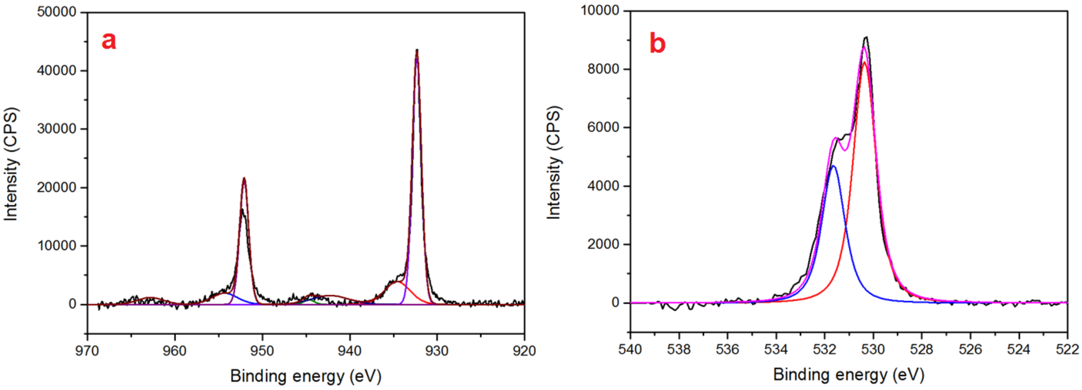

Figure 4.23: X-ray photoelectron spectroscopy (XPS) characterizations of the 3D printed OD-Cu electrocatalyst before electrochemical measurements: (a) Cu 2p and (b) O 1s regions.

4.1.2.2. 3D printed PD/OD-Cu electrocatalyst

The 3D printed PD/OD-Cu electrocatalyst was prepared on the surface of 3D printed OD-Cu electrocatalyst through a quick phopshidation process (15 min instead of 2 h of phosphidation using small amount of NaH_2PO_2) followed by electrochemical reduction of the Cu_3P layer. The preparation of a thin layer was prepared to be used as a precursor for phosphide derived (PD) Cu electrocatalyst. The plan was to create different types of active sites on the surface of the electrocatalyst derived from the copper oxides and copper phosphides. Having different kinds of actives sites may tune/change the interaction between the intermediates and may lead to the formation of different products.

Before the electrochemical reduction of Cu_3P layer, the XRD pattern of the thin Cu_3P electrocatalyst **(PD/OD Cu) (Figure 4.24)** confirmed the existence of the Cu_3P layer (ICSD # 15056 of Cu_3P) on the surface of the 3D printed OD-Cu electrocatalyst in addition to the strong peaks of Cu metal before the electrochemical reduction of Cu_3P layer indication that either incomplete coverage of the electrocatalyst with Cu_3P or the film is thin.

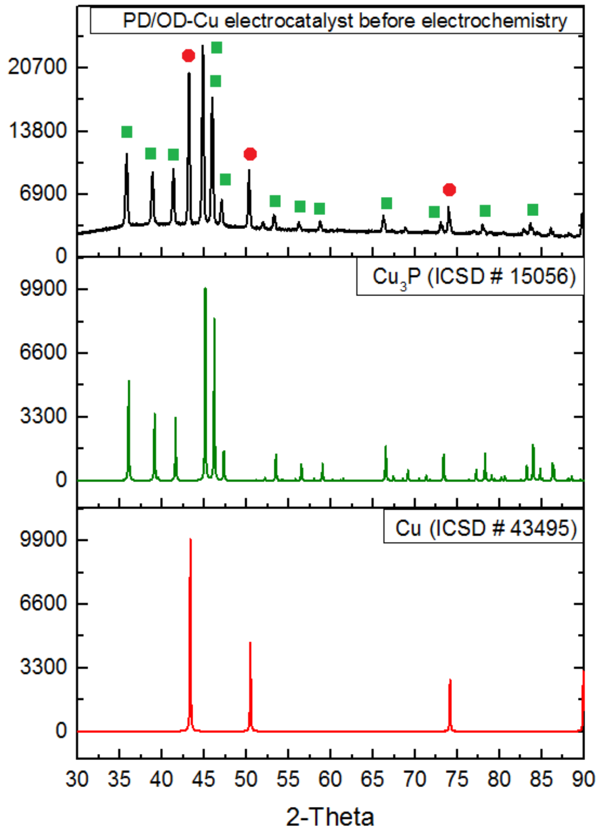

Figure 4.24: XRD patterns of the 3D printed PD/OD-Cu electrode before the electrochemical measurements. Red circles belong to Cu peaks and green squares belong to Cu_3P.

SEM images of the top-down view of the PD/OD-Cu electrocatalyst exhibited a rough polycrystalline surface with appearance close to that of the 3D printed OD-Cu electrocatalyst **(Figure 4.25)** due to the fast phosphidation process. The SEM image of the cross-section of PD/OD-Cu electrocatalyst showed that the thickness of the copper phosphide layer reached 107 μm **(Figure 4.27)**. SEM images of the cross-section view of the three plates showed the existence of copper phosphides deep in the internal parts of the electrocatalyst and mainly located on the surface of the pores **(Figure 4.28)**. EDX spectrum also confirmed the existence of the phosphorous on the surface of electrocatalyst **(Figure 4.29)**.

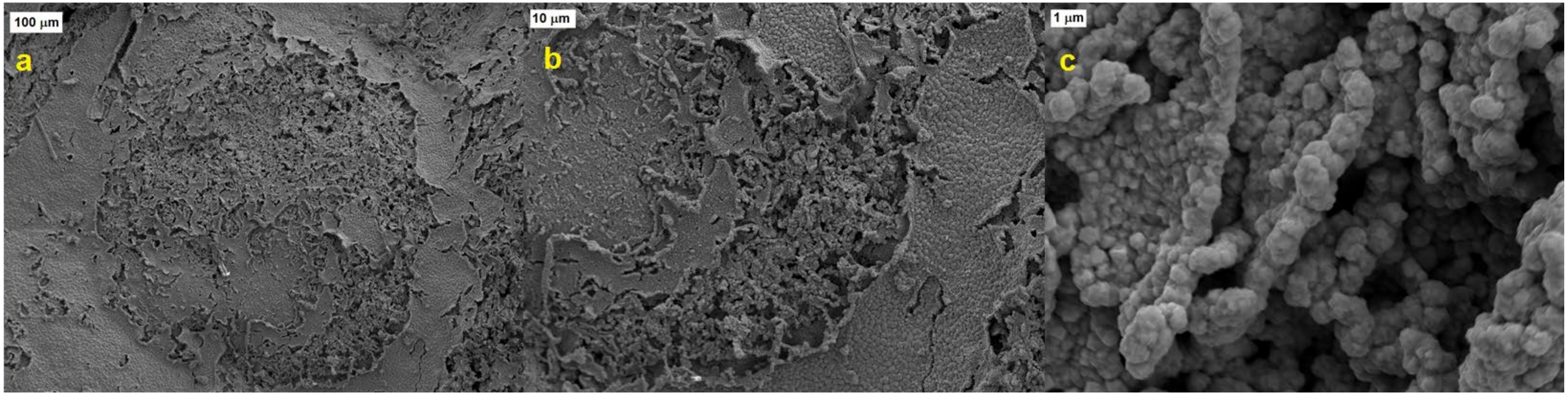

Figure 4.25: (a-c) SEM images of the 3D printed PD/OD Cu electrode before electrochemical measurements.

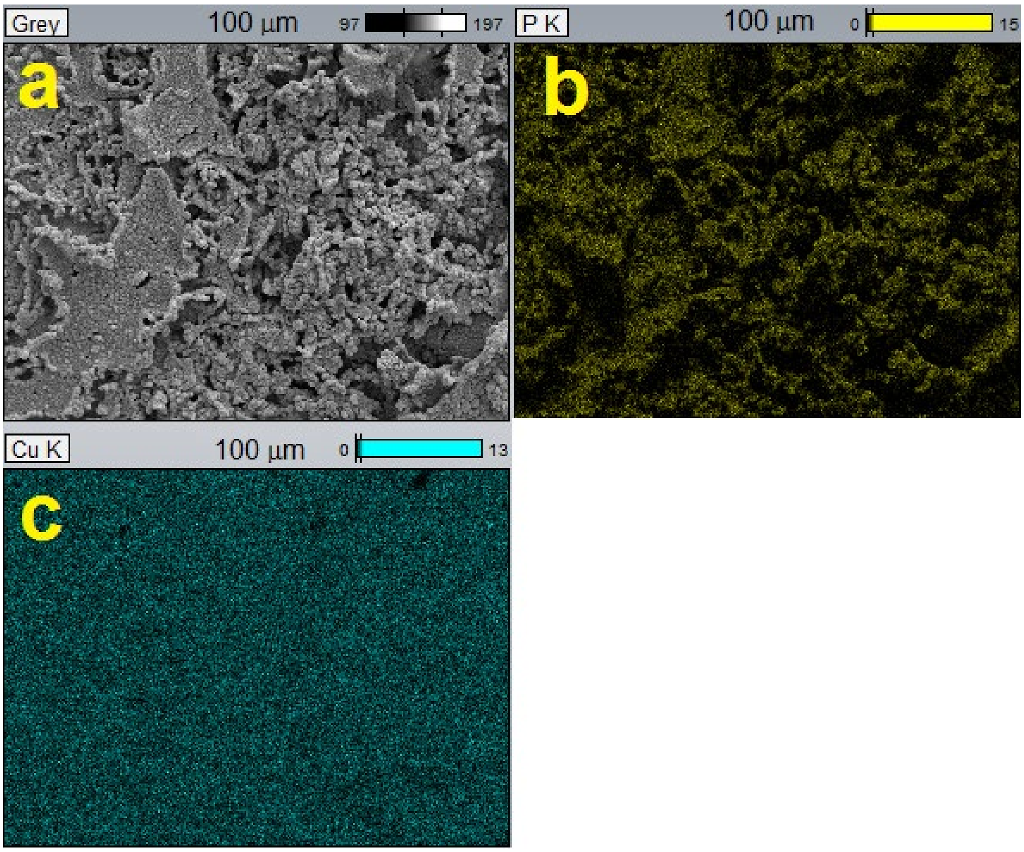

Figure 4.26: Elemental mapping of the top-view of the 3D printed PD/OD Cu electrode before electrochemical measurements. (a) SEM image of the 3D printed PD/OD-Cu electrode, (b) the distribution of phosphorous and (c) the distribution of Cu measured by the K-shell absorption.

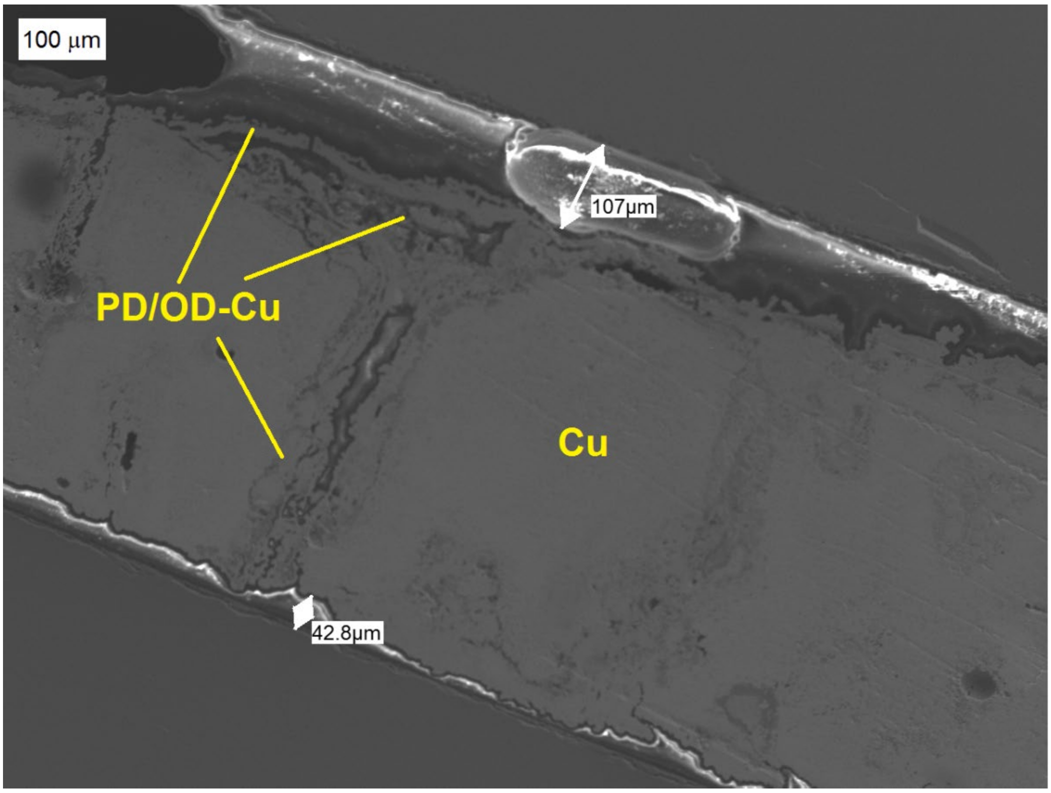

Figure 4.27: SEM image of the cross-section of the 3D printed PD/OD-Cu electrode.

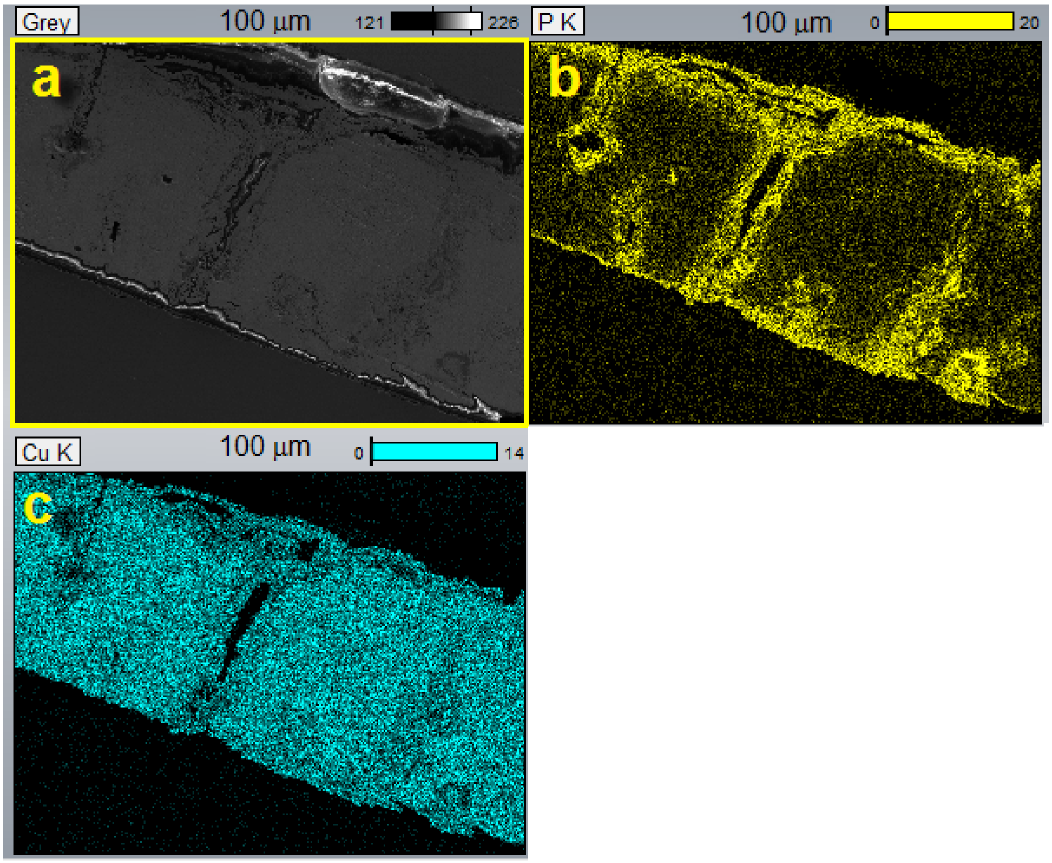

Figure 4.28: Elemental mapping of the cross-section view of the 3D printed PD/OD-Cu electrode. (a) SEM image of 3D printed the 3D printed PD/OD-Cu electrocatalyst, (b) the distribution of phosphorous and (c) Cu (below-left) measured by the K-shell absorption.

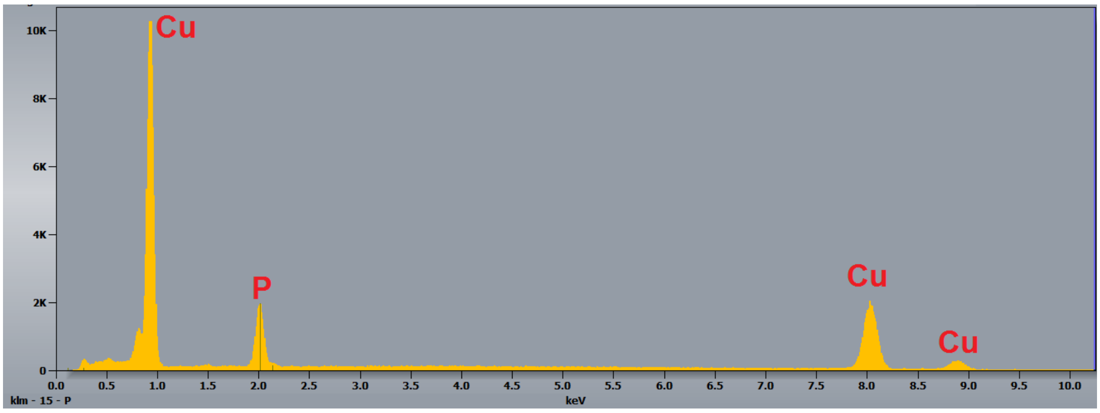

Figure 4.29: EDX spectrum of the 3D printed PD/OD Cu electrode before electrochemical measurements (%Cu was 84.10 % and %P was 15.90 %).

TEM images **(Figure 4.30)** of the 3D printed PD/OD Cu electrocatalyst (before electrochemistry) showed that it is made from nanocrystallites that covered the 3D printed copper plate. The Cu_3P nanoparticles have square appearance with width ranging between 38 - 25 nm **(Figure 4.30)**. The diffraction rings that appeared in **(Figure 4.30)** can be indexed as (300), (112), (113) and (220). HRTEM image **(Figure 4.30d)** showed interplanar spacing of 0.247 nm corresponds to (112).[259-261]

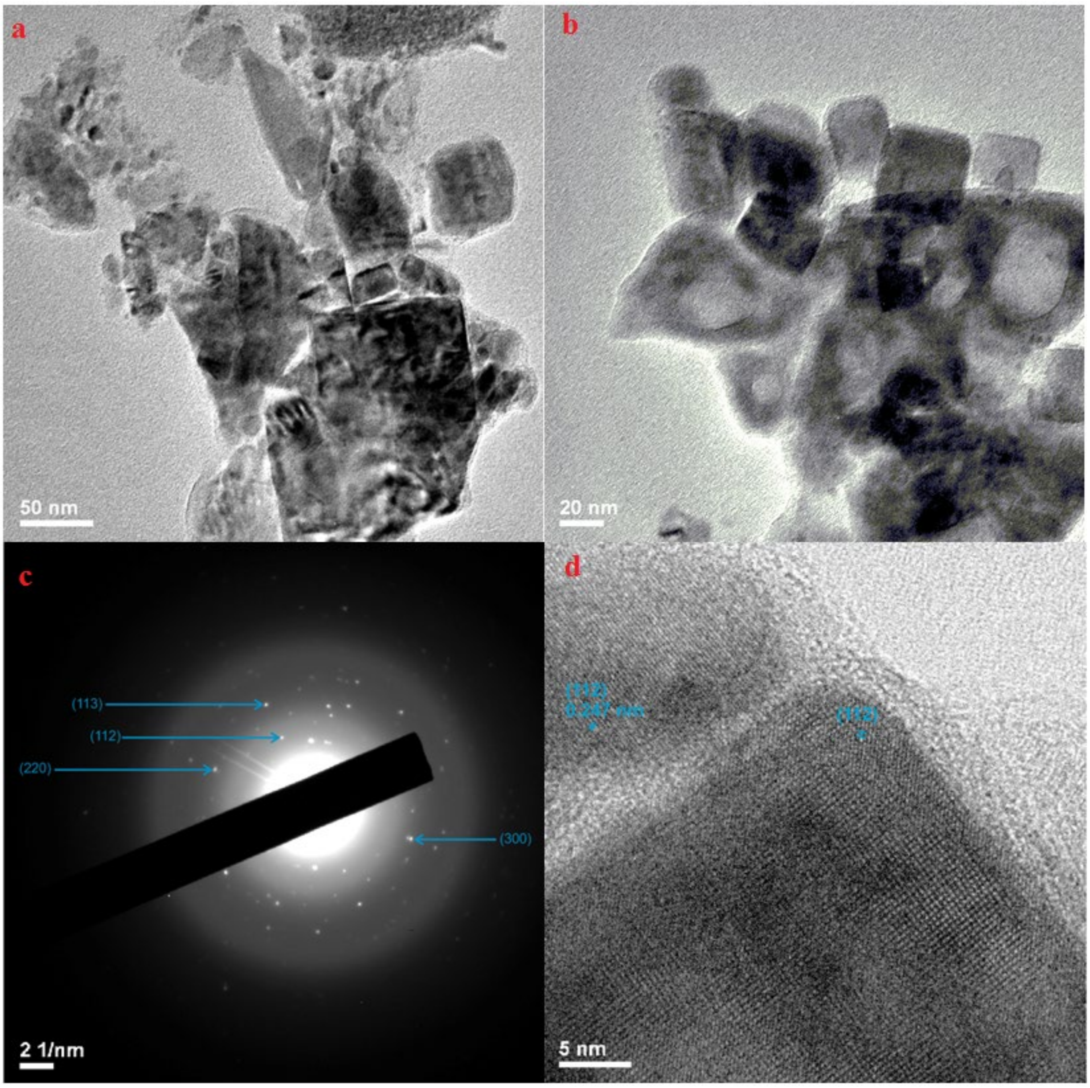

Figure 4.30: TEM images of the 3D printed PD/OD-Cu electrode before electrochemistry: a,b) low magnification TEM images, c) diffraction and d) HETEM image.

The XPS spectra of 3D printed PD/OD-Cu electrocatalyst (before the electrochemical reduction of the Cu_3P layer) confirmed the existence of Cu, P and O elements consistent to the EDX spectral data **(Figure 4.31)**. The XPS data showed the existence of Cu(II) and Cu(I) species on the surface of the electrocatalyst with ≈88 % for Cu(II) and ≈12 % for Cu(I), the majority of the Cu on the surface were either Cu(II) due to the incomplete phosphidation process of the surface during preparation and may have resulted from oxidation in air. The Cu 2p region **(Figure 4.31a)** showed peaks at 932.6 and 952.4 eV for Cu $2p_{3/2}$ assigned for corresponding to $Cu^{\delta+}$ in Cu_3P and Cu(I), respectively. Another two peaks at 934.9 and 952.5 eV assigned for $Cu^{\delta+}$ in Cu_3P and Cu(II) species of the Cu $2p_{1/2}$ peak, respectively.[259] The peaks at 942.9 and 963.3 eV are assigned for the satellites of Cu(II).[221] In the P 2p region **(Figure 4.31b)**, a big peak at 129.7 eV corresponds to the P ($2p_{3/2}$) and P

($2p_{1/2}$).[262] An additional peak appeared at 133.6 eV in the P 2p region, this is assigned to the oxidised phosphorus (phosphate).[259] The appearance of phosphate may be attributed to the incomplete phosphidation of the surface of the 3D printed OD-Cu electrocatalyst. The existence of oxygen peak in the XPS spectrum **(Figure 4.31c)** resulted from the oxidation of Cu_3P in air during storage.[261]

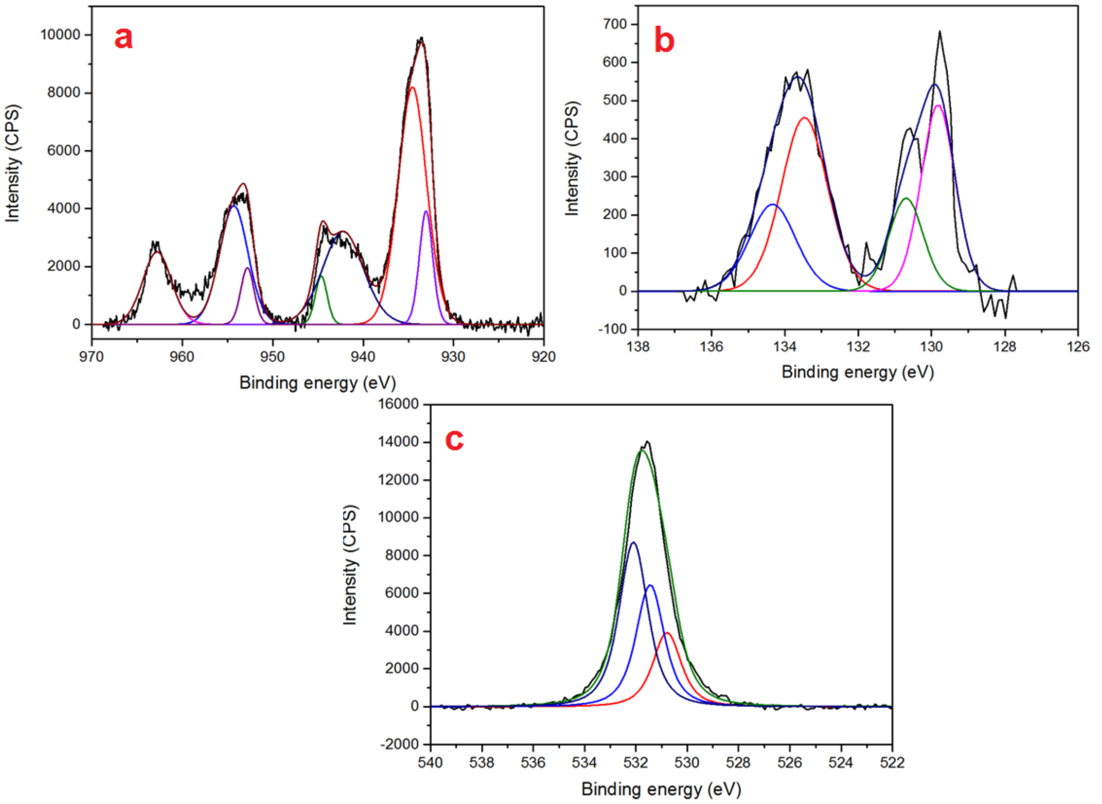

Figure 4.31: X-ray photoelectron spectroscopy (XPS) characterizations of the 3D printed PD/OD-Cu (before the electrochemical reduction of Cu_3P layer): (a) Cu 2p, (b) P 2p and (c) O 1s regions.

4.1.3. Electrochemical characterisation and electrocatalysis of Cu based electrocatalysts

The electrocatalytic performances of the electrocatalysts (electropolished Cu foil, OD-Cu foil, Cu_3P/Cu foil, 3D printed OD-Cu and PD/OD-Cu electrocatalysts) were studied through linear sweep voltammetry (LSV), capacitance measurements and chronoamperometric experiments (CA). The current efficiencies (CE%) of all the detected products are tabulated in **Table 4-2 and Table 4-4**.

4.1.3.1. Electropolished Cu foil

The LSV of the electropolished Cu **(Figure 4.32)** exhibited the electrochemical reduction of Cu_2O under N_2 at -0.36 V (RHE); the oxide may be formed during storage of the foil. The reported value is very close to that reported in literature -0.95 V vs Ag/AgCl (≈ -0.35 V vs RHE).[206]

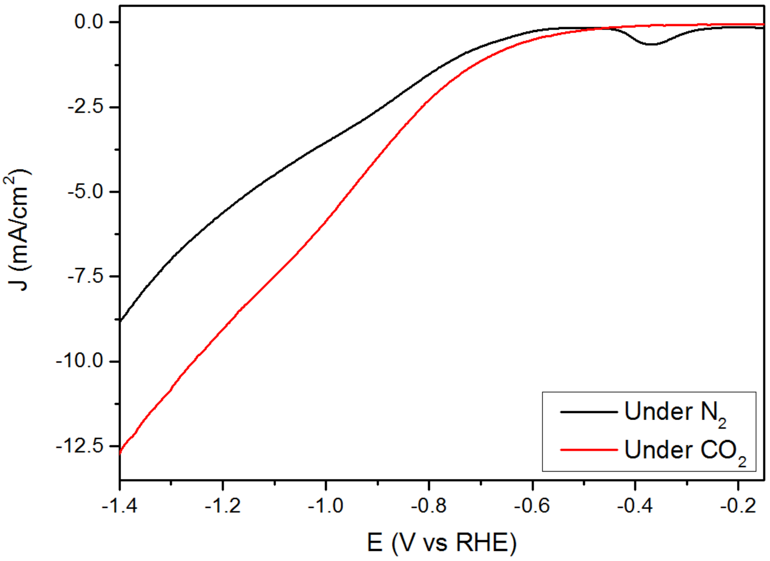

Figure 4.32: LSVs of Electropolished Cu foil in 0.1 M $KHCO_3$ saturated by N_2 and CO_2 with a scan rate of 20 mV/s.

At the most voltages, the current densities in the chronoamperometric experiments **(Figure 4.33)** were stable and became noisy at most negative voltages, this is attributed to the formation of gas bubbles. The gas bubbles have an effect on the current stability as they block some areas of the electrode surface till they release.[39] Bubbles also make the iR-compensation by the potentiostat difficult to keep the voltage constant while the bubbles evolve.[39] The current efficiencies of the different products were generally lower than that reported in literature **(Figure 4.34 and Table 4-2)**. There are several reasons for that and the main one is the mass transport limitation of CO_2 in the electrochemical cell.[39]

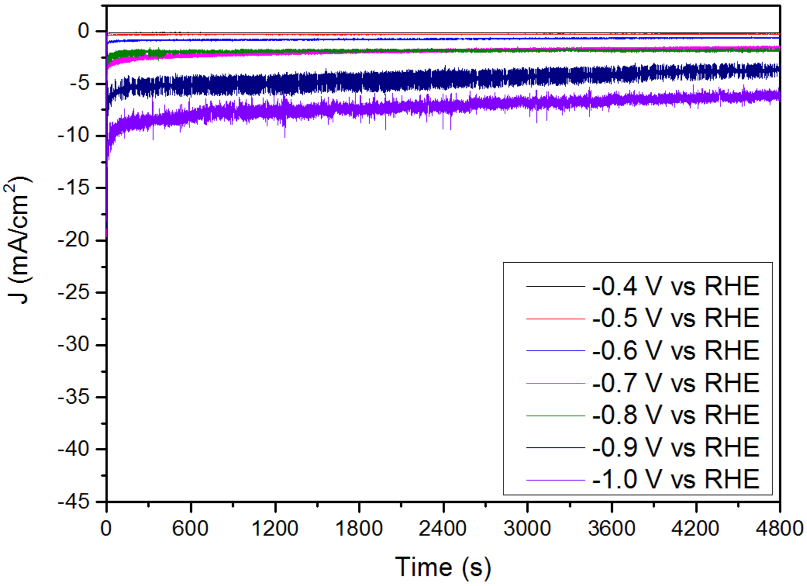

Figure 4.33: CAs experiments of electropolished Cu foil in 0.1 M $KHCO_3$ saturated by CO_2.

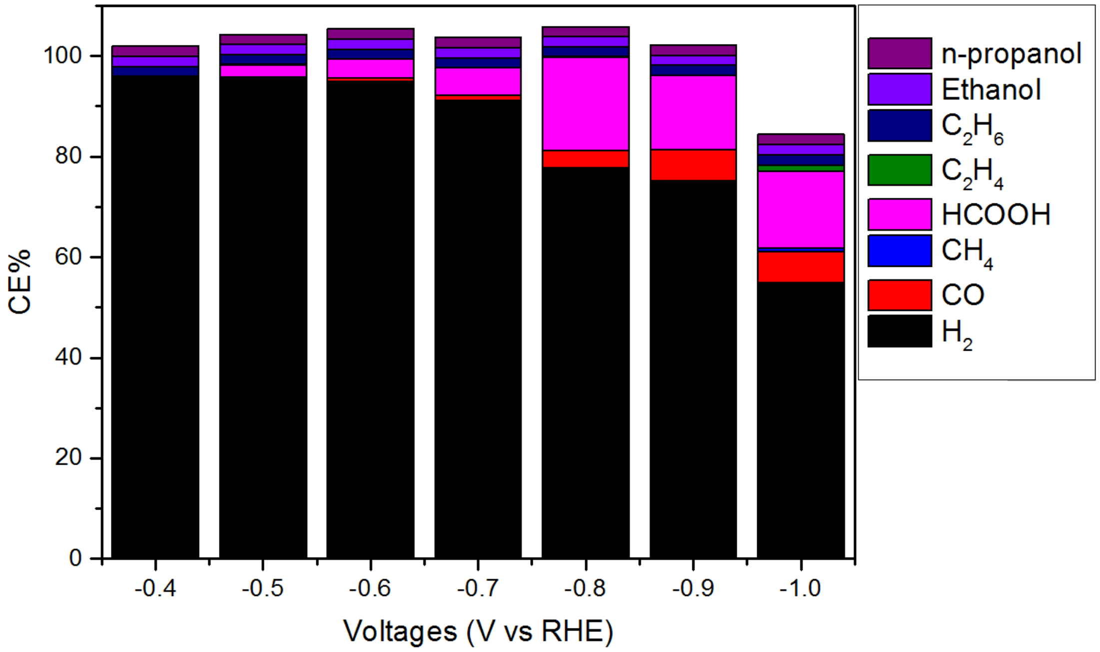

Figure 4.34: Current efficiencies % of all the detected products through CO2RR by the electropolished Cu foil.

Table 4-2: Current efficiencies of all the products using different copper based electrocatalysts in 0.1 M $KHCO_3$ saturated with CO_2.

CE% Electropolished Cu foil									
E (V)*	**H_2**	**CO**	**CH_4**	**HCOOH**	**C_2H_4**	**C_2H_6**	**C_2H_5OH**	**n-propanol**	**Total CE%**
-0.4	96	<0.5	-	-	-	-	-	-	96
-0.5	95.5	<0.5	-	2.5	-	-	-	-	98
-0.6	95	0.7	-	3.7	-	-	-	-	99
-0.7	91	1.0	-	5.5	-	-	-	-	98
-0.8	78	3.4	-	18.6	-	-	-	-	100
-0.9	75	6.0	0.01	14.8	<0.5	-	-	-	96
-1.0	55	6.0	0.55	15	1.3	-	-	-	78
CE% OD-Cu foil									
E (V)	**H_2**	**CO**	**CH_4**	**HCOOH**	**C_2H_4**	**C_2H_6**	**C_2H_5OH**	**n-propanol**	**Total CE%**
-0.4	91	6.0	-	3.0	-	-	-	-	100
-0.5	89	6.0	-	5.0	-	-	-	-	99
-0.6	68	12	-	14	-	-	-	-	93
-0.7	42	15	-	25	0.5	<0.5	-	-	83
-0.8	58	9	-	16	1.0	<0.5	<0.5	<0.5	85
-0.9	51	4.0	<0.5	8.7	2.8	<0.5	<0.5	<0.5	68
-1.0	57	1.5	<0.5	2.0	7.0	<0.5	<0.5	<0.5	68
CE% Cu_3P/ Cu foil									
E (V)	**H_2**	**CO**	**CH_4**	**HCOOH**	**C_2H_4**	**C_2H_6**	**C_2H_5OH**	**n-propanol**	**Total CE%**
-0.4	99	-	-	3.5	-	-	-	-	103
-0.5	92	-	-	6.0	-	-	-	-	98
-0.6	90	-	-	9.0	-	-	-	-	99
-0.7	94	<0.5	-	4.0	-	-	-	-	98
-0.8	97	<0.5	-	2.0	-	-	-	-	99
-0.9	95	<0.5	-	1.5	-	-	-	-	97

* All the reported voltages were versus RHE.

4.1.3.2. Oxide-derived Cu (OD-Cu) electrocatalyst

The absence of the electrochemical reduction of Cu_2O wave in the LVS graph was due to complete reduction of all the oxides prior to any electrochemical measurements **(Figure 4.35)**. As expected, the recorded current densities of OD-Cu foil were more than the electropolished Cu foil **(Figure 4.32)**.

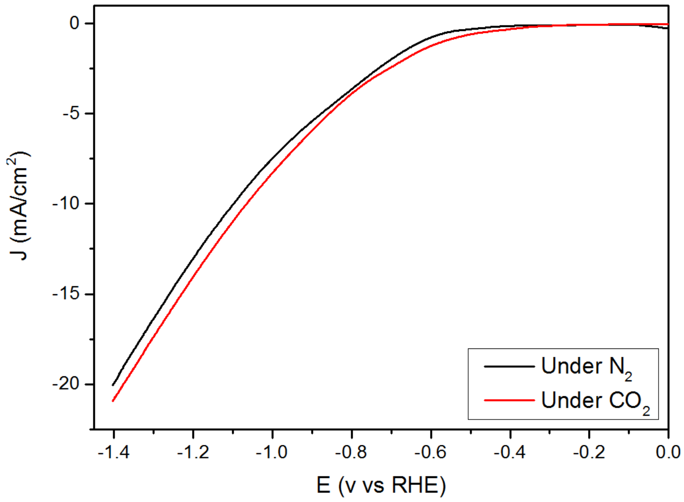

Figure 4.35: LSVs of OD-Cu foil in 0.1 M $KHCO_3$ saturated by N_2 and CO_2 with a scan rate of 20 mV/s.

The CE% of the gaseous and liquid products, are tabulated in **(Figure 4.38 and Table 4-2)**, resulting from CO2RR (chronoameprometric experiments) **(Figure 4.36)**, were lower than the reported values in literature.[191] The difference in the CE% values may be induced by the difference in the roughness factor (41.3) **(Figure 4.37) (Table 4-1)** as it is about 10 times the reported value in literature (4.7).[191] The highest CO2RR performance was observed at -0.7 V (RHE) where the CE% of CO reached about 15% and that of HCOOH reached about 25% **(Table 4-2)**. It is worth noting the total CE% declined at far negative voltage, this may be due to the evaporation of the volatile gaseous products **(Table 4-2)**.

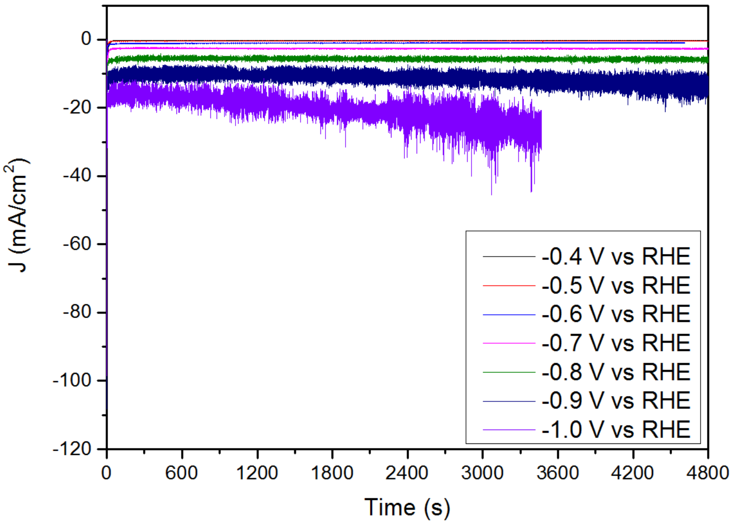

Figure 4.36: CA experiments of OD-Cu foil in 0.1 M $KHCO_3$ saturated by CO_2.

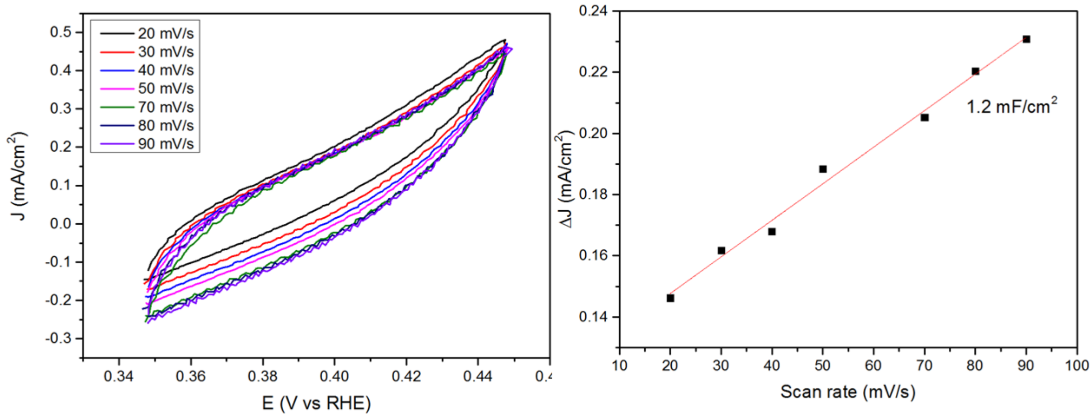

Figure 4.37: Measurement of the capacitance of the OD-Cu foil under N_2 in 0.1 M $KHCO_3$.

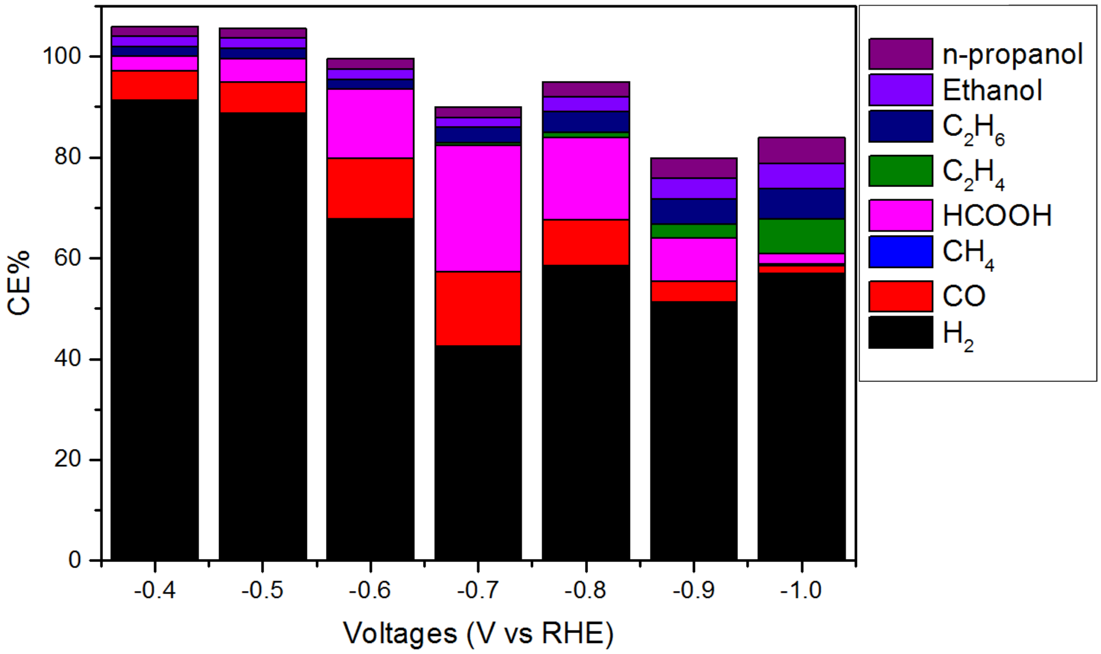

Figure 4.38: Current efficiencies % of all the detected products through CO2RR by the OD-Cu foil.

4.1.3.3. Cu_3P/Cu electrocatalyst

The LSV curves showed that the onsetpotential for CO2RR by Cu_3P/Cu was less negative than the electropolished Cu and more negative than that of OD-Cu foil. Under N_2 gas the electrochemical reduction of Cu(I) was observed at -0.36 V (RHE) **(Figure 4.39)**.

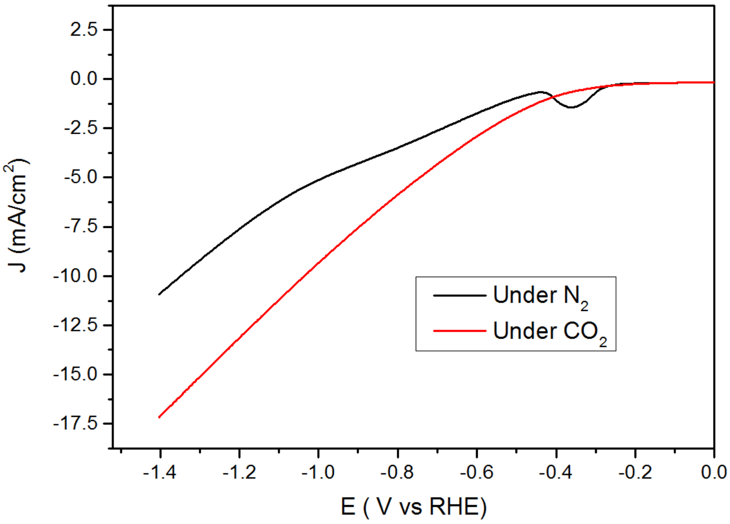

Figure 4.39: LSVs of Cu_3P/Cu foil in 0.1 M $KHCO_3$ saturated by N_2 and CO_2 with a scan rate of 20 mV/s.

The roughness factor of Cu_3P/Cu foil measured through capacitance measurements **(Figure 4.40)** (22.4) was about half that of OD-Cu (41.3) **(Table 4-1)**. Suggesting that the active surface area of the OD-Cu foil is about the double of that of Cu_3P/Cu foil.

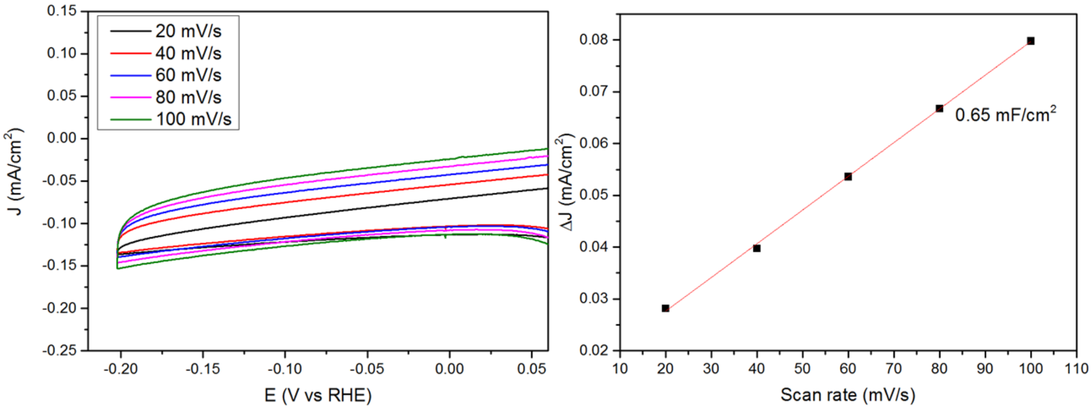

Figure 4.40: Measurement of the capacitance of the Cu_3P/Cu foil under N_2 in 0.1 M $KHCO_3$.

For the copper phosphide electrocatalyst the gaseous products were H_2 and CO and the vast majority was H_2 gas **(Figure 4.42 and Table 4-2)**. Formic acid was detected as well from Cu_3P/Cu electrocatalyst and the highest percentage did not exceed 10% at -0.6 V (RHE). Traces of CO were detected at different voltages during CAs experiments of Cu_3P/Cu foil that may suggest the weak interaction between CO_2 with the Cu_3P surface. Such performance is very different from Cu_3P/C electrocatalyst reported recently, Cu_3P/C exhibited CE% of CO up to 47% at -0.3 V (RHE). [221] Also the weak performance may be attributed to the partial/incomplete disconnection between the Cu_3P film and the bulk Cu metal. It is worth mentioning that at far negative voltage the current densities increased which may be attributed to the activation of more sites on the surface **(Figure 4.41)**.

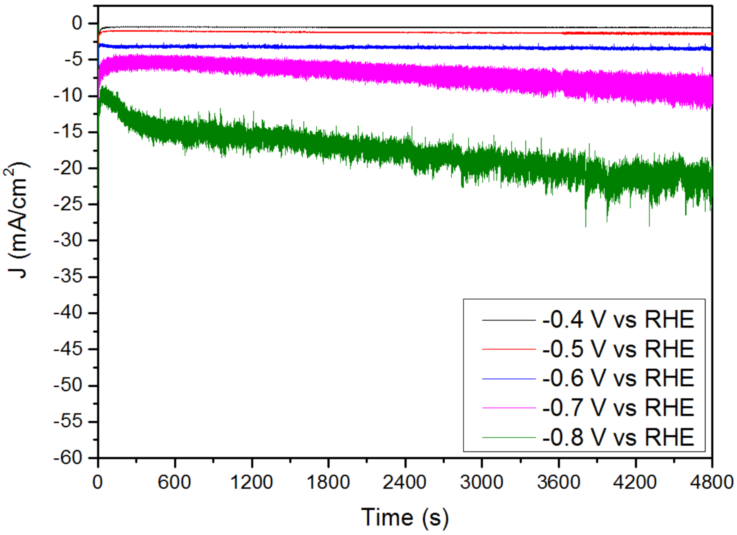

Figure 4.41: CA experiments of Cu_3P/Cu foil in 0.1 M $KHCO_3$ saturated by CO_2.

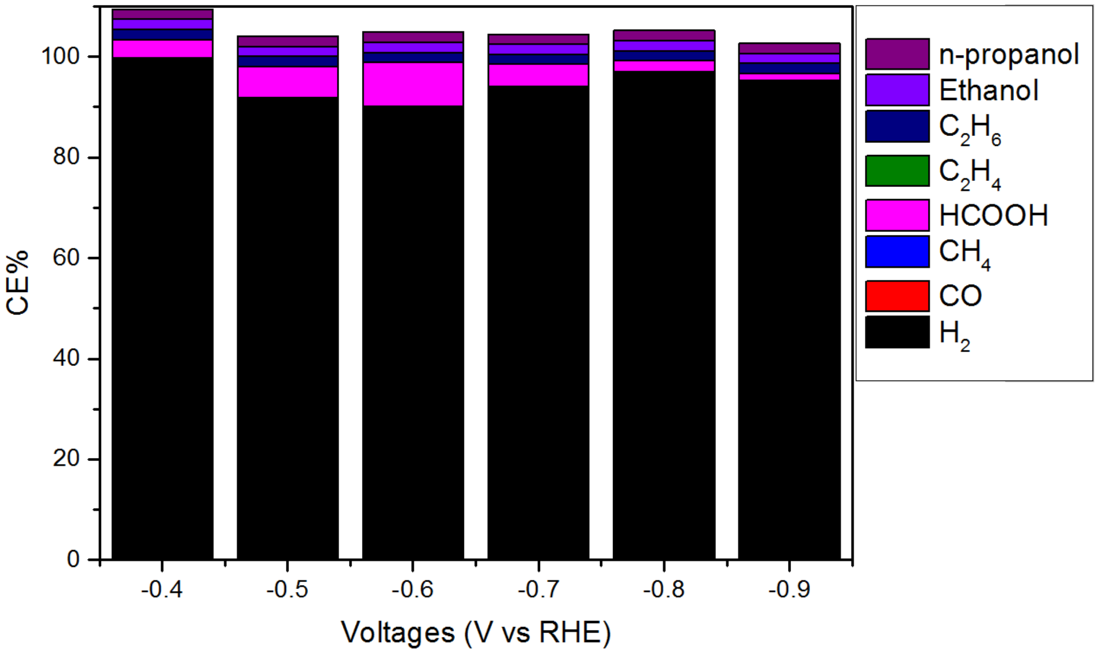

Figure 4.42: Current efficiencies % of all the detected products through CO2RR by the Cu_3P/Cu foil.

The XRD patterns after the electrochemical measurements confirmed the existence of the Cu_3P on the surface of the electrocatalyst after the chronoamperometric experiments **(Figure 4.43)**. After 40 mins of applying constant voltage, the peak of Cu° enhanced slightly suggesting the in-situ electrochemical reduction of Cu_3P during CO2RR **(Figure 4.43)**. Further investigations are required to confirm the existence of Cu_3P on the surface of the electrocatalyst through XPS. SEM images **(Figure 4.45)** after the electrochemical measurements showed the appearance of a layer on the surface of the Cu_3P/Cu foil may be a carbonates layer as the electrochemical measurements were performed in 0.1 M $KHCO_3$.

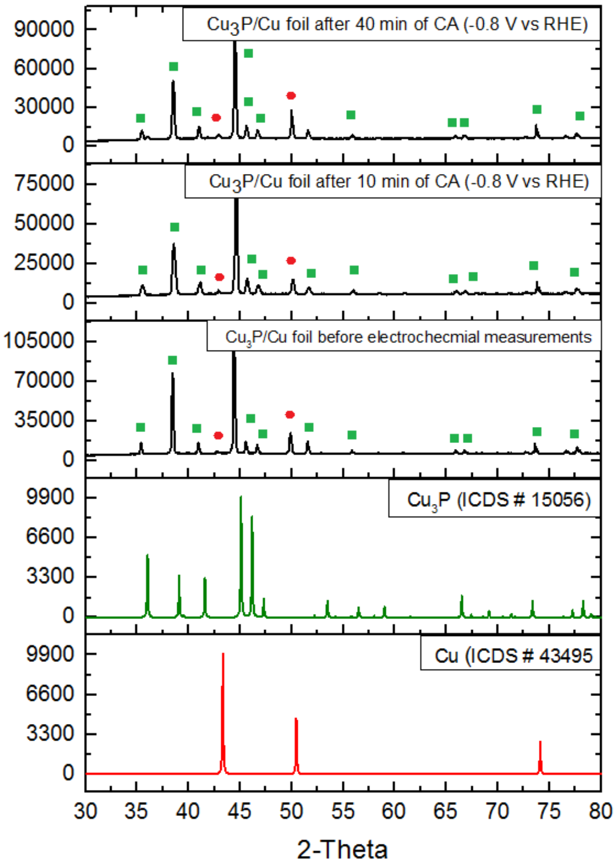

Figure 4.43: XRD patterns of the Cu_3P/Cu foil before and after electrochemical measurements (CA). Red balls belong to Cu peaks and green squares belong to Cu_3P.

The XPS spectra of Cu_3P/Cu foil after the electrochemical measurements confirmed the existence of Cu, P and O elements consistent to the EDX spectral data **(Figure 4.44)**. The XPS data showed the existence of Cu(II) and Cu(I) species on the surface of the electrocatalyst with ≈58 % for Cu(II) and ≈41 % for Cu(I), the majority of the Cu on the surface were either Cu(II), the enhancement of Cu(II) percentage, compared to Cu_3P/Cu foil before electrochemical measurements, can be resulted from the oxidation Cu^o (Cu^o may be formed during the CO2RR) and Cu(I) after the electrochemical measurements (and during storage of the sample). It is not clear which Cu compound/element was the active species(s) it may be Cu^o resulted from the in-situ reduction of Cu_3P and Cu_2O on the surface of Cu_3P/Cu foil or may be the Cu_3P only as the LSV **(Figure 4.39)** didn't show any electrochemical reduction of Cu(I) under CO_2. Further in-situ investigations are required to find/prove the active species. The Cu 2p region **(Figure 4.44a)** exhibited peaks at 932.4 and 952.9 eV for Cu $2p_{3/2}$ assigned for corresponding to $Cu^{\delta+}$ in Cu_3P and Cu(I), respectively. Another two peaks at 934.6 and 952.2 eV assigned for $Cu^{\delta+}$ in Cu_3P and Cu(II) species of the Cu $2p_{1/2}$ peak, respectively.[259] The peaks at 942.3 and 962.5 eV are assigned for the satellites of Cu(II).[221] In the P 2p region **(Figure**

4.44b), a big peak at 133.2 corresponds to the P ($2p_{3/2}$) and P ($2p_{1/2}$).[262] The existence of oxygen in the XPS spectrum resulted from the oxidation of Cu_3P in surface air during storage **(Figure 4.44c)**.[261]

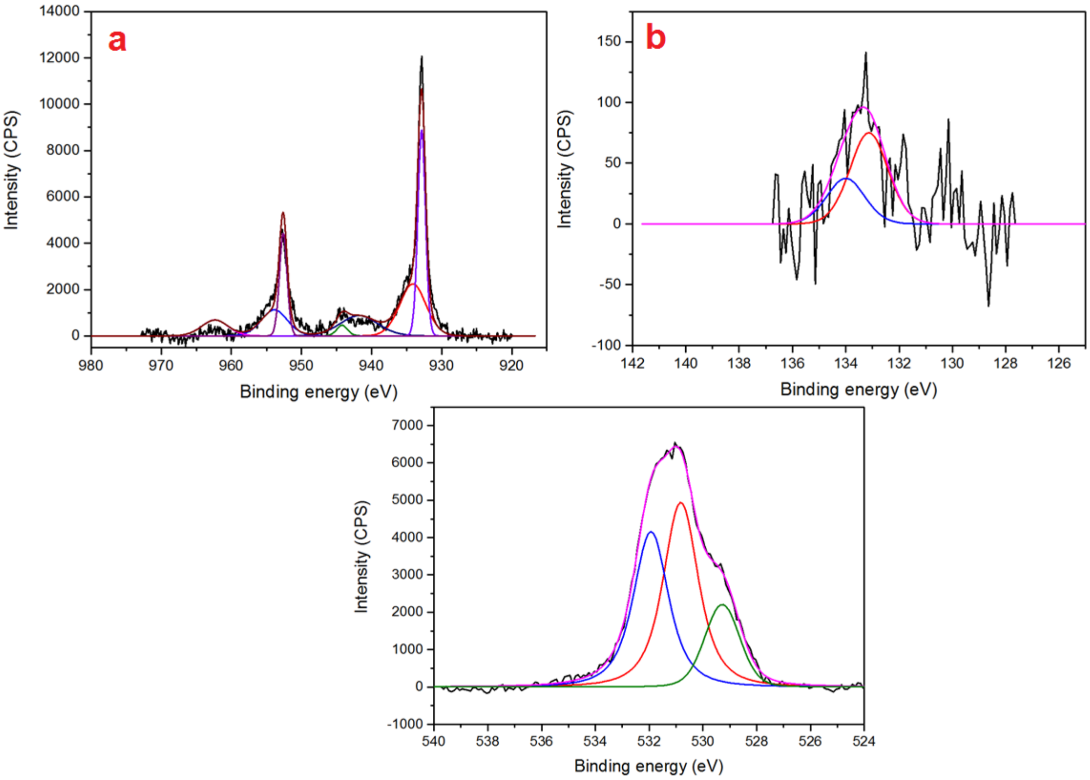

Figure 4.44: X-ray photoelectron spectroscopy (XPS) characterizations of Cu_3P/Cu foil after electrochemical measurements: (a) Cu 2p, (b) P 2p and (c) O 1s regions.

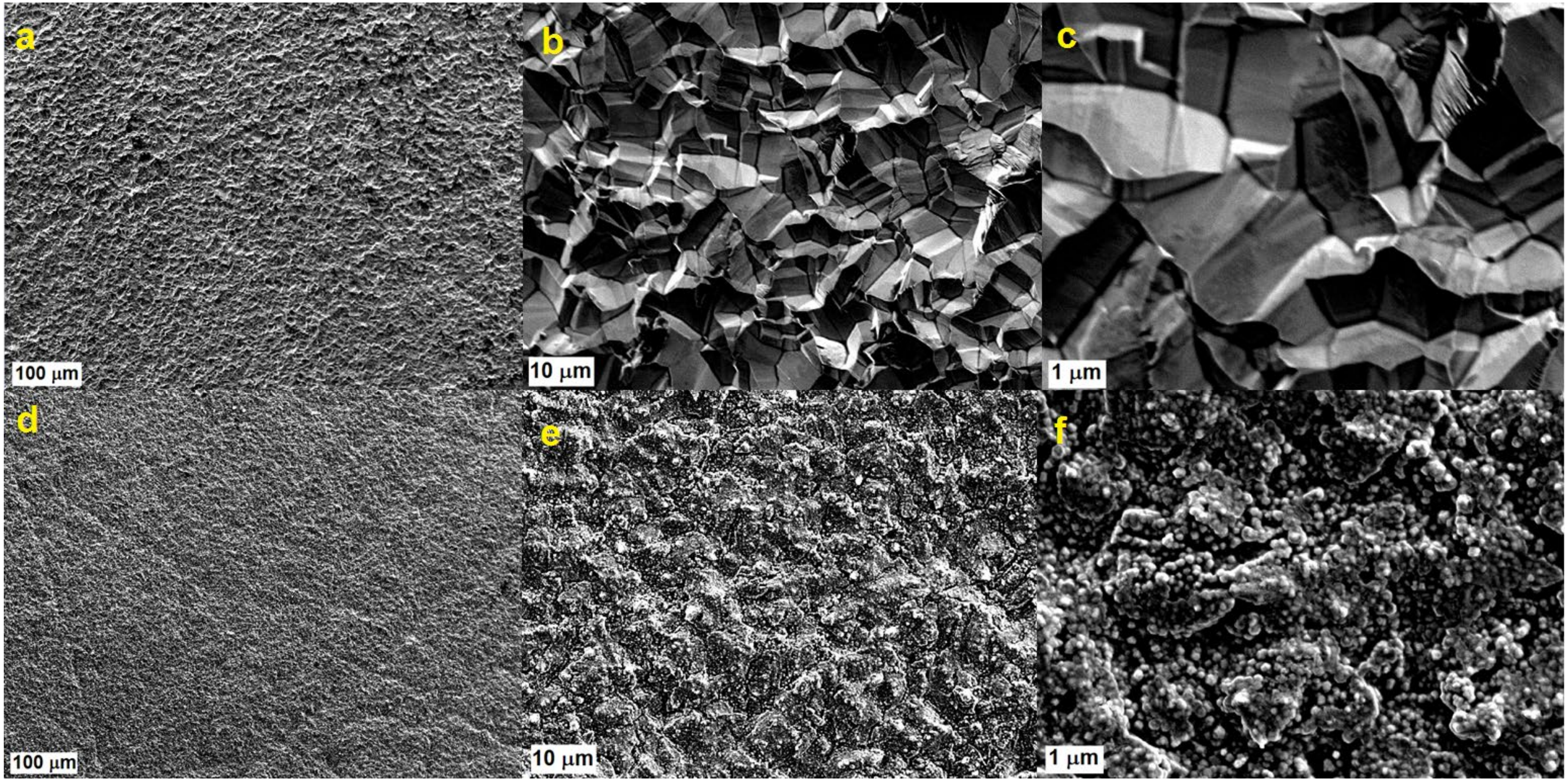

Figure 4.45: SEM images of the Cu_3P/Cu foil before (a-c) and after (d-f) electrochemistry.

4.1.3.4. 3D printed OD-Cu electrocatalyst

The LSV of the 3D printed OD-Cu electrocatalyst showed a weak peak of the electrochemical reduction of Cu_2O under N_2 gas at -0.365 V (RHE) **(Figure 4.46)**.

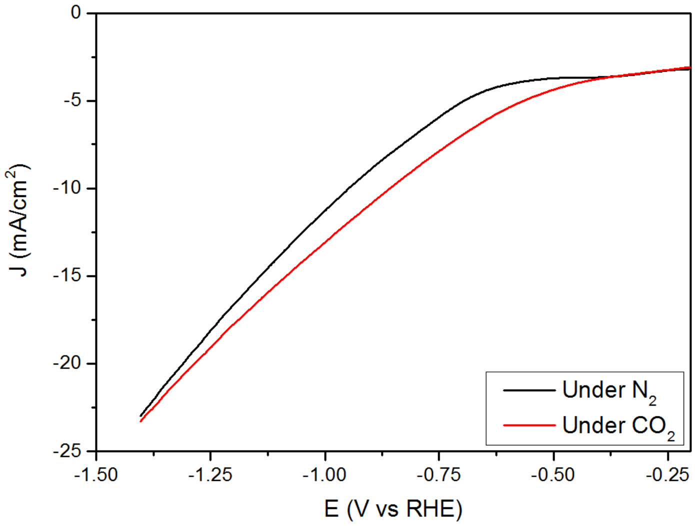

Figure 4.46: LSVs of the 3D printed OD-Cu electrode in 0.1 M $KHCO_3$ saturated by N_2 and CO_2 with a scan rate of 20 mV/s.

The roughness factor of the 3D printed OD-Cu electrocatalyst **(Figure 4.47)** is very high (1386.20) compared to that of OD-Cu foil (41.3) **(Table 4-1 and Table 4-3)**. The difference between the current density between the 3D printed OD-Cu electrode and OD-Cu foil was small **(Figure 4.35 and Figure 4.46)**. The 3D printed OD-Cu electrocatalyst may have a big actual surface area compared to smooth Cu foil but not all the sites are electrochemically active.

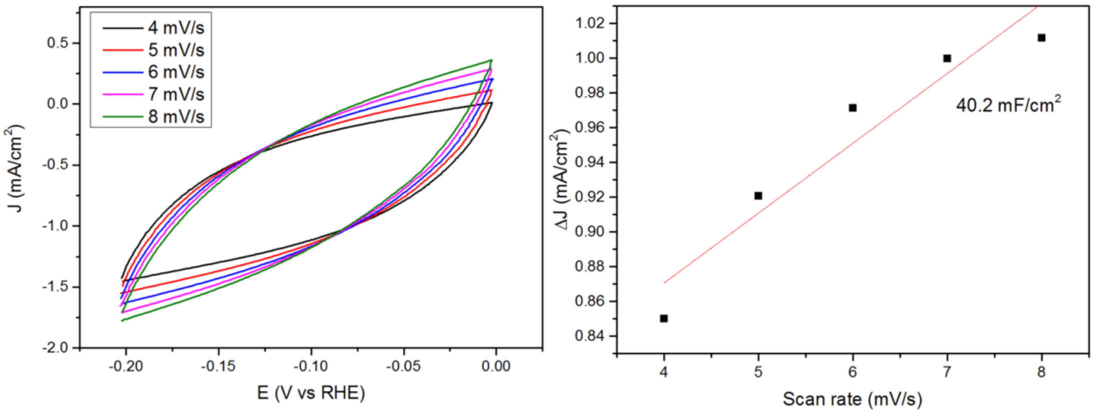

Figure 4.47: Measurement of the capacitance of the 3D printed OD-Cu electrode under N_2 in 0.1 M $KHCO_3$.

Table 4-3: Capacitance and roughness factor measurements of the 3D printed Cu electrocatalyst in 0.1 M $KHCO_3$ under N_2.

Electrocatalyst	**Capacitance**	**Roughness factor**
Cu foil	0.029	1
3D OD-Cu electrode	40.2	1386.20
3D PD/OD-Cu electrode	33.1	1141.38

The electrochemical performance of the 3D printed OD-Cu electrocatalyst was investigated through CO2RR (chronoamperometric experiments) **(Figure 4.49)**. The 3D printed OD-Cu exhibited poor product selectivity compared to OD-Cu foil. The main difference between the 3D-printed OD-Cu electrocatalyst and OD-Cu foil is the appearance of methanol as a product of CO2RR and the current efficiency (CE%) reached 1% at -0.8 V (RHE) **(Table 4-4)**. The CE% of HCOOH did not exceed 10 % at all the reported voltages **(Table 4-4)**.

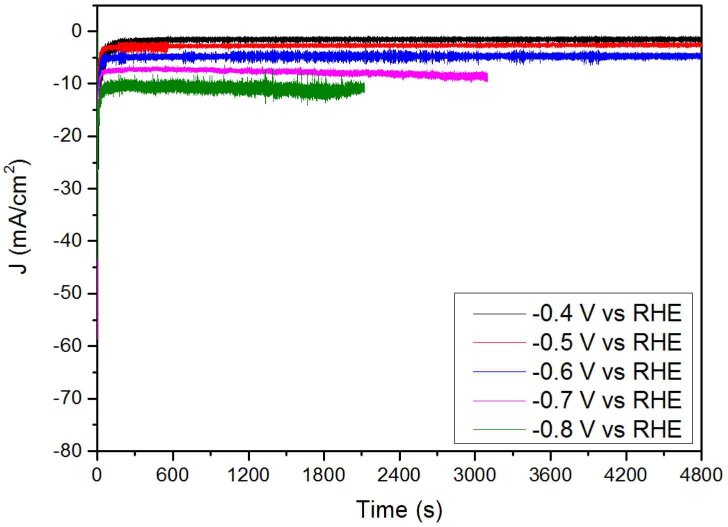

Figure 4.48: CA experiments of the 3D printed OD-Cu electrocatalyst in 0.1 M $KHCO_3$ saturated by CO_2.

Table 4-4: Current efficiencies of all the products using different electrocatalysts and the total current densities in 0.1 M $KHCO_3$ saturated with CO_2.

CE% 3D printed OD-Cu electrocatalyst										
E (V)	**H_2**	**CO**	**CH_4**	**HCOOH**	**C_2H_4**	**C_2H_6**	**CH_3OH**	**C_2H_5OH**	**n-propanol**	**Total CE%**
-0.4	94	2. 0	-	5.0	-	-	-	-	-	101
-0.5	88	2.0	-	6.0	-	-	-	-	-	96
-0.6	91	1.8	-	7.5	-	-	-	-	-	100
-0.7	77	3	-	7.0	<0.5	<0.5	<0.5	<0.5	<0.5	88
-0.8	75	4.0	-	8.5	<0.5	<0.5	1.00	<0.5	<0.5	89
CE% PD/OD-Cu electrocatalyst										
E (V)	**H_2**	**CO**	**CH_4**	**HCOOH**	**C_2H_4**	**C_2H_6**	**CH_3OH**	**C_2H_5OH**	**n-propanol**	**Total CE%**
-0.4	97	-	-	2.5	-	-	-	-	-	99.6
-0.5	93	-	-	4.7	-	-	-	-	-	98
-0.6	96	-	-	50	-	-	-	-	-	101
-0.7	93	<0.5	-	7.0	-	-	-	-	-	99.5
-0.8	99	<0.5	-	1.5	-	-	-	-	-	101

* All the reported voltages were versus RHE.

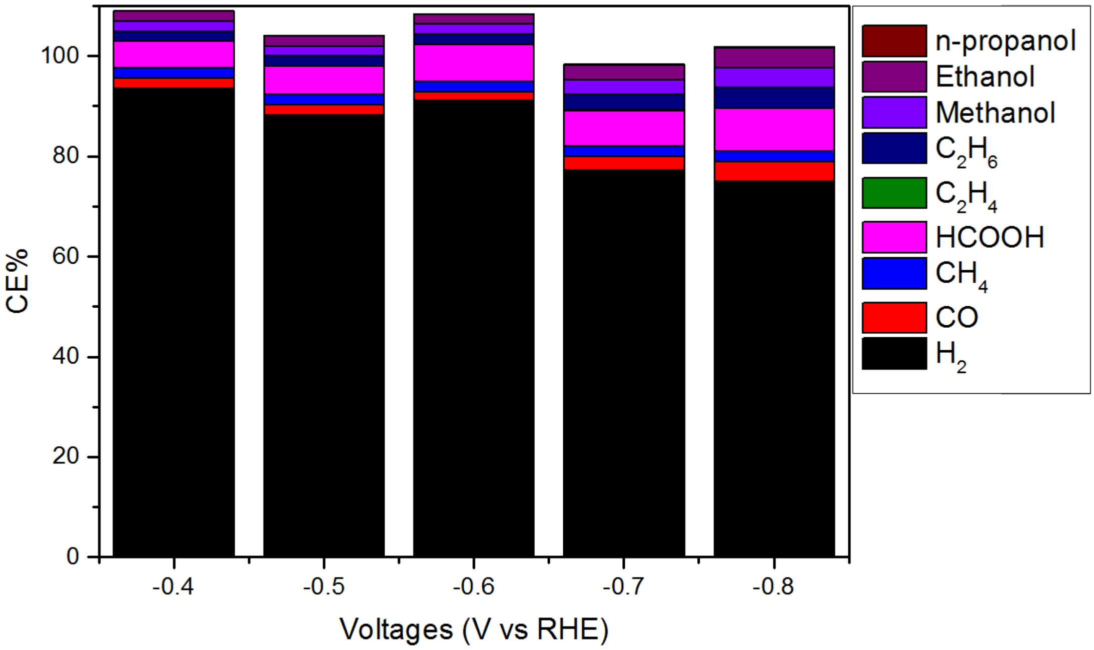

Figure 4.49: Current efficiencies % of all the detected products through CO2RR by the 3D printed OD-Cu electrocatalyst.

The XRD pattern **(Figure 4.50)** of the 3D printed OD-Cu electrocatalyst exhibited enhancement in the intensity of the peaks of the Cu_2O peaks formed during storage of the eleectrocatalyst in air. The SEM images of the 3D printed OD-Cu electrocatalyst **(Figure 4.52)** did not show significant change in the appearance and the morphology of the surface of the 3D printed OD-Cu electrocatalyst before and after the electrochemical measurements (CA).

The XPS spectra of the 3D printed OD-Cu electrocatalyst after the electrochemical measurements confirmed the existence of Cu, and O elements consistent to the EDX spectral data **(Figure 4.51)**. The XPS data showed the existence of Cu(II) and Cu(I) species on the surface of the electrocatalyst with ≈30.9 % for Cu(II) and ≈69.9 % for Cu(I), the majority of the Cu on the surface were Cu_2O. the enhancement in the intensity of Cu(II) peaks after electrochemistry compared to after electrochemistry may be attributed to the oxidation during in air and formation of $CuCO_3$ as the electrochemical measurements formed in 0.1 M $KHCO_3$. In the Cu 2p region **(Figure 4.51)**, showed peaks at 932.6 and 951.6 eV for Cu $2p_{3/2}$ assigned for Cu(I) (Cu_2O), respectively. Another two peaks at 934.3 and 954.1 eV assigned for Cu(II) of CuO.[259, 263] The peaks at 941.5 and 962.6 eV are assigned for the satellites of Cu(II).[221] The existence of oxygen in the XPS spectrum resulted from the oxidation of Cu in surface air during storage **(Figure 4.51)**.

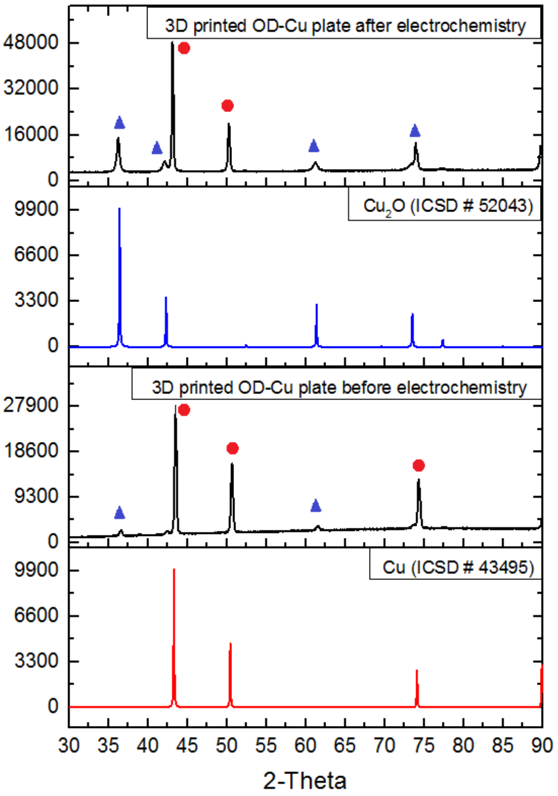

Figure 4.50: XRD patterns of the 3D printed OD-Cu electrode before and after electrochemistry. Red balls belong to Cu peaks and blue triangles for Cu$_2$O peaks.

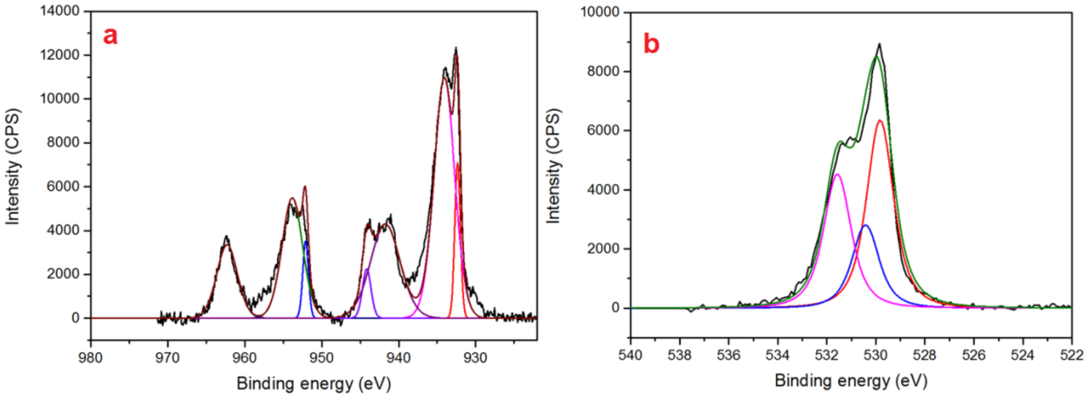

Figure 4.51: X-ray photoelectron spectroscopy (XPS) characterizations of the 3D printed OD-Cu electrocatalyst after electrochemical measurements: (a) Cu 2p and (b) O 1s regions.

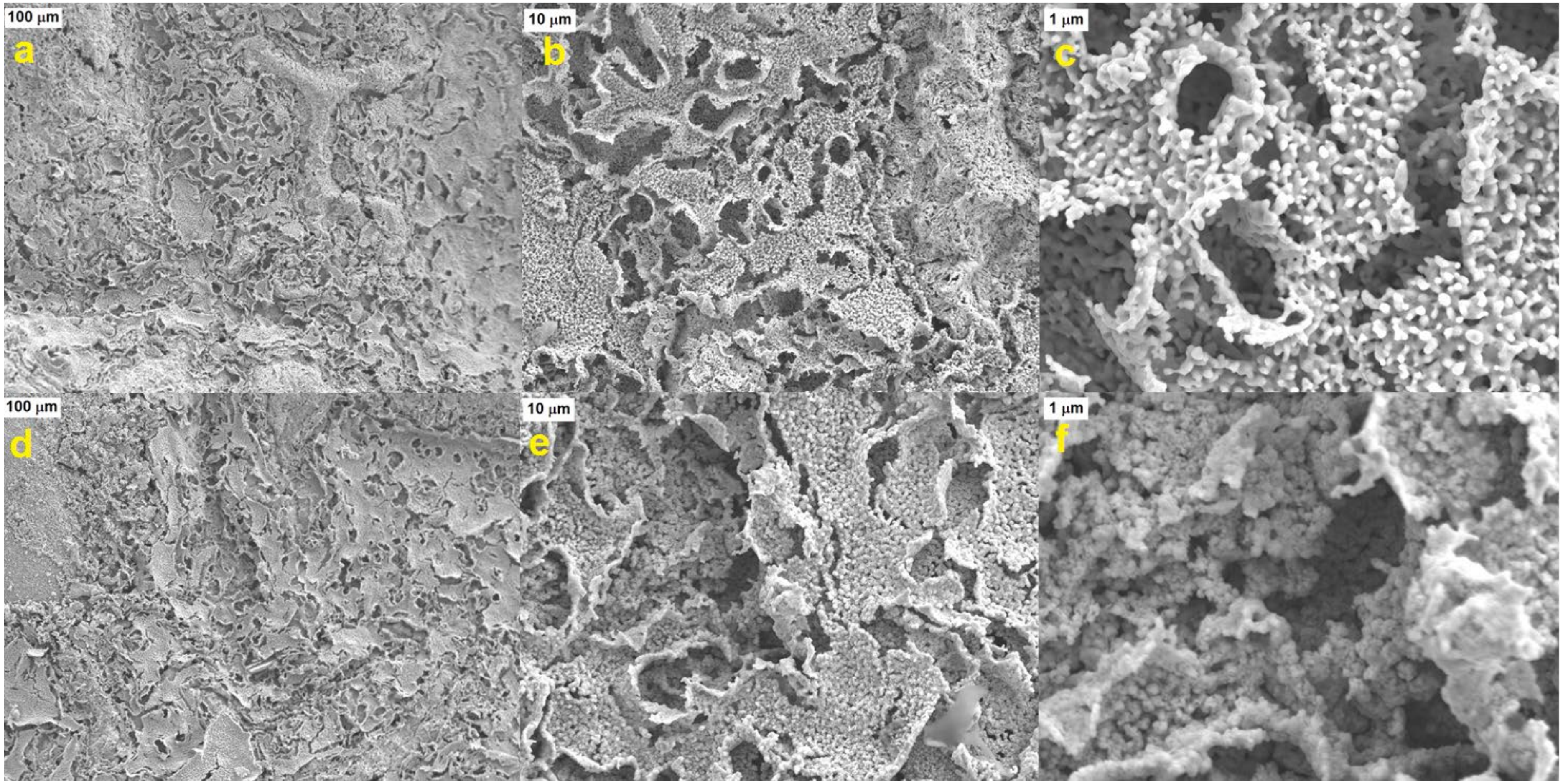

Figure 4.52: SEM images of the top-down view of the 3D printed OD-Cu electrode before (a-c) and after (d-f) electrochemical measurements.

4.1.3.5. 3D printed PD/OD-Cu electrocatalyst

The LSV of the 3D printed PD/OD-Cu electrocatalyst showed a weak wave of the electrochemical reduction of Cu_2O under N_2 gas at -0.37 V (RHE) **(Figure 4.53)**.

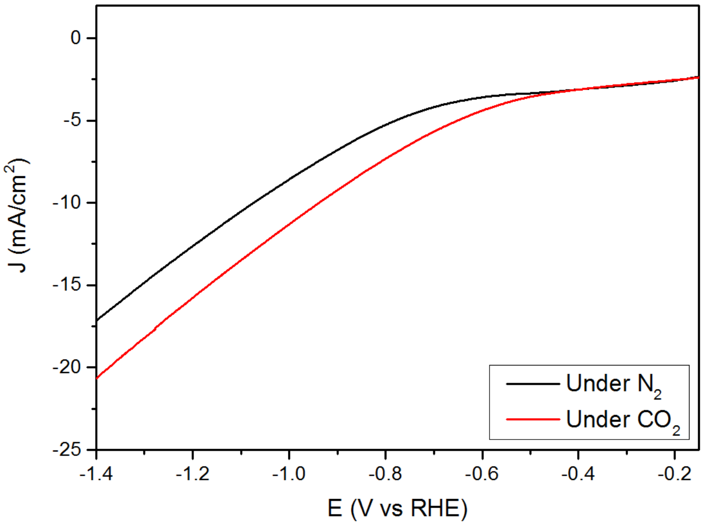

Figure 4.53: LSVs of the 3D printed PD/OD Cu electrode in 0.1 M $KHCO_3$ saturated by N_2 and CO_2 with a scan rate of 20 mV/s.

The roughness factor of the 3D printed PD/OD-Cu electrocatalyst **(Figure 4.54)** is very high (1141.38) **(Table 4-3)** but is lower than that of the 3D printed OD-Cu (1386.20) **(Table 4-1)**. The difference between the current density between the 3D printed OD-Cu electrode and OD-Cu foil was small **(Figure 4.35 and Figure 4.46)**. The 3D printed OD-Cu electrocatalyst may have big actual surface area compared to smooth Cu foil but not all the sites are electrochemically active.

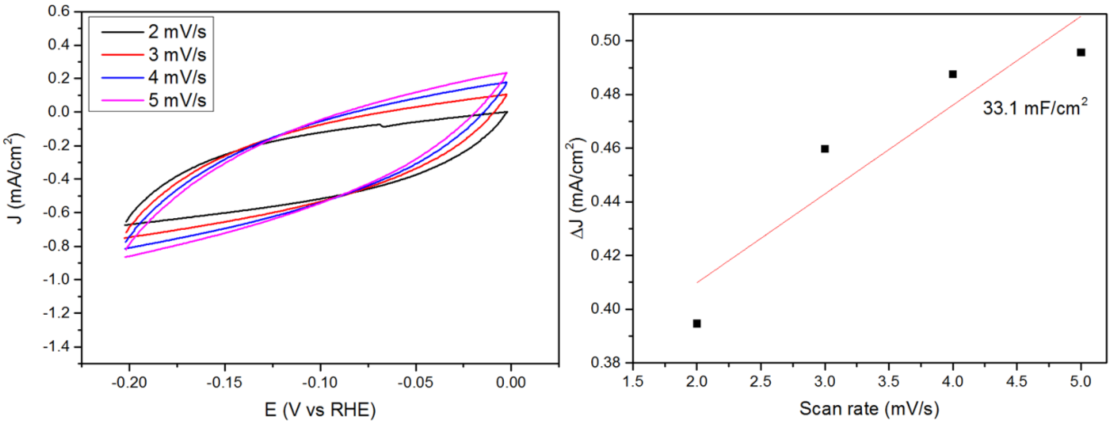

Figure 4.54: Measurement of the capacitance of the 3D printed PD/OD-Cu electrode under N_2 in 0.1 M $KHCO_3$.

The 3D printed PD/OD-Cu electrocatalyst showed the production of H_2 and formic acid with traced of CO at far negative voltages (-0.7 and -0.8 V RHE) **(Figure**

4.55). The CE% of the gaseous and liquid product showed that the 3D printed PD/OD-Cu eletcrocatalyst favours HER over CO2RR and all the CE% percentages of hydrogen were above 92% at all voltages **(Table 4-4)**.

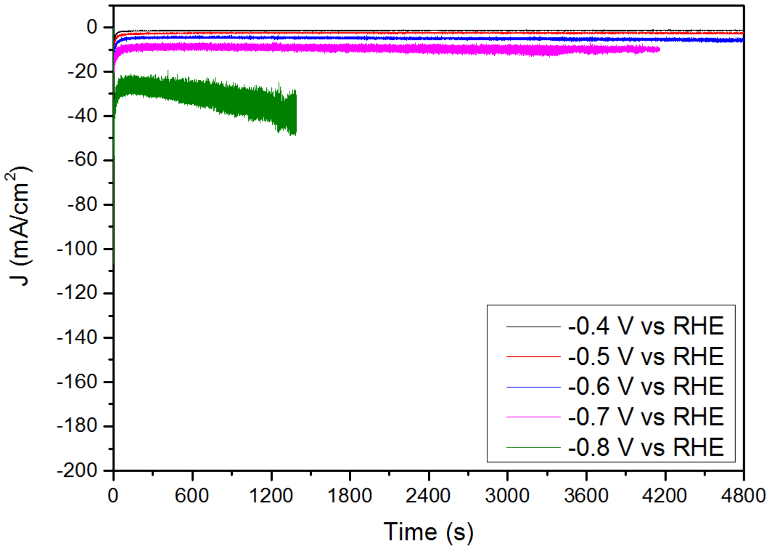

Figure 4.55: CA experiments of the 3D printed PD/OD-Cu electrode in 0.1 M $KHCO_3$ saturated by CO_2.

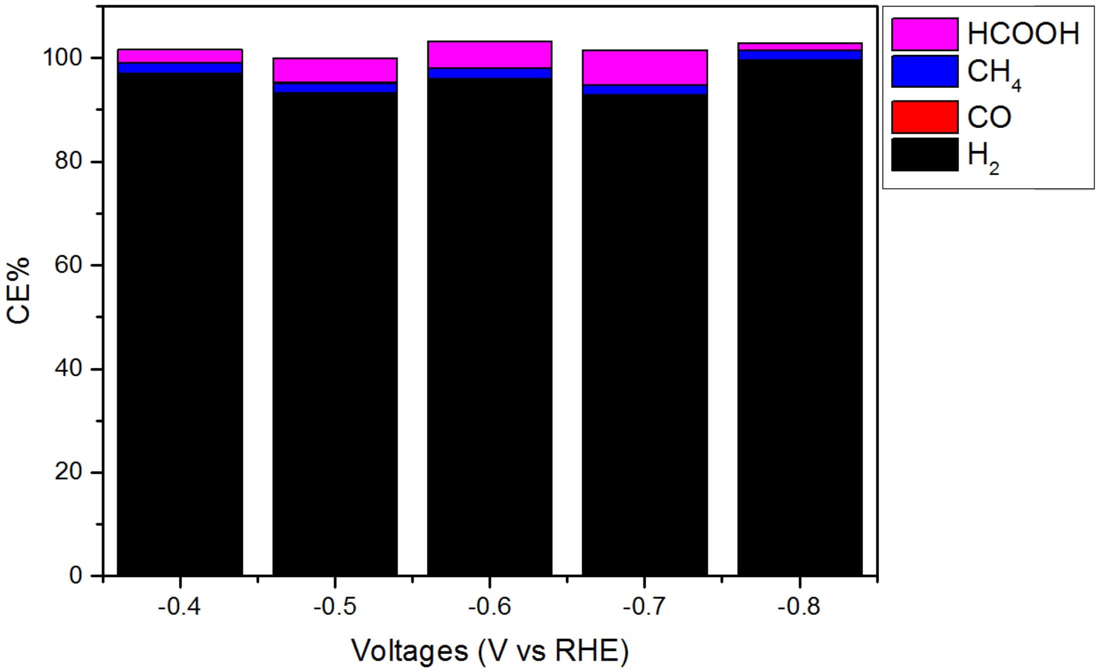

Figure 4.56: Current efficiencies % of all the detected products through CO2RR by the 3D printed PD/OD-Cu electrocatalyst.

The XRD pattern **(Figure 4.57)** of the 3D printed PD/OD-Cu electrocatalyst confirmed the existence of the Cu_3P peaks after the electrochemical measurements in addition to peaks belonging to Cu_2O. Further investigations are required to confirm the existence of Cu_3P on the surface of the electrocatalyst through XPS suggesting the electrochemical reduction of Cu_3P on the surface not the bulk Cu_3P which appeared in the XRD pattern.

The SEM images **(Figure 4.59)** did not show significant change in the appearance and the morphology of the surface of the 3D printed OD-Cu electrocatalyst before and after the electrochemical measurements (CA). Carbonates may be adsorbed on the surface as CO2RR was performed in 0.1 M $KHCO_3$.

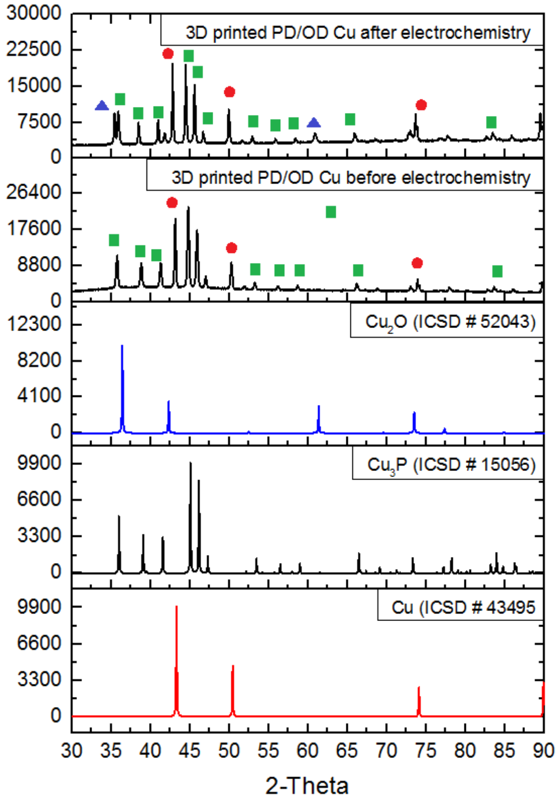

Figure 4.57: XRD patterns of the 3D printed PD/OD-Cu electrode before and after electrochemistry. Red balls belong to Cu peaks, green squares belong to Cu_3P and blue triangles for Cu_2O peaks.

The XPS spectra of 3D printed PD/OD-Cu elecrocatalyst after the electrochemical mesurements confirmed the existence of Cu, P and O elements consistent with the EDX spectral data **(Figure 4.58)**. The XPS data showed the existence of Cu(II) and Cu(I) species on the surface of the electrocatalyst with ≈79 % for Cu(II) and ≈20 % for Cu(I). The enhancement of Cu(I) after the electrochemical measurements compared to that before the electrochemical measurments, may be resulted from the in-situ electrochemical reduction of Cu(II) during CO2RR and the reoxidation of Cu^o during storage. It is not clear which Cu compound/element was the active species(s); it may be Cu^o resulted from the in-situ reduction of Cu_3P and Cu_2O on the surface of Cu_3P/Cu foil or may be the Cu_3P only as the LSV **(Figure 4.53)** didn't show any electrochemical reduction of Cu(I) under CO_2. Further in-situ investigations are required to find/prove the active species. In the Cu 2p region **(Figure 4.58a)**, showed peaks at 932.6 and 952.6 eV for Cu $2p_{3/2}$ assigned for corresponding to $Cu^{\delta+}$ in Cu_3P and Cu(I), respectively. Another two peaks at 934.7 and 954.6 eV assigned for $Cu^{\delta+}$ in Cu_3P and Cu(II) species of the Cu $2p_{1/2}$ peak, respectively.[259] The peaks at 942.5 and 963 eV are assigned for the satellites of Cu(II).[221] In the P 2p region **(Figure 4.58b)**, a big peak at 130.2 corresponds to the P ($2p_{3/2}$) and P ($2p_{1/2}$).[262] Additional peak appeared at 133.4 eV in the P 2p region assigned for the oxidised phosphorus (phosphate).[259] The enhancement of the peak of the phosphate may be attributed to the oxidation of the surface phosphide during storage and the weak peak of phosphide reflected the fact the Cu_3P layer was electroreduced prior to the electrochemical measurements. The existence of oxygen in the XPS spectrum resulted from the oxidation of Cu_3P in surface air during storage **(Figure 4.58c)**.[261]

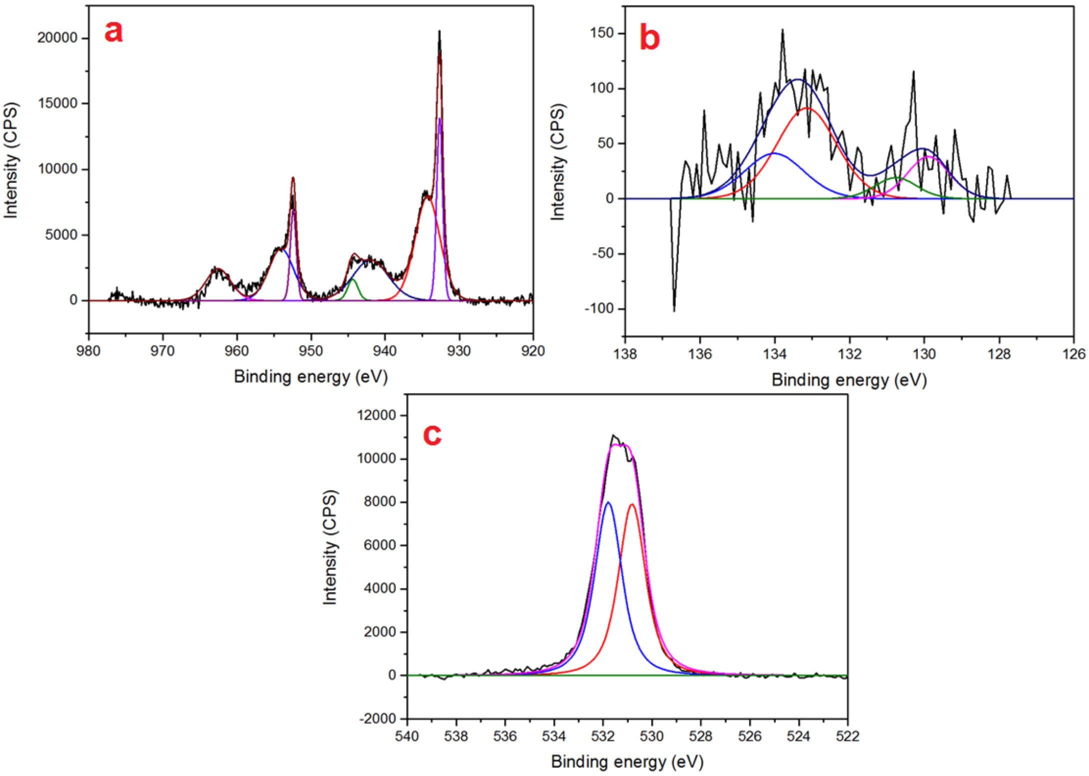

Figure 4.58: X-ray photoelectron spectroscopy (XPS) characterizations of 3D printed PD/OD-Cu electrocatalyst after the electrochemical measurements: (a) Cu 2p, (b) P 2p and (c) O 1s regions.

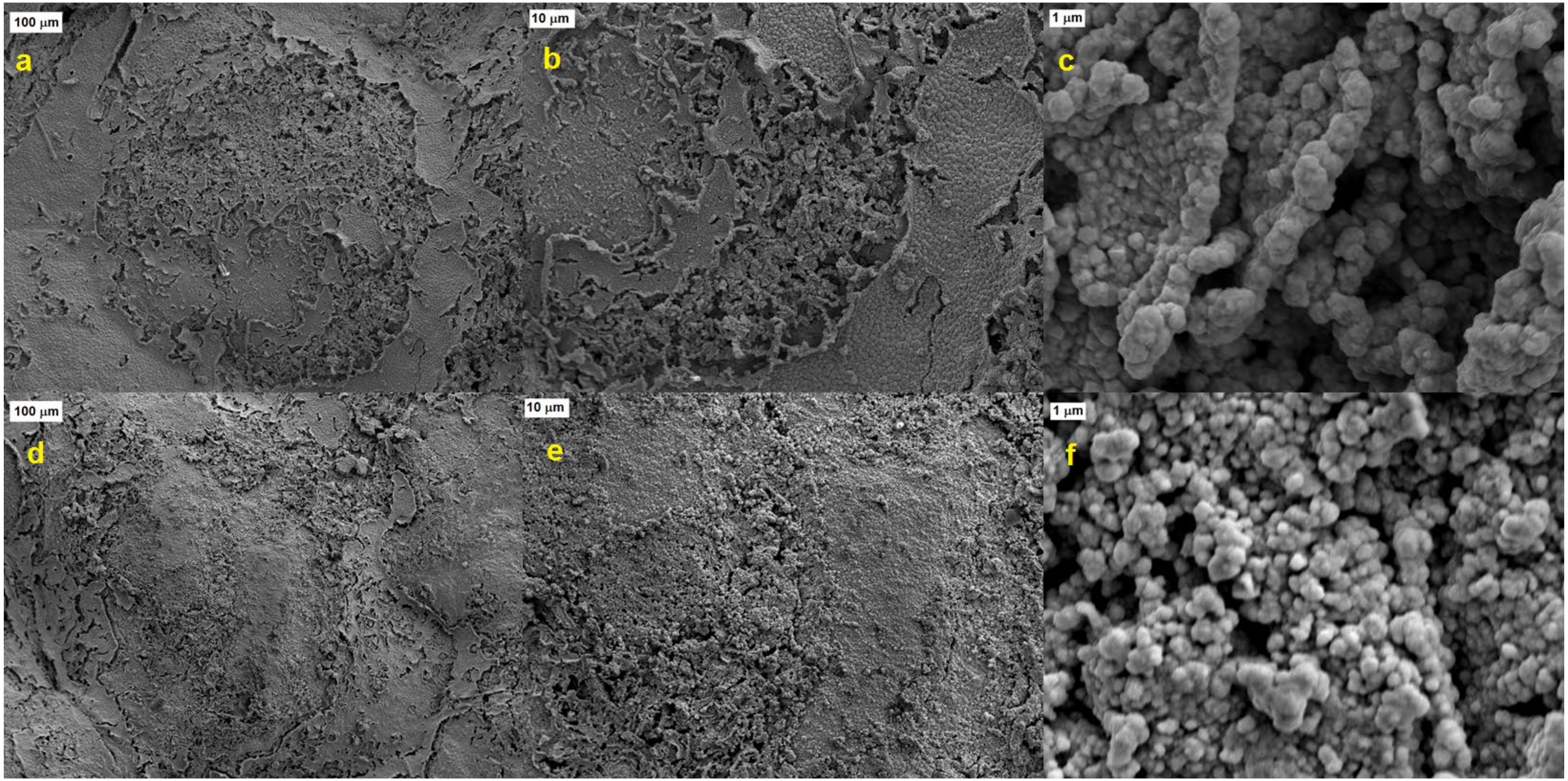

Figure 4.59: SEM images of the 3D printed PD/OD Cu electrode before (a-c) and after (d-f) electrochemical measurements.

4.1.4. Electrochemical impedance measurements

Electrochemical impedance spectroscopy was used to determine and study the charge-transfer resistance in CO_2 saturated 0.1 M $KHCO_3$ at different voltages. The Nyquist plots of the EIS spectra at different potentials exhibited two semi-circles **(Figure 4.60 - Figure 4.64)**. The equivalent circuit used is shown in **(Figure 4.65)** where R1 (solution resistance), R2//Q2 component (electrocatalyst transport behaviour) and R3//Q3 (electrochemical reduction reactions).[264] All the EIS data of the Cu based electrocatalysts were tabulated in **(Table 4-5)**. Moving to far negative voltage, the impedance values decreases, suggesting the a high rate of the faradaic reactions.[264]

For the Cu foils (electropolished Cu, OD-Cu and Cu_3P/Cu foils) the solution resistance (R1) lies between 3 - 7 ohm. R2 values were between 8 - 12 ohm without any significant change upon changing the voltages. The charge transfer resistances (R3) for the electropolished Cu were between (1981 - 32.54 ohm), for OD-Cu foil (408 - 7.3 ohm) and for Cu_3P/Cu foil (276 - 16 ohm). The charge transfer resistances (R3) values were generally high and decreased with moving to far negative voltages. The charge transfer resistances of the Cu_3P/Cu foil were low compared to that of electropolished Cu and OD-Cu foils, suggesting the feasibility of HER over CO2RR in the case of electropolished Cu and OD-Cu foils.

For the 3D printed Cu electrocatalysts (OD-Cu and PD/OD-Cu electrocatalysts), the solution resistance (R1) lies between 6 - 10 ohm. R2 values were between about 3 for the 3D printed OD-Cu electrocatalyst and about 9 ohm for PD/OD-Cu electrocatalyst. There was no significant change in the R1 and R2 values upon changing the voltages. The 3D printed OD-Cu electrocatalyst favour HER over CO2RR and the fast charge transfer for protons compared to CO_2. The charge transfer resistance of PD/OD-Cu were lower than that of OD Cu electrocatalyst, reflecting the favourability of the former one to reduce protons over CO_2 and the more feasible charge transfer to protons **(Table 4-5)**. The charge transfer resistances of the OD-Cu were higher than that of 3D printed OD-Cu electrocatalyst. Such behaviour may reflect that difference between the electrocatalytic activities of two electrocatalysts toward CO2RR and HER.

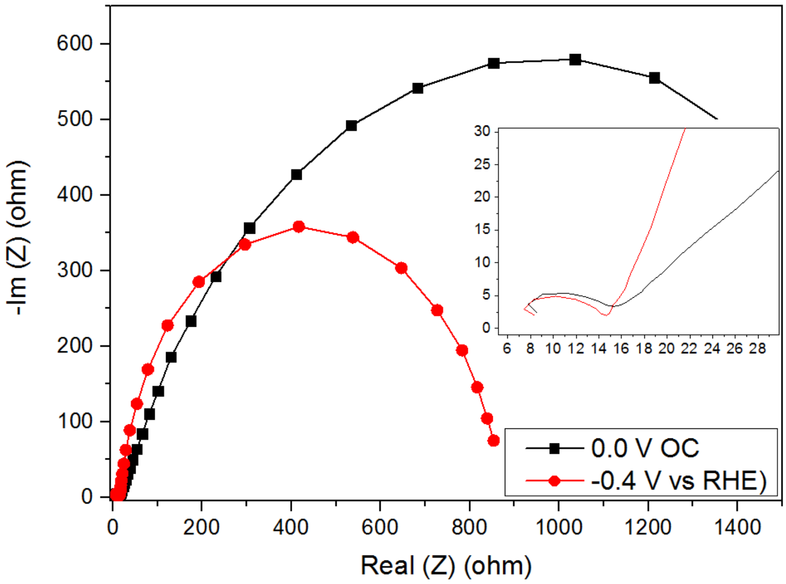

Figure 4.60: EIS spectra of electropolished Cu foil in 0.1 M $KHCO_3$ saturated by CO_2.

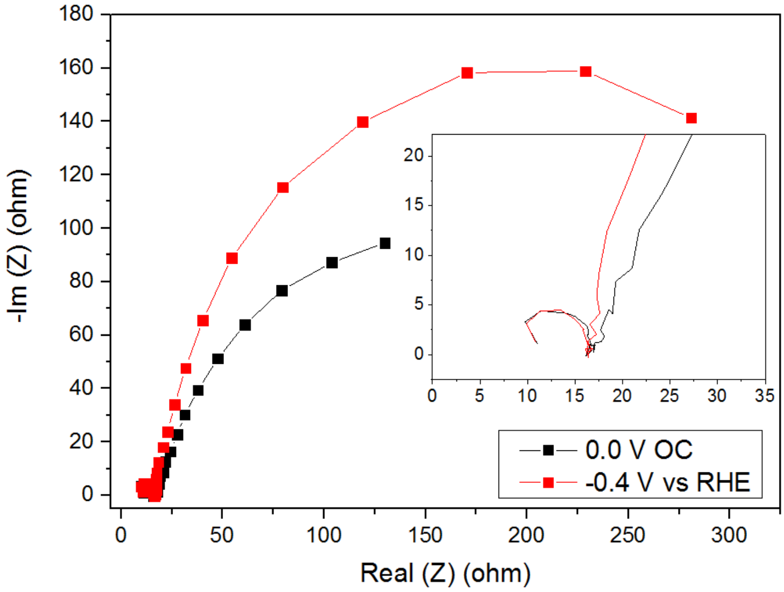

Figure 4.61: EIS spectra of OD-Cu foil in 0.1 M $KHCO_3$ saturated by CO_2.

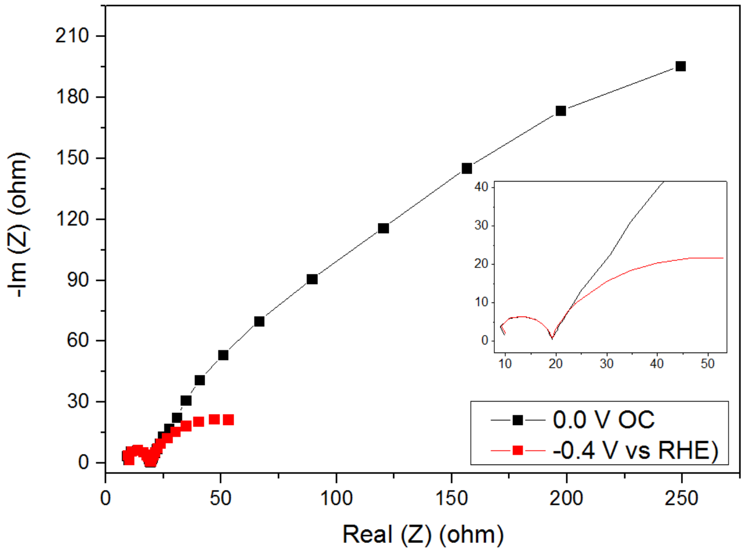

Figure 4.62: EIS spectra of Cu_3P/Cu foil in 0.1 M $KHCO_3$ saturated by CO_2.

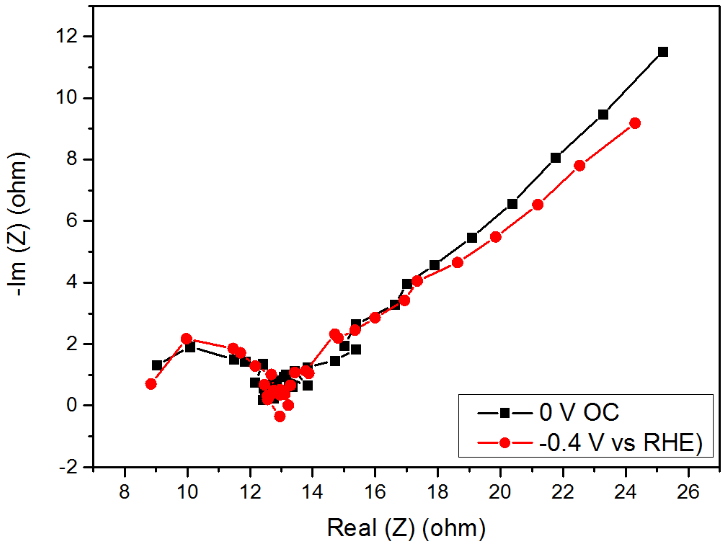

Figure 4.63: EIS spectra of the 3D printed OD-Cu electrocatalyst in 0.1 M $KHCO_3$ saturated by CO_2.

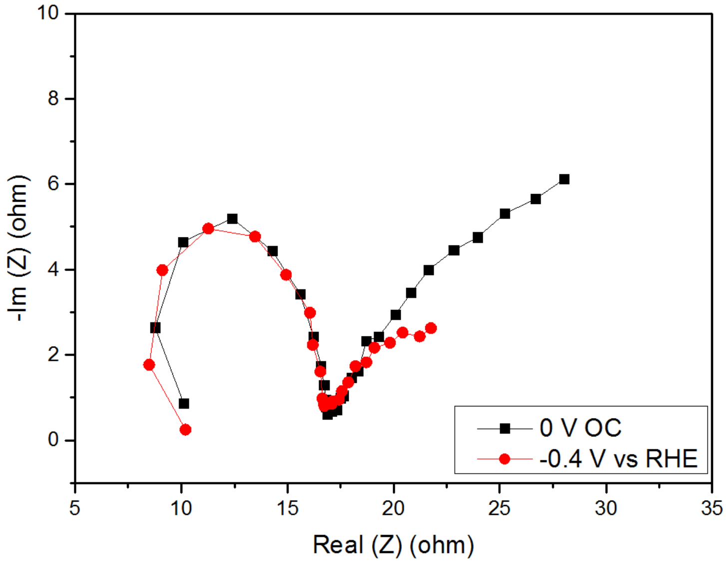

Figure 4.64: EIS spectra of the 3D printed PD/OD-Cu electrocatalyst in 0.1 M $KHCO_3$ saturated by CO_2.

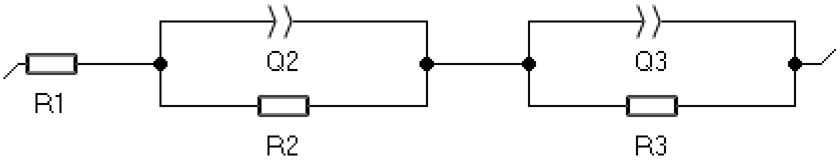

Figure 4.65: The equivalent electric circuit used for fitting the EIS data; R: resistance and Q: constant phase element.

Table 4-5: EIS data of all Cu based electrocatalysts foils in 0.1 M $KHCO_3$ saturated by CO_2.

Electropolished Cu foil						
	0.0 OC	**-0.4 V***	**-0.5 V**	**-0.6 V**	**-0.7 V**	**-0.8 V**
R1	3.338	4.28	5.259	4.95	6.726	6.747
Q2	1.62E-6	1.43E-6	6.10E-7	7.90E-6	7.06E-7	8.29E-7
a2	0.8667	0.9022	0.9897	0.7556	1	1
R2	12.05	10.77	9.3	10.86	8.372	8.179
Q3	3.94E-4	1.63E-4	2.15E-4	1.98E-4	1.18E-4	8.47E-5
a3	0.6858	0.8942	0.8548	0.886	0.8655	0.9189
R3	1981	853.6	248.3	113.8	72.03	44.18
OD-Cu electrocatalyst						
	0.0 OC	**-0.4 V**	**-0.5 V**	**-0.6 V**	**-0.7 V**	**-0.8 V**
R1	7.718	5.312	3.97	4.076	6.782	7.794
Q2	4.26E-7	7.86E-6	7.69E-7	9.9E-7	3.58E-7	5.41E-7
a2	1	0.7284	0.8968	0.871	1	1
R2	9.061	11.49	12.17	12.25	9.206	8.159
Q3	6.48E-3	2.44E-3	3.22E-3	1.40E-3	1.05E-3	1.16E-3
a3	0.7797	0.9051	0.8406	0.9039	0.9172	0.9168
R3	276.7	371.2	142.8	75.44	43.65	25.97
Cu_3P/Cu electrocatalyst						
	0.0 OC	**-0.4 V**	**-0.5 V**	**-0.6 V**	**-0.7 V**	**-0.8 V**
R1	7.106	6.216	6.277	6.476	6.395	6.198
Q2	4.99E-7	3.42E-7	3.47E-7	3.65E-7	4.35E-4	3.55E-7
a2	0.9881	1	1	1	1	1
R2	12.1	12.73	12.54	12.17	10.29	12.38
Q3	3.29E-3	1.58E-3	9.57E-4	9.63E-4	3.59E-7	9.92E-4
a3	0.782	0.7927	0.8561	0.8336	1	0.8501
R3	408.4	61.06	34.69	21.51	12.36	7.388
3D printed OD-Cu electrocatalyst						
	0.0 OC	**-0.4 V***	**-0.5 V**	**-0.6 V**	**-0.7 V**	**-0.8 V**
R1	8.71	8.775	9.33	9.60	10.45	10.21
Q2	1.75E-6	1.94E-6	2.47E-6	2.01E-6	3.01E-6	2.64E-6
a2	0.99	1	1	1	1	1
R2	3.77	3.85	3.52	3.47	3.00	3.11
Q3	6.60E-2	7.03E-2	7.13E-2	7.25E-2	5.70E-2	7.09E-2
a3	0.47	0.4654	0.48	0.48	0.54	0.39
R3	144.4	70.28	32.21	16.39	9.45	9.22
3D printed PD/OD-Cu electrocatalyst						
	0.0 OC	**-0.4 V**	**-0.5 V**	**-0.6 V**	**-0.7 V**	**-0.8 V**
R1	6.38	6.36	6.26	6.77	6.69	6.82
Q2	4.45E-7	6.04E-7	5.63E-7	4.51E-7	4.38E-7	4.43E-7
a2	1	1	1	1	1	1
R2	9.82	9.11	9.32	9.82	9.64	9.55
Q3	2.94E-2	4.67E-2	3.00E-2	5.04E-3	6.89E-3	7.49E-3
a3	0.408	0.28	0.34	0.67	0.64	0.64
R3	58.51	49.35	20.42	7.99	6.58	5.34

*all voltages were reported versus RHE.

4.2. Discussion

The current efficiencies (CE%) resulting from all the Cu based electrocatalyst (electropolished Cu, OD-Cu, Cu_3P/Cu, 3D-printed OD-Cu and PD/OD-Cu electrocatalysts) are tabulated in **Table 4-2 and Table 4-4**.

The reported CE% values for the electropolished Cu foil were low compared to that reported in literature[223] especially for gaseous product which may be attributed to the orientation preference of Cu plane observed in the XRD pattern **(Figure 4.1)**. The CE% of the products detected during the chronoamperometric experiments of OD-Cu foil were different from what is reported in literature.[191] At -1.0 V (RHE) the CE% of C_2H_4 reached about 7 % compared to about 40 % reported in litreraure.[191] The difference in the electrocatalytic performance may be induced by the mass transport and difference in roughness factor (41.3) for the OD-Cu foil in the current work compared to (4.7) reported in literature.[191] The total CE% at far negative voltages were low (67 - 68%) which may be due to the electrochemical setup being not optimised to collect all the volatile products. The CE% of the detected products resulting from the electrochemical reduction at Cu_3P/Cu foil showed its low electrocatalytic activity toward CO2RR. Negligible percentages of CO at all the voltages and a CE% of formic acid reached about 8 % at -0.6 V (RHE) were observed, suggesting weak interaction between the Cu_3P/Cu and CO_2. The difference between the CE% of the Cu_3P/Cu compared to what is reported from Cu_3P/C reported in literature[221] may be attributed to two things: firstly, having different substrates Cu and C, secondly, the difference in the roughness factors (ECSA) which may be reflected in the difference in electrocatalytic activity. It is worth noting that the highest FE% for CO (47%) were reported at low voltage (-0.3 V vs RHE).[221]

3D printing as a new methodology succeeded in preparing and building Cu based electrocatalysts. The 3D printed Cu based electrodes were prepared and exhibited a very rough morphology with high surface area resulted from the evolution of gases during the thermal treatment to remove the organic content. The electrochemical activities of the two 3D printed Cu based electrocatalyst were lower than that of Cu foils towards CO2RR. The 3D printed Cu based electrocatalyst showed high roughness factor but the current densities did not reflect this large surface area indicating that only portions of the surface area are active. The closest Cu based system to the 3D printed electrocatalyst are Cu based foams.[160 214, 264] Ju et al (2018) reported that Cu foam showed high FE% for H_2 (>60%) from - 0.5 to - 1.0 V (RHE).[264] The prepared Cu foams were of C_{dl} ranging between 10-12 mF/cm^2.[264] The FE% of formic acid and CO did not exceed 20% at the same voltage range and CO almost disappeared after -0.6 V (RHE). The reported behaviour of the Cu foam is very close to that of the 3D printed OD-Cu foil except more products were reported in the case of the 3D printed OD-Cu electocatalyst. It is worth noting that in the case of 3D printed OD-Cu and OD-Cu foils showed volatile products especially at far negative voltages **(Table 4-2 and Table 4-4)**. The electrochemical setup was not optimised for collecting volatile products. The decline in the CE% at far negative voltages may be attributed to the evaporation of the volatile products **(Table 4-2 and Table 4-4)**.

Cu_3P and phosphide derived Cu based electrocatalyst exhibited high CE% for H_2 **(Table 4-2 and Table 4-4)** compared to any other products (CO and formic acid) suggesting their favourability toward HER over CO2RR. The idea behind the preparation of phosphide and oxide derived Cu based electrocatalyst was to form different types of active sites derived from two different Cu based binary compounds. The concept was simple, which is to electroreduce CO_2 in two steps (tandem system). If we can have an active sites can produce CO at low overpotential at (Cu_3P or PD-Cu active sites), CO may interact with OD-Cu active sites to enhance the formation of C_2 hydrocarbons. Unfortunately, the performance of the PD/OD-Cu electrocatalyst was affected by the nature of the copper phosphide and its favourability toward HER over CO2RR. It is reported that Cu_3P/C can electroreduce CO_2 into CO and H_2 with FE% about 47% for CO.[221] The mentioned system was not used in the proposed reactor as the reported FE% values were at low current density <0.5 mA/cm^2.[221]

4.3. Conclusions

Copper phosphide on Cu foil favours the electrochemical reduction of protons over the electrochemical reduction of CO_2 into carbon based compounds. Cu_3P/Cu foil showed conversion of CO_2 into HCOOH and the highest percentage did not exceed 10% at -0.6 V (RHE). The interaction between CO_2 and Cu_3P seems to be very weak and that was reflected in the appearance of traces of CO at different voltages.

3D printer as a technology can be used for building metal based electrocatalyst and it is a flexible tool that can be used to design different electrode using different ingredients and it can also be used in future in mass production of electrodes. 3D printing also can be an efficient tool to prepare rough electrodes with high roughness factor. The performances of the elecrocatalyst toward CO2RR were low. Phosphide derived electrode could convert CO_2 into formate and hydrogen exclusively with only traces of CO.

5. Oxygen evolution reaction

Aims

In order to complete the second half reaction of the water splitting system (OER) at the anode in neutral (and acidic media), an electrocatalyst was required for water oxidation. A CoPi electrode was chosen for this purpose as an inexpensive electrocatalyst that can operate efficiently in a neutral medium.

Introduction

Generally, there are many parameters that can be used to benchmark different electrocatalysts including overpotential ($\eta = E_{applied} - E^{o}$) where E^{o} is the standard potential for the desired electrochemical reaction, Tafel slope, exchange current density and stability. Thus the theoretical potential for overall water splitting equals 1.23 V. Any efficient and environmentally friendly electrochemical (oxidation-reduction) system should work under low energy demand (low overpotential value) using inexpensive available materials.[265] Platinum works as an electrocatalyst for HER and OER at low overpotential and high current density but its rarity and high cost limits its usage in such systems. There are different cheap materials like graphite that can be used for water oxidation but they require a high energy demand (high overpotential).

Different transition-metal based compounds have been investigated as electrocatalysts for OER such as transition metal oxides and hydroxides. Such compounds can operate safely in alkaline media but dissolve in acidic media. In the current project, we are working in acidic and neutral media. Nocera et al reported the CoPi film for the oxygen evolving reaction in a neutral medium.[238] The CoPi film is a catalytically active material that can be formed on the surface of inert conducting substrates like ITO, CC, SS etc. upon anodic polarization at >1.0 V (vs NHE) in potassium phosphate (KPi) buffer solution (pH 7) containing 0.5 mM Co^{2+} salts.[238] CoPi has a low onset potential in neutral medium. Such activity is very useful and can minimize the energy demand for the suggested mini-reactor. The pH dependence of the catalytic performance suggested that the hydrogen phosphate anions act as proton acceptors.[266] Several studies have been used to elucidate the structure of CoPi films. Cobalt K-edge extended X-ray absorption fine structure (EXAFS) studies spectra suggested that CoPi contains edge-sharing molecular cobaltate clusters (MCCs) with the minimal structural unit shown in **(Figure 5.1 and Figure 5.2)**.[267]

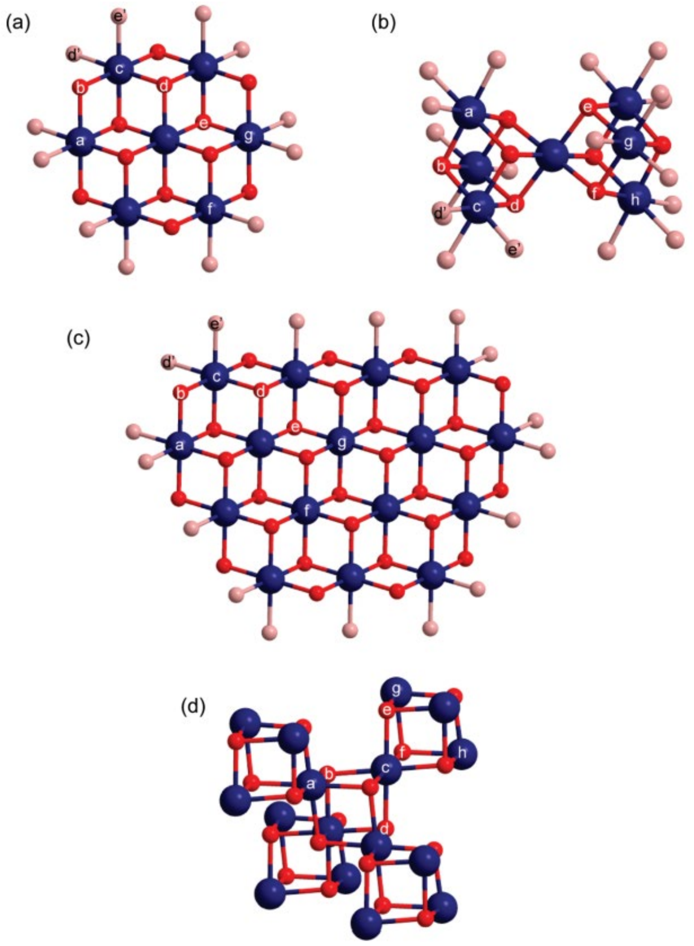

Figure 5.1: Structural models for CoPi (a) Edge-sharing molecular cobaltate cluster (MCC) of CoPi films deposited at 1.1 V (surface). Bridging oxo/hydroxo ligands are shown in red, and non-bridging oxygen ligands (including water, hydroxide, and phosphate, light red) complete the octahedral coordination geometry of each peripheral Co ion (blue). (b) Corner-sharing model for surface, (c) edge-sharing MCC for bulk CoPi and (d) Corner-sharing model for CoPi bulk. [268]

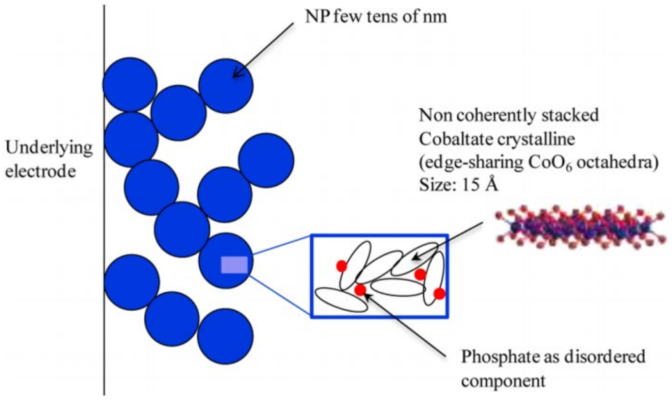

Figure 5.2: Structural sketch of CoPi films.[269]

In the current project, the hydrogen evolution reaction were performed in acidic and neutral media. In an acidic medium, there are plenty of compounds that can operate as cathode efficiently for HER. There are few examples for transition metal compounds that can work as anode (for water oxidation) in acidic medium such as Co_3O_4, MnO_x, $Co_2P/NiCo_2O_4$, $CoMnO_x$ and WC.[270, 271] These electrocatalysts suffer either from high onset potential, lack of long-term stability or both of them.

Table 5-1: Different non-noble electrocatalysts for OER in acidic and neutral media[270].

Electrocatalyst	medium	η_{10} (V)	Stability	Comments
CoPi/SS	0.1 M KPi	η_1= 0.41		
Co_3O_4 [272]	0.5 M H_2SO_4	0.570	12	
Co/CoP[273]	1.0 M PBS	1.51	12	E = 1.41 at 1 mA/cm^2
CoP@CoBiPi	0.1 M KBi			E = 1.35 at 1 mA/cm^2
MnO_x[274]	pH = 2.5	600		
CoP NA/CC[275]	1.0 M PBS 0.5 M H_2SO_4		1000 CV cycle	E = 1.55 at 1 mA/cm^2 E = 1.90 at 1 mA/cm^2
Co_2P/ $NiCo_2O_4$ [270]	1 M H_2SO_4	1.58	30 h	E = 1.25 at 1 mA/cm^2
$CoMnO_x$	pH = 2.5		50 h	b =70-80 mV/dec
N doped WC/ CFP[271]	0.5 M H_2SO_4	1.45	1.0 h	
NiFeP[276]	1.0 M H_2SO_4	η_{10} = 540	30 h	

Some data (overpotential were taken from figures). Stability tests were taken directly from the article as reported by the authors. CFP: carbon fibre paper, CC: carbon cloth, NA: nanoarrray.

In the current project, a chemical reactor was built in order to couple electrocatalysis (water electrolysis and CO2RR) and catalysis (hydrogenation and hydroformylation) steps within one setup. Water electrolysis is a clean and efficient source of hydrogen. The overall water splitting (electrolysis) system includes two processes; oxygen evolution reaction (OER) and hydrogen evolution reaction (HER). In an acidic medium, water oxidation occurs at the anode $H_2O \rightarrow 2H^+ + 2e^- + \frac{1}{2}O_2,\ E^o = 1.23\,V\,(NHE)$ and proton reduction at cathode $2H^+ + e^- \rightarrow H_2, E^o = 0\,V\,(NHE)$.

The main criteria of choosing the electrocatalyst for water oxidation were:

1- Electrocatalyst based on inexpensive earth abundant metals.
2- Operate in water in neutral and acidic media. (HER was performed in neutral and acidic media while CO_2 was performed in neutral medium only).
3- Ease to prepare
4- Efficient and stable electrocatalyst that can operate for at least 6-8 h.

For the hydrogenation reaction of styrene, FeP/CC prepared by electroplating was chosen as cathode for hydrogen evolution reaction through water electrolysis in acidic and near neutral media. CoPi/SS electrode was chosen as anode for water oxidation reaction at the anode in near neutral medium. For the hydroformylation of styrene, Au foil was chosen as cathode for the electrochemical production of H_2/CO via CO2RR. CoPi/SS was chosen as anode for water oxidation reaction at the anode in 0.1 M $KHCO_3$.

5.2. Results and discussions

The CoPi film was prepared on stainless steel mesh by applying 1.0 V vs Ag/AgCl for a certain time to achieve a charge density ranging between 50-60 mC/cm^2, this potential is sufficient to oxidize the surface Co^{2+} to Co^{3+} **(Figure 5.3)**.[7, 266, 267, 277]

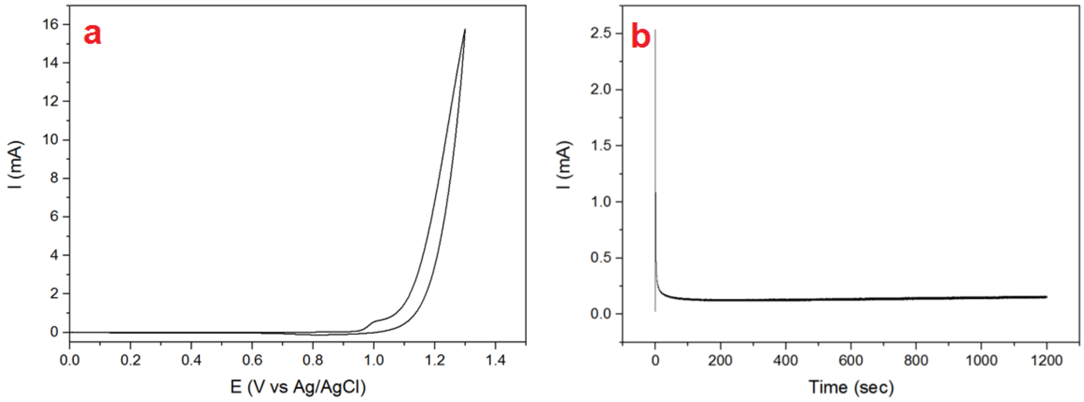

Figure 5.3: (a) Cyclic voltammogram in 0.1 M KPi electrolyte at pH 7.0 with 0.5 mM Co^{2+} present on SS (b) CA experiment in 0.1 M KPi electrolyte at pH 7.0 containing 0.5 mM at 1.1 V (Ag/AgCl).

The prepared electrode was characterized by SEM and EDX. SEM images **(Figure 5.4)** of CoPi prepared on stainless mesh (CoPi/SS) confirmed the formation of a layer of electrocatalyst. The EDX spectrum of CoPi/SS **(Figure 5.5)** and elemental mapping **(Figure 5.6)** confirmed the existence of Co, K and P elements but with different percentage on each substrate (*i.e.* Kanan et al reported; Co: 31.1 %, P:7.70 % and K: 7.71 %). A cyclic voltammogram **(Figure 5.3)** showed the existence of sharp oxidation waves due to oxygen evolution reaction.

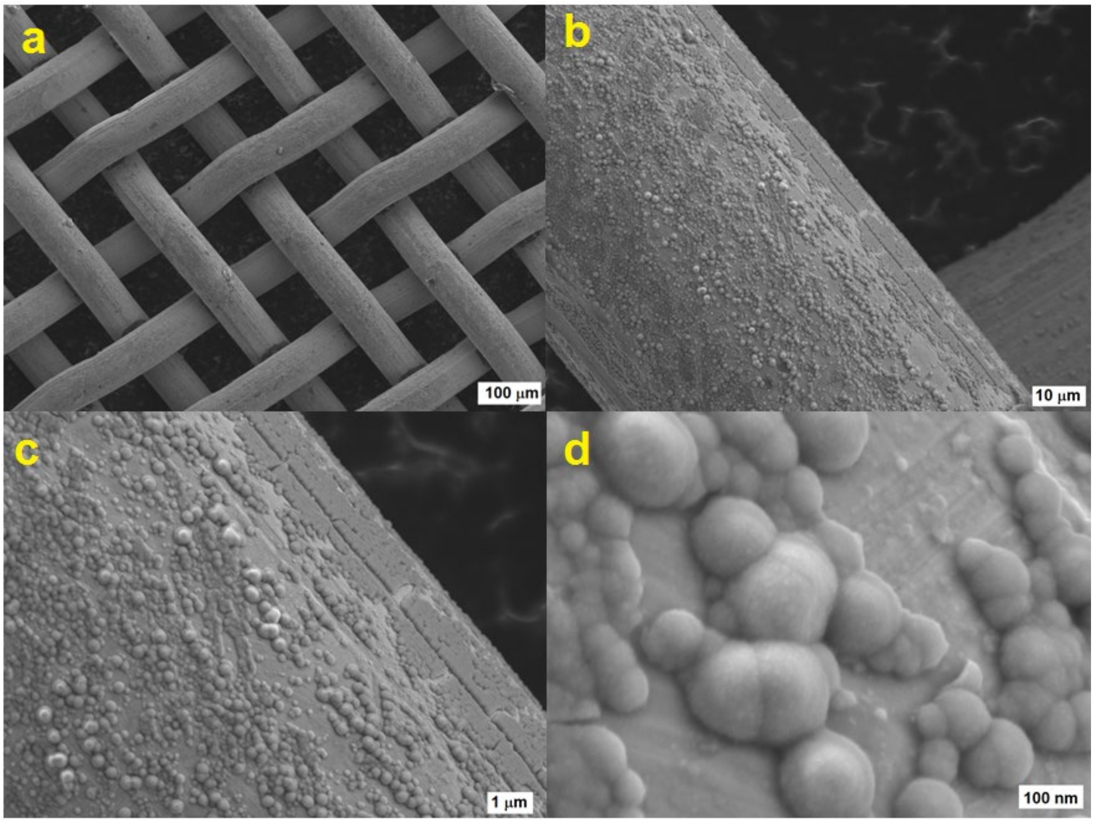

Figure 5.4: SEM images of CoPi/SS (a-c) and CoPi/CC (d-f).

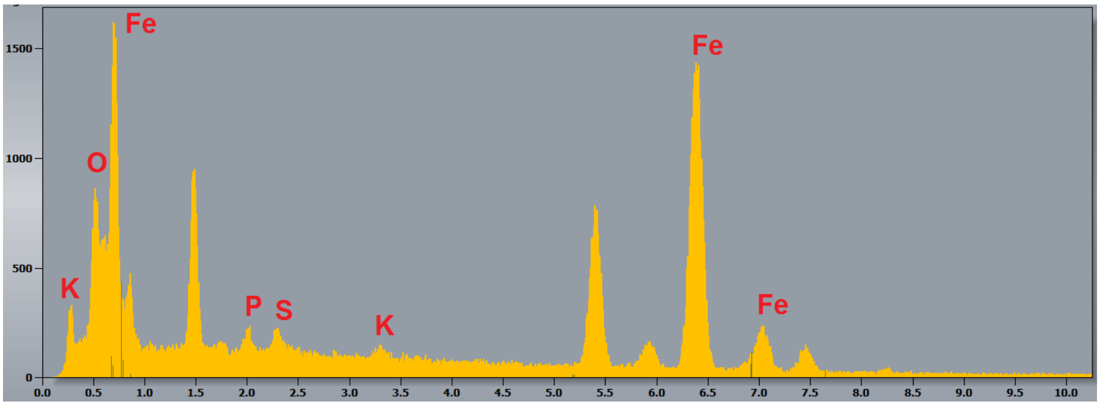

Figure 5.5: EDX spectrum of CoPi/SS (% Co: 1.32 %, % Fe: 89.56 %, % K: 0.76 %, % O: 7.20 % and % P: 1.16 %).

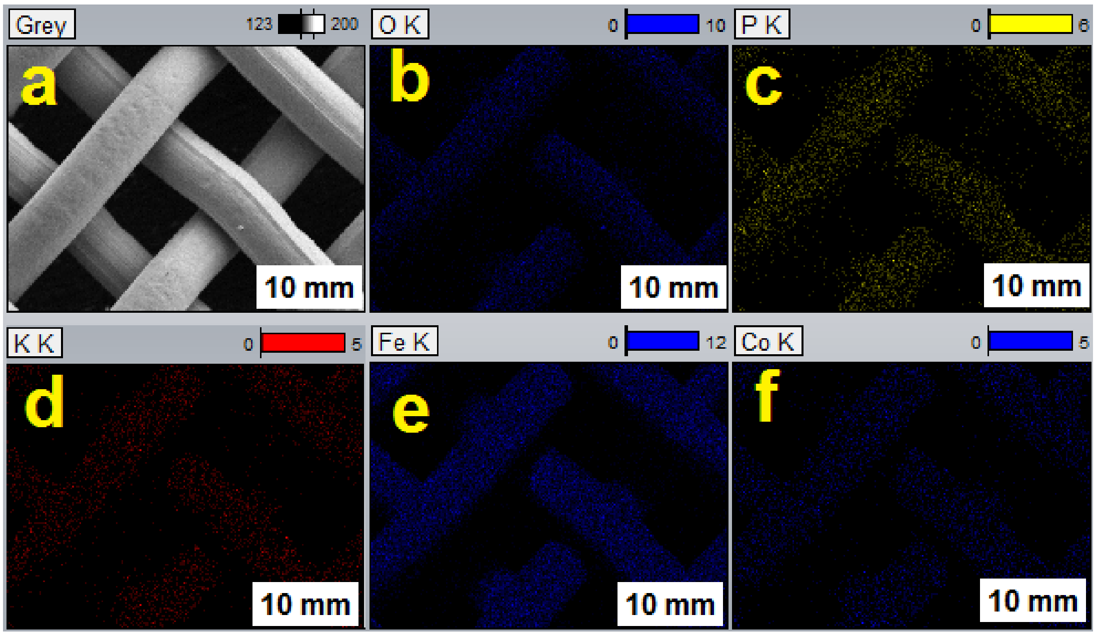

Figure 5.6: (a) SEM of the top-down of CoPi/SS), (b) the distribution of O, (c) the distribution of P, (d) the distribution of K, (e) the distribution of Fe and (f) the distribution of Co by the K-shell absorption.

According to the LSV experiments **(Figure 5.7 - Figure 5.10)**, in neutral medium, the overpotential required to maintain 31 mA/cm^2 (for the reactor experiments) by CoPi/SS and blank CC were 0.88 and 1.27 V, respectively. The two values are relatively high as the medium is neutral and CC is without electrocatalyst **(Figure 5.9)**. The overpotential required by CoPi/SS in 0.1 M $KHCO_3$ was 1.15 V to afford 20 mA/cm^2 **(Figure 5.8)**. In an acidic medium, the overpotential required to support the system with 31 mA/cm^2 was 0.86 V upon using blank CC and 0.97 V upon using carbon plate in 0.5 M H_2SO_4 **(Figure 5.7 and Figure 5.8)**. The required voltages are relatively high in all cases.

For the hydrogen evolution reaction in acidic medium (0.5 M H_2SO_4), blank carbon plate was chosen to work as counter electrode in the reactor as the required voltage is not too high if we considered the fact it does not support any electrocatalyst. Carbon cloth was not chosen as the prosity of the carbon cloth casue to the diffuision of electrolyte solution up to the crocodile clip casuing its oxidation in addition to the water oxidation. Carbon plate also lacks porosity that causes connections problems (corrosion of the crocodile clips) within the reactor in the preliminary trials. No electrocatalyst was prepared for OER in acidic medium (0.5 M H_2SO_4) as most of the reported electrocatalyst suffer either from low stability or operated at relatively high overpotential. For the hydrogen evolution reaction in near neutral medium (0.1 M KPi), CoPi/SS was chosen as a counter electrode to operate in 0.1 M KPi, in the preliminary work, CoPi/SS was efficient for oxygen evolution reaction and operated for 6 h without any significant changes.

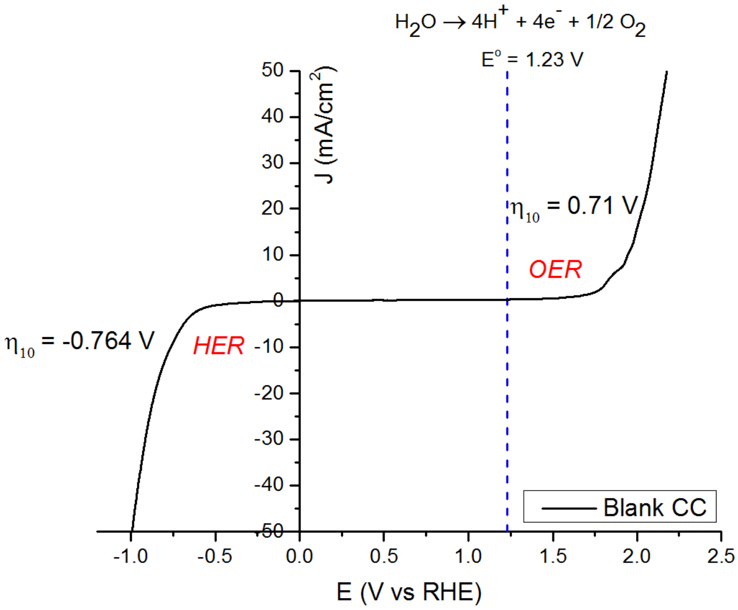

Figure 5.7: LSV of carbon cloth in 0.5 M H_2SO_4 at scan rate of 20 mV/s.

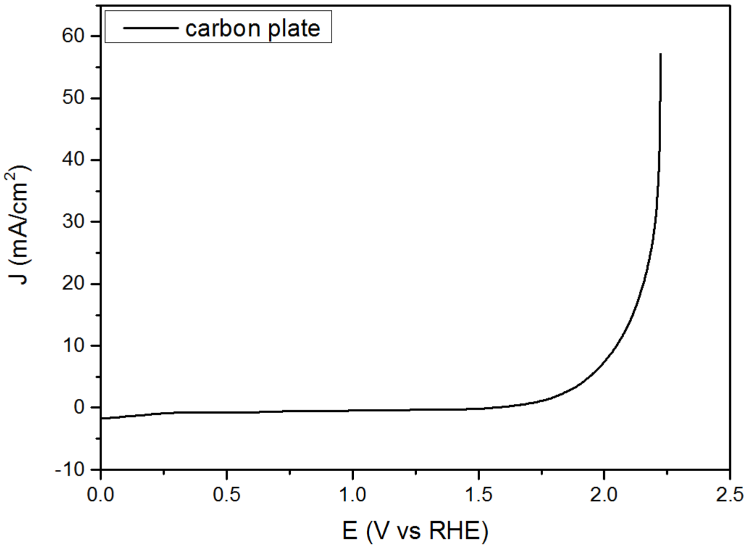

Figure 5.8: LSV of carbon plate in 0.5 M H_2SO_4 at scan rate of 20 mV/s.

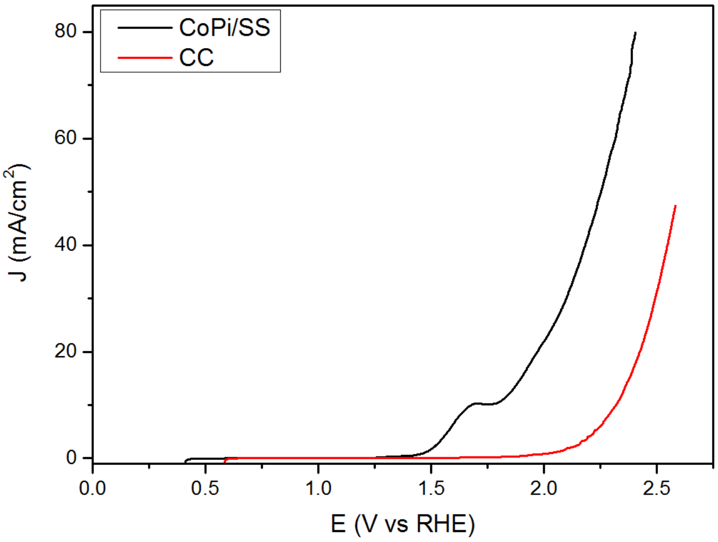

Figure 5.9: LSV of CoPi/SS and blank carbon cloth in 0.1 M KPi (pH=6.63) at scan rate of 20 mV/s.

For CO2RR, gold was chosen as a cathode as the prepared Cu based electrocatalysts did not give 1:1 ratio between CO:H_2 required for the chemical reactor. In 0.1 M $KHCO_3$, CoPi/SS was chosen to act as anode in the proposed reactor. CoPi/SS operate at a relatively high voltage for 20 mA/cm^2 as it operates in neutral medium which affect the kinetics of the water oxidation.

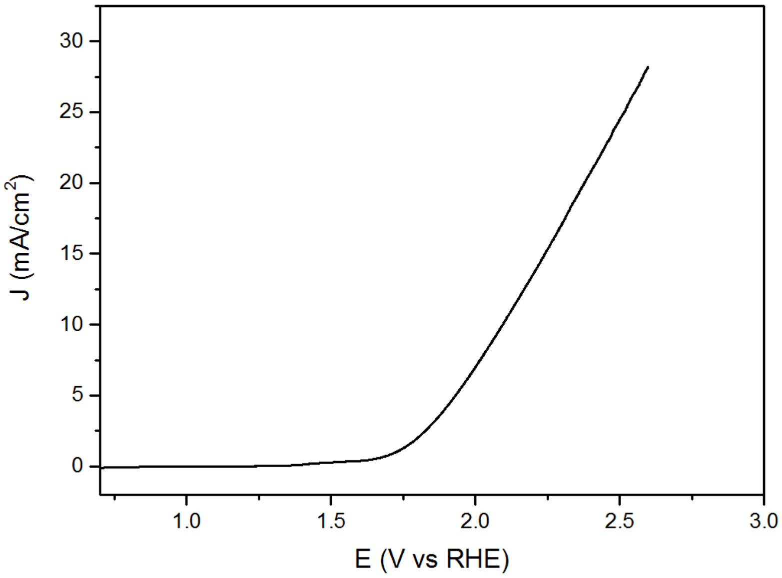

Figure 5.10: LSV of CoPi/SS plate in 0.1 M $KHCO_3$.

5.3. Conclusion

The CoPi/SS electrocatalyst for oxygen evolution reaction was chosen for the reactor to operate in 0.1 M KPi and in 0.1 M $KHCO_3$ for the HER and CO2RR experiments, respectively.

For HER in acidic medium, the capillary phenomenon caused problems upon using blank carbon cloth, thus carbon plate was chosen to work in reactor as anode (OER) in acidic medium (0.5 M H_2SO_4). For HER in near neutral medium, CoPi/SS was chosen for the reactor.

For the CO2RR setup, CoPi/SS was chosen also to work as anode in 0.1 M $KHCO_3$.

6. Water-tolerant, low pressure catalytic hydrogenation and hydroformylation of alkenes

Aims

The aim of this part of the project is to find catalytic systems that can perform hydrogenation and hydroformylation reactions in the proposed reactor. The criteria for choosing the catalysts were the following: operate under atmospheric pressure, be water-tolerant, and air insensitive. For hydroformylation, tolerance to CO_2 is also required. An important distinction is that in the proposed reactor hydrogenation will occur in a closed system whereas hydroformylation will occur under continuous flow.

For hydrogenation reaction, we tried to develop a new catalytic system [Ru@[MIL-101(SO3H)] based on $[Ru(PTA)_2Cl_2]$ and MOF. For hydroformylation reaction, Rh/6-DPPon system developed by Breit et al[15] was chosen to work in the proposed reactor.

Abstract

A new catalytic system was developed for the hydrogenation of alkene based on [Ru@[MIL-101(SO3H)]. The prepared catalyst was characterized and the catalytic activity was investigated, however at 1 atm H_2 the catalytic performance was too low. Therefore a commercial Pd/C (5%) catalyst was investigated and shown to be suitable for hydrogenation at room temperature and 1 atm H_2. For hydroformylation, Rh/6-DPPon showed the expected catalytic activity under an atmosphere of 1:1H_2 and CO as reported in the literature. In the presence of CO_2, the percentage of conversion of styrene to the corresponding aldehydes was about 53 % after h 8.

6.2. Results and discussions

6.2.1. Preparation of Ru@MOF catalyst for the hydrogenation of alkenes

Introduction

Hydrogen is a clean source of energy as it gives water as the only chemical product of its combustion according to the following equation: $2\ H_{2(g)} + O_{2(g)} \rightarrow 2\ H_2O_{(l)}$ + 286 kJ/mol. Hydrogen gas is highly flammable and can ignite in air starting from low concentrations (4 % by volume).[278] There are many catalytic reaction processes include the usage of hydrogen gas such as hydrogenation [9] and hydroformylation.[279] Such processes, in most cases, require high pressure of hydrogen; high pressure raises the risk of explosion of the reactor due to its high flammability. Working under low pressure of hydrogen can minimize such risk. Hydrogenation reaction is one of the best known processes based on metal complexes in organic chemistry and in industry.[280] Recently, two systems have been reported for hydrogenation reaction of alkenes (under 1 atm of H_2) based on a MOF $\{Cr_3(H_2O)_3O[(O_2C)C_6H_3(SO_3H)(CO_2)]_2[(O_2C)C_6H_3(SO_3)(CO_2)]\}\cdot nH_2O$ [MIL-101 (SO3H)] **(Figure 6.1)**.[240, 241] Takashima et al used Wilkinson's catalyst to prepare their hybrid system **(Figure 6.1)** while Rosseinsky used Crabtree's catalyst for their system **(Figure 6.2)**. Regarding our mini-reactor, the plan is to design a mini-reactor that can perform hydrogenation reaction of alkenes under 1 atm at room temperature. There are many reported systems that can fulfil this role but most of them are water and air sensitive.[281-285] The current project aims to make hydrogenation reaction system as simple as we can: a system that is water tolerant is not very air sensitive and can perform hydrogenation at low pressure. During hydrogen evolution reaction (HER) at a cathode electrode ($4H^+ + 4e^- \rightarrow 2H_2$, E° = 0.00 V vs. NHE). Water oxidation takes place at the anode electrode ($2H_2O \rightarrow 4H^+ + 4e^- + O_2$, E° = 1.23 V vs. NHE). The flow of oxygen gas from electrocatalytic cell into the catalytic reaction tube can kill the catalytic activity. Separating anode and cathode using Nafion membrane can maintain the activity. The hydrogen evolution reaction usually takes place in aqueous media (acidic, neutral and basic media) which may conflict the requirements of the hydrogenation reaction. In order to avoid such problem, drying the produced gases using a membrane may complicate the mini-reactor and increase the cost of the mini-reactor. Working with a catalytic system with relatively low water sensitivity may solve such problem. In order to have a system that is water tolerant and can do hydrogenation reaction, ruthenium complexes based on the PTA ligand have been chosen **(Figure 6.3)**. In the current project, we propose the preparation of one system combining [MIL-101(SO3H)] and [CpRu(PTA)$_2$Cl] to do hydrogenation at low pressure. MIL-101 is stable over months under an air atmosphere and stable also in various organic solvents at room temperature or under solvothermal conditions. [MIL-101(SO3H)] possesses two large pores of diameters 2.9 and 3.4 nm and their apertures of dimensions 1.2 × 1.3 and 1.4 × 1.5 nm, respectively **(Figure 6.1)**.[240, 242] The pores sizes can accommodate [CpRu(PTA)$_2$Cl] which has dimensions of ca. 1.04 x 0.65 nm.[243] [MIL-101(SO3H)] shows also high thermal (up to 270 °C) and chemical stability.[286] [MIL-101] MOFs generally exhibit excellent stability against moisture and other chemicals; water molecules can be removed under vacuum or by heating up to 423 K.[287] Such properties as well as its high adsorption capacities, make MIL-101 an efficient MOF to accommodate metal complexes.[242] Such a system may be able to catalyse the reaction and be water tolerant as the complex is water soluble. The ruthenium complex itself can do hydrogenation reaction under 30 bar of hydrogen gas.[244] The hydride form of the same complex can do the same reaction at relatively lower pressure (4 bar).[243, 288] In such a system, we will start with the chloride form of the complex and the corresponding hydride form might be prepared *in-situ* and do the hydrogenation reaction. There are two ways to couple $[CpRu(PTA)_2Cl]$ with MIL-101(SO3Na); in the first one both of them are heated together in acetonitrile under Ar and coupling may take place through ligand exchange. In the second option $[CpRu(PTA)(PTAH)Cl](PF_6)$ is prepared instead of $[CpRu(PTA)_2Cl]$ and coupling may happen through cation exchange with Na^+ ions. In the current project, heating the materials together was chosen for this purpose.

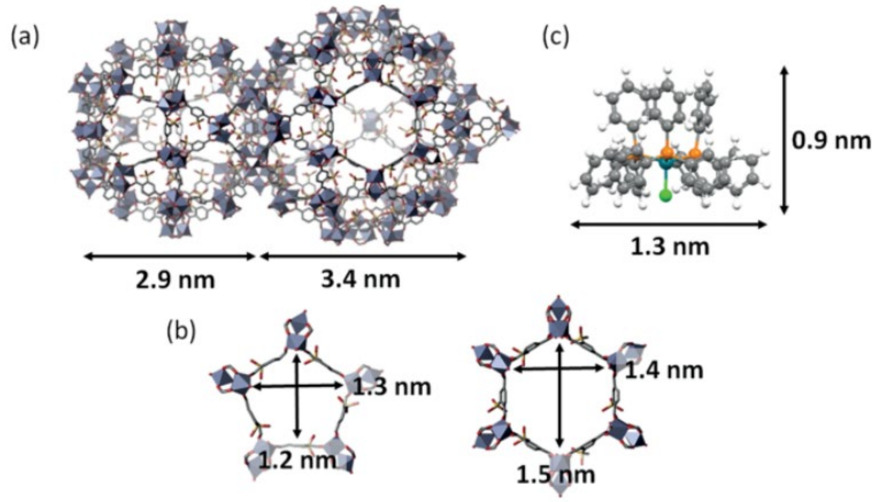

Figure 6.1: Structures of (a) MIL-101(SO3H) pores, (b) their pore apertures, and (c) Wilkinson's catalyst.[240]

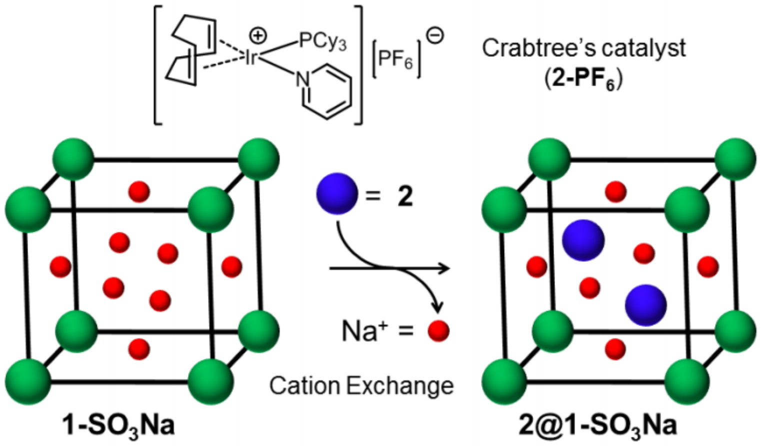

Figure 6.2: Interaction between Crabtree's catalyst (blue sphere) and sulfonated MIL-101(Cr) (1-SO3Na, cube) by exchange of the charge-balancing Na^+ cations (red sphere).[241]

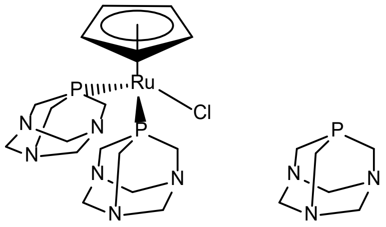

[CpRu(PTA)$_2$Cl] **PTA**

Figure 6.3: Structures of [CpRu(PTA)$_2$Cl] complex and PTA ligand.

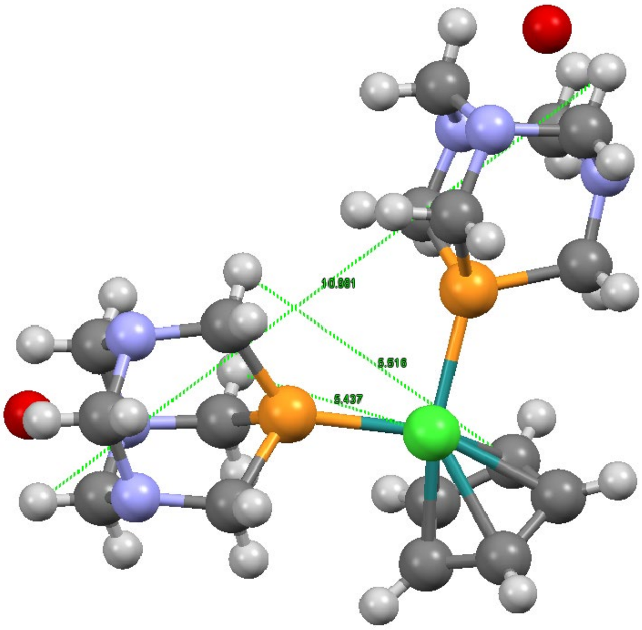

Figure 6.4: [CpRu(PTA)$_2$Cl] complex's dimensions.[243]

6.3. Results and discussions

NMR (^{1}H, ^{13}C and ^{31}P) spectra were used to characterize the prepared compounds (6-DPPon ligand and its precursors, [CpRu(PTA)$_2$Cl]) and [Rh(CO)$_2$(acac)]) and the spectral data are in good agreement with reported ones **(Experimental chapter p. 75 and Appendix-2)**.

Physical characterization of MIL-101(SO3H)

Regarding the Ru@MOF catalyst, the XRD **(Figure 6.5)** and TGA analysis **(Figure 6.6)** confirmed the formation of the desired MOF (MIL-101(SO3H). The elemental analysis of the prepared MOFs **(Table 6-1)** were measured with precise percentage for C and H and the percentage of S was less than the expected value, ICP-OES analysis is required for the analysis of Na, Ru and Cr metals in the prepared MOFs to confirm the molecular formula and the molecular mass. The BET measurements confirmed **(Table 6-2)** that the MIL-101(SO3H) and MIL-101(SO3Na) have high porosity with BET surface area = 1524.20 and 1563.11

m^2/g, respectively. The reported values were lower than the values reported by Rosseinsky et al[241] (2005 m^2/g for MIL-101(SO3H) and 1805 m^2/g for MIL-101(SO3Na)). The difference may reflect the difference in the pore volume for MIL-101(SO3H) it was 0.71 cm^3/g and for MIL-101(SO3Na) it was 0.72 cm^3/g while Rosseinsky et al[241] reported that 0.82 cm^3/g for MIL-101(SO3H) and 0.91 for MIL-101(SO3Na). It is not obvious why there is a difference between the reported values and measured ones, further investigation are required to study pore size.

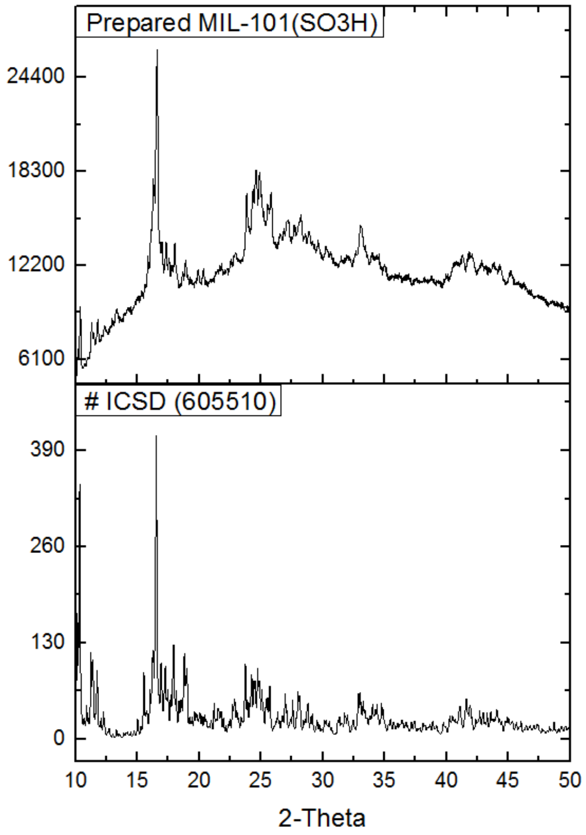

Figure 6.5: XRD pattern of MIL-101(SO3H).

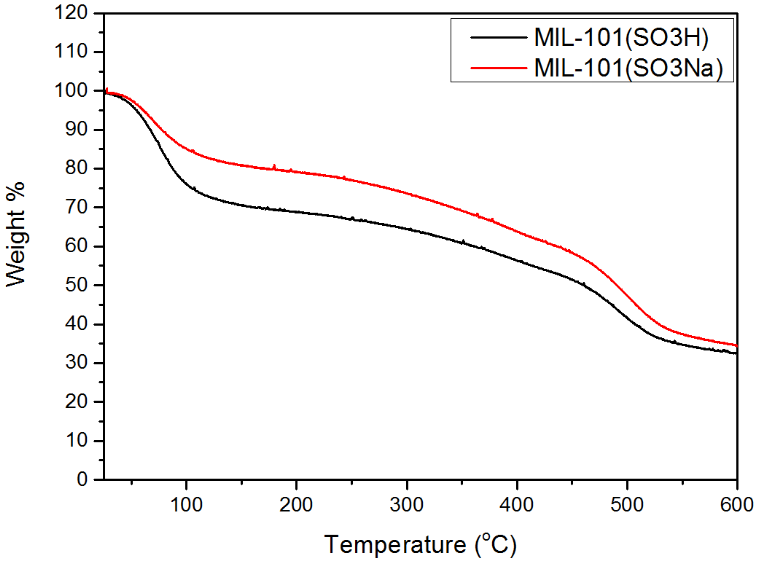

Figure 6.6: TGA of all MOFs.

Table 6-1: Elemental analysis of each MOF ([a] from CHN, S elemental analysis).

Element %	**MIL-101(SO3H)** $[H_{1.8}Na_{0.2}][Cr_3(\mu_3\text{-}O)(BDC\text{-}SO_3)_3].12(H_2O)$ $\mathbf{Cr_3C_{24}S_3O_{34}H_{34.8}Na_{0.2}}$ (M. wt. = 1124.6)		**MIL-101(SO3Na)** $[H_{0.2}Na_{1.8})][Cr_3(\mu_3\text{-}O)(BDC\text{-}SO_3)_3].12(H_2O)$ $\mathbf{Cr_3C_{24}S_3O_{34}H_{34.8}Na_{1.8}}$ (M. wt. = 1160.18)	
	Experimental	**Theoretical**	**Experimental**	**Theoretical**
C% [a]	25.10	25.61	25.14	24.8
H% [a]	3.68	3.10	3.03	3.00
S% [a]	5.30	8.55	6.61	8.27
Cr%	-	13.87	-	13.44
Na%	-	0.41	-	3.56

Table 6-2: BET surface area measurements of all prepared MOFs. *reported by Rosseinsky et al.[241]

Compound	**MIL-101(SO3H)**	**MIL-101(SO3Na)**
BET (m²/g)	1524.20 (1805)*	1563.11 (2005)*

Different characterization techniques were used including XRD, BET, elemental and thermal analyses were used to prove the formation of MIL-101(SO3H). No evidence supported the formation of the Ru@MOF catalyst. Further analyses are required to prove the formation of the catalyst. We decided to use Pd/C (5 %) for two reasons; first one that the time was not enough for the complete set of analysis and the second reason was that the catalytic activity was very weak and the catalyst cannot be used in the proposed reactor.

6.3.1. Catalysis

The determination of conversion percentage/ratio of hydroformylation and hydrogenation reactions was calculated through the integration of the ^{1}H-NMR spectra. In preliminary experiments, the catalytic reaction under the standard procedure reported in literature gave the expected results; full conversion of styrene into the expected products within the same time interval. Hydrogenation of styrene was performed using two catalytic systems: Ru@MOF and Pd/C (5%) in methanol while the hydroformylation of styrene was performed using Rh/6-DPPon catalytic system in water/surfactant (PTS) system. The surfactant was added because the styrene is not miscible with water; without a surfactant the styrene would be in a different layer (phase) on the top of the aqueous layer.

For the hydrogenation reaction of styrene using Ru@MOF catalyst, a weak catalytic activity was observed in DCM. For the hydrogenation reaction of styrene using Pd/C (5 %) within 12 h under H_2 balloon. For the hydroformylation reaction of styrene, the full conversion of styrene into the corresponding aldehydes occurred after 20 h under syngas (CO/H_2) balloon.

6.3.1.1. Test reactions for hydrogenation using (Ru@MOF and Pd/C)

The results of the hydrogenation reactions are tabulated in **(Table 6-3)**. The catalytic activity of the prepared catalyst (Ru@-MIL-101(SO3H) was very low under a H_2 balloon (about 2-3%) after 24 h **(Figure 6.7)**. Apparently, the catalyst requires a high pressure of hydrogen for efficient hydrogenation reaction. Upon using Pd/C (5%) catalyst under the standard conditions, the percentage of conversion of styrene to ethylbenzene was 100% within 12 h under a H_2 balloon **(Figure 6.8)**. The standard method included working under H_2 balloon for 12 h, 1 mol % of Pd and 1.15 mmole of styrene in 1.5 mL of methanol. Under standard conditions (H_2 balloon) only 42% of styrene was converted into ethylbenzene after 4 h of the reaction **(Figure 6.9)**.

Table 6-3: Summary of the results of the two hydrogenation reaction systems.

Starting conditions of the catalytic reactions (gas source)	**Solvent/ catalysis duration**	**Results and comments (Conversion percentage of styrene to the expected products)**
Ru@MOF (H_2 balloon)	DCM/ 24 h	About 2-3% conversion to ethylbenzene **(Figure 6.7)**
Standard system (Pd/C) (H_2 balloon)	CH_3OH/ 12 h	About 100 % conversion of styrene to ethylbenzene [a] **(Figure 6.8)**
Standard system (Pd/C (H_2 balloon)	CH_3OH/ 4 h	About 42 % conversion of styrene to ethylbenzene [a] **(Figure 6.9)**

[a] The percentage of conversion was determined by integrating the 1H-NMR spectra.

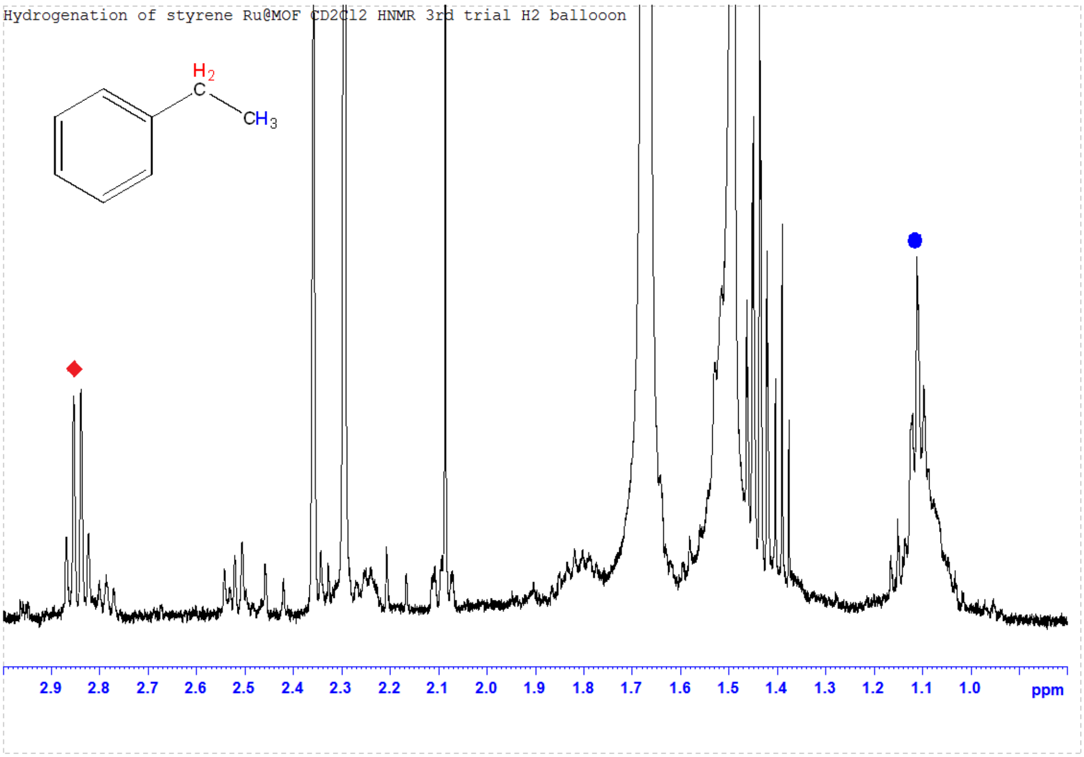

Figure 6.7: Hydrogenation of styrene using [Ru@MOF] catalyst under H_2 balloon.

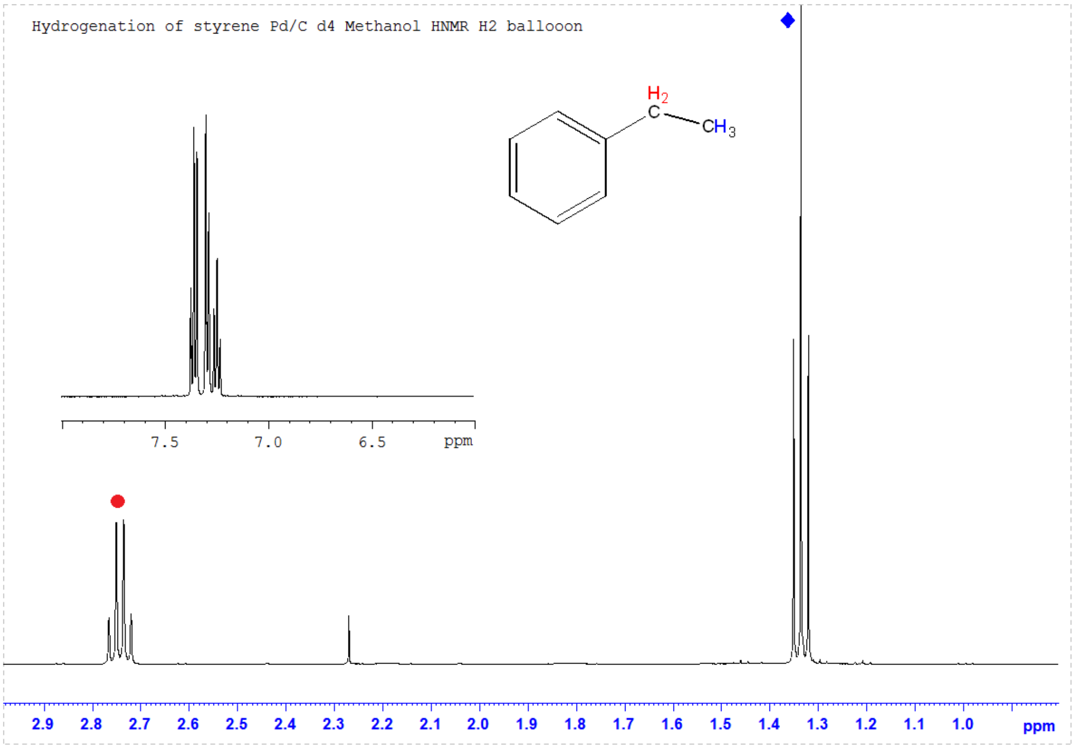

Figure 6.8: ^{1}H-NMR (MeOD-d_4) spectrum of products of hydrogenation of styrene under 1 atm of H_2 gas (Balloon).

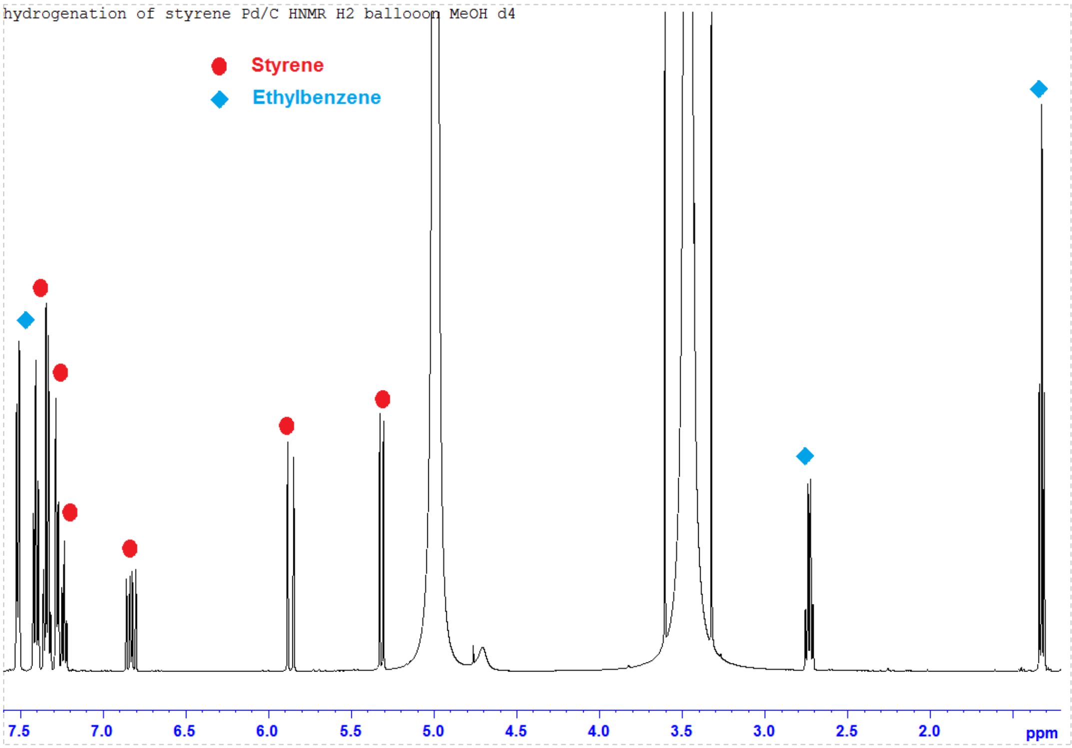

Figure 6.9: ^{1}H-NMR (MeOD-d_4) spectrum of products of hydrogenation of styrene under 1 atm of H_2 gas (balloon) for 4 h.

6.3.1.2. Test reactions for hydroformylation in water and tolerance to CO_2

All the results of the hydroformylation reaction using Rh/6-DPPon in PTS/H_2O are tabulated in **(Table 6-4).** Under the reported standard conditions, full conversion (about 100%) of styrene to the corresponding aldehydes (2-phenylpropanal and 3-phenylpropanal) was observed as expected without the existence of any peaks belong to styrene **(Figure 6.10)**. Conversion was measured through integrating peaks of the ^{1}H-NMR spectra.

It is worth noting that the ratio between the branched and linear aldehydes ranged between 54 - 59% in all experiments reported in the thesis while the reported percentage by Breit et al was 78 % for the branched aldehyde.[16] Further investigations are required to clarify the reason behind the difference between ratios between the linear and branched aldehydes.

Table 6-4: Summary of the results of the two hydroformylation systems.

Starting conditions of the catalytic reactions (gas source)	**Solvent/ catalysis duration**	**Results and comments (Conversion percentage of styrene to the expected products)**
Standard system (CO/H_2 balloon) (1.0 wt% of PTS)	H_2O/ 24 h	About 100 % conversion of styrene converted to 2-phenylpropanal and 3-phenylpropanal [a] **(Figure 6.10)**
Low partial pressure of CO/H_2 under CO_2 (1.0 wt% of PTS) (CO/H_2 and CO_2 balloons)	H_2O/ 20 h	About 28% of styrene converted to 2-phenylpropanal and 3-phenylpropanal **(Figure 6.11)** [a]
Increasing the wt% of PTS to 3% (CO_2 and CO/H_2 balloons)	H_2O/ 8 h	About 53% of styrene converted to 2-phenylpropanal and 3-phenylpropanal [a] **(Figure 6.12)**
Increasing the wt% of PTS to 3% (CO_2 and CO/H_2 balloons) with silicone oil	H_2O/ 8 h	About 10 % of styrene converted to 2-phenylpropanal and 3-phenylpropanal [a] **(Figure 6.13)**

[a]: ^{1}HNMR was used to detect the products and conversion percentages. All the solvents were used without any drying.

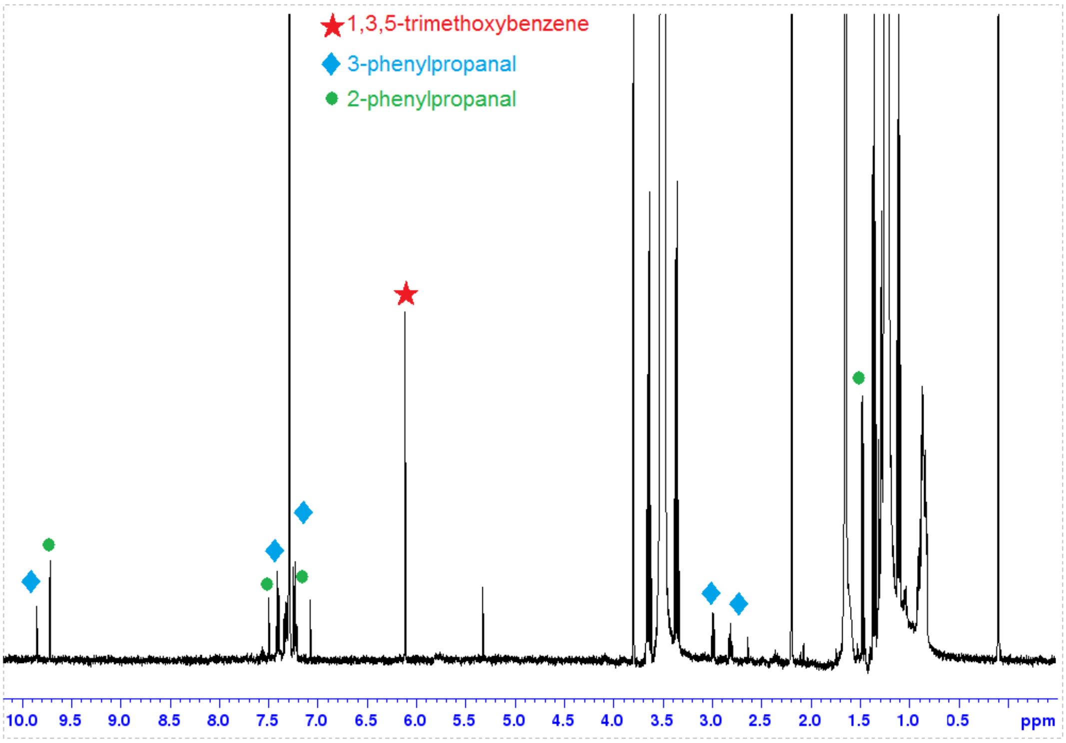

Figure 6.10: ^{1}H-NMR ($CDCl_3$) of products of the hydroformylation reaction of styrene under 1 atm of syngas under standard conditions.

Upon using CO_2 balloon in addition to syngas balloon (wt% of PTS was 1%) for 20 h, the styrene conversion was about 28% **(Figure 6.11)**. Increasing the wt% of the surfactant (PTS) to 3% enhanced the percentage of conversion to about 53% **(Figure 6.12)** with the existence of CO_2 balloon. In the proposed reactor, the continuous flow of CO_2 is required for CO2RR. The hydroformylation of styrene was performed under CO_2 atmosphere only to investigate the effect of CO_2 and no aldehydes were observed at the end of the reaction. The result suggested that there is no role by CO_2 in the catalytic reaction and the flow of CO_2 in the proposed reactor will not affect/interfere the hydroformylation reaction.

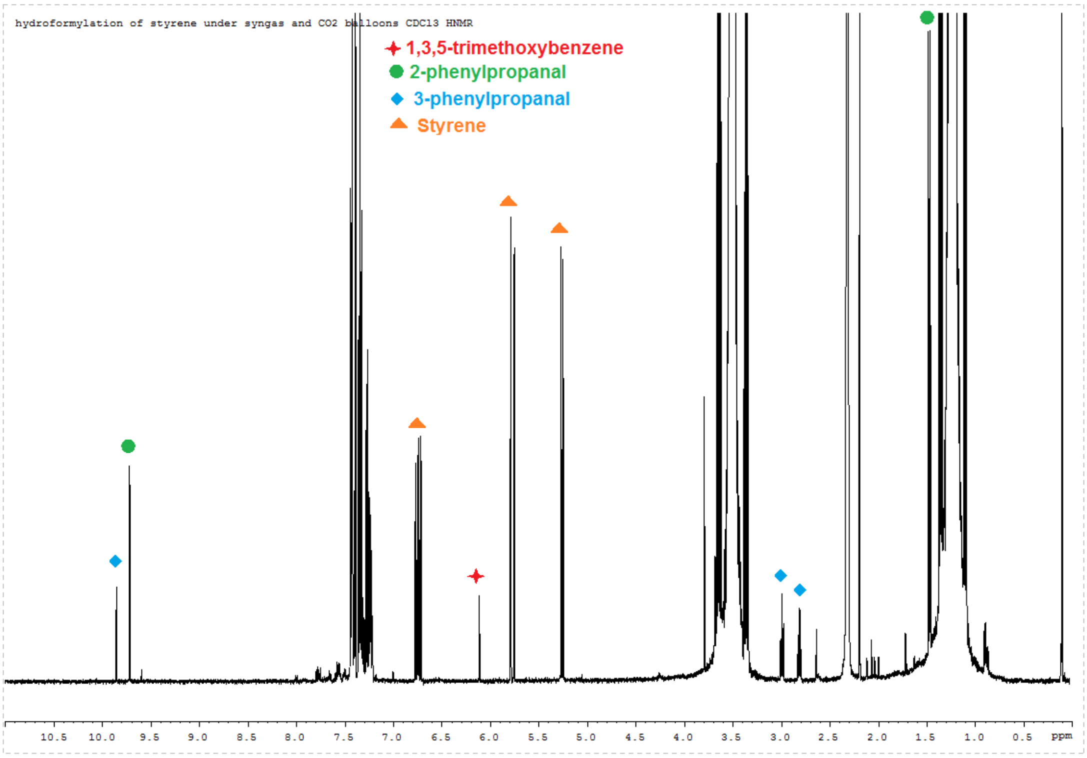

Figure 6.11: ^{1}H-NMR spectrum of products hydroformylation reaction of styrene under CO/H_2 and CO_2 balloons for 20 h.

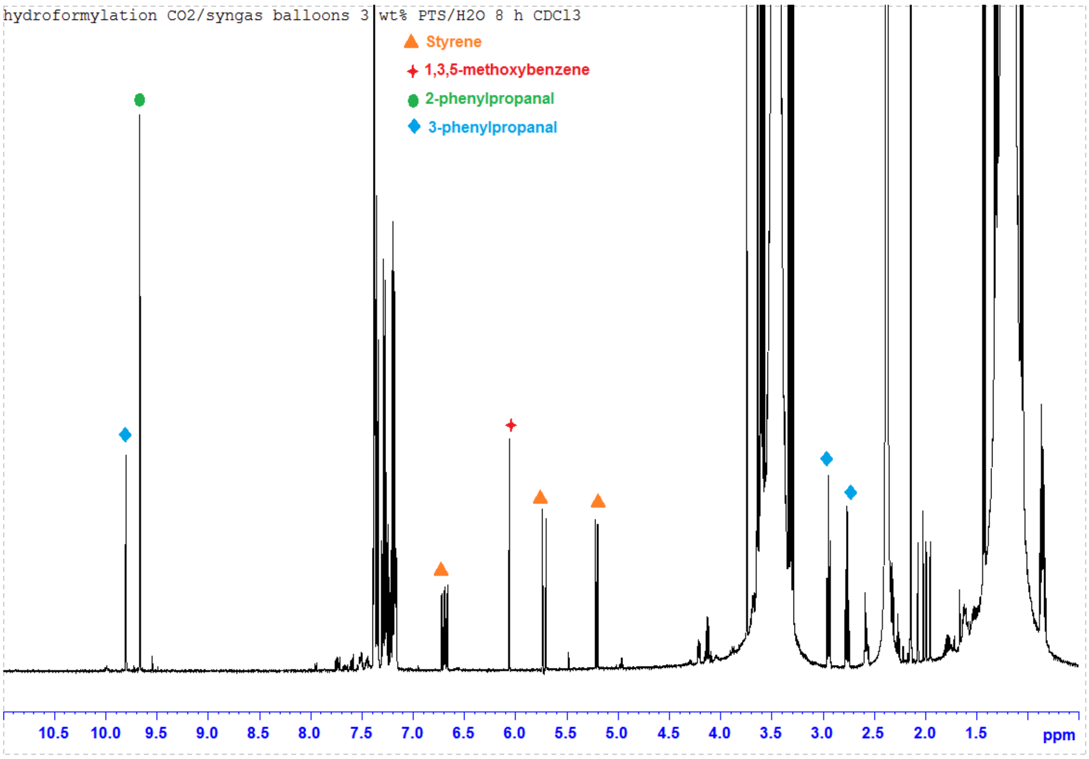

Figure 6.12: ^{1}H-NMR ($CDCl_3$) spectrum of products hydroformylation reaction of styrene under CO_2 and CO/H_2 balloons for 8 h in 3% (wt%) of PTS/H_2O.

In the proposed reactor, the electrocatalytic reduction of CO_2 required a continuous flow of CO_2 in order to improve the mass transport of CO_2 during the electrocatalysis. The reactor consists of two main parts: electrochemical cell that is connected to a tube containing the catalytic mixture containing surfactant (PTS). The flow of CO_2 will force the electroproduced gases (H_2/CO) into the catalytic tube to perform the hydroformylation reaction (the system is open and not sealed). The continuous flow of CO_2 resulted in the formation of foams due to the existence of the surfactant. The foaming phenomenon resulted in the flow of the catalytic mixture out of the catalytic tube. In order to supress/prevent the foaming formation, a commercially available silicone antifoam was added to the catalytic solution (2 drops only). The addition of silicone antifoam succeeded in preventing the foaming formation but it also affected the catalytic reaction. The percentage of conversion of styrene to the corresponding aldehydes was 10 % after 8 h of reaction under CO_2 and syngas balloons **(Figure 6.13)**. Without using silicon oil, the percentage of conversion of styrene to the corresponding aldehydes was about 53 % after 8 under CO_2 and syngas (CO/H_2) balloons. According to these results, upon using the proposed reactor the achievable conversion percentage may be low about 10 %.

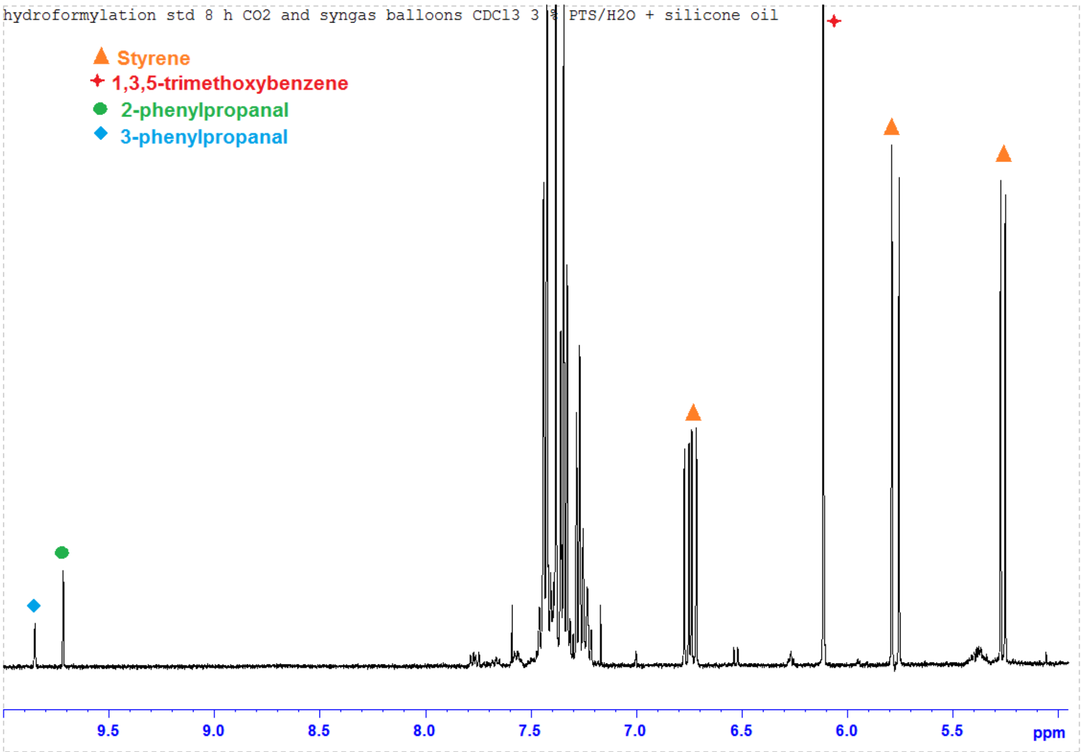

Figure 6.13: ^{1}H-NMR ($CDCl_3$) spectrum of products hydroformylation reaction of styrene under CO_2 and CO/H_2 balloons for 8 h in 3% (wt%) of PTS/H_2O in addition to silicon antifoam.

6.4. Conclusions

The prepared catalyst (Ru@MOF) could not be used for the proposed reactor due to low activity toward the hydrogenation of styrene at 1 atm. Commercially available Pd/C (5%) catalyst is suitable for the proposed reactor unlike the Ru@MOF catalyst which requires pressure more than 1 atm. We therefore turned to palladium on graphite instead as described in **chapter seven p.178**.

The chosen catalysts (Rh/6-DPPon) was able also to work efficiently in the under the reported standard method (20 h in PTS/H_2O). To mimic the expected phenomenon and conditions in the proposed reactor silicone antifoam was used to prevent the expected foaming formation. The silicone antifoam succeeded in preventing the foaming phenomenon and also supressed the catalytic conversion of styrene into the corresponding aldehydes to about 10 % instead of 53% without using it (8 h under CO_2 and syngas balloons).

Chapter 7

7. Mini-chemical reactor

Aims

The main goal of the project was to use solar-driven electrocatalysis for downstream chemical synthesis. Previous chapters have described the electrocatalytic reduction and oxidation reactions, and downstream catalytic reactions under mutually compatible conditions. The aim here was to integrate this knowledge into a functioning device. FeP/CC electrocatalyst was used to electroreduce protons into H_2 in acidic and near neutral media to perform hydrogenation reaction of styrene using the commercially available Pd/C catalyst.

For hydroformylation, considering the CE% of H_2 and CO using all the prepared Cu based electrocatalyst, no Cu based electrocatalyst gave the ideal stoichiometry of 1:1 $CO:H_2$ required for hydroformylation reaction, however OD-Cu foil did give a 3:1 ratio of $H_2:CO$ (in addition to formic acid) that could potentially be used. It is known that gold can electroreduce CO_2 into CO/H_2 exclusively at different voltages. As a proof of principal gold was used to electroreduce CO_2 into syngas mixture (H_2/CO) to perform the hydroformylation reaction of styrene using (Rh/6-DPPon system).

Abstract

Two reactors were built to couple/connect the electrocatalysis and catalysis systems. The two reactors were powered using a solar panel. The electroproduced H_2 was used for the hydrogenation of styrene and the setup succeeded in converting 100% of styrene within 6 h (standard method 12 h). Better engineering can make the system more efficient.

Gold was used for the electrochemical reduction of CO_2 into H_2/CO mixture. The electroproduced gases were used directly to perform the hydrofomylation reaction for styrene. Unfortunately, the reaction did not occur as the styrene left the catalytic vessel during the flow of CO_2. Furthermore, foaming of the catalytic reaction was also a serious issue.

7.2. Mini-reactor components

Two systems were designed for performing hydrogenation and hydroformylation of alkene reactions. The first system consisted of coupled hydrogen evolution reaction (HER) and hydrogenation (Pd/C) while the second one included the electrochemical reduction of CO_2 using a gold foil followed by hydroformylation of alkene using Rh/6-DPPon **(Figure 7.1)**. A glass frit was used to sparge the produced gas(s) within the catalytic solution. The idea behind using a glass frit is to provide the system with a high surface area in order to increase the rate of catalytic reaction (no magnetic stirring was involved). Standard glass was used for the electrochemical cell and catalytic reactor and it can undergo pressure up to 5 bar.

For the hydrogenation reaction, FeP/CC prepared by electroplating was used as cathode. Blank carbon plate and CoPi/SS were used as anode in acidic (0.5 M H_2SO_4) and near neutral media (0.1 M KPi), respectively.

For the hydroformylation reaction based system, gold was used as cathode and CoPi/SS was used as anode in 0.1 M $KHCO_3$. In prelimnary work, upon using gold foil (2 x 2 cm^2), the CE% of CO was about 64.78 and CE% of H_2 was 36.32 % at -20 mA/cm^2. The ratio between H_2:CO was not 1:1 but it is enough to try it in the reactor for the hydroformylation of styrene.

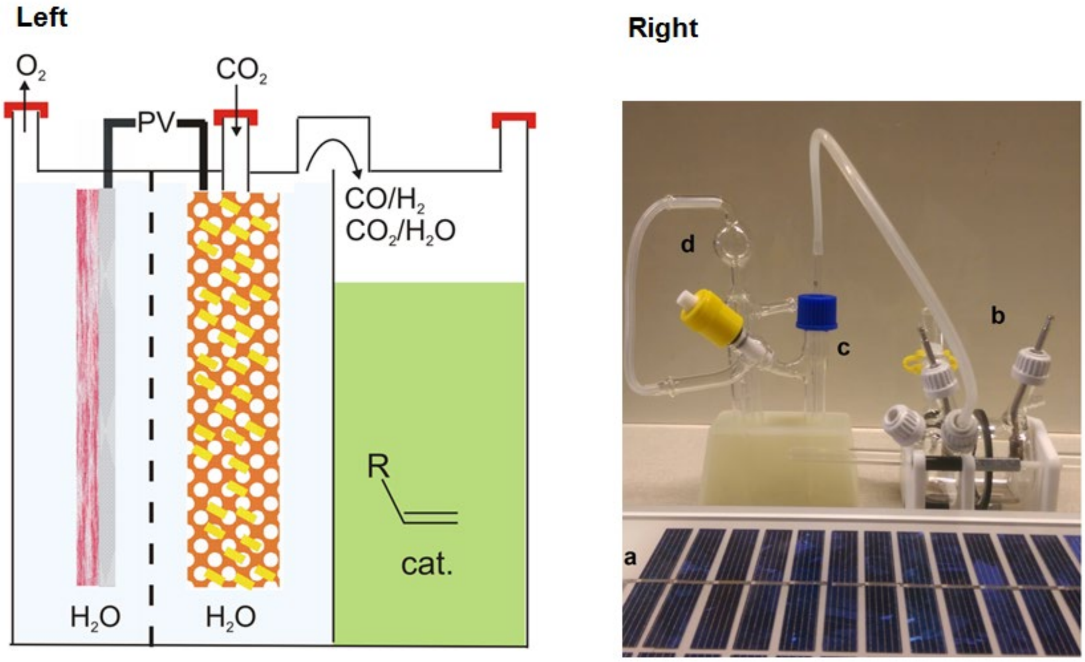

Figure 7.1: (left) a diagram of the mini-reactor components and (right) real components of the reactor; (a) solar panel, (b) electrochemical cell, (c) catalysis vessel and (d) bubbler.

7.3. Example of calculations for mini-reactor

The volume of headspace was about 36 mL. The expected partial pressure of the desired gas is 1 atm to avoid any pressure on the glassware. Assuming the electroproduced gases behave like ideal gases, we can apply the general gas law:

$$PV = nRT$$

Where P: the pressure, V: the volume, n: no. of moles, R: gas constant (0.082 L. atm. mol^{-1} . K^{-1}) and T: temperature in K (294 K).

$$n = \frac{PV}{RT} = \frac{1x\ 36\ x\ 10^{-3}}{0.082\ x\ 294} = 0.00149\ mol = 1.49\ mmol$$

For the hydrogen evolution reaction system $(2H^{+} + 2e^{-} \rightarrow H_2, E^{o} = 0.0\ V)$

$$Q = n\ x\ z\ x\ F = I\ x\ t$$

Where Q is the charge passed during electrolysis, n: no. of moles, I: current, t: time of electrolysis and F: Faraday constant. According to the experimental data mentioned in chapter three, the faradaic efficiency was 100% for hydrogen evolution reaction using FeP/CC prepared by electroplating method. The no of moles of styrene used was 1.15 mmol so the required no of mole of H_2 is $n_{H2} = 1.15\ mmol.$ Thus $n_e = 2\ x\ n_{H_2} = 2.3\ mmol,\ Q = I\ x\ t = nF = 221.91\ C$

For 4 h of electrolysis $\left(I = \frac{Q}{t} = \frac{221.91}{14400} = 15.41\ mA\right)$. Assuming the geometric surface area is $1.0\ cm^2$, thus $J = 15.41\ mA/cm^2$.

7.4. Results and Discussion

All the results of the catalytic systems based on the proposed reactor are tabulated in **(Table 7-1, Table 7-2)**.

7.4.1. Chemical reactor for hydrogenation reaction

The results of the hydrogenation reactions are tabulated in **(Table 7-1)**. Upon using the mini-reactor powered by power supply in 0.5 M H_2SO_4 (≈15 mA/cm^2, Q= 221.91 C, partial pressure of H_2 was less than 1 atm), the 1:1 ratio between styrene and H_2 was not enough for full conversion of styrene into ethylbenzene and about 5.2% of styrene was converted to ethylbenzene.

To prove/demonstrate the concept, a solar panel (illuminated by sun rays) was used to power the reactor. Upon the flow of ≈ 31 mA/cm^2 (average value) from the solar panel (Q= 489.6 C), the percentage of conversion of styrene to ethylbenzene reached 46 % after 4 h **(Figure 7.2)**. Thus a ratio of 1:2.2 between styrene and H_2 was insufficient to convert all the styrene into the corresponding alkane.

Table 7-1: Summary of the results of the two hydrogenation reaction systems.

Starting conditions of the catalytic reactions (gas source)	**Solvent/ catalysis duration**	**Results and comments (Conversion percentage of styrene to the expected products)**
Reactor powered by a DC power supply (≈ 15 mA/cm^2)	CH_3OH/ 4 h	About 5.2 % conversion of styrene to ethylbenzene ^{a}
Reactor powered by solar panels^a (≈ 34 mA/cm^2)	CH_3OH/ 4 h	About 46 % conversion of styrene to ethylbenzene ^{a} **(Figure 7.4)**
Reactor powered by solar panels^a (≈ 31 mA/cm^2) (Electrolysis in 0.5 M H_2SO_4)	CH_3OH/ 6 h	About 100 % conversion of styrene to ethylbenzene ^{a} **(Figure 7.6)**
Reactor powered by solar panels^b (≈31 mA/cm^2) (Electrolysis in 0.1 M KPi)*	CH_3OH/ 6 h	About 80 % conversion of styrene to ethylbenzene ^{a} **(Figure 7.8)**

The geometric surface area of the counter electrode was double that of the working electrode. ^{a}the solar panel was illuminated by Sun rays. ^{b}CoPi/SS was used as a counter electrode and a 300 W xenon lamp was used as a source of visible light (ILC 302UV).

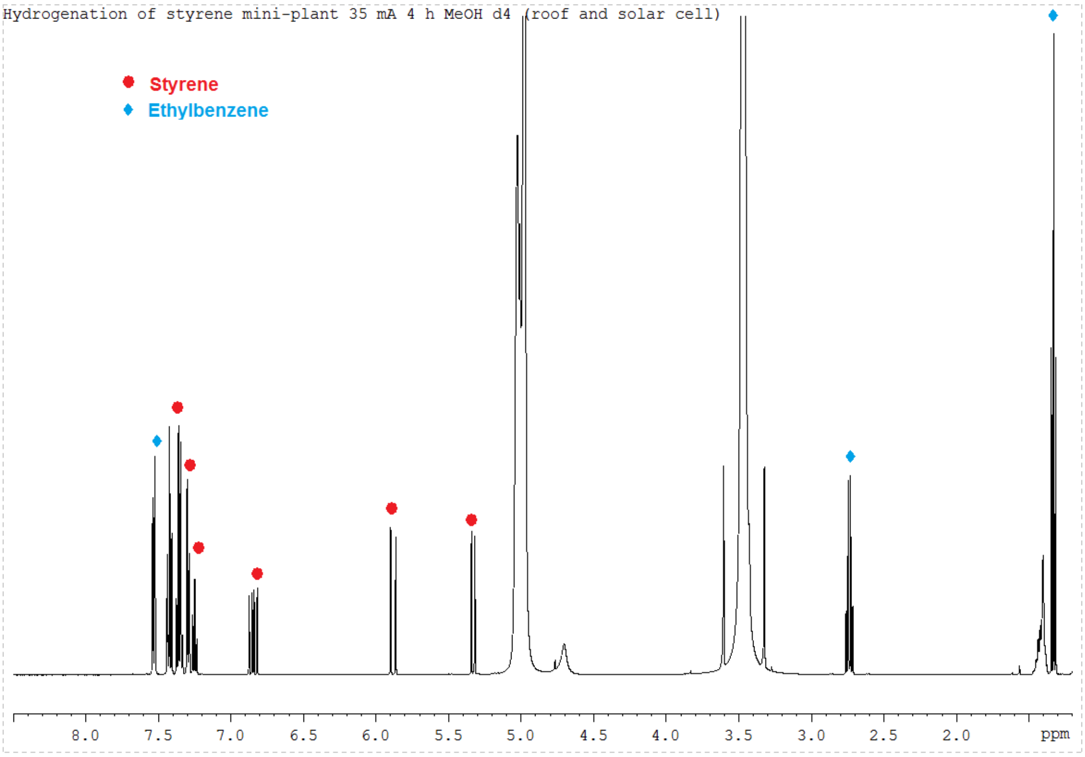

Figure 7.2: ^{1}H-NMR (MeOD-d$_4$) spectrum of the product of hydrogenation of styrene using the mini-reactor for 4 h (≈34 mA/cm^2) powered by solar panel.

To increase the amount of electroproduced H_2 without increasing the current density from 31 mA/cm^2 (and the cell voltage), the electrolysis time was increased to 6 h **(Figure 7.3)**. The charge passed during the electrolysis was 669.6 C, which is about 3 times the required charge of H_2. In acidic medium (0.5 M H_2SO_4), the cell voltage was about 1.87 V and current density was about 31.02 mA/cm^2 **(Figure 7.3)**.

After 6 h of electrolysis, the percentage of styrene conversion reached 100 % **(Figure 7.4)**. Thus, the ratio between styrene and H_2 1:3 is required for the full conversion of styrene to ethylbenzene. The difference between the rate of electroproduction of H_2 and the rate of hydrogenation may be the reason for the loss of two thirds of the electroproduced H_2.

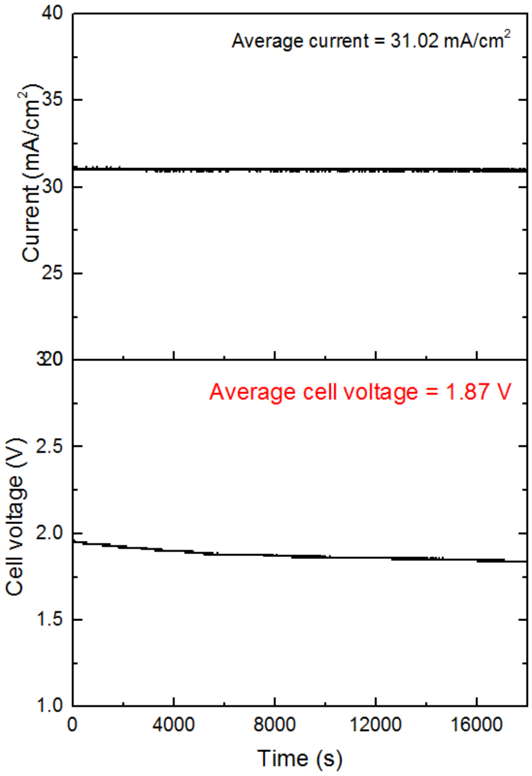

Figure 7.3: Electrochemical parameters (cell voltage and current) for the solar powered reactor in 0.5 M H_2SO_4.

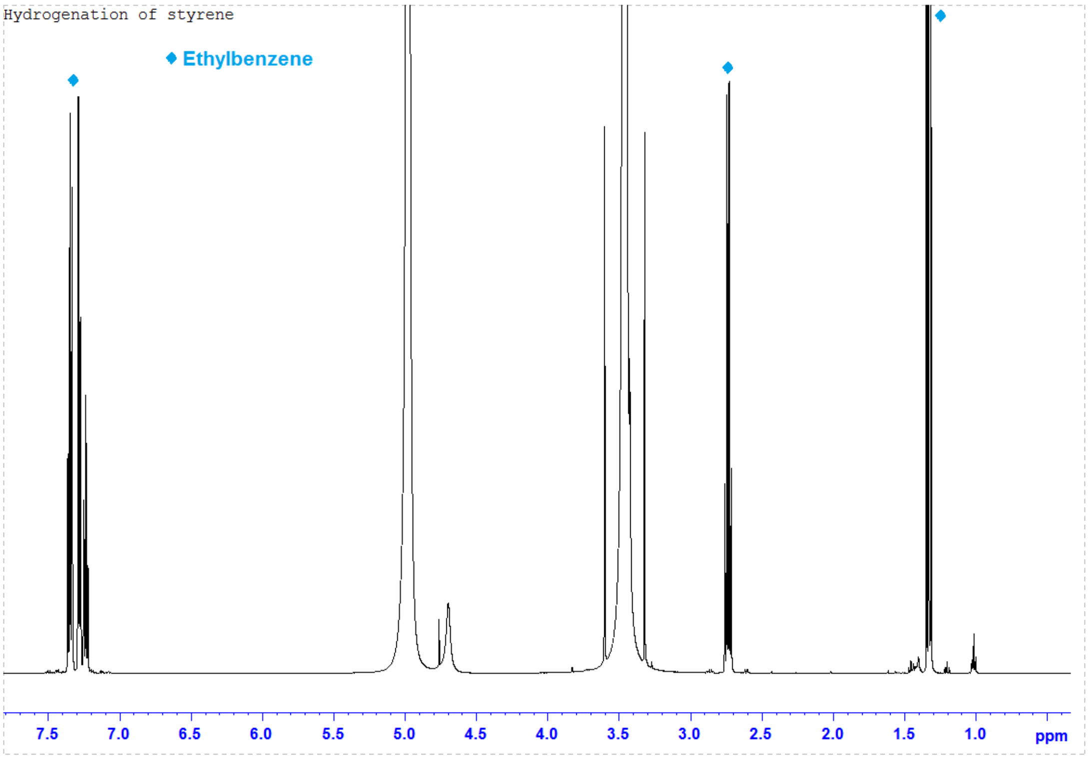

Figure 7.4: ^{1}H-NMR (MeOD-d_4) spectrum of products hydrogenation reaction of styrene under using the mini-reactor for 6 h (≈31 mA/cm^2) powered by solar panel in 0.5 M H_2SO_4.

A similar experiment was performed in near neutral medium (0.1 M KPi) with illumination of the solar panel by a xenon arc. The cell voltage was about 3.62 V and current was about 32.08 mA/cm^2 **(Figure 7.5)**. After 6 h of electrolysis, the percentage of styrene conversion reached about 90 % **(Figure 7.6)**. The reason that conversion percentage did not reach 100% may be due to side reactions or leakage in the system. It is worth mentioning that for this reaction the solar panel was illuminated using a 300 W xenon lamp. It was very difficult to wait and work under sun light in York as the weather is cloudy and rainy most of the days. Maintaining a constant current under the mentioned weather conditions was not achievable on many days.

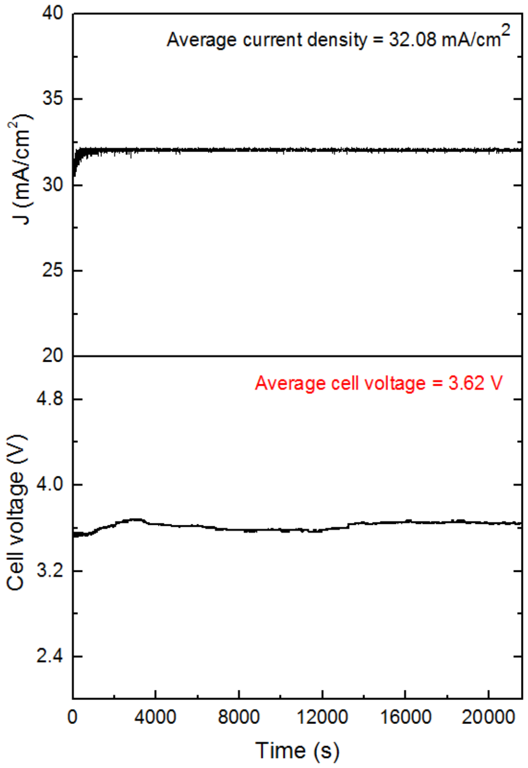

Figure 7.5: Electrochemical parameters (cell voltage and current) for the solar powered reactor in 0.1 M KPi.

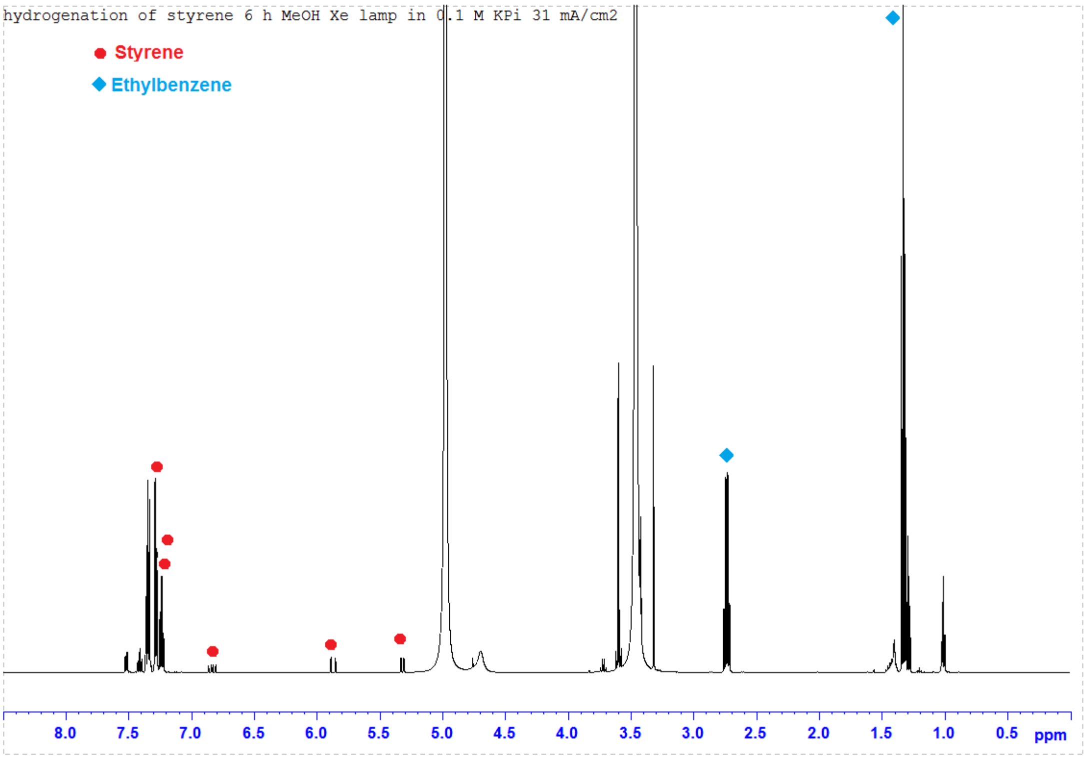

Figure 7.6: ^{1}H-NMR (MeOD-d_4) spectrum of products hydrogenation reaction of styrene using the mini-reactor for 6 h (≈31 mA/cm^2) powered by solar panel.

7.4.2. Chemical reactor for hydroformylation reaction

It is worth noting that all the trials and experiments in this section were performed using the reactor, while the solar panel was illuminated using a 300 W xenon lamp as described above.

Upon using the reactor, no reaction nor styrene were detected by ^{1}H-NMR indicating that the styrene left the catalytic solution while purging the catalytic mixture with CO_2 due to the volatility of the styrene. The styrene is a volatile organic compound and has a boiling point of 145 °C. Apparently, the reaction needs to be performed in a sealed system. Using a different substrate may be an option to avoid the volatility of the styrene.

Table 7-2: Summary of the results of the two hydroformylation systems.

Starting conditions of the catalytic reactions (gas source)	**Solvent/ catalysis duration**	**Results and comments (Conversion percentage of styrene to the expected products)** [a]
Reactor by solar panels (about ≈ 20 mA)[b] (Electrolysis in 0.1 M $KHCO_3$)	CH_3OH/ 8 h	**No reaction**

[a]: ^{1}HNMR was used to detect the products and conversion percentages. All the solvents were used without any drying, [b]: CoPi based on stainless steel was used as a counter electrode and Au was used as working electrode and a 300 W xenon lamp was used as a source of visible light (ILC 302UV).

7.4.3. Conclusions

The preliminary work proved the ability of the system to be used in the real world. The mini-chemical reactor worked efficiently for hydrogenation of styrene especially upon increasing the electroproduced H_2 three times than that required for the reaction (3 times the no of mmole of styrene). The same reaction was repeated in near neutral medium and the percentage of conversion was about 90%, which may be because of leakage or because the faradaic efficiency for H_2 was not 100 %.

The reactor did not work well for the hydroformylation reaction as the styrene left the catalytic mixture while the CO_2 was flowing.

8. Conclusions and future work

The current project aimed to prove the concept of using solar energy as the only source of energy for the production of useful chemicals through coupling electrocatalysis and catalysis steps in a single system using a reactor. The electrocatalysis step includes the electrochemical reduction of protons and CO_2 into H_2 and syngas, respectively. The catalytic step involves using two catalysts for the hydrogenation (using the electroproduced H_2) and hydroformylation (using the electroproduced syngas) of alkenes. To achieve the mentioned goal, different criteria were chosen to simplify the system and to work in lab scale. The chosen criteria faced multiple challenges, below a summary of the criteria, challenges and the future work that can be done to improve the reactor further:

8.1. The consumption of relatively low energy

Using efficient electrocatalysts for the electrochemical reduction of protons and CO_2 can minimise the energy demand as they can operate under low overpotential ($\eta = E_{applied} - E^{o}$).

For the hydrogenation evolution reaction (HER), iron phosphide was chosen for the electrochemical reduction of protons. The iron phosphides were prepared through two methods; electroplating and spray-pyrolysis. The two electrocatalysts exhibited good catalytic activities in terms of overpotential, durability and stability. FeP/C prepared by spray pyrolysis can operate with overpotential (η_{10}) of 98 mV while that prepared by electroplating has overpotential of 65 mV in 0.5 M H_2SO_4. The mass loading of FeP/C electrocatalyst prepared by the electroplating method is about 10 times that of the one prepared by spray pyrolysis. The catalytic activities of the two FeP/CC electrocatalysts were compared in terms of overpotential, Tafel slopes, capacitance measurements, stability and durability. The ability of the two electrocatalysts to operate in near neutral medium (pH = 5.8 - 6.3) has been investigated. The electrocatalyst prepared by spray pyrolysis operates at (η_{10}) 190 mV while that prepared by electroplating is 136 mV in phosphate buffer solution. The two electrocatalysts were able to produce H_2 required for the reactor. FeP/CC prepared by electroplating was chosen to work in the reactor as it operates at low overpotential compared to FeP/CC prepared by spray-pyrolysis. It is worth noting the FeP/CC prepared by electroplating operates at 65 mV to afford -10 mA/cm^2 compared to 34 mV reported in literature.[70] The main reason behind the difference between the two values may be due to using two different kinds of carbon cloth (the substrate). Generally, carbon cloth has relatively weak electroactivity that is reflected in the capacitance value. In the future, using carbon cloth of better properties may be an option to improve the interaction between the electrocatalyst and the carbon cloth and subsequently improve the electrocatalytic performances.

The reactor setup for the hydroformylation of styrene required 1:1 H_2:CO mixture. For the electrochemical reduction of CO_2 we used two different approaches; firstly using Cu_3P as an electrocatalyst and secondly using 3D printing as a potential technology for building a Cu based electrocatalyst for CO2RR. Copper phosphide on Cu foil favours the hydrogen evolution reaction over the electrochemical reduction of CO_2. Cu_3P/Cu foil showed conversion of CO_2 into HCOOH and the highest percentage did not exceed 10% at -0.6 V (RHE). Such behaviour may be attributed to the weak interaction between CO_2 and Cu_3P. We did not observe the reported behaviour in literature during our work on the current project from Cu_3P/Cu[221] where Cu_3P/C gives 47 % at -0.3 V (RHE) (FE% of H_2 was 53 %).[221] The difference between the two may be due to having two different substrates: in the literature Cu_3P was prepared on carbon while in the current project it was prepared on Cu foil.

In the future, using different electrocatalysts based on Cu such as Cu derived from Cu_2O inverse opals,[196] Ag and Au based electrocatalyst which can give FE% for CO up to 50 % and/or more through CO2RR.

A 3D printer can be used as a technology for building metal based electrocatalysts and it is a flexible tool that can be used to design different electrode using different ingredients and it can also be used in future in mass production of electrodes. 3D printing also can be an efficient tool to prepare rough electrodes with high roughness factor. The performances of the electrocatalyst toward CO2RR were low. The phosphide derived electrode could convert CO_2 into formate and hydrogen exclusively with only traces of CO.

In the future, building different structures of different geometries can be done for better electrocatalyic performance. The prepared ink can be developed for better printing and for structures having better resolution. Generally, working with electrocatalysts that can operate at high current density and absolute current (>200 mA/cm^2 required for industrial scale) is very important for the future of the CO2RR field generally and for future developing of the reactor.

8.2. Working with an electrocatalyst in aqueous media without using any sacrificial agents

Water was chosen as a solvent and to act as source of protons required for the electrochemical reduction of protons and CO_2 as the following:

$$2H^+ + 2e^- \rightarrow H_2, \qquad E^o = 0.0\,V$$

$$CO_2 + 2H^+ + 2e^- \rightarrow \mathrm{CO} + H_2O, \qquad E^o = -0.51\,V$$

Using water benefited us by avoiding using acids as protons source upon working in non-aqueous media.

8.3. Working under room temperature and atmospheric pressure

The chosen electrocatalysts and catalysts for the reactor can operate under room temperature and atmospheric pressure. Thus no special glass was used and standard glass which can withstand pressure up to 5 bar. The custom-made electrochemical cell was a two compartment cell and the two chambers were separated by a Nafion-117 membrane.

In the future, using different kinds of electrode like gas diffusion electrode may lead to radical changes in the electrochemical design and materials used in reactor.

8.4. Catalysts for the hydrogenation and hydroformylation of styrene

The main theme of the project was to work using catalysts and electrocatalysts based on inexpensive earth abundant materials. For the catalytic reactions (hydroformylation and hydrogenation reaction), there are molecular catalysts with metal centres such as Fe and Co. The use of water as a solvent in the electrocatalytic reduction of protons and CO_2 required using catalysts that are not water sensitive nor air sensitive. Unfortunately, the metal complexes based on Fe and Co suffer either from air/water sensitivity and operate at high pressure. Pd/C and Rh/D-DPPon catalysts proved their ability to be used in the reactor.

The Ru@MOF catalyst was prepared and characterized and tested to work as a catalyst for the hydrogenation of alkene. Unfortunately, the catalyst did not give any significant catalytic activity at 1 atm and cannot be used in the reactor. In the future, Ru@MOF catalyst can be developed and the operational method can be optimised and tested using different alkenes.

8.5. The complementary oxidation reaction

The electrocatalytic reactions (HER and CO2RR) were performed in water. The water oxidation was the expected reaction at the anode. The thermodynamic barrier $(E^o = 1.23\,V)$ is relatively high in addition to kinetic barriers that increased the total energy further.

$$H_2O \rightarrow\ 2H^+ +\ 2e^- + 1/2\,O_2, \qquad\qquad E^o = 1.23\,V$$

Working with electrocatalysts for OER was very difficult in acidic medium as the most of the reported electrocatalysts suffer from either low stability or operated at high overpotential (or both of them).

In neutral medium, using CoPi supported on stainless steel mesh was a good choice for the electrocatalytic process. It worked efficiently for 6-8 h in the reactor experiments.

In the future, working in a basic medium may increase the options of the electrocatalysts for OER compared to that in neutral and acidic media. Working in basic medium would affect also the electrocatalysts choices for the hydrogen evolution reaction.

8.6. Using solar panel.

The main concept of the project based on using solar energy as the only energy sources for the reactor. The weather in York usually is rainy and cloudy except few days per month during the summer. It was very difficult to wait and work under sun light in York as the weather is cloudy and rainy most of the days. Maintaining a constant current under the mentioned weather conditions was not achievable in many days. It was very difficult to perform the reactor based experiments outdoors because of the weather conditions. Thus using a xenon lamp was inevitable to illuminate the solar panel connected to the reactor.

In the future using a DC power supply can save more time and may simplify the setup further but it would be less realistic and against the main concept of the project which is using solar energy (or any renewable source of electricity in real world).

8.7. Reactor experiments

As mentioned above there were chemical and engineering challenges faced the project goal. Having a professional help from an engineer could be valuable in the future development of the reactor. A better design of the reactor can be also considered to minimise any loss of gas and to minimise resistance in the electrochemical cell.

Using silicone antifoam was a successful idea to prevent the foaming formation due to the continuous flow of CO_2 within the surfactant containing catalytic mixture. The silicone oil worked as expected and it prevent the foaming formation but it also suppressed the catalytic reaction to 10 % instead of 53 % under the same conditions. The volatility of styrene was a problem in the hydroformylation reaction experiments as the flow of CO_2 forced the styrene out of the catalytic tube. Reaction can be optimised but I didn’t have enough time to optimise the reaction.

In the future, using less volatile alkenes would be a good choice to test the setup. Finding a catalytic system that does not require using surfactant would be a good option to avoid the foaming formation and subsequently avoid using additional chemicals (antifoam).

Appendix-1

Table A1.1: Possible half-reactions of electrochemical reduction of CO_2.

Product	Electrochemical reduction half-reactions	$E^o\ (V)$ vs (SHE) pH = 7	$E^o\ (V)$ vs (SHE) pH = 0	no of (e^-)	Standards NMR data			
					Chemical shift (^{1}H)	**Nucleus**	**Splitting/J coupling (Hz)**	**^{13}C**
Bicarbonate	*Electrolyte*	-		-	-	$KH\mathbf{C}O_3$	-	162.9
DMSO	*Internal standard*	-		-	2.6	$(\mathbf{C}H_3)_3SO$	s	39.6
Carboxylate radical	$CO_2 + e^- \rightleftharpoons CO_{2}^{\cdot}$	-1.90	-	1				
Hydrogen	$2H^+ + 2e^- \rightleftharpoons H_2$	-0.414	0.0	2				
Carbon monoxide	$CO_{2(g)} + 2H^+ + 2e^- \rightleftharpoons CO_{(g)} + H_2O$	-0.51	-0.106	2				
	$CO_{2(g)} + 2H_2O_{(l)} + 2e^- \rightleftharpoons CO_{(g)} + H_2O$	-	-0.934					
Formic acid	$CO_{2(g)} + 2H^+ + 2e^- \rightleftharpoons HCOOH_{(l)}$	-0.61	-0.250	2	8.33	$H\mathbf{C}OOH$	s	171.77
	$CO_{2(g)} + 2H_2O_{(l)} + 2e^- \rightleftharpoons HCOO^-_{(aq)}$	-	-1.078					
Oxalic acid	$2CO_{2(g)} + 2H^+ + 2e^- \rightleftharpoons (COOH)_{2(aq)}$	−0.87	-0.500	2	8.20	$(\mathbf{C}OOH)_2$	s (br)	161
	$2CO_{2(g)} + 2e^- \rightleftharpoons (COO^-)_{2(aq)}$	-	-0.590					
Formaldhyde	$CO_{2(g)} + 4H^+ + 4e^- \rightleftharpoons HCHO_{(l)} + H_2O_{(l)}$	-0.48	-0.070	4				
	$CO_{2(g)} + 3H_2O_{(l)} + 4e^- \rightleftharpoons HCHO_{(l)} + 4OH^-$	-	-0.898					
Acetic acid	$CO_{2(g)} + 4H^+ + 4e^- \rightleftharpoons CH_3COOH$	-0.26	-	4	2.08	$\mathbf{C}H_3COOH$	s	23.74
Carbon	$CO_{2(g)} + 4H^+ + 4e^- \rightleftharpoons C_{(s)} + 2H_2O$	-	0.210	4				
	$CO_{2(g)} + 2H_2O_{(l)} + 4e^- \rightleftharpoons C_{(s)} + 4OH^-$	-	−0.627					
Methanol	$CO_{2(g)} + 6H^+ + 6e^- \rightleftharpoons CH_3OH_{(l)} + H_2O_{(l)}$	-0.38	0.016	6	3.34	$\mathbf{C}H_3OH$	s	59.75
	$CO_{2(g)} + 5H_2O_{(l)} + 6e^- \rightleftharpoons CH_3OH_{(l)} + 6OH^-$	-	-0.812					
Glyoxal	$CO_2 + 6H^+ + 6e^- \rightleftharpoons (HCO)_2 + 2H_2O$	-0.16	-	6		$(OH)_2\mathbf{C}H\mathbf{C}H(OH)_2$	s	91.39
Methane	$CO_{2(g)} + 8H^+ + 8e^- \rightleftharpoons CH_{4(g)} + 2H_2O$	-0.24	0.169	8				
	$CO_{2(g)} + 6H_2O_{(l)} + 8e^- \rightleftharpoons CH_{4(g)} + 2H_2O$	-	-0.659					
Glycolaldehyde	$2CO_2 + 7H_2O + 8e^- \rightleftharpoons (OH)_2CHCH_2OH + 8OH^-$	-0.03	-	8	3.43 5.04	$(OH)_2CH\mathbf{C}H_2OH$ $(OH)_2\mathbf{C}HCH_2OH$	d, 5.15 t, 5.12	65.42 90.62
Acetaldehyde	$2CO_2 + 8H_2O + 10e^- \rightleftharpoons CH_3CH(OH)_2 + 10OH^-$	0.05	-	10	9.55 5.13 2.12 1.20	$CH_3\mathbf{C}HO$ $CH_3\mathbf{C}H(OH)_2$ $\mathbf{C}H_3CHO$ $\mathbf{C}H_3CH(OH)_2$	q, 2.93 q, 5.37 d, 2.93 d, 5.37	206.9 88.57 30.89 23.50
Ethylene glycol	$2CO_2 + 10e^- + 10H^+ \rightleftharpoons HOCH_2CH_2OH + 2H_2O$	0.20	-	10	3.55	$HOCH_2CH_2OH$	S	
Ethylene	$2CO_{2(g)} + 12H^+ + 12e^- \rightleftharpoons C_2H_{4(g)} + 4H_2O_{(l)}$	−0.34	0.064	12				

Appendix-1

	$2CO_{2(g)} + 8H_2O_{(l)} + 12e^- \rightleftharpoons C_2H_{4(g)} + 12OH^-$	-	-0.764					
Ethanol	$2CO_2 + 12H^+ + 12e^- \rightleftharpoons CH_3CH_2OH_{(l)} + 3H_2O_{(l)}$	−0.33	0.084	12	1.06 3.53	$\mathbf{C}H_3CH_2OH$ $CH_3\mathbf{C}H_2OH$	t, 7.08 q, 7.32	17.63 58.30
	$2CO_2 + 9H_2O_{(l)} + 12e^- \rightleftharpoons CH_3CH_2OH_{(l)} + 12OH^-$	-	-0.744					
Methylglyoxal	$3CO_2 + 12e^- + 12H^+ \rightleftharpoons C_3H_4O_2 + 4H_2O$	0.02 RHE		12				
Ethane	$2CO_2 + 10H_2O + 14e^- \rightleftharpoons C_2H_6 + 14OH^-$	−0.27		14				
Hydroxyacetone	$2CO_2 + 14H^+ + 14e^- \rightleftharpoons CH_3C(=O)CH_2OH + 4H_2O$	0.46		14	2.02 4.25	$\mathbf{C}H_3C(=O)CH_2OH$ $CH_3C(=O)\mathbf{C}H_2OH$	s s	25.63 68.36
Acetone	$CO_2 + 16H^+ + 16\ e^- \rightleftharpoons CH_3COCH_3$	-0.14		16	2.1	$\mathbf{C}H_3CO\mathbf{C}H_3$	s	30.44
Propionaldehyde	$3CO_2 + 16e^- + 11H_2O \rightleftharpoons CH_3CH_2CHO + 16OH^-$	0.14		16	9.57 4.85 2.44 1.47 0.92	$CH_3CH_2\mathbf{C}HO$ $CH_3CH_2\mathbf{C}H(OH)_2$ $CH_3\mathbf{C}H_2CHO$ $\mathbf{C}H_3CH_2CH(OH)_2$ $\mathbf{C}H_3CH_2CHO$	s t, 5.87 q, 7.32 dt, 7.57, 12.94 t, 7.32	209.6 92.77 37.34 30.45 5.54
Allyl Alcohol	$3CO_2 + 16e^- + 11H_2O \rightleftharpoons CH_2{=}CHCH_2OH + 16OH^-$	0.11		16	5.17 5.9 3.99	$\mathbf{C}H_2{=}CHCH_2OH$ $CH_2{=}\mathbf{C}HCH_2OH$ $CH_2{=}CH\mathbf{C}H_2OH$	d, 17.33 m dt, 5.13, 1.46	115.74 136.86 62.96
n-Propanol	$3CO_2 + 13H_2O + 18e^- \rightleftharpoons CH_3CH_2CH_2OH + 18OH^-$	−0.32		18	0.77 1.42 3.44	$\mathbf{C}H_3CH_2CH_2OH$ $CH_3\mathbf{C}H_2CH_2OH$ $CH_3CH_2\mathbf{C}H_2OH$	t, 7.57 sextet, 7.32 6.49	10.36 25.41 64.43
2,3-Furandiol	$4CO_2 + 14e^- + 14H^+ \rightleftharpoons C_4H_4O_3 + 5H_2O$	0.01 RHE		14	6.145 7.030		d d	

The standard potential under standard conditions (SHE based values were at 1.0 atm and 25 °C and were calculated according to the standard Gibbs energies of the reactants in reactions) and their expected NMR spectral data collected from literature.[39, 116, 122-129, 289, 290] All these reported products were electroproduced via different electrocatalysts including copper.

Table A1.2: Different electrocatalysts for hydrogen evolution reaction in 0.5 M H_2SO_4.

#	Electrode/substrate	Method	Loading $(mg)/cm^2$	Tafel slope	η_{10}
1	FeP(NWA)/CP[89]	Hydrothermal	0.6	53	31
2	FeP/Carbon cloth[70]	*Electroplating*	4.9	29.2	34
3	$Fe_{0.5}Co_{0.5}P$/CC[291]	-	2.2	30	37
4	FeP/CC[98]	Dip-coating	4.2	32	39
5	u-CoP/Ti[292]	-	3.6	49.3	45
6	MoP/PC[83]	Pyrolysis	0.24	51	45
7	Fe_3P/FTO[101]			57	49
8	MoP/GCE[81]	-	0.86	54	50
9	FeP NPs/Ti[293]		~1.0	37	50
10	FeP@OMC/CC[255]		1.3	39	51
11	FeP/C NPs /GC[83]		0.23	49	52
12	Fe@FeP/CNT[109]		1.6	55	53
13	FeP/ VAGNs[294]	Electrodeposition	0.776	42	53
14	FeP Nanowires /Ti[108]	Hydrothermal	3.2	38	55
15	FeP nanorods/ CC[92]	Hydrothermal	~1.5	45	58
16	FeP_2 nanowires[80]	-	45	37	61
17	MoP|S/Ti foil[84]	-	3.0	50	64
18	P-Fe_2N/rGO[106]			48.7	64.8
19	***FeP/Carbon cloth***	***Electroplating***	***4.66 – 4.96***	***69***	***65***
20	Vc-FeP(NP)/Ti[104]			49	65
21	CoP/CC[24]	Hydrothermal	0.92	51	67
22	FeP nanocrystals[91]	Solvent-deficient	~0.337	56	70
23	FeP NR/Ti[295]			39	70
24	FeP@GPC[296]	Pyrolysis of MOF		68	72
25	FeP/FTO[101]			66	83
26	FeP(NRA)/Ti[297]	Hydrothermal	0.60	60	85
27	CoP/Copper disk[93]	-	-	50	85
28	Fe_2P/GCE[298]	Hydrothermal	0.36	49	88
29	FeP(NTA)/CP[299]	-	1.6	35.5	88
30	CoP/Ti[300]	Electrodeposition	2.0	43	90
31	MoP NP[301]	Solution-phase	~1.0	45	90
32	FeP nanowires[80]	-	60	39	96
33	Ni-doped FeP(NP)/Ti[71]	Spray-pyrolysis	1.1	43	101
34	Fe_2P/GCE[302]		0.47	52.2	101
35	***FeP/Carbon cloth***	***Spray-pyrolysis***	***0.4 – 0.5***	***87***	***102***
36	FeP/Ti[303]	Hydrothermal			104
37	FeP NWs/rGO[248]		0.204	58.5	107
38	Petaloid FeP/C[304]		0.28	57	110
39	FeP NPs/CS[96]	Solvothermal	0.23	58	112
40	FeP-NCNT(NP)/GCE[79]	Hydrothermal		59	113
41	C-coated FeP MC [305]	Facile solution		56	115
42	FeP/FTO[101]			76	116
43	FeP/Ti[95]	Electrodeposition	1.5	66	116
44	CoP/C NCs[91]			58	117
45	WP(NP)/Ti[306]			54	120
46	FeP(NR)/GCE[307]		0.2	55	120
47	Ni_5P4-Ni_2P(NSA)/NF[308]			79	120
48	FeP/graphene sheets[82]	Solvothermal	0.28	50	123
49	Ni_2P-CNT(NP)/GCE[309]			53	124
50	MoP(NP)/GCE[81]			54	125
51	Ni_2P(NP)/Ti [a 245]			60	125
52	Ni_2P(NP)/GCE[a 310]			87	125
53	CoP nanotube[311]			60	129
54	FeP NPs@NC[105]	-	1.4	67	130
55	WP NAs/CC[86]			69	130

56	$CoSe_2$(NP)/CP[312]			42.1	137
57	Ni_2P/Ti[245]			60	η_{20}=138
58	Ni_5P_4(NSA)/Ni[313]			40	140
59	Cu_3P NW/CF[94]			67	143
60	FeP/Ti[71]	*Spray-pyrolysis*	1.0	31	144
61	FeP microsphere[110]		0.5	58	144
62	FeP nanoparticles [249]	Hydrothermal	0.72	64	154
63	Fe_2P/Ti[100]		40 µg	67	155
64	CoP-RGO[314]			70.2	156.87
65	Pure FeP[91]			138	157
66	FeP NPs[105]			72	172
67	Fe_2P/Fe[315]			55	191
68	FeP_2/C NPs /GC[316]		0.425	66	η_1 = 220
69	FeP@NC[21]	Urea-assisted		73	233
70	FeP nanosheets[78]			67	240
71	FeP/Ti[100]			85	250
72	Ni_2P/C NCs[91]			92	~253
73	FeS_2 film[317]	-	-	62.5	η_4=190-270
74	$FeSe_2$ film[317]	-	-	65.3	η_4=190-270
75	Porous FeP nanosheet[78]	Anion-exchange		67	η_{20}=325

CC: Carbon cloth, PC: Porous carbon, G: graphene; α-INS: iron-nickel sulfide; NCNT: nitrogen-doped carbon nanotubes; CNT: carbon nanotubes; NWA: nanowire array; NSA: nanosheet array; NRA: nanorod array, NTA: nanotube array, MC: microcube, NP: nanoparticles, NS: nanosheets; NR:nanorods, CP: carbon fiber paper, Ti: titanium foil, NF: nickel foam, Fe: iron foil, GCE: glassy carbon electrode, Ni: nickel foil, [a]: (1M H_2SO_4), CS: Candle soot, u: urchin-like, NC: N-codoped carbon, CFP: carbon fiber paper, HNA: hierarchical nanowires array, HNA: hierarchical nanowires array, VAGNs: vertically aligned graphene nanosheets, Vc-FeP : Fe-vacancy-rich FeP, FTO: fluorine-doped tin oxide, OMC: ordered mesoporous carbon.

Table A1.3: Reported data of different electrocatalysts for hydrogen evolution reaction in neutral solution.

#	Electrode/substrate	Electrolyte solution	Loading (mg)/cm^2	b	η_{10} mV
1	CoW(OH)$_x$ [318]	1.0 M PBS	-	149	73.6
2	NiW(OH)$_x$ [318]	1.0 M PBS	-		76.2
3	Co-doped NiSe [319]	1.0 M PBS			82
4	1Co-ns [320]	0.1 M tris-HNO_3	2	48	η_{onset}= 84
5	MoP_2 NS/CC[321]	1.0 M PBS		98	85
6	$Zn_{0.3}Co_{2.7}S_4$ [322]	0.1M PBS			90
7	Ni-C-N NSs [323]	1.0 M PBS			92.1
8	CoP/CC [24]	1.0 M PBS	0.92		106
9	FeP NPs [293]	1.0 M PBS	4.2	-	102
10	RuP_x@NPC	1.0 M PBS		59	110
11	FeP/CC[98]	1.0 M PBS	70		115
12	CoP@BCN [324]	1.0 M PBS			122
13	Co_2P@NPG [325]	1.0 M PBS			130
14	**FeP/CC (electroplating)**	**0.1 M KPi**	**4.66 – 4.96**		**136**
15	MoP NPs@NC [326]	1.0 M PBS		71	136
16	CoP nanosheet array [300]		2.0	58	149
17	Mo_2C@NC [62]	1.0 M PBS			156
18	Cobalt-sulfide/ FTO [327]	1.0 M PBS	-	93	165
19	Co–P–B/rGO [328]				168
20	Ni_3S_2/NF [329]	1.0 M PBS			170
21	Ni_2P/Ni [87]	1.0 M PBS		142	170

22	np-CoP NWs/Ti [330]	1.0 M PBS		125	178
23	NiMoZn [331]	0.1 M PBS			187
24	MoP NA/CC [332]	1.0 M PBS		94	187
25	**FeP/CC (Spray pyolysis)**	**0.1 M KPi**	**0.4 – 0.5**		**190**
26	WP nanorod array [86]		2.0	125	200
27	FeP NPs/Ti [95]	1 M PBS	1.5	99	200
28	WP_2 NPs/W [333]	1 M PBS	-	95	201
29	FeP NPs on CC[92]	1 M PBS	1.5	71	202
30	Mo_2C [334]	1 M PBS			204
31	$CuMoS_4$ crystals [335]	0.1M KPi	0.003		η_2= 210
32	MoP_2 NPs/Mo [336]	1.0 M PBS		81	211
33	rGO-$FePS_3$ [337]				220
34	Mo_2C/MoP@NPC [338]	1.0 M PBS	-	125	228
35	15-h-CoS_2 [339]	1.0 M PBS	-	129	240
36	Co/N-codoped [340]				240
37	WP_2 submicroparticles [341]		0.5	92	244
38	CoN_x/C [342]		2.0		247
39	3D MoS_2/N-Gas [343]		0.7	230	261
40	$CoWS_x$/FTO [344]	1.0 M PBS	-	78	271
41	Co-C-N [345]	1.0 M PBS	-	107	276
42	Co/CoO_x/CN [346]	1.0 M PBS			280
43	Co_9S_8@C [347]		0.28		280
44	$CoMoS_x$/FTO [344]	1.0 M PBS	-	85	282
45	WP_2 NRs [348]	1.0 M PBS	-	79	298
46	H2-CoCat [349]	0.5 M KPi	58.9 $\mu g/cm^2$	140	325
47	Ni-S film [350]	1.0 M KPi	81.5 $\mu g/cm^2$	77	330
48	CNF@CoS_2 [258]	1.0 M PBS	-	163	360
49	CoNC/GD [351]	1.0 M PBS	-	207	368
50	$NiWS_x$/FTO [344]	1.0 M PBS	-	96	373
51	FeP NPs@NPC [105]	1.0 M PBS	-	58	386
52	$FePS_3$ [337]				395
53	Co-NRCNTs [352]	1.0 M PBS	-	-	540

Table A1.4: Reported Copper based electrocatalysts for CO2RR.

Electrocatalysts	**Method of preparation**	**Voltage V vs RHE**	**Current density J -mA.cm^{-2}**	**Faradaic efficiencies of major products (FE%)**	**Electrolyte**	**Stability (h)**	**(Year)**
Cu oxides electrocatalysts							
3 C cm^{-2} Cu_2O [353]	Electrodeposition on Cu	-1.1	37	C_2H_4 (33%), CH_4 (4%)	0.1 M $KHCO_3$	~6.0	(2014)
11 C cm^{-2} Cu_2O [353]	Electrodeposition on Cu	-0.4	~1.0	CO (30%)	0.1 M $KHCO_3$	N/A	(2014)
Cu_2O with (110) orientation [353]	Electrodeposition on Cu plate	-1.5	-	HCOOH (20%), C_2H_4 (19%), C_2H_6 (6%)	0.1 M $KHCO_3$	N/A	(2014)
Cu_2O [180]	Electrodeposition	-0.95 Ag/AgCl	-	C_2H_4 (26%), C_2H_5OH (11.32%)	0.1 M $KHCO_3$	N/A	(2016)
Cu_2O/Cu [354]	Electrodeposition	-1.9 Ag/AgCl	12	CO (~5%), CH_4 (~5%), C_2H_4 (~25%)	0.5 M $KHCO_3$	N/A	(2015)
Cu_2O/GDE [164]	-	-1.39 Ag/AgCl	10	CH_3OH (42.3%), C_2H_5OH (10.1%), n-propanol (2.4%)	0.5 M $KHCO_3$	N/A	(2016)
Cu_2O/ZnO/GDE [164]	-	-1.16 Ag/AgCl	10	CH_3OH (27.5%), C_2H_5OH (3.9%)	0.5 M $KHCO_3$	N/A	(2016)
CuO NP/ TiO_2 [355]	-	−0.85	~8.0	C_2H_5OH (37.5%), acetone (4.3%), n-propanol (5.6%)	0.5 M $KHCO_3$	N/A	(2018)
Cu_xO/GDC ($Cu_xO_{180\text{-}2}$) [356]	-	-1.25 SHE	20.5	HCOOH (59%)	0.5 M $KHCO_3$	N/A	(2014)
Cu_2O film/Cu disc (0.9 μm) [191]	Electrodeposited onto polished Cu discs	-0.99	25	C_2H_5OH (8.66%) C_2H_4 (40.25%)	0.1 M $KHCO_3$	N/A	(2015)
Cu_2O film/Cu disc (3.6 μm) [191]	Electrodeposited onto polished Cu discs	-0.99	38	C_2H_5OH (16.37%) C_2H_4 (34.26%)	0.1 M $KHCO_3$	N/A	(2015)
Cu_2O NP/ RRDE [357]	Lab scale CHFS system	-0.8	~0.2	HCOOH (66%)	0.5 M $KHCO_3$	N/A	(2018)
Polyaniline/Cu_2O nanocomposite [358]	-	-0.3 V SCE	-	HCOOH (30.4%) CH_3COOH (63.0%)	0.1 M TBAP/ MeOH	N/A	(2014)
Graphene/ Cu_2O [359]	-	−0.9 Ag/AgCl	~0.5	C_2H_5OH (9.93%)	0.5 M $NaHCO_3$	N/A	(2017)
Cu_2O (WE) Co_3O_4 (CE) [360]	Brush coating on graphite plates	2.0 1.5 1.5 2.0	-	C_2H_5OH (98.1%), HCOOH (36.6%) C_2H_5OH (55.21%), HCOOH (25.1%)	0.5 M $NaHCO_3$ 0.5 M Na_2CO_3	N/A	(2016)
Ultra-fine CuO NP [361]	Lab scale CHFS system	-0.75	~3.5	HCOOH (61%)	0.5 M $KHCO_3$	24	(2016)
2-methylpyridine /Cu_2O/ZnO [362]	-	-1.03	1.0	CH_3OH (16.86%)	0.5 M $KHCO_3$	N/A	(2017)
Plasma-Activated	Electropolishing of Cu foil/	−1.0	-	C_2H_4 (45.4%), C_2H_5OH (10%), n-	0.1 M $KHCO_3$	N/A	(2017)

Cu [225]	plasma etcher			propanol (3.5%)			
Plasma-Activated Cu [225]	Electropolishing of Cu foil/ plasma etcher	−1.0	-	C_2H_4 (47.3%), C_2H_5OH (11.7%), n-propanol (2.5%)	0.1 M $KHCO_3$ + 0.3M KCl	N/A	(2017)
Plasma-Activated Cu [225]	Electropolishing of Cu foil/ plasma etcher	−1.0	-	C_2H_4 (45.0%), C_2H_5OH (11.1%), n-propanol (2.3%)	0.1 M $KHCO_3$ + 0.3M KBr	N/A	(2017)
Plasma-Activated Cu [225]	Electropolishing of Cu foil/ plasma etcher	−1.0	-	C_2H_4 (47.6%), C_2H_5OH (11.4), n-propanol (2.7%)	0.1 M $KHCO_3$ + 0.3M KI	N/A	(2017)
CuO/N-doped C (CuO/NxC-700) [363]	Reduction/oxidation	-1.25	118	C_2H_4 (36%), HCOOH (2.5%), C_2H_5OH (5-6%)	0.1M $NaHCO_3$	N/A	(2018)
Cu_2O/C [364]	-	2.5	5.4	C_2H_4 (15%), CH_3OH (19%)	-	N/A	(2013)
Cl-induced bi-phasic Cu_2O-Cu [128]	Electrodeposition	-1.6	~6.0	C_2H_4 (22%), C_2H_5OH (24%), n-propanol (8.7%), CH_4 (1.4%)	0.1 M KCl	7.0	(2015)
Plasma-activated Cu foil [189]	Cu foils were treated in O_2 and H_2 plasmas	-0.65 -0.92	1.7 18	CO (~55%) C_2H_4 (60%), CH_4 (4.0%)	0.1 M $KHCO_3$	5.0	(2016)
Plasma-Activated Cu-Nanocubes [205]	Electropolishing/ anodizing Cu foils	−1.0	23	C_2H_5OH (~22%), n-propanol (~9%), C_2H_4 (45%), CH_4 (3%)	0.1 M $KHCO_3$	N/A	(2017)
Thermally oxidized Cu_xO [365]	Annealing (773 K 1.5 h)	-0.6 V	-	CO (25%), HCOOH (28%), CH_3COOH (7%)	0.1 M $KHCO_3$	N/A	(2014)
Cu_2O(1)-carbon paper [366]	Airbrushing a catalytic ink onto a porous carbon paper	−1.30 Ag/AgCl	6.93	CH_3OH (45.7%)	0.5 M $KHCO_3$	5.0	(2015)
Cu_2O thin Cu film[367]	Electrodeposition	-0.4	~5.0	CH_3OH (38%)	0.5 M $KHCO_3$	N/A	(2011)
Cu_2O (30 wt%) impregnated MWCNT[368]	-	-0.8	~8.0	CH_3OH (38%)	0.5 M $NaHCO_3$	N/A	(2016)
Oxide-derived copper electrocatalysts							
Cu-CDots nanocorals[369]	-	-0.7	~4.2	HCOOH (79%)	0.5 M $KHCO_3$	5.0	(2017)
Cu NW array (8.1 μm) [124]	Annealing/ reduction electrochemically	-1.1	-	HCOOH (17.5%), C_2H_4 (17.4%), C_2H_6 (2.4%), CO (7.6%), C_2H_5OH (3.8%), n-propanol (7.8%)	0.1 M $KHCO_3$	5.0	(2016)
Cu NW array (3.0 μm) [124]	Annealing/ reduction electrochemically	-1.1	-	HCOOH (20.7%), C_2H_4 (14.2%), CO (10%), n-propanol (7.8%)	0.1 M $KHCO_3$	5.0	(2016)
Annealed Cu foil (12 h) [156]	Annealing Cu/ electrochemically, reducing Cu_2O	-0.55 -0.85	2.60 -	HCOOH (38.8%), CO (30.1%) HCOOH (10.2%), C_2H_4 (3.9%), CO (6.4%), C_2H_5OH (4.7%), C_2H_6 (6.6%)	0.1 M $KHCO_3$	7.0	(2012)
Cu_2O-Derived	Electrodeposition on Cu foil	−1.0	~20	Cu: C_2H_4 (32.1%), C_2H_5OH (16.4%)	0.1 M $KHCO_3$	12	(2015)

$(Cu/PdCl_2)$ [122]				$Cu/(PdCl_2$ in electrolyte): C_2H_6 (30.1%)			
OD-Cu NW [194]	Wet chemistry/ annealing	-0.6	~0.6	CO (~50%), HCOOH (~30%)	0.1 M $KHCO_3$	N/A	(2015)
Mesoporous Oxide-derived Cu Foam [195]	Cu foam electro-deposited/ planar Cu wafer coupons	-0.8	5–7	C_2H_4 & C_2H_6 (55%)	0.5 M $NaHCO_3$	N/A	(2016)
Cu−Sn/OD-Cu [175]	Annealing/ reduction/ electrodeposition Sn	−0.6	1.0	CO (>90%)	M $KHCO_3$	14	(2016)
Sn NP/Cu_xO NW [370]	Sn electroless plating bath	-0.8	4.5	CO (90%)	0.1 M $KHCO_3$	12	(2016)
OD-Cu particles [192]	Mechanical polishing/hydrothermal	-0.98	~27	C_2H_5OH (11.8%), C_2H_4 (42.6), n-propanol (5.4%)	0.1 M $KHCO_3$	N/A	(2016)
Cu_2O-derived Cu disc [371]	Mechanical polishing Cu discs/ hydrothermal method	-0.83 -0.98	-	n-propanol (8.2%) C_2H_4 (23.19%), C_2H_5OH (8.52%), n-propanol (4.9%)	0.1 M $KHCO_3$	N/A	(2017)
CuO-derived Cu/ NRA [372]	Electrochemical reduction of CuO NRA	−0.816	~11	C_2H_4, C_2H_6 & C_2H_5OH (~40%)	0.1 M $KHCO_3$	N/A	(2017)
Nanostructured oxide-derived Cu [373]	Commercial /Electrodeposition	-1.1	-	C_2H_4 (28%)	0.1 M $KHCO_3$	N/A	(2017)
Oxide-derived copper disc [374]	Electrodeposition	-0.95	-	C_2H_4 (31.9%)	0.1 M $KHCO_3$	N/A	(2017)
Thick Oxide-Derived Copper [375]	Mechanical polishing/ Hydrothermal method	−0.98	~35	C_2H_4 (26.7%)	0.1 M $KHCO_3$	N/A	(2017)
Cu from Cu_2O inverse opals [196]	Electrochemical reduction of Cu(II) acetate	− 0.6	1.2	CO (45.3%), HCOOH (33.6%)	0.1 M $KHCO_3$	10	(2018)
Oxide-Derived Cu [376]	-	−1.0	27.5	C_2H_5OH (7.2%), C_2H_4 (11.8%), C_{2+} (3.5%)	0.1 M $CsHCO_3$	N/A	(2017)
Oxide-Derived Cu [377]	Electropolishing/ annealing/electroreduction	-0.33	-	C_2H_5OH (~30%), C_3H_7CHO (5%)	0.1 M KOH	N/A	(2016)
Copper nitride based electrocatalyst							
Cu on Cu_3N [220]	Ligand exchange/ electroreduction	-0.95	~14	C_2H_4 (39%), C_2H_5OH (19%), n-propanol (6%)	0.1 M $KHCO_3$	32	(2018)
Sulfur-derived/based copper electrocatalysts							
Cu_2S–Cu[131]	-	-0.92 V	54.8 1.3	C_{2+} (13.7% in flow cell) C_{2+} (9.6% in H-cell)	1M KOH 0.1 M $KHCO_3$	17	(2018)
Cu_2S–Cu-V[131]	-	-0.92 V	126 7.3	C_{2+} (32%) in flow cell C_{2+} (23.1%) in H-cell	1M KOH 0.1 M $KHCO_3$	17	(2018)
S-doped Cu_2O-derived Cu [215]	Mechanical polishing/ electrodeposition/ reduction/immersion in NH^+	-0.8	10.7	HCOOH (75%)	0.1 M $KHCO_3$	12	(2018)

	polysulfide solution						
Cu_2S-derived Cu [214]	Anodization of Cu foam/thermal treatment	-2.0 Ag/Ag^+	5.3	HCOOH (85%)	MeCN/ 0.5M $BmimBF_4$	N/A	(2016)
Sulfide-Derived Cu [216]	Pulsed electro-deposition/electrolysis	-0.8	-	HCOOH (~63%)	0.1 M $KHCO_3$	N/A	(2018)
Active CuS_x [378]	Electrodeposition on Cu	−0.85	6.75	HCOOH (75.7%)	0.1 M $KHCO_3$	N/A	(2018)
Desulfurized CuS_x [378]	Electroreduction	−0.85	4.85	HCOOH (29.3%)	0.1 M $KHCO_3$	N/A	(2018)
S-Modified Cu/GDL[185]	-	−0.8	~27	HCOOH (80%)	0.1 M $KHCO_3$	12	(2018)
Halide derived/based Cu based electrocatalysts							
Cu-halide confined mesh [379]	Commercial	−2.4 Ag/AgCl	-	C_2H_4 (60.5−79.5%)	3.0 M KX X = Br, I, Cl	N/A	(2004)
Cu_2O–CuBr films [224]	-	−2.1 Ag/AgCl	-	C_2H_4 (17%)	-	10	(2017)
CuCl-derived Cu [223]	Electropolishing/ wet oxidation/ electroreduction	-2.6 Ag/AgCl	17	C_{2+} (73%): C_2H_4 (56%)	0.1 M $KHCO_3$	N/A	(2018)
Cu NP [222]	Electrodeposition on Cu foil	-0.99	~15	CO (~3%), C_2H_4 (~16%), CH_4 (~6%)	0.1 M $KHCO_3$	N/A	(2015)
Copper phosphide electrocatalyst							
Cu_3P/C[221]	Phosphidation of MOF (HKUST-1)	-0.3		CO (47%)	$KHCO_3$	N/A	(2019)
Copper selenide electrocatalyst							
$Cu_{2-x}Se_y$[213] $Cu_{1.63}Se$(1/3)	Hydrothermal	-2.1 Ag/Ag^+	J_{total}= 41.5 J_{CH3OH}=32.2	CH_3OH (77.6%)	$[Bmim]PF_6$ (30 wt %)/ CH_3CN/H_2O (5 wt%)	25	(2019)
Tandem (sequential) systems based on copper electrocatalysts							
Tandem Au/Cu electrocatalyst [178]	Physical vapour deposition of Au on Cu	-0.9	3.40	Alcohols (<5%), CO (~24%), HCOOH (~9%)	0.1 M $KHCO_3$	N/A	(2018)
Cu dots (2.4%)/Ag[177]	-	-1.0	~11.8	Oxygenates (41.3%)	0.1 M $CsHCO_3$	N/A	(2018)

*Some values were taken from the graphical results within each article. N/A: in most of the cases the authors at least reported 1-3 h CA experiments for their Cu based electrocatalysts. The vast majority of the unreported synthesis procedures were based on wet chemistry and usually started with either mechanical or electropolishing. All the reported electrolytes were saturated with CO_2 (pH = 6.8). NP: nanoparticle, GCE: glassy carbon electrode, NW: nanowires, GDE: Gas Diffusion Electrodes, OD: oxide-derived, NC: nanocrystal, NRA: nanoribbon arrays, GDL: carbon gas diffusion layer, GDC: Gas diffusion carbon, CHFS: continuous hydrothermal flow synthesis, RRDE: Rotating ring-disc electrode, TBAP: tetrabutylammonium perchlorate, V: vacancies, NR: nanorods.

Appendix-2

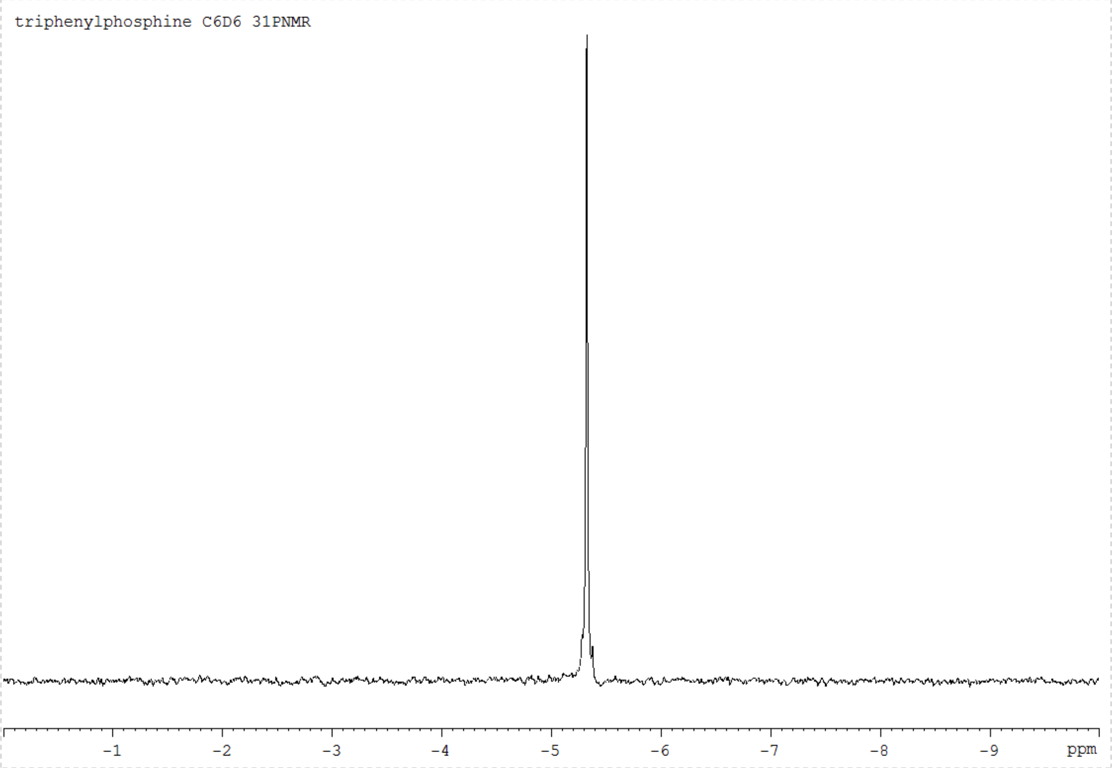

Figure A2.1: ^{31}P-NMR spectrum of triphenylphosphine in C_6H_6.

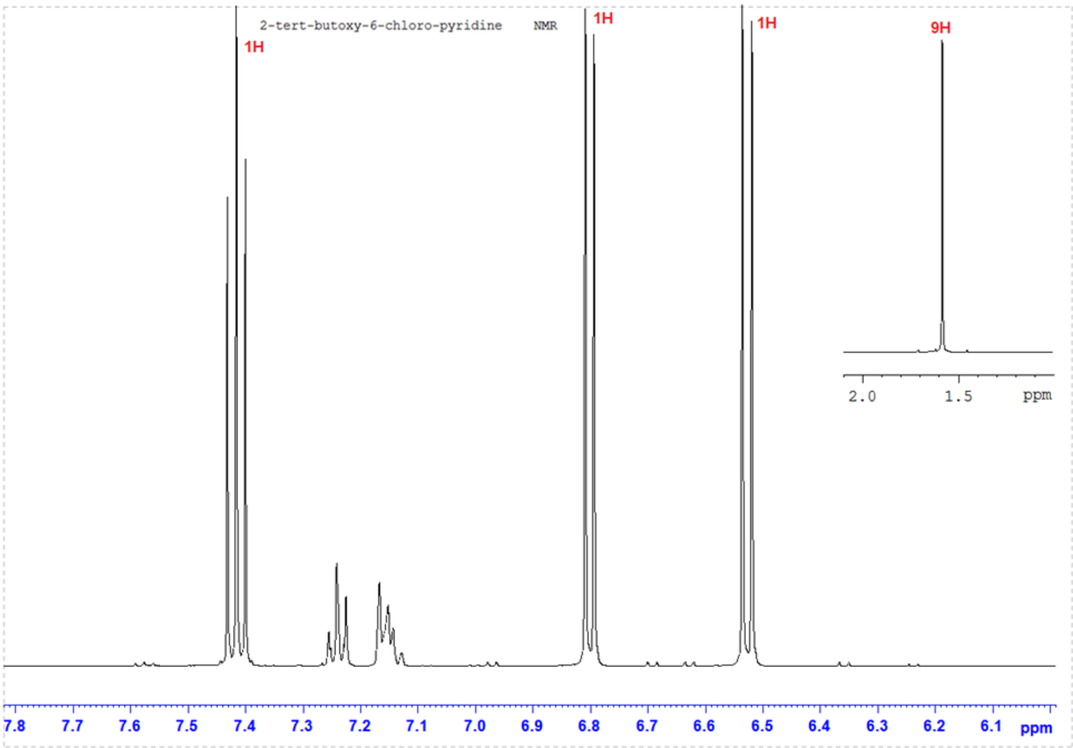

Figure A2.2: ^{1}H-NMR spectrum of 2-tert-butoxy-6-chloro-pyridine (1) in $CDCl_3$.

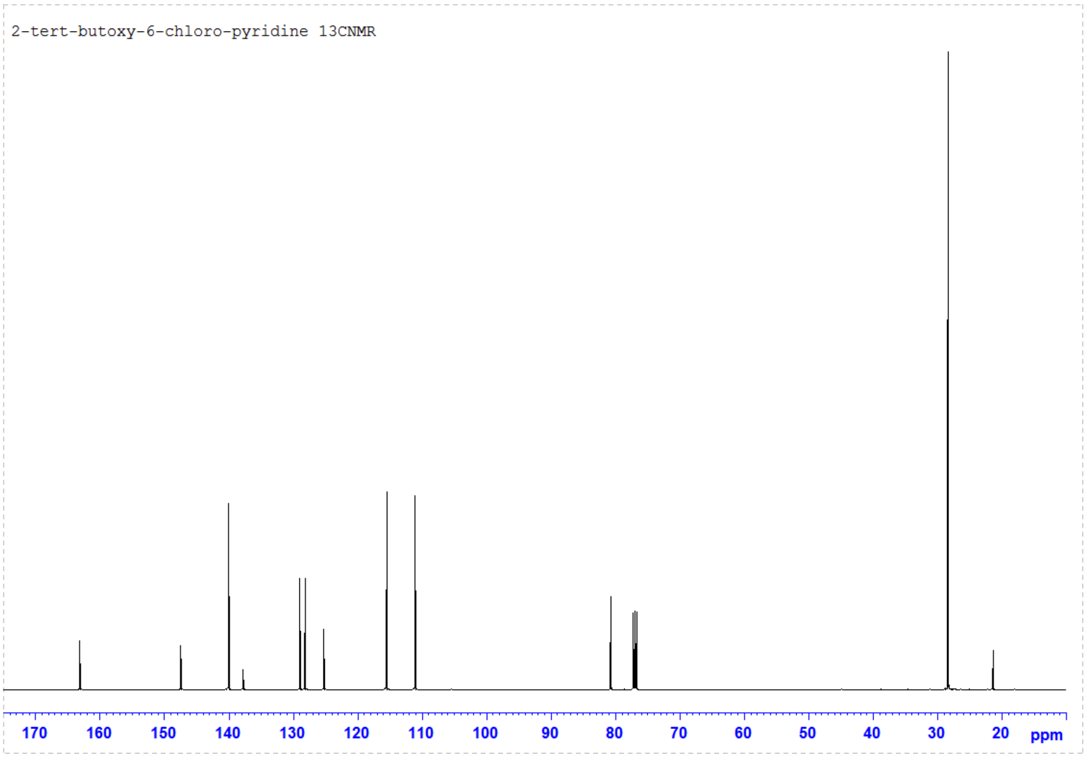

Figure A2.3: ^{13}C-NMR spectrum of 2-tert-butoxy-6-chloro-pyridine (1) in $CDCl_3$.

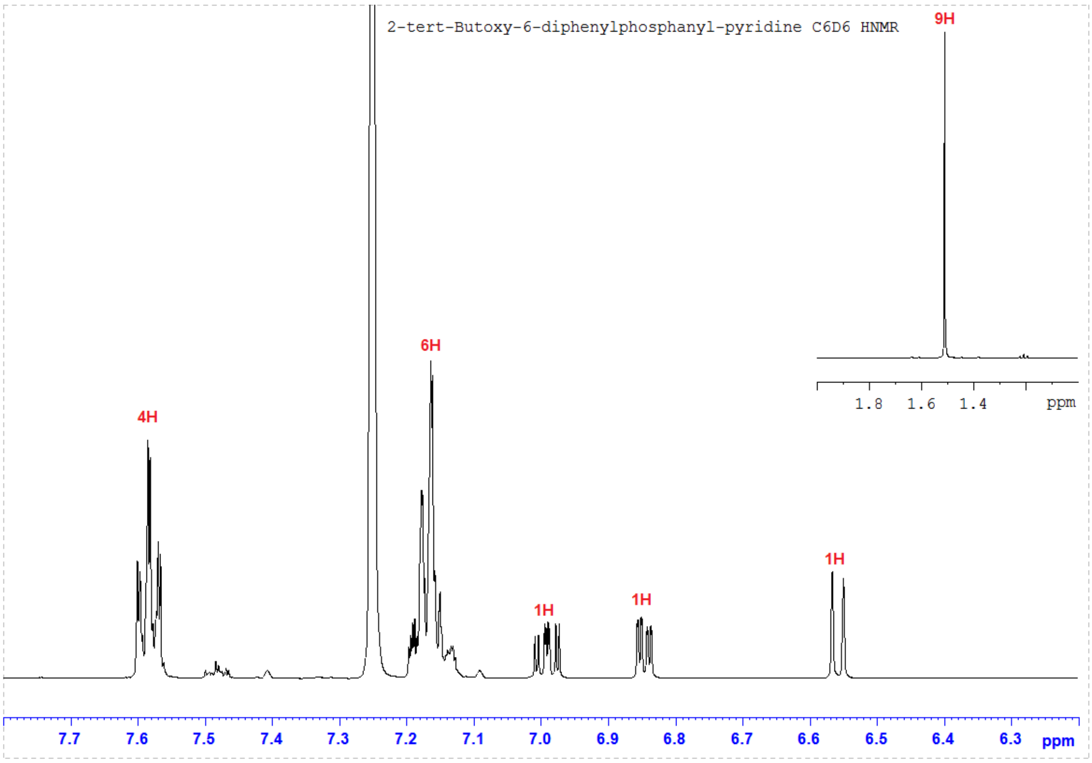

Figure A2.4: ^{1}H-NMR spectrum of 2-tert-butoxy-6-diphenylphosphanyl-pyridine (2) in C_6D_6.

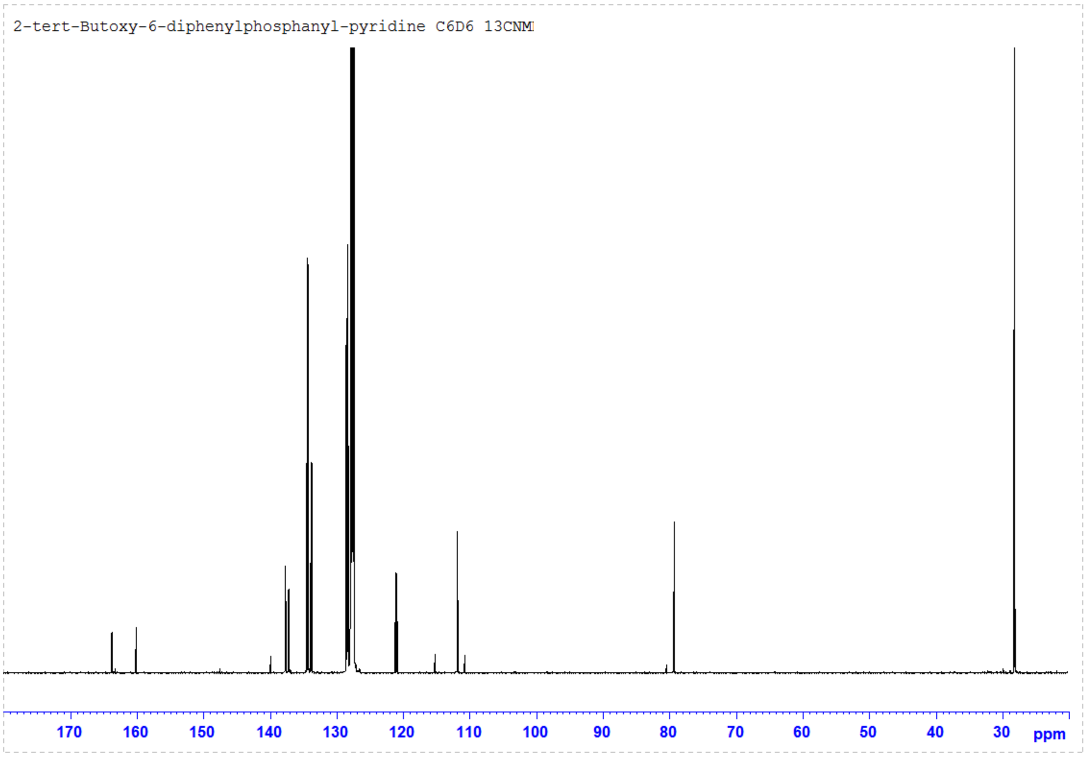

Figure A2.5: ^{13}C-NMR spectrum of 2-tert-butoxy-6-diphenylphosphanyl-pyridine (2) in C_6D_6.

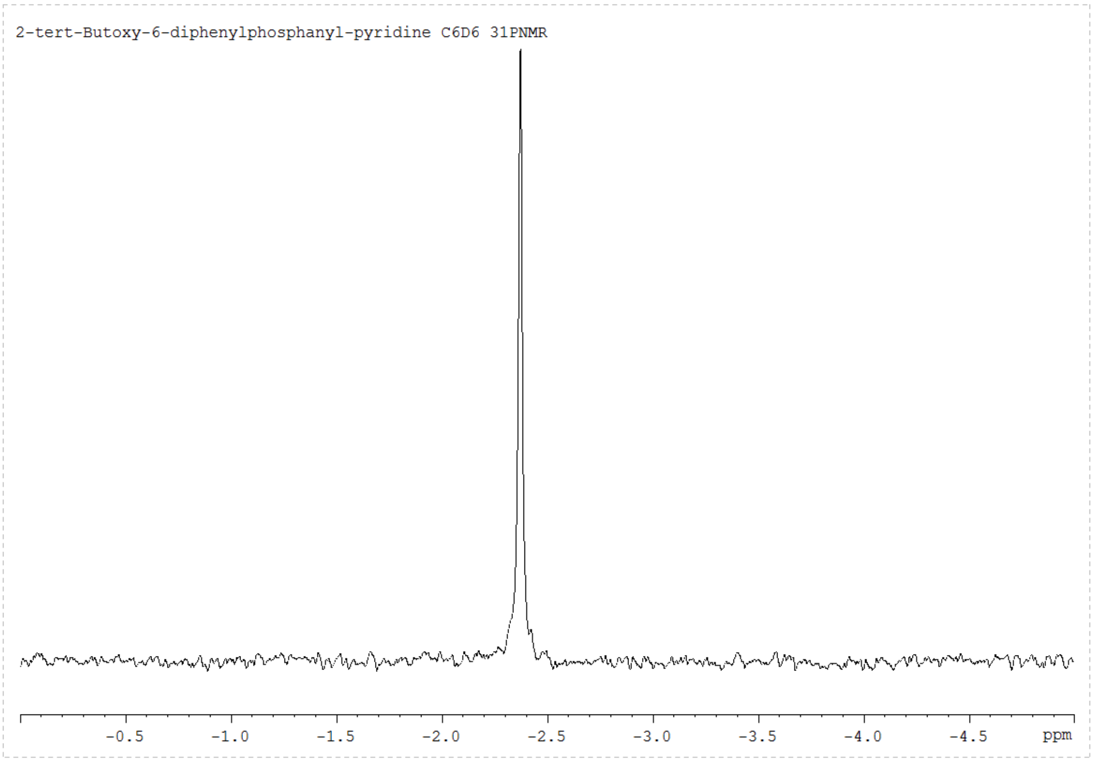

Figure A2.6: ^{31}P-NMR spectrum of 2-tert-butoxy-6-diphenylphosphanyl-pyridine (2) in C_6D_6.

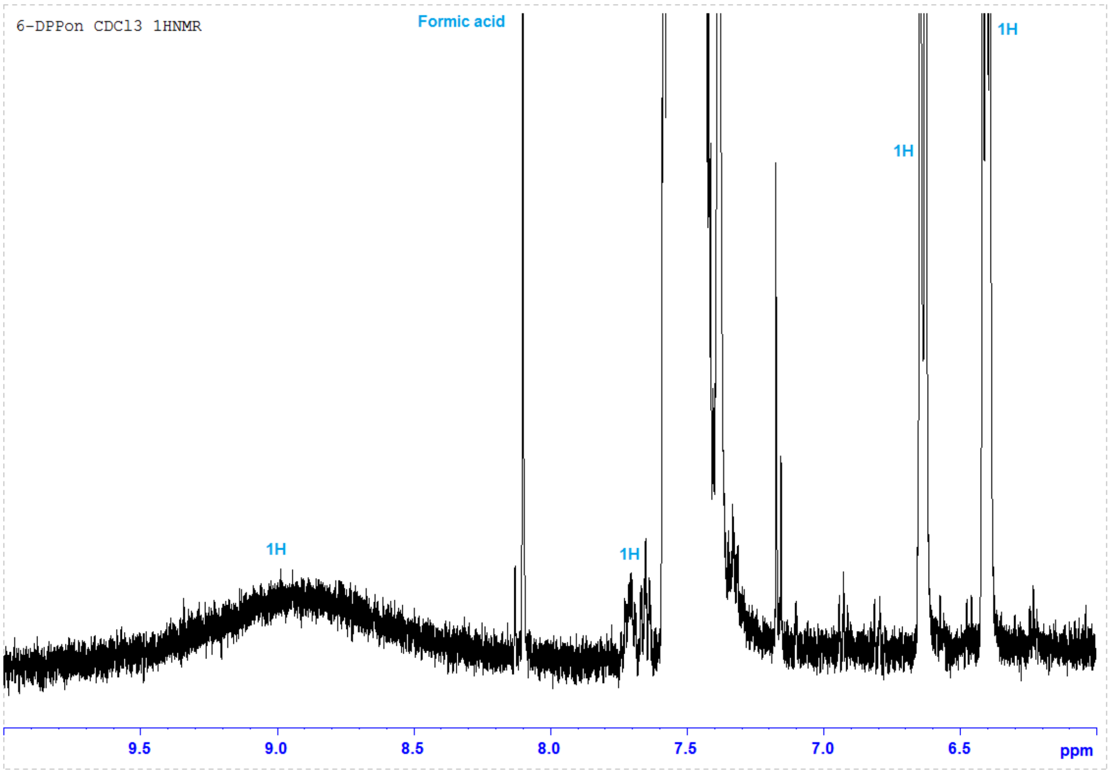

Figure A2.7: ^{1}H-NMR spectrum of 6-diphenylphosphanyl-1H-pyridin-2-one (6-DPPon) (3) in $CDCl_3$.

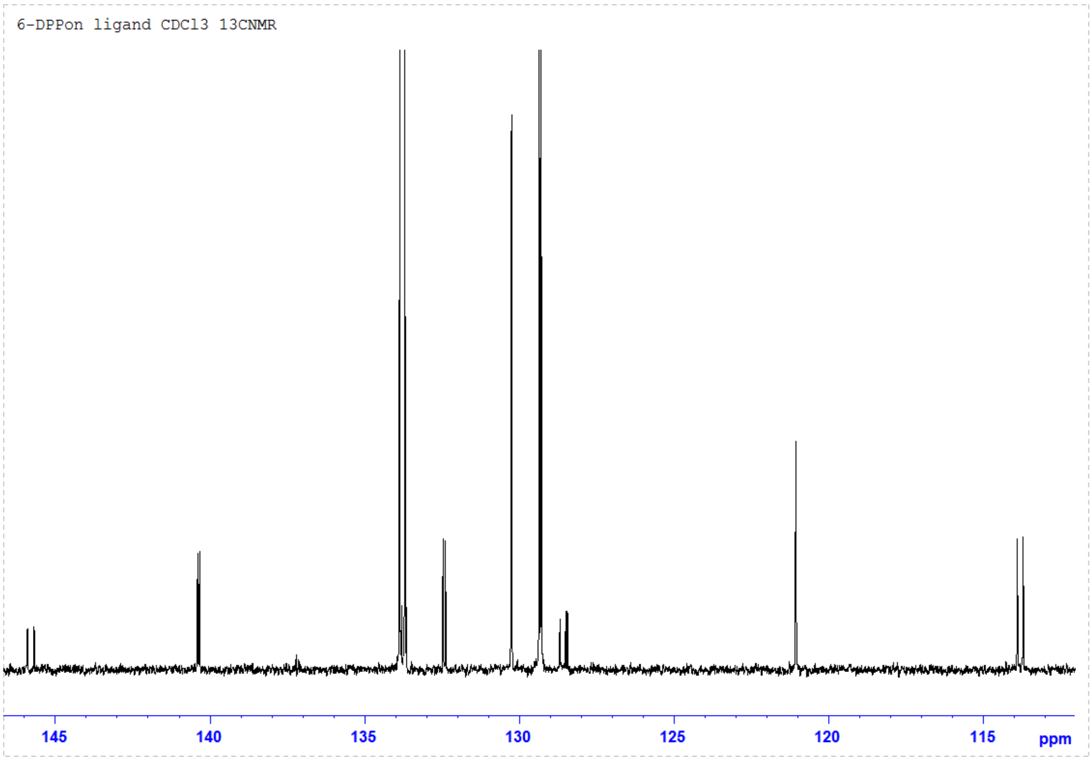

Figure A2.8: ^{13}C-NMR spectrum of 6-diphenylphosphanyl-1H-pyridin-2-one (6-DPPon) (3) in $CDCl_3$.

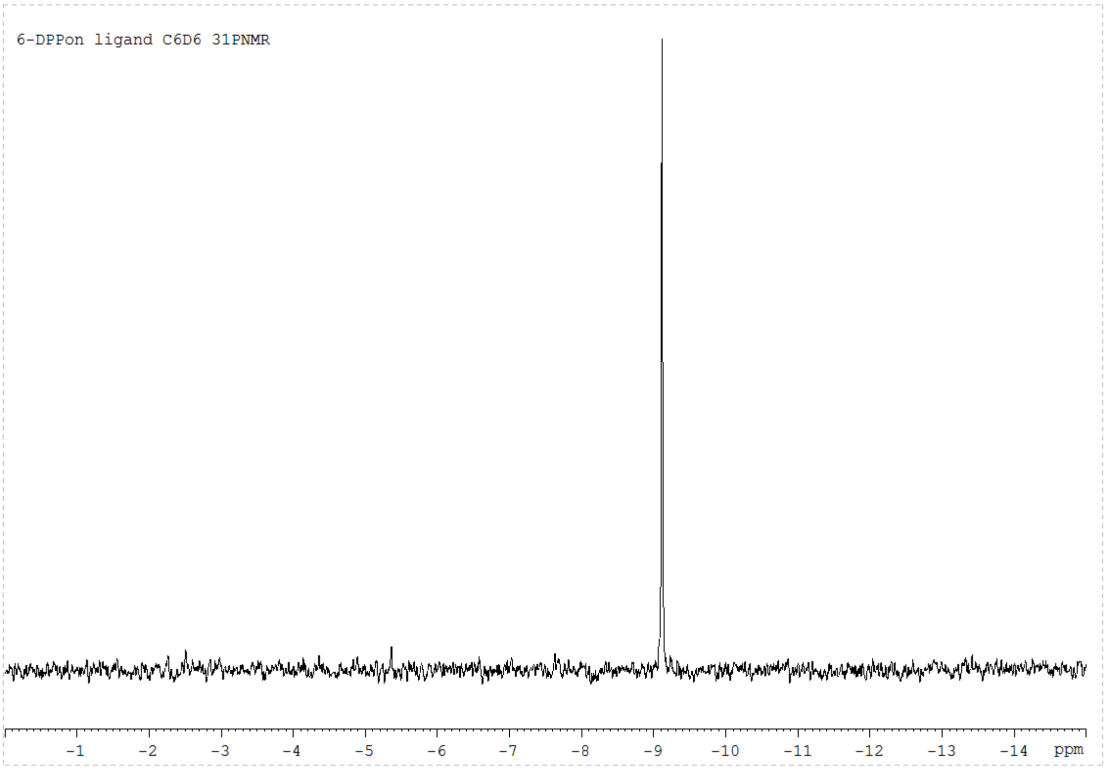

Figure A2.9: ^{31}P-NMR spectrum of 6-diphenylphosphanyl-1H-pyridin-2-one (6-DPPon) (3) in $CDCl_3$.

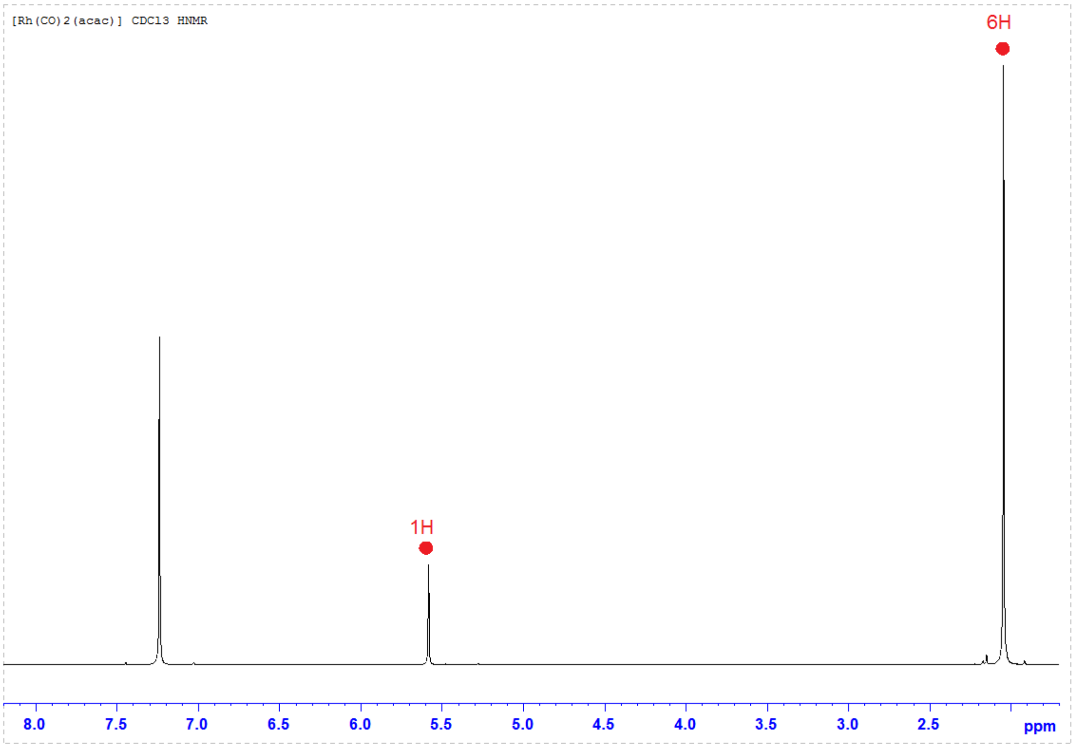

Figure A2.10: ^{1}H-NMR spectrum of $[Rh(CO)_2(acac)]$ in $CDCl_3$.

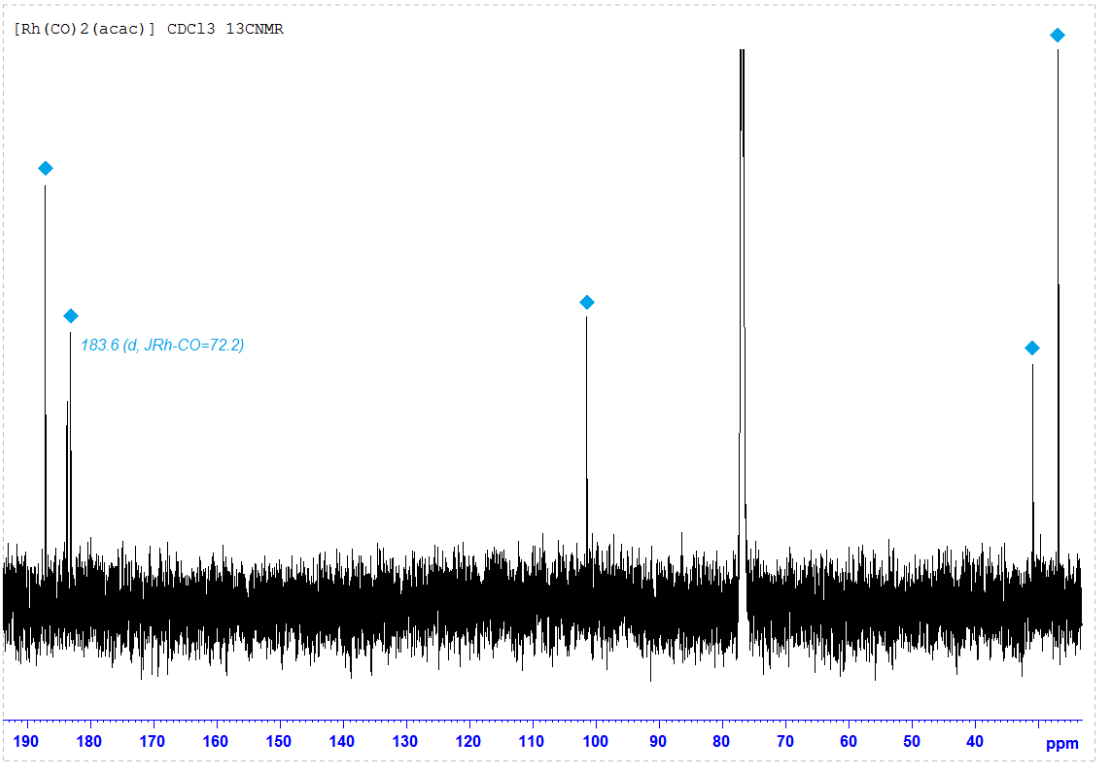

Figure A2.11: ^{13}C-NMR spectrum of $[Rh(CO)_2(acac)]$ in $CDCl_3$.

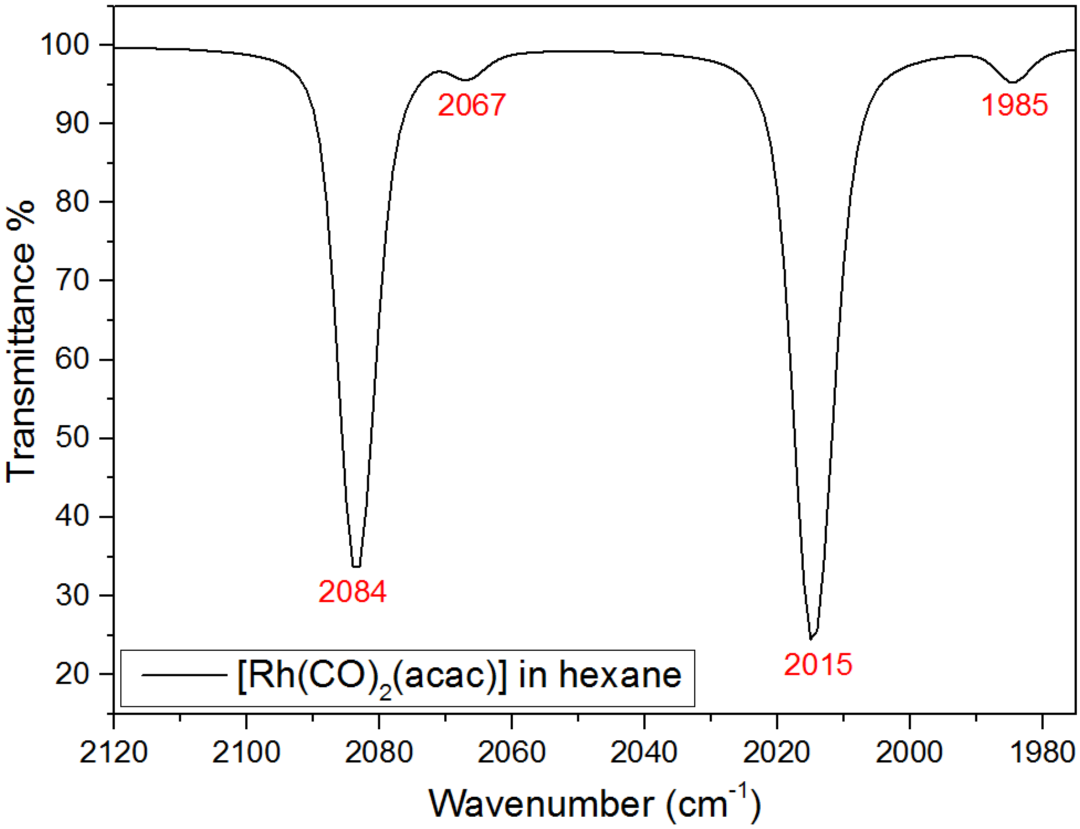

Figure A2.12: IR spectrum of $[Rh(CO)_2(acac)]$ in hexane.

Appendix-3

Important definitions, considerations and methods that can affect and used for the evaluation of electrocatalysts:

Current density (J) and Exchange current density (Jº)

Current density: It is the current in (mA) normalized by the geometric area of working electrode in cm^2:

$$J = \frac{i}{A}\ (mA/cm^2) \qquad \text{Eq. A3.1}$$

Exchange current density: It is the current density at equilibrium where rate of oxidation equals rate of reduction, the rate at such state called exchange current. Exchange current can be used as a measure for the feasibility of the electrode kinetics.[38] A system with a high exchange current density suggests having a high activity. For instance Pt has exchange current (10^{-2} A/cm^2) compared to Zn (10^{-11} A/cm^2) which means the hydrogen evolution from Pt is more likely than that from Zn. When exchange current is normalized by the electrode area (cm^2), it becomes exchange current density (for heterogeneous catalysis):

$$J^o = \frac{I^o}{A}\ (mA/cm^2) \qquad \text{Eq. A3.2}$$

Overpotential $(\boldsymbol{\eta})$

It is the difference between the applied potential and standard potential; a low value reflects efficient electrocatalysts ($\eta = E_{applied} - E^o$) **(Figure A3.1)**. **Onset potential:** voltage applied between working electrode at which the desired product is produced in a detectable amount (*eg.* 0.5 - 1.0 mA/cm^2).[48]

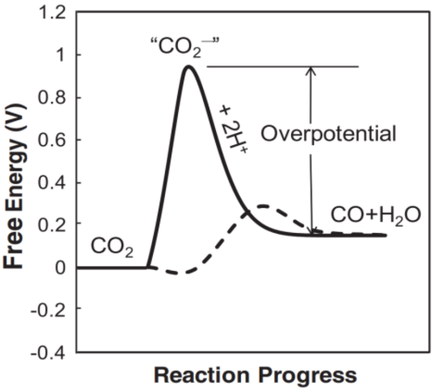

Figure A3.1: Schematic diagram of CO2RR in water in absence (solid) and presence (dashed) of electrocatalyst.[380]

Electrochemical considerations for CO2RR:

The electrocatalytic system of CO2RR can be described according to the following model:

$$E_{cell} = E^n + \eta_{ohmic} + \eta_{act} + \eta_{mt} \qquad \text{Eq. A3.3}$$

Where E_{cell} is the cell voltage, E^n is standard potential. The overpotentials: η_{ohmic} , η_{act} and η_{mt} are due to ohmic resistance, anodic and cathodic kinetic activation overpotetnial and overpotential due to limited mass transfer at the anode and cathode.[381] The contributions of each item can be modelled in a $J-V$ curve **(Figure A3.2)** and depend on the operating conditions.[381] At low current densities, the system is under kinetic control (can be described via Tafel equation). At high current densities, mass transfer limitation appears.[381]

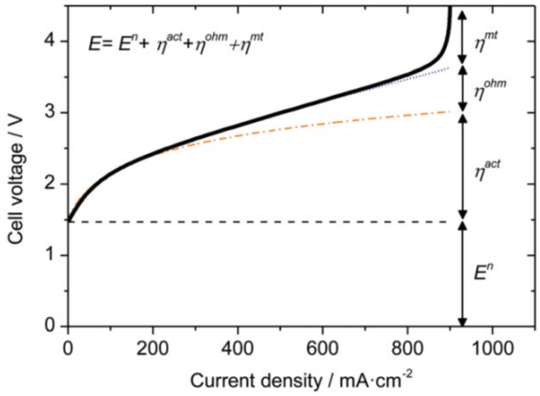

Figure A3.2: Current density-voltage curve of electrolyser able to produce CO (cathode) and O_2 (anode) including limiting factors (kinetic, ohmic and mass transport limitations).[381]

Tafel equation and Tafel plots

Tafel plot is a plot between voltages versus the Log of the current density. To apply the Tafel equation the system should be under kinetic control; no mass transfer limitation and no ohmic drop. The $J-V$ data obtained from LSV experiment with low scan rate. Tafel equation: In electrochemical kinetics, it correlates the rate of reaction with overpotential.

$$\eta = a + b\ Log\ J = \frac{-2.3\ RT}{\alpha nF} \log j^o + \frac{2.3RT}{\alpha nF}\ Log\ J \qquad \text{Eq. A3.4}$$

Where J and j^o are the current and the exchange current densities, respectively, α: charge transfer coefficient, n: number of electrons transferred, F: Faraday constant, R: ideal gas constant, and T is the temperature. **Tafel Plot:** Plot between $Log\ J$ vs overpotential(η). Tafel slop (***b***) can be used for determination of reaction mechanism for HER and CO2RR as the following:

For HER reaction: can proceed via three possible steps in acidic media.[26, 38, 41, 43, 44, 46, 47] Volmer step which involve the electrochemical hydrogen adsorption:

$$H_3O^+ + e^- + M \rightarrow MH_{ads} + H_2O, b = \frac{2.3RT}{\alpha F} \approx 120\ mV/dec$$

And the rate of Volmer step can be determined via the following equation:

$$v_1 = k_1(1-\theta) - k_{-1}\theta$$

Heyrovsky step which is an electrochemical desorption[382]:

$$MH_{ads} + e^- + H^+ \rightarrow \mathrm{M} + H_2, b = \frac{2.3RT}{\alpha F} \approx 40\ mV/dec.$$

And the rate of Heyrovsky step can be determined via the following equation:[382]

$$\nu_2 = k_2\theta - k_{-2}(1-\theta)$$

Tafel step which is a chemical desorption step:

$$2MH_{ads} \rightarrow 2\mathrm{M} + H_2,\ b = \frac{2.3RT}{\alpha F} \approx 30\ mV/dec.$$

And the rate of Tafel step can be determined via the following equation:[382]

$$\nu_3 = k_3\theta^2 - k_{-3}(1-\theta)^2$$

Where θ is the surface coverage and k is the rate constant.

For CO2RR, $b = 118\,mV/dec$ mV/dec means the generation of $CO_2^{\cdot}$ is the rate determining step for the electroreduction of $CO_2^{\cdot}$ $b = 59\,mV/dec$ means that there is a fast one electron transfer pre-equilibrium step before a chemical rate determining step.[6, 383] (J: Current density, α: charge transfer coefficient, n: no of electron in balanced electrochemical equation and F: faradaic constant).

Some thermodynamic considerations

The change in Gibbs free energy is correlated to the cell potential via $\Delta\ = -\mathrm{nFE_{cell}}$, where n is no of electrons and F is the faradaic efficiency. *i.e.* a spontaneous reaction has –ve Δ value and +ve $\mathrm{E_{cell}}$. The change in Gibbs free energy also is related to equilibrium constant $\Delta\ = -\mathrm{RT}\ln K$. **(Table A1.1)** summarized the standard Nernst potentials for all the potential products from CO2RR, the variation in the potentials with temperature can be calculated through Gibbs-Helmholtz equation **(Eq. A3.5)**:[3]

$$E(T) = \frac{-\Delta G}{nF} = -\frac{(\Delta H - T\Delta S)}{nF} \qquad \text{Eq. A3.6}$$

where ΔH and ΔS are the enthalpy and entropy change, respectively. The effect of the entropy is negligible compared to enthalpy change as it is the driving force.[3]

Stability and Durability of electrocatalysts

The stability of the electrocatalyst can be investigated through applying constant current or constant voltage and monitoring the overpotential or current as a function of time as in case of HER electrocatalysts. The durability of any electrocatalyst can be tested by applying multiple thousands of CV cycles and perform LSV after and before the CV cycles. The two tests can show if the catalyst started to be deactivated or not.

Electrochemical active surface area measurements (ECSA)

The electrochemical active surface area of the working electrodes can be determined through two methods (second method was described in the experimental chapter). First method involves the usage of the ferri/ferrocyanide redox couple ($[Fe(CN)_6]^{3-/4-}$) [131] by recording it through CV. By applying Randles-Sevcik equation **(Eq. A3.8)**, it is possible to obtain the ECSA at room temperature:

$$I_p = (2.69\ x\ 10^5)\ n^{\frac{3}{2}}\ A\ D^{\frac{1}{2}}\ C\ v^{\frac{1}{2}} \qquad \text{Eq. A3.7}$$

Electrochemical impedance spectroscopy (EIS)

EIS is used to investigate the kinetics of HER and interactions at electrode/electrolyte interface. In a simple Randles circuit **(Figure A3.3)**, the resistance value at high frequency corresponds to solution resistance (R_Ω) and the diameter of the semicircle corresponds to charge transfer resistance (R_{ct}). A low (R_{ct}) reflect a fast reaction rate.[48] EIS usually performed at η_{10} with frequency range between 10^5-0.01 Hz.[48]

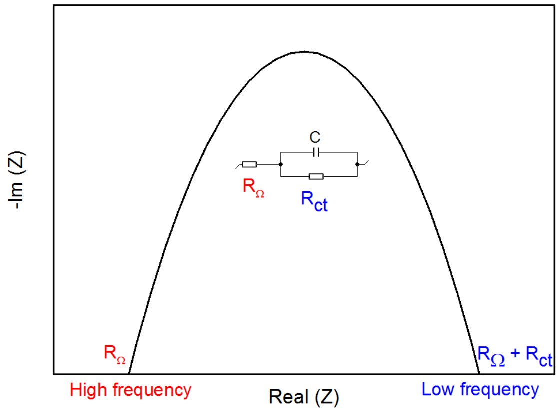

Figure A3.3: Randles circuit and its Nyquist plot.

The solubility of CO_2 on water limits the current

The solubility of CO_2 in water is low compared to that in non-aqueous media. The following equation explains the reason of why the solubility of CO_2 limits the current:

$$i_L = nFK_mC_b \qquad \text{Eq. A3.8}$$

Where F is the Faraday constant, K_m is the mass transfer coefficient, n is the electron stoichiometric coefficient and C_b is the bulk concentration of CO_2 ($[CO_2]$ = 30 mM at STP).[158]

The equilibria of CO_2 species in water[384]

Upon dissolving CO_2 in water, a rapid equilibrium takes place:[385] $CO_{2(g)} = CO_{2(aq)}$. Thermodynamic equilibria of CO_2 species in water play important role in CO2RR,[384] as the pH of the solution depends on other species like HCO_3^- and CO_3^{2-}**(Figure A3.4)**.

$$CO_2 + H_2O = HCO_3^- + H^+ \qquad \text{Eq. A3.9}$$

$$pH = pK_{a1} + log[HCO_3^-] - \log[CO_2] \qquad \text{Eq. A3.10}$$

Where pK_{a1} is $\log K_{a1}$ for the **(Eq. A3.11)** (the equilibrium constant) and equals 6.35 at 25 °C.

$$[CO_2] = \frac{P(CO_2)}{K_c} \qquad \text{Eq. A3.11}$$

$$pH = pK_{a1} + log[HCO_3^-] - \log\frac{P(CO_2)}{K_c} \qquad \text{Eq. A3.12}$$

$$pH = 7.82 + log[HCO_3^-] - \log P(CO_2) \qquad \text{Eq. A3.13}$$

K_c is Henry's constant and equals 3.38 x 10^{-2} mol. L^{-1}. atm^{-1} at 25 °C. For electrolyte solutions $[HCO_3^-]$ of concentrations 0.1 and 0.5 M the pH of these solutions are 6.82 and 7.52, respectively, at $P(CO_2) = 1\ atm$.

$$HCO_3^- = CO_3^{2-} + H^+ \qquad \text{Eq. A3.14}$$

$$pH = pK_{a2} + \log\frac{[CO_3^{-2}]}{[HCO_3^-]} \qquad \text{Eq. A3.15}$$

Where pK_{a2} is the equilibrium constant and equals 10.33 at 25 °C. By combining **(Eq. A3.13)** and **(Eq. A3.16)**, $P(CO_2)$ can be calculated:

$$P(CO_2) = pK_{a1} - pK_{a2} - \log K_c + \log\ [HCO_3^-] - \log\ \frac{[CO_3^{-2}]}{[HCO_3^-]} \qquad \text{Eq. A3.16}$$

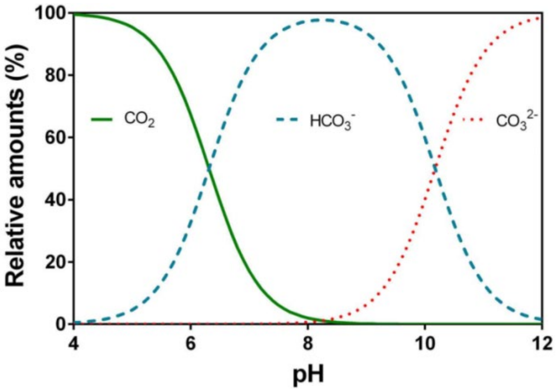

Figure A3.4: Distribution species diagram of carbonate species as a function of pH. [386]

It is worth noting that at the electrode during the electrolysis, the solution is not necessarily at equilibrium and OH^- anions are generated at the electrode in case of the involvement of H_2O in the electrochemical reaction.[384] Thus the local pH at the interface between electrode and electrolyte solution is higher than that of the bulk solution. The following chemical processes take place in the diffusion layer:[384]

- Slow hydration of $CO_{2(aq)}$ and carbonic acid (H_2CO_3) with K_H = 2.6 x 10^{-3} at 25 °C:[385]

$$CO_{2(aq)} + H_2O = H_2CO_3 \qquad \text{Eq. A3.17}$$

- Dissociation constant of carbonic acid (K_o = 1.7 x 10^{-4} at 25 °C), (Fast reactions), $H_2CO_3 = HCO_3^- + H^+$, thus it is better to show the formation of bicarbonate (ionization reaction) as the following:

$CO_{2(aq)} + H_2O = HCO_3^- + H^+$ ($K_1 = K_HK_o$= 4.4 x 10^{-7}), as less than 1% of CO_2 exist as H_2CO_3 .[385]

- Dissociation of HCO_3^-:

$$HCO_3^- = H^+ + CO_3^{-2}, K_2 = 4.7 \times 10^{-11} \text{ at } 25\ ^oC \qquad \text{Eq. A3.18}$$

- There are other equilibria take place: At high pH: $CO_2 + HO^- = HCO_3^-$, slow reaction with $K_{1'} \approx 3 \times 10^7$ M^{-1}. In solutions containing CO_3^{-2} "carbonate catalysis" takes place: $CO_{2(aq)} + CO_3^{-2} + H_2O = 2HCO_3^-$. Also some other instantaneous reactions occur such as:

$$H_2CO_3 + HO^- = HCO_3^- + H_2O \qquad \text{Eq. A3.19}$$

$$HCO_3^- + HO^- = CO_3^{2-} + H_2O \qquad \text{Eq. A3.20}$$

Isotope-Labelled $^{13}CO_2$ studies for CO2RR

Comparing the electrochemical performance and electroproduced compounds of any electrocatalyst under CO_2 and under N_2 or Ar is an effective and inexpensive method to determine the source of carbon in the produced products. Labelled studies can be used to investigate the source of C of the products resulted from CO2RR (CO_2/CO_3^{2-}).[387] Using labelled ^{13}C can be used to identify the source of C. Labelled $^{13}CO_2$ can be used or labelled electrolyte ($KH^{13}CO_3$). i.e. $KH^{13}CO_3$ can be prepared through bubbling KOH solution with $^{13}CO_2$ till the pH of the solution reaches the required pH. Gases products such as CO can be analysed using GC-MS can be used and signals at m/z = 28 and 29 can be used to identify the product.[388] For liquid products, ^{13}C and ^1H NMR are efficient technique to determine the source of the C by observing the change in the signal in ^{13}CNMR spectrum with and without using labelled ^{13}C under one condition which is having sufficient and detectable concentration.[389] Labelled ^{13}C lead to additional splitting in the adjacent H atoms and can be observed in ^{1}HNMR **(Figure A3.5)**.[390]

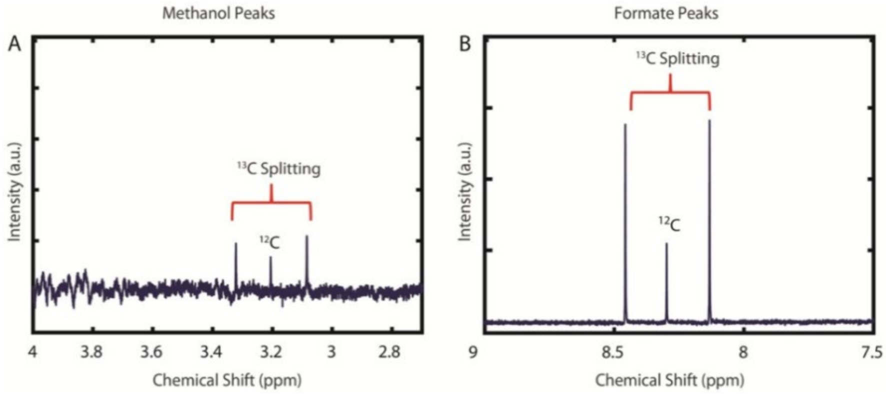

Figure A3.5: ^1H NMR spectrum upon using $^{13}CO_2$.[390]

Abbreviation list

acacH	Acetylacetone
b.p.	Boiling point
CA	Chronoamperometry
CC	Carbon cloth
CE%	Current efficiency
CO2RR	CO_2 reduction reaction
CP	Chronopotentiometry
CV	Cyclic Voltammetry
DMSO	Dimethyl sulfoxide
EDX (EDS)	Energy-dispersive X-ray spectroscopy
EIS	Electrochemical impedance
FDM	Fused deposition method
FE%	Faradaic efficiency
FID	Flame ionization detector
GC	Gas chromatography
HER	Hydrogen evolution reaction
HRTEM	High-resolution TEM
HPMC	Hydroxylpropyl methyl cellulose
LSV	Linear Sweep Voltammetry
OC	Open circuit potential
OD	Oxide derived
PD	Phosphide derived
PEI	Polyethylineimine
PLA	Polylactic acid polymer
PTS	Polyoxyethanyl-α-tocopheryl sebacate
RHE	Reversal hydrogen electrode
SEM	Scanning electron microscope
SS	Stainless steel mesh
TCD	Thermal conductivity detector
TEM	Transmission electron microscopy
XRD	X-Ray powder diffraction
XPS	X-ray photoelectron spectroscopy
3D printing	Processes used to synthesize three dimensional structures
6-DPPon	6-diphenylphosphanyl-2-pyridone

References

1. J. He, K. E. Dettelbach, D. A. Salvatore, T. Li and C. P. Berlinguette, *Angew. Chem. Int. Ed.*, 2017, **56**, 6068-6072.
2. C. Costentin, M. Robert and J.-M. Savéant, *Acc. Chem. Res.*, 2015, **48**, 2996-3006.
3. S. Hernández, M. Amin Farkhondehfal, F. Sastre, M. Makkee, G. Saracco and N. Russo, *Green Chem.*, 2017, **19**, 2326-2346.
4. K. P. Kuhl, T. Hatsukade, E. R. Cave, D. N. Abram, J. Kibsgaard and T. F. Jaramillo, *J. Am. Chem. Soc.*, 2014, **136**, 14107-14113.
5. T. Wang, H. Xie, M. Chen, A. D'Aloia, J. Cho, G. Wu and Q. Li, *Nano Energy*, 2017, **42**, 69-89.
6. D. D. Zhu, J. L. Liu and S. Z. Qiao, *Adv. Mater.*, 2016, **28**, 3423-3452.
7. A. Tatin, C. Comminges, B. Kokoh, C. Costentin, M. Robert and J.-M. Savéant, *Proc. Natl. Acad. Sci. U.S.A.*, 2016, **113**, 5526.
8. W. Zhu, R. Michalsky, Ö. Metin, H. Lv, S. Guo, C. J. Wright, X. Sun, A. A. Peterson and S. Sun, *J. Am. Chem. Soc.*, 2013, **135**, 16833-16836.
9. P. J. Chirik, *Acc. Chem. Res.*, 2015, **48**, 1687-1695.
10. F.-X. Felpin and E. Fouquet, *Chem. Eur. J.*, 2010, **16**, 12440-12445.
11. S. Nishimura, *Handbook of Heterogeneous Catalytic Hydrogenation for Organic Synthesis*, Wiley and sons, New York, 2001.
12. P. N. Rylander, *Hydrogenation Methods*, Academic Press, New York, 1985.
13. P. N. Rylander, *Ullmann's Encyclopedia of Industrial Chemistry*, Wiley-VCH, Weinheim, 2005.
14. M. Hudlickey, *Reductions in Organic Chemistry*, ACS, Washington, 1996.
15. B. Breit and W. Seiche, *J. Am. Chem. Soc.*, 2003, **125**, 6608-6609.
16. A. T. Straub, M. Otto, I. Usui and B. Breit, *Adv. Synth. Catal.*, 2013, **355**, 2071-2075.
17. M. T. Jensen, M. H. Rønne, A. K. Ravn, R. W. Juhl, D. U. Nielsen, X.-M. Hu, S. U. Pedersen, K. Daasbjerg and T. Skrydstrup, *Nat. Commun.*, 2017, **8**, 489.
18. J. M. Ogden, *Annu. Rev. Energy Env.*, 1999, **24**, 227-279.
19. S. Kumar, *Clean Hydrogen Production Methods*, Springer, 2015.
20. D. S. Tarnay, *Int. J. Hydrogen Energy*, 1985, **10**, 577-584.
21. S. Gao, Y. Liu, G.-D. Li, Y. Guo, Y. Zou and X. Zou, *Electrochim. Acta*, 2016, **199**, 99-107.
22. T. D. Tran, M. T. T. Nguyen, H. V. Le, D. N. Nguyen, Q. D. Truong and P. D. Tran, *Chem. Commun.*, 2018, **54**, 3363-3366.
23. E. J. Popczun, C. G. Read, C. W. Roske, N. S. Lewis and R. E. Schaak, *Angew. Chem.*, 2014, **126**, 5531-5534.
24. J. Tian, Q. Liu, A. M. Asiri and X. Sun, *J. Am. Chem. Soc.*, 2014, **136**, 7587-7590.
25. J. D. Benck, T. R. Hellstern, J. Kibsgaard, P. Chakthranont and T. F. Jaramillo, *ACS Catal*, 2014, **4**, 3957-3971.
26. Y. Yan, B. Xia, Z. Xu and X. Wang, *ACS Catal*, 2014, **4**, 1693-1705.
27. F. H. Saadi, A. I. Carim, J. M. Velazquez, J. H. Baricuatro, C. C. L. McCrory, M. P. Soriaga and N. S. Lewis, *ACS Catal*, 2014, **4**, 2866-2873.
28. Y.-R. Zheng, M.-R. Gao, Z.-Y. Yu, Q. Gao, H.-L. Gao and S.-H. Yu, *Chem. Sci.*, 2015, **6**, 4594-4598.
29. B. Cao, G. M. Veith, J. C. Neuefeind, R. R. Adzic and P. G. Khalifah, *J. Am. Chem. Soc.*, 2013, **135**, 19186-19192.
30. W.-F. Chen, K. Sasaki, C. Ma, A. I. Frenkel, N. Marinkovic, J. T. Muckerman, Y. Zhu and R. R. Adzic, *Angew. Chem. Int. Ed.*, 2012, **51**, 6131-6135.
31. H. Vrubel and X. Hu, *Angew. Chem. Int. Ed.*, 2012, **51**, 12703-12706.

32. W. F. Chen, C. H. Wang, K. Sasaki, N. Marinkovic, W. Xu, J. T. Muckerman, Y. Zhu and R. R. Adzic, *Energy Environ. Sci.*, 2013, **6**, 943-951.
33. M. Fan, H. Chen, Y. Wu, L.-L. Feng, Y. Liu, G.-D. Li and X. Zou, *J. Mater. Chem. A*, 2015, **3**, 16320-16326.
34. S.-S. Tong, X.-J. Wang, Q.-C. Li and X.-J. Han, *Chinese J Anal Chem*, 2016, **44**, 1447-1457.
35. X. Zou and Y. Zhang, *Chem. Soc. Rev.*, 2015, **44**, 5148-5180.
36. A. Eftekhari, *Int. J. Hydrogen Energy*, 2017, **42**, 11053-11077.
37. M. Ciobanu, J. P. Wilburn, M. L. Krim and D. E. Cliffel, in *Handbook of Electrochemistry*, ed. C. G. Zoski, Elsevier, Amsterdam, 2007, DOI: https://doi.org/10.1016/B978-044451958-0.50002-1, pp. 3-29.
38. L. R. F. Allen J. Bard, *Electrochemical Methods: Fundamentals and Applications*, John Wiley and Sons, New York, 2001.
39. K. P. Kuhl, E. R. Cave, D. N. Abram and T. F. Jaramillo, *Energy Environ. Sci.*, 2012, **5**, 7050-7059.
40. Y. Li, *IEEE Nanotechnol. Mag.*, 2014, **8**, 22-28.
41. Y. Liang, Y. Li, H. Wang and H. Dai, *J. Am. Chem. Soc.*, 2013, **135**, 2013-2036.
42. M. Zeng and Y. Li, *J. Mater. Chem. A*, 2015, **3**, 14942-14962.
43. E. Gileadi, *Physical Electrochemistry: Fundamentals, Techniques and Applications*, John Wiley and Sons, 2011.
44. A. Lasia, *Handbook of fuel cells : fundamentals, technology, and applications*, John Wiley and Sons Chichester, 2010.
45. A. B. Laursen, A. S. Varela, F. Dionigi, H. Fanchiu, C. Miller, O. L. Trinhammer, J. Rossmeisl and S. Dahl, *J. Chem. Educ.*, 2012, **89**, 1595-1599.
46. S. Trasatti, *J. Electroanal. Chem.*, 1972, **39**, 163-184.
47. H. Tributsch and J. C. Bennett, *J. Electroanal. Chem.*, 1977, **81**, 97-111.
48. J. Wang, F. Xu, H. Jin, Y. Chen and Y. Wang, *Adv. Mater.*, 2017, **29**, 1605838.
49. B. E. Conway and B. V. Tilak, *Electrochim. Acta*, 2002, **47**, 3571-3594.
50. Y. Li, H. Wang, L. Xie, Y. Liang, G. Hong and H. Dai, *J. Am. Chem. Soc.*, 2011, **133**, 7296-7299.
51. J. O. M. Bockris and E. C. Potter, *J. Electrochem. Soc.*, 1952, **99**, 169-186.
52. L. Liao, S. Wang, J. Xiao, X. Bian, Y. Zhang, M. D. Scanlon, X. Hu, Y. Tang, B. Liu and H. H. Girault, *Energy Environ. Sci.*, 2014, **7**, 387-392.
53. J. A. Keith, K. A. Grice, C. P. Kubiak and E. A. Carter, *J. Am. Chem. Soc.*, 2013, **135**, 15823-15829.
54. J. Hu, C. Zhang, X. Meng, H. Lin, C. Hu, X. Long and S. Yang, *J. Mater. Chem. A*, 2017, **5**, 5995-6012.
55. K. Elbert, J. Hu, Z. Ma, Y. Zhang, G. Chen, W. An, P. Liu, H. S. Isaacs, R. R. Adzic and J. X. Wang, *ACS Catal*, 2015, **5**, 6764-6772.
56. C. G. Morales-Guio, L.-A. Stern and X. Hu, *Chem. Soc. Rev.*, 2014, **43**, 6555-6569.
57. S. Lu and Z. Zhuang, *Sci. China Mater.*, 2016, **59**, 217-238.
58. R. Parsons, *Trans. Faraday Soc.*, 1958, **54**, 1053-1063.
59. M. Chatti, J. L. Gardiner, M. Fournier, B. Johannessen, T. Williams, T. R. Gengenbach, N. Pai, C. Nguyen, D. R. MacFarlane, R. K. Hocking and A. N. Simonov, *Nat. Catal.*, 2019, **2**, 457-465.
60. S. Jiménez Sandoval, D. Yang, R. F. Frindt and J. C. Irwin, *Phys. Rev. B*, 1991, **44**, 3955-3962.
61. H. Pan, *Sci. Rep.*, 2014, **4**, 5348.
62. Y. Liu, G. Yu, G.-D. Li, Y. Sun, T. Asefa, W. Chen and X. Zou, *Angew. Chem. Int. Ed.*, 2015, **54**, 10752-10757.

63. F.-X. Ma, H. B. Wu, B. Y. Xia, C.-Y. Xu and X. W. Lou, *Angew. Chem. Int. Ed.*, 2015, **54**, 15395-15399.
64. R. Ma, Y. Zhou, Y. Chen, P. Li, Q. Liu and J. Wang, *Angew. Chem. Int. Ed.*, 2015, **54**, 14723-14727.
65. S. Carenco, D. Portehault, C. Boissière, N. Mézailles and C. Sanchez, *Chem. Rev.*, 2013, **113**, 7981-8065.
66. Z. Gholamvand, D. McAteer, C. Backes, N. McEvoy, A. Harvey, N. C. Berner, D. Hanlon, C. Bradley, I. Godwin, A. Rovetta, M. E. G. Lyons, G. S. Duesberg and J. N. Coleman, *Nanoscale*, 2016, **8**, 5737-5749.
67. A.-M. Alexander and J. S. J. Hargreaves, *Chem. Soc. Rev.*, 2010, **39**, 4388-4401.
68. M. S. Faber and S. Jin, *Energy Environ. Sci.*, 2014, **7**, 3519-3542.
69. X. F. Lu, L. Yu and X. W. Lou, *Sci. Adv.*, 2019, **5**, eaav6009.
70. X. Yang, A.-Y. Lu, Y. Zhu, S. Min, M. N. Hedhili, Y. Han, K.-W. Huang and L.-J. Li, *Nanoscale*, 2015, **7**, 10974-10981.
71. W. L. Kwong, C. C. Lee and J. Messinger, *J. Phys. Chem. C*, 2017, **121**, 284-292.
72. S. Liu, Y. Qian and L. Xu, *Solid State Commun.*, 2009, **149**, 438-440.
73. Y. Shi and B. Zhang, *Chem. Soc. Rev.*, 2016, **45**, 1529-1541.
74. P. E. R. Blanchard, A. P. Grosvenor, R. G. Cavell and A. Mar, *Chem. Mater.*, 2008, **20**, 7081-7088.
75. J. Kibsgaard, T. F. Jaramillo and F. Besenbacher, *Nat. Chem.*, 2014, **6**, 248.
76. Y. Lin, M. Liu, Y. Pan and J. Zhang, *J. Mater. Sci.*, 2017, **52**, 10406-10417.
77. S. T. Oyama, X. Wang, Y. K. Lee, K. Bando and F. G. Requejo, *J. Catal.*, 2002, **210**, 207-217.
78. Y. Xu, R. Wu, J. Zhang, Y. Shi and B. Zhang, *Chem. Commun.*, 2013, **49**, 6656-6658.
79. Q. Liu, Z. Pu, A. M. Asiri and X. Sun, *Electrochim. Acta*, 2014, **149**, 324-329.
80. C. Y. Son, I. H. Kwak, Y. R. Lim and J. Park, *Chem. Commun.*, 2016, **52**, 2819-2822.
81. P. Xiao, M. A. Sk, L. Thia, X. Ge, R. J. Lim, J.-Y. Wang, K. H. Lim and X. Wang, *Energy Environ. Sci.*, 2014, **7**, 2624-2629.
82. Z. Zhang, B. Lu, J. Hao, W. Yang and J. Tang, *Chem. Commun.*, 2014, **50**, 11554-11557.
83. S. Han, Y. Feng, F. Zhang, C. Yang, Z. Yao, W. Zhao, F. Qiu, L. Yang, Y. Yao, X. Zhuang and X. Feng, *Adv. Funct. Mater.*, 2015, **25**, 3899-3906.
84. J. Kibsgaard and T. F. Jaramillo, *Angew. Chem. Int. Ed.*, 2014, **53**, 14433-14437.
85. Y. Pan, Y. Liu, J. Zhao, K. Yang, J. Liang, D. Liu, W. Hu, D. Liu, Y. Liu and C. Liu, *J. Mater. Chem. A*, 2015, **3**, 1656-1665.
86. Z. Pu, Q. Liu, A. M. Asiri and X. Sun, *ACS Appl. Mater. Interfaces*, 2014, **6**, 21874-21879.
87. Y. Shi, Y. Xu, S. Zhuo, J. Zhang and B. Zhang, *ACS Appl. Mater. Interfaces*, 2015, **7**, 2376-2384.
88. T. Tian, L. Ai and J. Jiang, *RSC Adv.*, 2015, **5**, 10290-10295.
89. C. Lv, Z. Peng, Y. Zhao, Z. Huang and C. Zhang, *J. Mater. Chem. A*, 2016, **4**, 1454-1460.
90. T. Helmenstine, Abundance of elements on earth, https://sciencenotes.org/abundance-of-elements-in-earths-crust-periodic-table-and-list/).
91. Z. Gao, Q. Gao, Z. Liu, C. Zhang, X. Zhang, X. Liu, R. Wang and N. Li, *RSC Adv.*, 2016, **6**, 114430-114435.
92. Y. Liang, Q. Liu, A. M. Asiri, X. Sun and Y. Luo, *ACS Catal*, 2014, **4**, 4065-4069.

93. F. H. Saadi, A. I. Carim, E. Verlage, J. C. Hemminger, N. S. Lewis and M. P. Soriaga, *J. Phys. Chem. C*, 2014, **118**, 29294-29300.
94. J. Tian, Q. Liu, N. Cheng, A. M. Asiri and X. Sun, *Angew. Chem. Int. Ed.*, 2014, **53**, 9577-9581.
95. Z. Pu, C. Tang and Y. Luo, *Int. J. Hydrogen Energy*, 2015, **40**, 5092-5098.
96. Z. Zhang, J. Hao, W. Yang, B. Lu and J. Tang, *Nanoscale*, 2015, **7**, 4400-4405.
97. C. Deng, J. Xie, Y. Xue, M. He, X. Wei and Y.-M. Yan, *RSC Adv.*, 2016, **6**, 68568-68573.
98. J. Tian, Q. Liu, Y. Liang, Z. Xing, A. M. Asiri and X. Sun, *ACS Appl. Mater. Interfaces*, 2014, **6**, 20579-20584.
99. N. K. Chaudhari, P. Yu, B. Kim, K. Lee and J. Li, *Dalton Transactions*, 2018, **47**, 16011-16018.
100. G. Cho, H. Kim, Y. S. Park, Y.-K. Hong and D.-H. Ha, *Int. J. Hydrogen Energy*, 2018, **43**, 11326-11334.
101. D. E. Schipper, Z. Zhao, H. Thirumalai, A. P. Leitner, S. L. Donaldson, A. Kumar, F. Qin, Z. Wang, L. C. Grabow, J. Bao and K. H. Whitmire, *Chem. Mater.*, 2018, **30**, 3588-3598.
102. S. Yao, V. Forstner, P. W. Menezes, C. Panda, S. Mebs, E. M. Zolnhofer, M. E. Miehlich, T. Szilvási, N. Ashok Kumar, M. Haumann, K. Meyer, H. Grützmacher and M. Driess, *Chem. Sci.*, 2018, **9**, 8590-8597.
103. Y. Du, Z. Li, Y. Liu, Y. Yang and L. Wang, *Appl. Surf. Sci.*, 2018, **457**, 1081-1086.
104. W. L. Kwong, E. Gracia-Espino, C. C. Lee, R. Sandström, T. Wågberg and J. Messinger, *ChemSusChem*, 2017, **10**, 4544-4551.
105. Z. Pu, I. S. Amiinu, C. Zhang, M. Wang, Z. Kou and S. Mu, *Nanoscale*, 2017, **9**, 3555-3560.
106. P. Yu, L. Wang, Y. Xie, C. Tian, F. Sun, J. Ma, M. Tong, W. Zhou, J. Li and H. Fu, *Small*, 2018, **14**, 1801717.
107. X. Peng, A. M. Qasim, W. Jin, L. Wang, L. Hu, Y. Miao, W. Li, Y. Li, Z. Liu, K. Huo, K.-y. Wong and P. K. Chu, *Nano Energy*, 2018, **53**, 66-73.
108. P. Jiang, Q. Liu, Y. Liang, J. Tian, A. M. Asiri and X. Sun, *Angew. Chem. Int. Ed.*, 2014, **53**, 12855-12859.
109. X. Li, W. Liu, M. Zhang, Y. Zhong, Z. Weng, Y. Mi, Y. Zhou, M. Li, J. J. Cha, Z. Tang, H. Jiang, X. Li and H. Wang, *Nano Lett.*, 2017, **17**, 2057-2063.
110. X. Guo, Z. Feng, Z. Lv, Y. Bu, Q. Liu, L. Zhao, C. Hao, G. Li and Q. Lei, *ChemElectroChem*, 2017, **4**, 2052-2058.
111. R. Warren, J. Price, E. Graham, N. Forstenhaeusler and J. VanDerWal, *Science*, 2018, **360**, 791-795.
112. T. L. Root, J. T. Price, K. R. Hall, S. H. Schneider, C. Rosenzweig and J. A. Pounds, *Nature*, 2003, **421**, 57-60.
113. K. Hasselmann, *Science*, 1997, **276**, 914-915.
114. R. A. Kerr, *Science*, 2007, **316**, 188-190.
115. S. S. Myers, A. Zanobetti, I. Kloog, P. Huybers, A. D. B. Leakey, A. J. Bloom, E. Carlisle, L. H. Dietterich, G. Fitzgerald, T. Hasegawa, N. M. Holbrook, R. L. Nelson, M. J. Ottman, V. Raboy, H. Sakai, K. A. Sartor, J. Schwartz, S. Seneweera, M. Tausz and Y. Usui, *Nature*, 2014, **510**, 139.
116. Z. Sun, T. Ma, H. Tao, Q. Fan and B. Han, *Chem*, 2017, **3**, 560-587.
117. K. E. Dalle, J. Warnan, J. J. Leung, B. Reuillard, I. S. Karmel and E. Reisner, *Chem. Rev.*, 2019, **119**, 2752-2875.
118. M. Mikkelsen, M. Jørgensen and F. C. Krebs, *Energy Environ. Sci.*, 2010, **3**, 43-81.
119. A. M. Appel, J. E. Bercaw, A. B. Bocarsly, H. Dobbek, D. L. DuBois, M. Dupuis, J. G. Ferry, E. Fujita, R. Hille, P. J. A. Kenis, C. A. Kerfeld, R. H. Morris, C. H. F. Peden, A. R. Portis, S. W. Ragsdale, T. B. Rauchfuss, J. N.

H. Reek, L. C. Seefeldt, R. K. Thauer and G. L. Waldrop, *Chem. Rev.*, 2013, **113**, 6621-6658.

120. J. Shi, Y. Jiang, Z. Jiang, X. Wang, X. Wang, S. Zhang, P. Han and C. Yang, *Chem. Soc. Rev.*, 2015, **44**, 5981-6000.
121. O. S. Bushuyev, P. De Luna, C. T. Dinh, L. Tao, G. Saur, J. van de Lagemaat, S. O. Kelley and E. H. Sargent, *Joule*, 2018, **2**, 825-832.
122. C. S. Chen, J. H. Wan and B. S. Yeo, *J. Phys. Chem. C*, 2015, **119**, 26875-26882.
123. Z. Han, R. Kortlever, H.-Y. Chen, J. C. Peters and T. Agapie, *ACS Cent. Sci.*, 2017, **3**, 853-859.
124. M. Ma, K. Djanashvili and W. A. Smith, *Angew. Chem. Int. Ed.*, 2016, **55**, 6680-6684.
125. D. Raciti, L. Cao, K. J. T. Livi, P. F. Rottmann, X. Tang, C. Li, Z. Hicks, K. H. Bowen, K. J. Hemker, T. Mueller and C. Wang, *ACS Catal*, 2017, **7**, 4467-4472.
126. D. Ren, N. T. Wong, A. D. Handoko, Y. Huang and B. S. Yeo, *J. Phys. Chem. Lett.*, 2016, **7**, 20-24.
127. K. U. D. Calvinho, A. B. Laursen, K. M. K. Yap, T. A. Goetjen, S. Hwang, N. Murali, B. Mejia-Sosa, A. Lubarski, K. M. Teeluck, E. S. Hall, E. Garfunkel, M. Greenblatt and G. C. Dismukes, *Energy Environ. Sci.*, 2018, **11**, 2550-2559.
128. S. Lee, D. Kim and J. Lee, *Angew. Chem. Int. Ed.*, 2015, **54**, 14701-14705.
129. J. Qiao, Y. Liu, F. Hong and J. Zhang, *Chem. Soc. Rev.*, 2014, **43**, 631-675.
130. B. Endrődi, G. Bencsik, F. Darvas, R. Jones, K. Rajeshwar and C. Janáky, *Prog. Energy Combust. Sci.*, 2017, **62**, 133-154.
131. T.-T. Zhuang, Z.-Q. Liang, A. Seifitokaldani, Y. Li, P. De Luna, T. Burdyny, F. Che, F. Meng, Y. Min, R. Quintero-Bermudez, C. T. Dinh, Y. Pang, M. Zhong, B. Zhang, J. Li, P.-N. Chen, X.-L. Zheng, H. Liang, W.-N. Ge, B.-J. Ye, D. Sinton, S.-H. Yu and E. H. Sargent, *Nat. Catal.*, 2018, **1**, 421-428.
132. A. A. Peterson and J. K. Nørskov, *J. Phys. Chem. Lett.*, 2012, **3**, 251-258.
133. C. Chen, J. F. Khosrowabadi Kotyk and S. W. Sheehan, *Chem*, 2018, **4**, 2571-2586.
134. I. Ganesh, *Renewable and Sustainable Energy Reviews*, 2014, **31**, 221-257.
135. D. Du, R. Lan, J. Humphreys and S. Tao, *J. Appl. Electrochem.*, 2017, **47**, 661-678.
136. C. Long, X. Li, J. Guo, Y. Shi, S. Liu and Z. Tang, *Small Methods*, 2019, **3**, 1800369.
137. B. Kumar, J. P. Brian, V. Atla, S. Kumari, K. A. Bertram, R. T. White and J. M. Spurgeon, *Catal. Today*, 2016, **270**, 19-30.
138. Z.-L. Wang, C. Li and Y. Yamauchi, *Nano Today*, 2016, **11**, 373-391.
139. W. Zhu, B. M. Tackett, J. G. Chen and F. Jiao, *Top. Curr. Chem.*, 2018, **376**, 41.
140. J. He, N. J. J. Johnson, A. Huang and C. P. Berlinguette, *ChemSusChem*, 2018, **11**, 48-57.
141. M. K. Birhanu, M.-C. Tsai, A. W. Kahsay, C.-T. Chen, T. S. Zeleke, K. B. Ibrahim, C.-J. Huang, W.-N. Su and B.-J. Hwang, *Advanced Materials Interfaces*, 2018, **5**, 1800919.
142. H. Xie, T. Wang, J. Liang, Q. Li and S. Sun, *Nano Today*, 2018, **21**, 41-54.
143. in *Activation of Small Molecules*, DOI: 10.1002/9783527609352.ch1.
144. R. Kas, R. Kortlever, H. Yılmaz, M. T. M. Koper and G. Mul, *ChemElectroChem*, 2015, **2**, 354-358.
145. A. S. Varela, M. Kroschel, T. Reier and P. Strasser, *Catal. Today*, 2016, **260**, 8-13.
146. F. Calle-Vallejo and M. T. M. Koper, *Angew. Chem.*, 2013, **125**, 7423-7426.

147. A. A. Peterson, F. Abild-Pedersen, F. Studt, J. Rossmeisl and J. K. Nørskov, *Energy Environ. Sci.*, 2010, **3**, 1311-1315.
148. D. Raciti, M. Mao, J. H. Park and C. Wang, *Catal. Sci. Technol.*, 2018, **8**, 2364-2369.
149. D. Ren, J. Fong and B. S. Yeo, *Nat. Commun.*, 2018, **9**, 925.
150. M. Dunwell, X. Yang, B. P. Setzler, J. Anibal, Y. Yan and B. Xu, *ACS Catal*, 2018, **8**, 3999-4008.
151. Y. Hori, H. Wakebe, T. Tsukamoto and O. Koga, *Surf. Sci.*, 1995, **335**, 258-263.
152. Y. Hori, R. Takahashi, Y. Yoshinami and A. Murata, *J. Phys. Chem. B*, 1997, **101**, 7075-7081.
153. Y. Hori, A. Murata and R. Takahashi, *J. Chem. Soc., Faraday Trans. 1*, 1989, **85**, 2309-2326.
154. S. Ma, M. Sadakiyo, R. Luo, M. Heima, M. Yamauchi and P. J. A. Kenis, *J. Power Sources*, 2016, **301**, 219-228.
155. Y. Hori, *Modern Aspects of Electrochemistry*, Springer, 2008.
156. C. W. Li and M. W. Kanan, *J. Am. Chem. Soc.*, 2012, **134**, 7231-7234.
157. R. Reske, H. Mistry, F. Behafarid, B. Roldan Cuenya and P. Strasser, *J. Am. Chem. Soc.*, 2014, **136**, 6978-6986.
158. A. Taheri Najafabadi, *Int. J. Energy Res.*, 2013, **37**, 485-499.
159. E. L. Clark, J. Resasco, A. Landers, J. Lin, L.-T. Chung, A. Walton, C. Hahn, T. F. Jaramillo and A. T. Bell, *ACS Catal*, 2018, **8**, 6560-6570.
160. S. Sen, D. Liu and G. T. R. Palmore, *ACS Catal*, 2014, **4**, 3091-3095.
161. K. Manthiram, B. J. Beberwyck and A. P. Alivisatos, *J. Am. Chem. Soc.*, 2014, **136**, 13319-13325.
162. D. Raciti, K. J. Livi and C. Wang, *Nano Lett.*, 2015, **15**, 6829-6835.
163. R. Kas, K. K. Hummadi, R. Kortlever, P. de Wit, A. Milbrat, M. W. J. Luiten-Olieman, N. E. Benes, M. T. M. Koper and G. Mul, *Nat. Commun.*, 2016, **7**, 10748.
164. J. Albo and A. Irabien, *J. Catal.*, 2016, **343**, 232-239.
165. C.-T. Dinh, T. Burdyny, M. G. Kibria, A. Seifitokaldani, C. M. Gabardo, F. P. García de Arquer, A. Kiani, J. P. Edwards, P. De Luna, O. S. Bushuyev, C. Zou, R. Quintero-Bermudez, Y. Pang, D. Sinton and E. H. Sargent, *Science*, 2018, **360**, 783-787.
166. K. Klingan, T. Kottakkat, Z. P. Jovanov, S. Jiang, C. Pasquini, F. Scholten, P. Kubella, A. Bergmann, B. Roldan Cuenya, C. Roth and H. Dau, *ChemSusChem*, 2018, **11**, 3449-3459.
167. A. Bagger, W. Ju, A. S. Varela, P. Strasser and J. Rossmeisl, *ChemPhysChem*, 2017, **18**, 3266-3273.
168. Y. Wang, D. Wang, C. J. Dares, S. L. Marquard, M. V. Sheridan and T. J. Meyer, *Proc. Natl. Acad. Sci. U.S.A.*, 2018, **115**, 278-283.
169. G. Kyriacou and A. Anagnostopoulos, *J. Electroanal. Chem.*, 1992, **328**, 233-243.
170. R. J. Lim, M. Xie, M. A. Sk, J.-M. Lee, A. Fisher, X. Wang and K. H. Lim, *Catal. Today*, 2014, **233**, 169-180.
171. Y. Wang, J. Zhou, W. Lv, H. Fang and W. Wang, *Appl. Surf. Sci.*, 2016, **362**, 394-398.
172. R. Reske, M. Duca, M. Oezaslan, K. J. P. Schouten, M. T. M. Koper and P. Strasser, *J. Phys. Chem. Lett.*, 2013, **4**, 2410-2413.
173. Z.-Y. Chang, S.-J. Huo, J.-M. He and J.-H. Fang, *Surfaces and Interfaces*, 2017, **6**, 116-121.
174. S. Ma, M. Sadakiyo, M. Heima, R. Luo, R. T. Haasch, J. I. Gold, M. Yamauchi and P. J. A. Kenis, *J. Am. Chem. Soc.*, 2017, **139**, 47-50.
175. S. Sarfraz, A. T. Garcia-Esparza, A. Jedidi, L. Cavallo and K. Takanabe, *ACS Catal*, 2016, **6**, 2842-2851.

176. Q. Li, J. Fu, W. Zhu, Z. Chen, B. Shen, L. Wu, Z. Xi, T. Wang, G. Lu, J.-j. Zhu and S. Sun, *J. Am. Chem. Soc.*, 2017, **139**, 4290-4293.
177. Y. Lum and J. W. Ager, *Energy Environ. Sci.*, 2018, **11**, 2935-2944.
178. C. G. Morales-Guio, E. R. Cave, S. A. Nitopi, J. T. Feaster, L. Wang, K. P. Kuhl, A. Jackson, N. C. Johnson, D. N. Abram, T. Hatsukade, C. Hahn and T. F. Jaramillo, *Nat. Catal.*, 2018, **1**, 764-771.
179. A. S. Varela, C. Schlaup, Z. P. Jovanov, P. Malacrida, S. Horch, I. E. L. Stephens and I. Chorkendorff, *J. Phys. Chem. C*, 2013, **117**, 20500-20508.
180. R. B. Sandberg, J. H. Montoya, K. Chan and J. K. Nørskov, *Surf. Sci.*, 2016, **654**, 56-62.
181. D. Ren, B. S.-H. Ang and B. S. Yeo, *ACS Catal*, 2016, **6**, 8239-8247.
182. E. L. Clark, C. Hahn, T. F. Jaramillo and A. T. Bell, *J. Am. Chem. Soc.*, 2017, **139**, 15848-15857.
183. M. Watanabe, M. Shibata, A. Kato, M. Azuma and T. Sakata, *J. Electrochem. Soc.*, 1991, **138**, 3382-3389.
184. H. Yoshio, M. Akira, I. Shin-ya, Y. Yuzuru and K. Osamu, *Chem. Lett.*, 1989, **18**, 1567-1570.
185. T. Shinagawa, G. O. Larrazábal, A. J. Martín, F. Krumeich and J. Pérez-Ramírez, *ACS Catal*, 2018, **8**, 837-844.
186. H. Shin, Y. Ha and H. Kim, *J. Phys. Chem. Lett.*, 2016, **7**, 4124-4129.
187. R. M. Arán-Ais, D. Gao and B. Roldan Cuenya, *Acc. Chem. Res.*, 2018, **51**, 2906-2917.
188. C. Hahn, T. Hatsukade, Y.-G. Kim, A. Vailionis, J. H. Baricuatro, D. C. Higgins, S. A. Nitopi, M. P. Soriaga and T. F. Jaramillo, *Proc. Natl. Acad. Sci. U.S.A.*, 2017, **114**, 5918-5923.
189. H. Mistry, A. S. Varela, C. S. Bonifacio, I. Zegkinoglou, I. Sinev, Y.-W. Choi, K. Kisslinger, E. A. Stach, J. C. Yang, P. Strasser and B. R. Cuenya, *Nat. Commun.*, 2016, **7**, 12123.
190. P. Yang, Z.-J. Zhao, X. Chang, R. Mu, S. Zha, G. Zhang and J. Gong, *Angew. Chem. Int. Ed.*, 2018, **57**, 7724-7728.
191. D. Ren, Y. Deng, A. D. Handoko, C. S. Chen, S. Malkhandi and B. S. Yeo, *ACS Catal*, 2015, **5**, 2814-2821.
192. A. D. Handoko, C. W. Ong, Y. Huang, Z. G. Lee, L. Lin, G. B. Panetti and B. S. Yeo, *J. Phys. Chem. C*, 2016, **120**, 20058-20067.
193. X. Wang, A. S. Varela, A. Bergmann, S. Kühl and P. Strasser, *ChemSusChem*, 2017, **10**, 4642-4649.
194. M. Ma, K. Djanashvili and W. A. Smith, *PCCP*, 2015, **17**, 20861-20867.
195. A. Dutta, M. Rahaman, N. C. Luedi, M. Mohos and P. Broekmann, *ACS Catal*, 2016, **6**, 3804-3814.
196. X. Zheng, J. Han, Y. Fu, Y. Deng, Y. Liu, Y. Yang, T. Wang and L. Zhang, *Nano Energy*, 2018, **48**, 93-100.
197. P. De Luna, R. Quintero-Bermudez, C.-T. Dinh, M. B. Ross, O. S. Bushuyev, P. Todorović, T. Regier, S. O. Kelley, P. Yang and E. H. Sargent, *Nat. Catal.*, 2018, **1**, 103-110.
198. J.-F. Xie, Y.-X. Huang, W.-W. Li, X.-N. Song, L. Xiong and H.-Q. Yu, *Electrochim. Acta*, 2014, **139**, 137-144.
199. T. N. Huan, P. Simon, G. Rousse, I. Génois, V. Artero and M. Fontecave, *Chem. Sci.*, 2017, **8**, 742-747.
200. A. Dutta, M. Rahaman, M. Mohos, A. Zanetti and P. Broekmann, *ACS Catal*, 2017, **7**, 5431-5437.
201. H. Xiao, W. A. Goddard, T. Cheng and Y. Liu, *Proc. Natl. Acad. Sci. U.S.A.*, 2017, **114**, 6685-6688.
202. M. Favaro, H. Xiao, T. Cheng, W. A. Goddard, J. Yano and E. J. Crumlin, *Proc. Natl. Acad. Sci. U.S.A.*, 2017, **114**, 6706-6711.

203. M. Fields, X. Hong, J. K. Nørskov and K. Chan, *J. Phys. Chem. C*, 2018, **122**, 16209-16215.
204. A. Eilert, F. Cavalca, F. S. Roberts, J. Osterwalder, C. Liu, M. Favaro, E. J. Crumlin, H. Ogasawara, D. Friebel, L. G. M. Pettersson and A. Nilsson, *J. Phys. Chem. Lett.*, 2017, **8**, 285-290.
205. D. Gao, I. Zegkinoglou, N. J. Divins, F. Scholten, I. Sinev, P. Grosse and B. Roldan Cuenya, *ACS Nano*, 2017, **11**, 4825-4831.
206. Y. Lum and J. W. Ager, *Angew. Chem. Int. Ed.*, 2018, **57**, 551-554.
207. A. Verdaguer-Casadevall, C. W. Li, T. P. Johansson, S. B. Scott, J. T. McKeown, M. Kumar, I. E. L. Stephens, M. W. Kanan and I. Chorkendorff, *J. Am. Chem. Soc.*, 2015, **137**, 9808-9811.
208. X. Feng, K. Jiang, S. Fan and M. W. Kanan, *ACS Cent. Sci.*, 2016, **2**, 169-174.
209. C. W. Li, J. Ciston and M. W. Kanan, *Nature*, 2014, **508**, 504.
210. J.-J. Velasco-Vélez, T. Jones, D. Gao, E. Carbonio, R. Arrigo, C.-J. Hsu, Y.-C. Huang, C.-L. Dong, J.-M. Chen, J.-F. Lee, P. Strasser, B. Roldan Cuenya, R. Schlögl, A. Knop-Gericke and C.-H. Chuang, *ACS Sustainable Chem. Eng.*, 2019, **7**, 1485-1492.
211. Y. Lum and J. W. Ager, *Nat. Catal.*, 2019, **2**, 86-93.
212. K. Chan, C. Tsai, H. A. Hansen and J. K. Nørskov, *ChemCatChem*, 2014, **6**, 1899-1905.
213. D. Yang, Q. Zhu, C. Chen, H. Liu, Z. Liu, Z. Zhao, X. Zhang, S. Liu and B. Han, *Nat. Commun.*, 2019, **10**, 677.
214. Q.-G. Zhu, X.-F. Sun, X.-C. Kang, J. Ma, Q.-L. Qian and B.-X. Han, *Acta Phys-Chim. Sin.*, 2016, **32**, 261-266.
215. Y. Huang, Y. Deng, A. D. Handoko, G. K. L. Goh and B. S. Yeo, *ChemSusChem*, 2018, **11**, 320-326.
216. K. R. Phillips, Y. Katayama, J. Hwang and Y. Shao-Horn, *J. Phys. Chem. Lett.*, 2018, **9**, 4407-4412.
217. X. F. Hu and C. J. Hirschmugl, *Phys. Rev. B*, 2005, **72**, 205439.
218. R. García-Muelas, F. Dattila, T. Shinagawa, A. J. Martín, J. Pérez-Ramírez and N. López, *J. Phys. Chem. Lett.*, 2018, **9**, 7153-7159.
219. I. Kasatkin, P. Kurr, B. Kniep, A. Trunschke and R. Schlögl, *Angew. Chem. Int. Ed.*, 2007, **46**, 7324-7327.
220. Z.-Q. Liang, T.-T. Zhuang, A. Seifitokaldani, J. Li, C.-W. Huang, C.-S. Tan, Y. Li, P. De Luna, C. T. Dinh, Y. Hu, Q. Xiao, P.-L. Hsieh, Y. Wang, F. Li, R. Quintero-Bermudez, Y. Zhou, P. Chen, Y. Pang, S.-C. Lo, L.-J. Chen, H. Tan, Z. Xu, S. Zhao, D. Sinton and E. H. Sargent, *Nat. Commun.*, 2018, **9**, 3828.
221. M. Peng, S. Ci, P. Shao, P. Cai and Z. Wen, *Journal of Nanoscience and Nanotechnology*, 2019, **19**, 3232-3236.
222. C. S. Chen, A. D. Handoko, J. H. Wan, L. Ma, D. Ren and B. S. Yeo, *Catal. Sci. Technol.*, 2015, **5**, 161-168.
223. M. G. Kibria, C.-T. Dinh, A. Seifitokaldani, P. De Luna, T. Burdyny, R. Quintero-Bermudez, M. B. Ross, O. S. Bushuyev, F. P. García de Arquer, P. Yang, D. Sinton and E. H. Sargent, *Adv. Mater.*, 2018, **30**, 1804867.
224. N. R. de Tacconi, W. Chanmanee, B. H. Dennis and K. Rajeshwar, *J. Mater. Res.*, 2017, **32**, 1727-1734.
225. D. Gao, F. Scholten and B. Roldan Cuenya, *ACS Catal*, 2017, **7**, 5112-5120.
226. D. Gao, I. T. McCrum, S. Deo, Y.-W. Choi, F. Scholten, W. Wan, J. G. Chen, M. J. Janik and B. Roldan Cuenya, *ACS Catal*, 2018, **8**, 10012-10020.
227. J. S. Manzano, Z. B. Weinstein, A. D. Sadow and I. I. Slowing, *ACS Catal*, 2017, **7**, 7567-7577.
228. C. R. Tubío, J. Azuaje, L. Escalante, A. Coelho, F. Guitián, E. Sotelo and A. Gil, *J. Catal.*, 2016, **334**, 110-115.

229. K. Sun, T.-S. Wei, B. Y. Ahn, J. Y. Seo, S. J. Dillon and J. A. Lewis, *Adv. Mater.*, 2013, **25**, 4539-4543.
230. M. D. Symes, P. J. Kitson, J. Yan, C. J. Richmond, G. J. T. Cooper, R. W. Bowman, T. Vilbrandt and L. Cronin, *Nat. Chem.*, 2012, **4**, 349.
231. https://megadepot.com/resource/a-guide-to-3d-printing).
232. R. M. Langford and C. Clinton, *Micron*, 2004, **35**, 607-611.
233. R. M. Langford and M. Rogers, *Micron*, 2008, **39**, 1325-1330.
234. P. Chen, L.-K. Wang, G. Wang, M.-R. Gao, J. Ge, W.-J. Yuan, Y.-H. Shen, A.-J. Xie and S.-H. Yu, *Energy Environ. Sci.*, 2014, **7**, 4095-4103.
235. Y. Li, W. Zhou, H. Wang, L. Xie, Y. Liang, F. Wei, J.-C. Idrobo, S. J. Pennycook and H. Dai, *Nat. Nanotechnol.*, 2012, **7**, 394.
236. S. Y. Lee, H. Jung, N.-K. Kim, H.-S. Oh, B. K. Min and Y. J. Hwang, *J. Am. Chem. Soc.*, 2018, **140**, 8681-8689.
237. C. F. C. Lim, Doctor of Philosophy, University of Canterbury, 2017.
238. M. W. Kanan and D. G. Nocera, *Science*, 2008, **321**, 1072.
239. J. R. Shapley, ed., *Inorganic Syntheses*, Wiley and sons, Hoboken, New Jersey, 2004.
240. Y. Takashima, Y. Fukuhara, Y. Sato, T. Tsuruoka and K. Akamatsu, *Eur. J. Inorg. Chem.*, 2017, **2017**, 5344-5349.
241. A. Grigoropoulos, A. I. McKay, A. P. Katsoulidis, R. P. Davies, A. Haynes, L. Brammer, J. Xiao, A. S. Weller and M. J. Rosseinsky, *Angew. Chem. Int. Ed.*, 2018, **57**, 4532-4537.
242. G. Férey, C. Mellot-Draznieks, C. Serre, F. Millange, J. Dutour, S. Surblé and I. Margiolaki, *Science*, 2005, **309**, 2040-2042.
243. B. J. Frost and C. A. Mebi, *Organometallics*, 2004, **23**, 5317-5323.
244. D. N. Akbayeva, L. Gonsalvi, W. Oberhauser, M. Peruzzini, F. Vizza, P. Brüggeller, A. Romerosa, G. Sava and A. Bergamo, *Chem. Commun.*, 2003, 264-265.
245. Z. Pu, Q. Liu, C. Tang, A. M. Asiri and X. Sun, *Nanoscale*, 2014, **6**, 11031-11034.
246. S. Marini, P. Salvi, P. Nelli, R. Pesenti, M. Villa, M. Berrettoni, G. Zangari and Y. Kiros, *Electrochim. Acta*, 2012, **82**, 384-391.
247. N. Pentland, J. O. M. Bockris and E. Sheldon, *J. Electrochem. Soc.*, 1957, **104**, 182-194.
248. Y. Yan, L. Thia, B. Y. Xia, X. Ge, Z. Liu, A. Fisher and X. Wang, *Adv. Sci.*, 2015, **2**, 1500120.
249. L. Tian, X. Yan and X. Chen, *ACS Catal*, 2016, **6**, 5441-5448.
250. M. H. Suliman, A. Adam, M. N. Siddiqui, Z. H. Yamani and M. Qamar, *Carbon*, 2019, **144**, 764-771.
251. S. Gao, M. Yang, S. Li, J. Xia, J. Mei, S. Xie and H. Liu, *Sustainable Energy & Fuels*, 2019, **3**, 823-830.
252. Y.-J. Gu, W. Wen and J.-M. Wu, *J. Mater. Chem. A*, 2018, **6**, 21078-21086.
253. D. Ye, Y. Yu, J. Tang, L. Liu and Y. Wu, *Nanoscale*, 2016, **8**, 10406-10414.
254. J. D. Benck, Z. Chen, L. Y. Kuritzky, A. J. Forman and T. F. Jaramillo, *ACS Catal*, 2012, **2**, 1916-1923.
255. Z. Liu, Z. Gao, F. Luo, S. Yuan, K. Wang, N. Li and X. Li, *ChemCatChem*, 2018, **10**, 3441-3446.
256. C.-T. Dinh, A. Jain, F. P. G. de Arquer, P. De Luna, J. Li, N. Wang, X. Zheng, J. Cai, B. Z. Gregory, O. Voznyy, B. Zhang, M. Liu, D. Sinton, E. J. Crumlin and E. H. Sargent, *Nature Energy*, 2019, **4**, 107-114.
257. T. Shinagawa and K. Takanabe, *J. Phys. Chem. C*, 2016, **120**, 24187-24196.
258. H. Gu, Y. Huang, L. Zuo, W. Fan and T. Liu, *Inorg. Chem. Front.*, 2016, **3**, 1280-1288.

259. S. Wei, K. Qi, Z. Jin, J. Cao, W. Zheng, H. Chen and X. Cui, *ACS Omega*, 2016, **1**, 1367-1373.
260. A. Han, H. Zhang, R. Yuan, H. Ji and P. Du, *ACS Appl. Mater. Interfaces*, 2017, **9**, 2240-2248.
261. C.-C. Hou, Q.-Q. Chen, C.-J. Wang, F. Liang, Z. Lin, W.-F. Fu and Y. Chen, *ACS Appl. Mater. Interfaces*, 2016, **8**, 23037-23048.
262. S. Liu, C. Liu, J. Guo and W. Yan, *Micro Nano Lett.*, 2018, **13**, 190-194.
263. R. Daiyan, W. H. Saputera, Q. Zhang, E. Lovell, S. Lim, Y. H. Ng, X. Lu and R. Amal, *Advanced Sustainable Systems*, 2019, **3**, 1800064.
264. J. Zeng, K. Bejtka, W. Ju, M. Castellino, A. Chiodoni, A. Sacco, M. A. Farkhondehfal, S. Hernández, D. Rentsch, C. Battaglia and C. F. Pirri, *Appl. Catal. B-Environ.*, 2018, **236**, 475-482.
265. Y. Wang, B. Kong, D. Zhao, H. Wang and C. Selomulya, *Nano Today*, 2017, **15**, 26-55.
266. W. Xu and H. Wang, *Chinese Journal of Catalysis*, 2017, **38**, 991-1005.
267. U. A. M. Bediako D.K., Nocera D.G., *Catalytic Oxygen Evolution by Cobalt Oxido Thin Films*, Springer, Cham, 2015.
268. M. W. Kanan, J. Yano, Y. Surendranath, M. Dincă, V. K. Yachandra and D. G. Nocera, *J. Am. Chem. Soc.*, 2010, **132**, 13692-13701.
269. C. Costentin, T. R. Porter and J.-M. Savéant, *J. Am. Chem. Soc.*, 2016, **138**, 5615-5622.
270. Y. Liu, F. Yang, W. Qin and G. Yang, *J. Colloid Interface Sci.*, 2019, **534**, 55-63.
271. N. Han, K. R. Yang, Z. Lu, Y. Li, W. Xu, T. Gao, Z. Cai, Y. Zhang, V. S. Batista, W. Liu and X. Sun, *Nat. Commun.*, 2018, **9**, 924.
272. J. S. Mondschein, J. F. Callejas, C. G. Read, J. Y. C. Chen, C. F. Holder, C. K. Badding and R. E. Schaak, *Chem. Mater.*, 2017, **29**, 950-957.
273. Z.-H. Xue, H. Su, Q.-Y. Yu, B. Zhang, H.-H. Wang, X.-H. Li and J.-S. Chen, *Adv. Energy Mater.*, 2017, **7**, 1602355.
274. M. Huynh, C. Shi, S. J. L. Billinge and D. G. Nocera, *J. Am. Chem. Soc.*, 2015, **137**, 14887-14904.
275. T. Liu, L. Xie, J. Yang, R. Kong, G. Du, A. M. Asiri, X. Sun and L. Chen, *ChemElectroChem*, 2017, **4**, 1840-1845.
276. F. Hu, S. Zhu, S. Chen, Y. Li, L. Ma, T. Wu, Y. Zhang, C. Wang, C. Liu, X. Yang, L. Song, X. Yang and Y. Xiong, *Adv. Mater.*, 2017, **29**, 1606570.
277. M. W. Kanan, Y. Surendranath and D. G. Nocera, *Chem. Soc. Rev.*, 2009, **38**, 109-114.
278. M. N. Carcassi and F. Fineschi, *Energy*, 2005, **30**, 1439-1451.
279. C. C. Piet W. N. M. Van Leeuwen, ed., *Rhodium Catalyzed Hydroformylation*, Springer, Dordrecht.
280. in *The Handbook of Homogeneous Hydrogenation*, pp. 1279-1324.
281. J. Chen, C. Chen, C. Ji and Z. Lu, *Org. Lett.*, 2016, **18**, 1594-1597.
282. S. Monfette, Z. R. Turner, S. P. Semproni and P. J. Chirik, *J. Am. Chem. Soc.*, 2012, **134**, 4561-4564.
283. T. N. Gieshoff, U. Chakraborty, M. Villa and A. Jacobi von Wangelin, *Angew. Chem. Int. Ed.*, 2017, **56**, 3585-3589.
284. S. C. Bart, E. Lobkovsky and P. J. Chirik, *J. Am. Chem. Soc.*, 2004, **126**, 13794-13807.
285. R. Xu, S. Chakraborty, S. M. Bellows, H. Yuan, T. R. Cundari and W. D. Jones, *ACS Catal*, 2016, **6**, 2127-2135.
286. P. Á. Szilágyi, P. Serra-Crespo, I. Dugulan, J. Gascon, H. Geerlings and B. Dam, *CrystEngComm*, 2013, **15**, 10175-10178.
287. S. Bhattacharjee, C. Chen and W.-S. Ahn, *RSC Adv.*, 2014, **4**, 52500-52525.
288. C. A. Mebi and B. J. Frost, *Organometallics*, 2005, **24**, 2339-2346.

289. R. P. Allen J. Bard, Joseph Jordan, *Standard Potentials in Aqueous Solution*, Marcel Dekker, Inc, New York and Basel, 1985.
290. C. W. Lee, K. D. Yang, D.-H. Nam, J. H. Jang, N. H. Cho, S. W. Im and K. T. Nam, *Adv. Mater.*, 2018, **30**, 1704717.
291. C. Tang, L. Gan, R. Zhang, W. Lu, X. Jiang, A. M. Asiri, X. Sun, J. Wang and L. Chen, *Nano Lett.*, 2016, **16**, 6617-6621.
292. D. Zhou, L. He, W. Zhu, X. Hou, K. Wang, G. Du, C. Zheng, X. Sun and A. M. Asiri, *J. Mater. Chem. A*, 2016, **4**, 10114-10117.
293. J. F. Callejas, J. M. McEnaney, C. G. Read, J. C. Crompton, A. J. Biacchi, E. J. Popczun, T. R. Gordon, N. S. Lewis and R. E. Schaak, *ACS Nano*, 2014, **8**, 11101-11107.
294. D. Li, Q. Liao, B. Ren, Q. Jin, H. Cui and C. Wang, *J. Mater. Chem. A*, 2017, **5**, 11301-11308.
295. J. J. Gao, Luo P., Qiu H-J, Wang Y., *Nanotechnology*, 2017, **28**, 105705.
296. Y. Yao, N. Mahmood, L. Pan, G. Shen, R. Zhang, R. Gao, F.-e. Aleem, X. Yuan, X. Zhang and J.-J. Zou, *Nanoscale*, 2018, **10**, 21327-21334.
297. R. Liu, S. Gu, H. Du and C. M. Li, *J. Mater. Chem. A*, 2014, **2**, 17263-17267.
298. Y. Zhang, H. Zhang, Y. Feng, L. Liu and Y. Wang, *ACS Appl. Mater. Interfaces*, 2015, **7**, 26684-26690.
299. Y. Yan, B. Y. Xia, X. Ge, Z. Liu, A. Fisher and X. Wang, *Chem. Eur. J.*, 2015, **21**, 18062-18067.
300. Z. Pu, Q. Liu, P. Jiang, A. M. Asiri, A. Y. Obaid and X. Sun, *Chem. Mater.*, 2014, **26**, 4326-4329.
301. J. M. McEnaney, J. C. Crompton, J. F. Callejas, E. J. Popczun, A. J. Biacchi, N. S. Lewis and R. E. Schaak, *Chem. Mater.*, 2014, **26**, 4826-4831.
302. M. Liu, L. Yang, T. Liu, Y. Tang, S. Luo, C. Liu and Y. Zeng, *J. Mater. Chem. A*, 2017, **5**, 8608-8615.
303. M. Liu and J. Li, *ChemistrySelect*, 2017, **2**, 9472-9478.
304. F. Wang, X. Yang, B. Dong, X. Yu, H. Xue and L. Feng, *Electrochem. Commun.*, 2018, **92**, 33-38.
305. X. Zhu, M. Liu, Y. Liu, R. Chen, Z. Nie, J. Li and S. Yao, *J. Mater. Chem. A*, 2016, **4**, 8974-8977.
306. J. M. McEnaney, J. Chance Crompton, J. F. Callejas, E. J. Popczun, C. G. Read, N. S. Lewis and R. E. Schaak, *Chem. Commun.*, 2014, **50**, 11026-11028.
307. H. Du, S. Gu, R. Liu and C. M. Li, *Int. J. Hydrogen Energy*, 2015, **40**, 14272-14278.
308. X. Wang, Y. V. Kolen'ko, X.-Q. Bao, K. Kovnir and L. Liu, *Angew. Chem. Int. Ed.*, 2015, **54**, 8188-8192.
309. Y. Pan, W. Hu, D. Liu, Y. Liu and C. Liu, *J. Mater. Chem. A*, 2015, **3**, 13087-13094.
310. L. Feng, H. Vrubel, M. Bensimon and X. Hu, *PCCP*, 2014, **16**, 5917-5921.
311. D. Kim, J. Resasco, Y. Yu, A. M. Asiri and P. Yang, *Nat. Commun.*, 2014, **5**, 4948.
312. D. Kong, H. Wang, Z. Lu and Y. Cui, *J. Am. Chem. Soc.*, 2014, **136**, 4897-4900.
313. M. Ledendecker, S. Krick Calderón, C. Papp, H.-P. Steinrück, M. Antonietti and M. Shalom, *Angew. Chem. Int. Ed.*, 2015, **54**, 12361-12365.
314. M. Li, X. Liu, Y. Xiong, X. Bo, Y. Zhang, C. Han and L. Guo, *J. Mater. Chem. A*, 2015, **3**, 4255-4265.
315. C. G. Read, J. F. Callejas, C. F. Holder and R. E. Schaak, *ACS Appl. Mater. Interfaces*, 2016, **8**, 12798-12803.
316. J. Jiang, C. Wang, J. Zhang, W. Wang, X. Zhou, B. Pan, K. Tang, J. Zuo and Q. Yang, *J. Mater. Chem. A*, 2015, **3**, 499-503.

317. D. Kong, J. J. Cha, H. Wang, H. R. Lee and Y. Cui, *Energy Environ. Sci.*, 2013, **6**, 3553-3558.
318. L. Zhang, P. F. Liu, Y. H. Li, C. W. Wang, M. Y. Zu, H. Q. Fu, X. H. Yang and H. G. Yang, *ACS Catal*, 2018, **8**, 5200-5205.
319. B. Liu, Y.-F. Zhao, H.-Q. Peng, Z.-Y. Zhang, C.-K. Sit, M.-F. Yuen, T.-R. Zhang, C.-S. Lee and W.-J. Zhang, *Adv. Mater.*, 2017, **29**, 1606521.
320. Z.-S. Cai, Y. Shi, S.-S. Bao, Y. Shen, X.-H. Xia and L.-M. Zheng, *ACS Catal*, 2018, **8**, 3895-3902.
321. W. Zhu, C. Tang, D. Liu, J. Wang, A. M. Asiri and X. Sun, *J. Mater. Chem. A*, 2016, **4**, 7169-7173.
322. Z.-F. Huang, J. Song, K. Li, M. Tahir, Y.-T. Wang, L. Pan, L. Wang, X. Zhang and J.-J. Zou, *J. Am. Chem. Soc.*, 2016, **138**, 1359-1365.
323. J. Yin, Q. Fan, Y. Li, F. Cheng, P. Zhou, P. Xi and S. Sun, *J. Am. Chem. Soc.*, 2016, **138**, 14546-14549.
324. H. Tabassum, W. Guo, W. Meng, A. Mahmood, R. Zhao, Q. Wang and R. Zou, *Adv. Energy Mater.*, 2017, **7**, 1601671.
325. M. Zhuang, X. Ou, Y. Dou, L. Zhang, Q. Zhang, R. Wu, Y. Ding, M. Shao and Z. Luo, *Nano Lett.*, 2016, **16**, 4691-4698.
326. Z. Pu, I. S. Amiinu, X. Liu, M. Wang and S. Mu, *Nanoscale*, 2016, **8**, 17256-17261.
327. Y. Sun, C. Liu, D. C. Grauer, J. Yano, J. R. Long, P. Yang and C. J. Chang, *J. Am. Chem. Soc.*, 2013, **135**, 17699-17702.
328. J. Linnemann, L. Taudien, M. Klose and L. Giebeler, *J. Mater. Chem. A*, 2017, **5**, 18420-18428.
329. L.-L. Feng, G. Yu, Y. Wu, G.-D. Li, H. Li, Y. Sun, T. Asefa, W. Chen and X. Zou, *J. Am. Chem. Soc.*, 2015, **137**, 14023-14026.
330. S. Gu, H. Du, A. M. Asiri, X. Sun and C. M. Li, *PCCP*, 2014, **16**, 16909-16913.
331. J. P. Torella, C. J. Gagliardi, J. S. Chen, D. K. Bediako, B. Colón, J. C. Way, P. A. Silver and D. G. Nocera, *Proc. Natl. Acad. Sci. U.S.A.*, 2015, **112**, 2337.
332. Z. Pu, S. Wei, Z. Chen and S. Mu, *Appl. Catal. B-Environ.*, 2016, **196**, 193-198.
333. Z. Pu, I. S. Amiinu and S. Mu, *Energy Technol.*, 2016, **4**, 1030-1034.
334. H. Yu, H. Fan, J. Wang, Y. Zheng, Z. Dai, Y. Lu, J. Kong, X. Wang, Y. J. Kim, Q. Yan and J.-M. Lee, *Nanoscale*, 2017, **9**, 7260-7267.
335. P. D. Tran, M. Nguyen, S. S. Pramana, A. Bhattacharjee, S. Y. Chiam, J. Fize, M. J. Field, V. Artero, L. H. Wong, J. Loo and J. Barber, *Energy Environ. Sci.*, 2012, **5**, 8912-8916.
336. Z. Pu, I. Saana Amiinu, M. Wang, Y. Yang and S. Mu, *Nanoscale*, 2016, **8**, 8500-8504.
337. D. Mukherjee, P. M. Austeria and S. Sampath, *ACS Energy Lett.*, 2016, **1**, 367-372.
338. J.-Q. Chi, W.-K. Gao, J.-H. Lin, B. Dong, K.-L. Yan, J.-F. Qin, Z.-Z. Liu, Y.-M. Chai and C.-G. Liu, *J. Colloid Interface Sci.*, 2018, **513**, 151-160.
339. H. Zhang, Y. Li, G. Zhang, P. Wan, T. Xu, X. Wu and X. Sun, *Electrochim. Acta*, 2014, **148**, 170-174.
340. S. Gao, G.-D. Li, Y. Liu, H. Chen, L.-L. Feng, Y. Wang, M. Yang, D. Wang, S. Wang and X. Zou, *Nanoscale*, 2015, **7**, 2306-2316.
341. Z. Xing, Q. Liu, A. M. Asiri and X. Sun, *ACS Catal*, 2015, **5**, 145-149.
342. H.-W. Liang, S. Brüller, R. Dong, J. Zhang, X. Feng and K. Müllen, *Nat. Commun.*, 2015, **6**, 7992.
343. Y. Hou, B. Zhang, Z. Wen, S. Cui, X. Guo, Z. He and J. Chen, *J. Mater. Chem. A*, 2014, **2**, 13795-13800.

344. P. D. Tran, S. Y. Chiam, P. P. Boix, Y. Ren, S. S. Pramana, J. Fize, V. Artero and J. Barber, *Energy Environ. Sci.*, 2013, **6**, 2452-2459.
345. Z.-L. Wang, X.-F. Hao, Z. Jiang, X.-P. Sun, D. Xu, J. Wang, H.-X. Zhong, F.-L. Meng and X.-B. Zhang, *J. Am. Chem. Soc.*, 2015, **137**, 15070-15073.
346. H. Jin, J. Wang, D. Su, Z. Wei, Z. Pang and Y. Wang, *J. Am. Chem. Soc.*, 2015, **137**, 2688-2694.
347. L.-L. Feng, G.-D. Li, Y. Liu, Y. Wu, H. Chen, Y. Wang, Y.-C. Zou, D. Wang and X. Zou, *ACS Appl. Mater. Interfaces*, 2015, **7**, 980-988.
348. H. Du, S. Gu, R. Liu and C. M. Li, *J. Power Sources*, 2015, **278**, 540-545.
349. S. Cobo, J. Heidkamp, P.-A. Jacques, J. Fize, V. Fourmond, L. Guetaz, B. Jousselme, V. Ivanova, H. Dau, S. Palacin, M. Fontecave and V. Artero, *Nat. Mater.*, 2012, **11**, 802.
350. N. Jiang, L. Bogoev, M. Popova, S. Gul, J. Yano and Y. Sun, *J. Mater. Chem. A*, 2014, **2**, 19407-19414.
351. Y. Xue, J. Li, Z. Xue, Y. Li, H. Liu, D. Li, W. Yang and Y. Li, *ACS Appl. Mater. Interfaces*, 2016, **8**, 31083-31091.
352. X. Zou, X. Huang, A. Goswami, R. Silva, B. R. Sathe, E. Mikmeková and T. Asefa, *Angew. Chem. Int. Ed.*, 2014, **53**, 4372-4376.
353. R. Kas, R. Kortlever, A. Milbrat, M. T. M. Koper, G. Mul and J. Baltrusaitis, *PCCP*, 2014, **16**, 12194-12201.
354. D. Kim, S. Lee, J. D. Ocon, B. Jeong, J. K. Lee and J. Lee, *PCCP*, 2015, **17**, 824-830.
355. J. Yuan, J.-J. Zhang, M.-P. Yang, W.-J. Meng, H. Wang and J.-X. Lu, *Catalysts*, 2018, **8**, 171.
356. M. Fan, Z. Bai, Q. Zhang, C. Ma, X.-D. Zhou and J. Qiao, *RSC Adv.*, 2014, **4**, 44583-44591.
357. X. Zhu, K. Gupta, M. Bersani, J. A. Darr, P. R. Shearing and D. J. L. Brett, *Electrochim. Acta*, 2018, **283**, 1037-1044.
358. A. N. Grace, S. Y. Choi, M. Vinoba, M. Bhagiyalakshmi, D. H. Chu, Y. Yoon, S. C. Nam and S. K. Jeong, *Appl. Energ.*, 2014, **120**, 85-94.
359. R. A. Geioushy, M. M. Khaled, A. S. Hakeem, K. Alhooshani and C. Basheer, *J. Electroanal. Chem.*, 2017, **785**, 138-143.
360. V. S. K. Yadav and M. K. Purkait, *Journal of Science: Advanced Materials and Devices*, 2016, **1**, 330-336.
361. K. Gupta, M. Bersani and J. A. Darr, *J. Mater. Chem. A*, 2016, **4**, 13786-13794.
362. J. Albo, G. Beobide, P. Castaño and A. Irabien, *J. CO2 Util.*, 2017, **18**, 164-172.
363. H.-J. Yang, H. Yang, Y.-H. Hong, P.-Y. Zhang, T. Wang, L.-N. Chen, F.-Y. Zhang, Q.-H. Wu, N. Tian, Z.-Y. Zhou and S.-G. Sun, *ChemSusChem*, 2018, **11**, 881-887.
364. L. M. Aeshala, R. G. Uppaluri and A. Verma, *J. CO2 Util.*, 2013, **3-4**, 49-55.
365. A. T. Garcia-Esparza, K. Limkrailassiri, F. Leroy, S. Rasul, W. Yu, L. Lin and K. Takanabe, *J. Mater. Chem. A*, 2014, **2**, 7389-7401.
366. J. Albo, A. Sáez, J. Solla-Gullón, V. Montiel and A. Irabien, *Appl. Catal. B-Environ.*, 2015, **176-177**, 709-717.
367. M. Le, M. Ren, Z. Zhang, P. T. Sprunger, R. L. Kurtz and J. C. Flake, *J. Electrochem. Soc.*, 2011, **158**, E45-E49.
368. M. Irfan Malik, Z. O. Malaibari, M. Atieh and B. Abussaud, *Chem. Eng. Sci.*, 2016, **152**, 468-477.
369. S. Guo, S. Zhao, J. Gao, C. Zhu, X. Wu, Y. Fu, H. Huang, Y. Liu and Z. Kang, *Nanoscale*, 2017, **9**, 298-304.
370. Y. Zhao, C. Wang and G. G. Wallace, *J. Mater. Chem. A*, 2016, **4**, 10710-10718.

371. Y. Huang, A. D. Handoko, P. Hirunsit and B. S. Yeo, *ACS Catal*, 2017, **7**, 1749-1756.
372. F.-S. Ke, X.-C. Liu, J. Wu, P. P. Sharma, Z.-Y. Zhou, J. Qiao and X.-D. Zhou, *Catal. Today*, 2017, **288**, 18-23.
373. Y. Pang, T. Burdyny, C.-T. Dinh, M. G. Kibria, J. Z. Fan, M. Liu, E. H. Sargent and D. Sinton, *Green Chem.*, 2017, **19**, 4023-4030.
374. D. Ren, N. W. X. Loo, L. Gong and B. S. Yeo, *ACS Sustainable Chem. Eng.*, 2017, **5**, 9191-9199.
375. A. D. Handoko, K. W. Chan and B. S. Yeo, *ACS Energy Lett.*, 2017, **2**, 2103-2109.
376. Y. Lum, B. Yue, P. Lobaccaro, A. T. Bell and J. W. Ager, *J. Phys. Chem. C*, 2017, **121**, 14191-14203.
377. E. Bertheussen, A. Verdaguer-Casadevall, D. Ravasio, J. H. Montoya, D. B. Trimarco, C. Roy, S. Meier, J. Wendland, J. K. Nørskov, I. E. L. Stephens and I. Chorkendorff, *Angew. Chem. Int. Ed.*, 2016, **55**, 1450-1454.
378. Y. Deng, Y. Huang, D. Ren, A. D. Handoko, Z. W. Seh, P. Hirunsit and B. S. Yeo, *ACS Appl. Mater. Interfaces*, 2018, **10**, 28572-28581.
379. H. Yano, T. Tanaka, M. Nakayama and K. Ogura, *J. Electroanal. Chem.*, 2004, **565**, 287-293.
380. B. A. Rosen, A. Salehi-Khojin, M. R. Thorson, W. Zhu, D. T. Whipple, P. J. A. Kenis and R. I. Masel, *Science*, 2011, **334**, 643-644.
381. A. J. Martín, G. O. Larrazábal and J. Pérez-Ramírez, *Green Chem.*, 2015, **17**, 5114-5130.
382. F. Safizadeh, E. Ghali and G. Houlachi, *Int. J. Hydrogen Energy*, 2015, **40**, 256-274.
383. E. Gileadi, *Electrode Kinetics for Chemists, Engineers, and Materials Scientists*, John Wiley and Sons, Weinheim, Germany 1993.
384. Y. Hori, in *Modern Aspects of Electrochemistry*, eds. C. G. Vayenas, R. E. White and M. E. Gamboa-Aldeco, Springer New York, New York, NY, 2008, pp. 89-189.
385. F. R. Keene, in *Electrochemical and Electrocatalytic Reactions of Carbon Dioxide*, ed. B. P. Sullivan, Elsevier, Amsterdam, 1993, pp. 1-18.
386. O. Pedersen, T. Colmer and K. Sand-Jensen, *Frontiers in Plant Science*, 2013, **4**.
387. J. Wu, Y. Huang, W. Ye and Y. Li, *Adv. Sci.*, 2017, **4**, 1700194.
388. D. Hursán and C. Janáky, *ACS Energy Lett.*, 2018, **3**, 722-723.
389. S. A. Francis, J. M. Velazquez, I. M. Ferrer, D. A. Torelli, D. Guevarra, M. T. McDowell, K. Sun, X. Zhou, F. H. Saadi, J. John, M. H. Richter, F. P. Hyler, K. M. Papadantonakis, B. S. Brunschwig and N. S. Lewis, *Chem. Mater.*, 2018, **30**, 4902-4908.
390. E. R. Cave, J. H. Montoya, K. P. Kuhl, D. N. Abram, T. Hatsukade, C. Shi, C. Hahn, J. K. Nørskov and T. F. Jaramillo, *PCCP*, 2017, **19**, 15856-15863.